UNIVERSIDAD DE CANTABRIA
Departamento de Física Moderna
y
CSIC-UC
Instituto de Física de Cantabria

Dinámica de polarización y modos transversales de VCSELs sometidos a inyección óptica

Ana Quirce Teja

Tesis Doctoral

2012

UNIVERSIDAD DE CANTABRIA
Departamento de Física Moderna
y
CSIC-UC
Instituto de Física de Cantabria

Dinámica de polarización y modos transversales de VCSELs sometidos a inyección óptica

Memoria presentada por la Licenciada

Ana Quirce Teja

para optar al grado de Doctor

Realizada bajo la supervisión del

Dr. **Ángel Valle Gutiérrez**

Santander, 2012

Dr. Ángel Valle Gutiérrez, Profesor titular de la Universidad de Cantabria, certifica:

Que la presente Memoria, titulada **"Dinámica de polarización y modos transversales de VCSELs sometidos a inyección óptica"**, ha sido realizada, bajo su dirección, por Ana Quirce Teja, y constituye su Tesis para optar al grado de Doctor por la Universidad de Cantabria. Asimismo emite su conformidad para que dicha memoria sea presentada y tenga lugar, posteriormente, la correspondiente lectura.

Santander, a 3 de Octubre de 2012

Fdo.: Dr. Ángel Valle Gutiérrez

A mi familia.

Agradecimientos

Quisiera expresar en unas pocas líneas mi más sincero y sentido agradecimiento a todas aquellas personas que de un modo u otro, antes y/o durante, directa o indirectamente han contribuido a este trabajo.

En primer lugar quiero dar las gracias profundamente a mi director de Tesis, Ángel Valle, porque él, es el verdadero culpable de que hoy esté escrita esta Tesis, sin su confianza, nada de ésto hubiera sido posible. Gracias por guiarme y adentrarme en el mundo de los VCSELs, por tus sabios consejos y por la ayuda brindada en todo momento.

También quiero expresar mi agradecimiento a Luis Pesquera, por su apoyo y fructíferas conversaciones de una ayuda inestimable. A ambos, gracias.

Gracias también al grupo de Física Estadística y No Lineal del Instituto de Física de Cantabria y en especial a los que estuvieron o todavía están en el despacho 114, Clara, Diego, Jorge, Marta, Pablo, Sarah y Silvia, por los buenos momentos compartidos juntos, por brindarme su ayuda y consejos siempre que han sido necesarios y por hacerme sentir tan a gusto en su compañía. Gracias.

Muchas gracias también a la profesora Maria Susana Torre del Instituto de Física "Arroyo Seco", Facultad de Ciencias Exactas, Universidad Nacional del Centro de la Provincia de Buenos Aires

(UNCPBA), por sus aportaciones teóricas, de gran ayuda para comprender y entender mejor nuestros experimentos. Gracias.

Of course, along these four intensive years of Ph.D., I have been very lucky for having the opportunity of travelling and visiting other universities whom I can not forget to thank for your welcome and fruitful collaborations. Chronologically beginning, firstly I want to thank to the people of the University of Essex (UK), Prof. Michael J. Adams, Prof. Ian Henning and especially Dr. Antonio Hurtado for their hospitality and the effort spent together in the laboratory. Also the students I had the chance to meet especially to Kevin, for their great help both professionally and personally from the outset, for his company at lunch and for all the good times shared in Colchester and its surroundings; and of course, thanks to Nadir for their immense kindness and intensity night laboratory work in order to let me work in the laboratory the maximum time. To everybody, thanks.

I want to thank the people of Bates College (USA) too, especially Prof. Hong Lin and her family, for their warm welcome and kindness and for giving me the opportunity to learn and work alongside. Thanks also to their students David, Yu and Ross, because with them I learnt in the laboratory, and in general, thanks to all the people of the Department of Physics and Astronomy that I had the fortune to meet, because everyone made my stay very enjoyable.

Agradecer también a toda la gente que conocí en el Departamento de Tecnología Fotónica y Bioingeniería de la E.T.S. de Ingenieros de Telecomunicación de la Universidad Politécnica de Madrid. Agradecer especialmente al Prof. Ignacio Esquivias su oportunidad para trabajar en su grupo y su excelente acogida, también a los profesores Santiago Aguilera y Jose Manuel García Tijero. Muchas gracias también al Dr. Antonio, por su amabilidad y ayuda, por el trabajo realizado juntos en el laboratorio y por las conversaciones y buenos ratos compartidos. Valerio, Pawel y Borja

por las agradables charlas mantenidas y en general y junto a los mencionados anteriormente al resto de profesores y estudiantes con los que he compartido cada día agradables comidas. A todos, gracias.

Por supuesto a mi familia y especialmente a mis padres, porque son ellos quienes más se merecen esta Tesis y porque también han sido decisivos para la realización de este trabajo. No tengo palabras que expresen mi inmenso agradecimiento a ambos y siempre me sentiré en deuda con ellos. Gracias por todo lo que me habéis dado, vuestra ayuda, vuestro apoyo y por estar siempre ahí. También a mis hermanos Javier y Alejandro, por soportar en la andadura de mi Tesis, mi mal humor en innumerables ocasiones, por su admiración e inmenso cariño y por las risas que siempre compartimos. Gracias a todos.

Con la misma intensidad quiero agradecer a Jose, que en todos los años que llevamos juntos, nunca ha dejado de confiar en mi, por su cariño, por su paciencia infinita, por su apoyo, por su ayuda y por un sin fin de cosas que lo convierten en uno de los motores fundamentales de mi vida y como no, por el trabajo realizado codo con codo en esta Tesis, porque parte de este trabajo, es también suyo. Gracias.

No pueden faltar tampoco mis amigos, siempre presentes de un modo u otro, a todos os doy las gracias y en especial a quienes por cercanía a mi área, habéis vivido más de cerca estos cuatro años de Tesis doctoral: A las físicas de la UC: Clara, Lara y Montse, porque nuestra amistad se remonta a los inicios de la carrera de Física y desde entonces, hemos vivido y compartido muy buenos y divertidos momentos. Momentos que seguro, seguiremos compartiendo aunque sea en la distancia. A Rocío y Carmen por los buenos ratos compartidos dentro y fuera de la facultad. A Carolina, porque ella ha puesto directamente su granito de arena en esta Tesis trabajando juntas en el laboratorio. A los amigos que tuve la suerte de conocer en el máster especialmente a: Irene con quien tengo un montón de cosas en común, por compartir

nuestros agobios y mejor aún, nuestras alegrías, paseos, charlas...y Diego, gracias por todos los buenos y divertidos momentos que disfruto en tu compañía, por todas nuestras charletas variopintas y por supuesto, también por acercarme un poquito Italia. A Sebastian, por haberme hecho disfrutar de la docencia, por su valentía para leer mi Tesis o al menos, intentarlo y por las divertidas e interesantes charlas que mantenemos vía e-mail. *Vielen Dank*. No pueden faltar aquí Soraya y Vero, Soraya porque sus palabras siempre me reconfortan y Vero, por los "veintimuchos" años de amistad que compartimos. A todos, gracias.

Dynamics of the polarization and transverse modes of VCSELs subject to optical injection

A dissertation submitted in partial fulfillment of the requirements for the degree of

Philosophy Doctor

by

Ana Quirce Teja

UNIVERSIDAD DE CANTABRIA
Departamento de Física Moderna
&
CSIC-UC
Instituto de Física de Cantabria

2012

"Persistence is the virtue by which all other virtues bear fruit"

Arturo Graf

CONTENTS

Motivations and Outline

The theoretical foundations of the laser were suggested by Albert Einstein at the beginning of the last century proving Planck's law of radiation. Einstein proposed, besides the absorption caused by interaction of an electron with the existing optical radiation, the existence of two different processes for light emission: the spontaneous emission of photons (which was already known) and the stimulated emission.

Coherent sources of electromagnetic radiation were first generated at radio frequencies in the late 1800s. By the mid-20th century, coherent frequencies had increased to the microwave region near 10^9 Hz with applications to Radar during the war years and later in support of commercial aviation. The precursor to the laser was the MASER ("Molecular Amplification by Stimulated Emission of Radiation"). Gordon, Zeiger and Townes at Columbia University demonstrated the amplification of microwaves using energy stored in molecules. The demonstration of the MASER led to a converted effort to extend stimulated emission to optical frequencies.

It was until 1960 that Theodore H. Maiman achieved to generate red laser radiation from stimulated emission of a rod of synthetic ruby crystal. The development of laser technology had begun. In a single step, the frequency range was extended by five orders of magnitude to the visible spectral range.

For modern optical communications, however, significant progress was not made possible until the invention of semiconductor lasers in 1962 and the demonstration of heterostructures. However, the use of the semiconductor lasers became practical only after 1970, when these devices operating continuously at room temperature became available. Since then, semiconductor lasers have been developed extensively.

The first nanodevice was a quantum-well laser, this device was possible due to major advances in epitaxy technologies in the late 1970s, with the inventions of molecular beam epitaxy (MBE) and metalorganic chemical vapor deposition (MOCVD).

Once 1300- and 1500-nm wavelengths were identified as desirable regimes for long-distance fiber transmission, significant research focused on developing materials and devices operating at these wavelength regimes. Single wavelength lasers were recognized to be critical for long-distance transmission in fiber. Distributed feedback (DFB) or distributed Bragg reflector (DBR) structures were introduced to control the emission spectra of the diode lasers.

Vertical cavity surface emitting lasers (VCSELs) were realized because it became possible to grow very complex structures that required hundreds of layers of deposition by MBE or MOCVD [Willner 2012]. VCSELs have great potential to be applied in applications such as all-optical signal processing, optical switching, and optical storage [Kawaguchi 1997], [Kawaguchi 1994], [Koyama 2006] due to their characteristics like single-longitudinal mode operation, high coupling efficiency to optical fibers due to their circular aperture that together with the cylindrical symmetric of the resonant cavity support a low divergence and a circular

beam profile. For this reason, the efficiency coupling of the emitted light into a fiber is higher than in EELs (Edge Emitting Lasers).

Besides, their reduce volume assures VCSELS have lower threshold currents, higher power conversion efficiency and higher modulation bandwidth than EELs. Furthermore, because VCSELs emit light perpendicular to the substrate, they can be tested on the wafer. They can be fabricated in large two-dimensional arrays easily reducing manufacturing costs. [Koyama 2006]. Also, short-wavelength (850 nm) VCSELs are used as low cost sources in single-mode fiber metropolitan area [Koyama 2006], [Chang 2003], [Chrostowski 2006]. In addition, high modulation speed and low production cost allow VCSELs to be applied in high-volume data communication applications such as gigabit Ethernet, 10-Gbit Ethernet, and the fiber channel [Yu 2003]. These advantages make the VCSELs ideal candidates for use as stable sources in present and future optical telecommunication network.

Although VCSELs are intrinsically single-longitudinal mode devices, they usually show complex polarization characteristics [Changhasnain 1991], [Sanmiguel 1995], [Choquette 1995], [Valle 1996], [MartinRegalado 1997], [Ryvkin 1999] and multi-transverse mode dynamics [Changhasnain 1991], [Vakhshoori 1993], [Valle 1995], [Buccafusca 1996], [Mulet 2002], [Zhang 2004]. The light emitted by a VCSEL is commonly linearly polarized along one of two orthogonal directions, and polarization switching (PS) between the two linearly polarized modes is often observed when the injection current or temperature is varied. Understanding and controlling the VCSEL polarization is crucial for their use in polarization-sensitive applications.

The study of optical injection effects in VCSELs is interesting because in contrast with EELs, the intrinsic polarization degree of freedom plays a key role in the dynamical response of the device under optical injection. Optical injection consists of injecting light from a laser into another laser. External injection of light in a laser

diode is a technique that is commonly employed to achieve optical bistability. This has attracted attention due to its potential applications in all-optical signal processing, optical switching, and optical storage [Kawaguchi 1994].

Polarization switching and polarization bistability (PB) in VCSELs subject to optical injection have undergone considerable research effort in the last years [Pan 1993], [Hong 2000], [Gatare 2006a], [Gatare 2007a]. Recently, attention has been focused on the analysis of PS and PB in long-wavelength VCSELs emitting in the region of 1550nm [Jeong 2008], [Hurtado 2008b], [Valle 2008], [Hurtado 2009b], [Hurtado 2009c], [Marki 2008], [Katayama 2008a] and different practical applications, including logic gates [Marki 2008], flip-flop operation [Katayama 2008a] and a buffer memory [Katayama 2008b] have been reported. Wide hysteresis cycles could enhance the potential practical use of these devices in the aforementioned applications whose operation principle is based in the width of the appearing hysteresis cycles associated to the bistability, for use in optical signal processing and optical switching applications in present and future optical telecommunication networks. All-optical processing of high-speed signals is expected to be a key technology in future photonic networks.

Optical injection in semiconductor lasers has been shown to lead to a wealth of complex dynamics and bifurcations, such as period-one state, period doubling, quasiperiodicity, chaos and injection locking [Wieczorek 2005]. Nonlinear dynamics of optically injected semiconductor lasers is interesting from a practical point of view because the period-one oscillation state is one of the potential candidates for carrying message in a radio-over-fiber (RoF) system [Chan 2006] that holds great promise for 4G mobile communications systems [Qi 2011a]. Then, nonlinear dynamics of optically injected semiconductor lasers can also be used for photonic microwave generation. Compared with conventional microwave generation by electronic circuitry with multiple stages of frequency doubling, photonic microwave signal generation

have advantages of lower cost, longer transmission distance, higher speed, low power consumption, less system complexity and the ability to generate tunable microwave signals with higher frequencies. Characterization of the maximum frequency achievable in a photonic microwave system is of interest because it sets the bandwidth limit of the system [Qi 2011a].

In summary, the main aim of this thesis is the study of how external optical injection affects light emitted by Vertical-Cavity Surface-Emitting Lasers (VCSELs). We analyze the nonlinear dynamics and the properties of polarization and transverse modes of a VCSEL subject to optical injection. This thesis is mainly experimental although we have made some theoretical work to understand and compare with the experimental results. We have worked mostly with 1550 nm-single-mode and multimode VCSELs. Typically, we have used an all-fiber setup although some experimental results using 850-nm VCSELs working in free space are also reported.

The present thesis is organized as follows. In chapter 1, we present the basic concepts for semiconductor lasers and we describe the more relevant characteristics of the EELs and VCSELs.

In chapter 2, the basic principles of the semiconductor laser dynamics are described. We present a simple model based on the rate equation approach for semiconductor lasers. We study the steady state solutions and we perform a small signal analysis of the rate equations. The concept of relative intensity noise and its calculation using small signal analysis are described.

In chapter 3, we describe the emission properties of VCSELs. We present the light-current characteristics and besides, we describe the thermal behavior and polarization properties of VCSELs. It is known that VCSELs can emit in several transverse modes, this phenomenon being attributed to Spatial Hole Burning which is explained briefly. We describe the Spin Flip Model, that is a model commonly used to explain the polarization behavior of VCSELs, and in particular the polarization switching found in these

devices. The main aim in this work is study the effects of the optical injection in VCSELs, so we describe the previous work on optical injection in semiconductor lasers, and in particular in VCSELs with an special phocus on the phenomenon of polarization switching associated with the optical injection.

In chapter 4, we describe our measurement equipment and present their most relevant characteristics.

In chapter 5, we study experimentally the relative intensity noise for different free-running multimode vertical-cavity surface-emitting lasers. We have considered VCSELs emitting in two and three transverse modes. For VCSELs emitting in two parallel polarized transverse modes, two resonance peaks appear in the noise spectra of the individual modes and total power of the VCSEL. RIN spectra of multimode VCSELs depend on the applied bias current in a similar way to that previously found in theory. For VCSELs emitting in three transverse modes with different polarizations we have found that the VCSEL polarization plays an important role in determining the multi-peaked structure of noise spectra.

In chapter 6, we study theoretically and experimentally the bistability properties of the polarization switching in a 1550-nm single-mode VCSEL subject to orthogonal optical injection. First, we study bistability as a function of the frequency detuning between the injected light and the orthogonal linear polarization of the VCSEL. We have found three different bistable regions. We study the widths of bistable regions as a function of the injected power and we find that the width of one of the three regions is more than seven times larger than previously reported results. Second, we study the bistability properties of the polarization switching as a function of the injected optical power. We have found three different shapes of polarization bistability, anticlockwise, clockwise and X-shape bistability. A good overall qualitative agreement is found between the theoretical and experimental results.

In chapter 7, we analyze the nonlinear dynamics appearing in

a 1550-nm single mode VCSEL subject to parallel and orthogonal optical injection. For both types of injection, we measure stability maps identifying the boundaries between regions of different nonlinear dynamics. For orthogonal optical injection we measure simultaneously time traces of the output of both linear polarizations of the VCSEL. We study the output signal for different values of the bias current, injected power and different detunings (the difference between the frequency of the master laser and the frequency of the orthogonal polarization of the VCSEL). Using these simultaneous traces, we analyze the correlation properties between both linear polarizations. For positive frequency detunings we usually find that the orthogonal polarization is the only polarization that contributes to the dynamics of the total power. We only find correlated dynamics in both linear polarizations for large values of the bias current and for small values of the optical injection strength near the border of the periodic region. For negative frequency detunings we find anticorrelated dynamics, characterized by broadened power spectra which is related to large values of the dispersion of the time between pulses. A good overall qualitative agreement is found between theory and experiments.

In chapter 8, we study the dynamics characteristics of an all-optical inverter based on polarization switching in long-wavelength VCSELs. All optical processing of high-speed signals is expected to be a key technology in future photonic networks. Using polarization switching (PS) of a 1550-nm single mode VCSEL we demonstrate an all-optical inverter. For different pulsed optical inputs we analyze the dynamic behavior of the all-optical inverter. We consider low and high-frequency pulsed optical injection, identifying proper operation conditions for all-optical inversion. The PS based on all-optical inverter is demonstrated with a 2.5 Gb/s non- return-to-zero (NRZ) input signal.

In chapter 9, modal selection induced by parallel polarized optical injection is studied experimentally in a VCSEL with emission

in two transverse modes that are linearly polarized in a direction referred as parallel. The selection of the fundamental transverse mode can be achieved when the two transverse modes have parallel polarizations. The selection of the fundamental mode is accompanied by locking of that mode to the optically injected signal for large enough values of the detuning. We also find bistability for this process when the wavelength of the optical injection increases beyond a minimum value.

In chapter 10, due to the interest for all-optical signal processing and optical switching/routing applications in long-haul optical networks applications where 1550 nm technology is dominant, we have analyzed experimentally the optical power polarization bistability induced in a long-wavelength multi-transverse mode VCSEL under orthogonal optical injection. Bistability with very wide hysteresis cycles is measured for the fundamental and the high-order transverse mode of the device. The shape of the associated hysteresis cycle is different for each of the two transverse modes. The high-order transverse mode has a squared shape for the input/output characteristic which is of particular interest for obtaining good quality all-optical inversion and all-optical regeneration.

In chapter 11, we have studied the effect of orthogonal optical injection on a short-wavelength multi-transverse mode VCSEL. The injected beam comes from a similar VCSEL. Both of them work around 850 nm wavelength. In contrast to the previously described experimental work free-space beams are used in the experimental setup. We show that when the receptor emits in several strong transverse modes with parallel polarization, optical injection can induce polarization switching in all of them while only one mode is locked to the external frequency. The induced switching can occur for a few microwatts of the injected beam. Periodic oscillations and low-frequency irregular pulsations are observed as well.

In chapter 12, we study the effects of injecting light from of a

short-wavelength multi-transverse mode VCSEL, on a similar multimode device. We also term this injection scheme as "two-frequency optical injection" because the master VCSEL emits in two transverse modes. We find polarization switching with and without frequency locking for relative small detunings. Besides polarization switching, we demonstrate two types of instabilities. All of them are mapped in the plane of frequency detuning versus injected power.

In chapter 13, we report theoretically a new method of photonic generation of microwave signals using a multi-transverse mode VCSEL subject to two-frequency optical injection. We show that double injection locking involving two transverse modes can be obtained in these systems. Comparison with a similar single transverse mode VCSEL subject to similar two- frequency optical injection shows that multi-transverse mode operation of the VCSEL enhances the performance of the photonics microwave generation system. Broad tuning ranges extended into the THz band, and narrow linewidths are demonstrated in our system. We show that the maximum frequency of the generated microwave signals can be substantially increased if multimode VCSELs are used instead of single-mode VCSELs.

In chapter 14, we present a summary with the main conclusions of this thesis.

CHAPTER 1

Introduction to Semiconductor Lasers: basic concepts

Due to their low cost, small size, high reliability and facility to be driven using conventional low voltage power supplies, semiconductor lasers have become a broadly used coherent light source in nowadays life. In telecommunications they send signals for thousands of kilometers along optical fibers. In consumer electronics, they are used to read/write data on compact disks, CD-ROMs and DVDs. These lasers find applications in laser printers, laser pointers, optical sensing and so on because they can work in a wide wavelength range: from the visible to the infrared region. In this chapter, we present the basic physical concepts of the semiconductor lasers together with a short description about Edge Emitting Lasers (EEL) and Vertical Cavity Surface Emitting Lasers (VCSELs). We highlight the advantages of VCSELs.

1.1. Basic Concepts

The laser is a coherent optical oscillator, this means that it generates a coherent signal through resonant oscillation without an input signal. Therefore, no external optical field is injected into the optical cavity for laser oscillation. The amplifier in a laser is the pumped active medium. The active medium may be a collection of atoms, molecules, or ions in the solid, liquid or gaseous form. Gain saturation is a basic property of laser amplifiers. Feedback is obtained by placing the active medium in an optical resonator, which reflects the light back and forth between two high-reflectivity mirrors separated a suitable distance. The mirrors may be planar or spherical and may either be in the form of discrete components located outside the gain medium or be attached to the ends of the gain medium. Usually, one of the mirrors is almost 100% reflecting, so that a small fraction of optical energy comes out of the resonator. Frequency selection is achieved by the resonant amplifier and by the resonator, which admits only certain modes.

Semiconductor lasers are based on p-n junctions of semiconductor materials. The p-type region has an abundance of holes (majority carriers) and few mobile electrons (minority carriers), the n-type region has an abundance of mobile electrons and few holes. In the case of n-type semiconductor, the excess electrons occupy the conduction-band states, normally empty in undoped (intrinsic) semiconductors. The Fermi level, lying in the middle of the bandgap for intrinsic semiconductors, moves toward the conduction band as the dopant concentration increases. It means, that in a heavily doped n-type semiconductor, the Fermi level E_{fc} lies inside the conduction band; such semiconductors are said to be degenerated. Similarly, the Fermi level E_{fv} moves toward the valence band for p-type semiconductors. Under heavy doping the Fermi level E_{fv} lies inside the valence band. The charge impurities left behind generate an electric field that is strong enough to prevent further diffusion of electrons and holes in

equilibrium conditions [Agrawal 2002].

When a p-n junction is forward biased by applying an external voltage, the electric field generated is reduced, this reduction results in diffusion of electrons and holes across the junction. A basic double heterostructure can be either P-p-N or P-n-N. For instance, in Figure 1.1 we show a schematic representation of the energy level diagram of a double P-p-N heterostructure semiconductor laser which consists of two heterojunctions. Electrons injected from the n-region can not be diffused beyond the barrier at the P-p junction. Similarly, holes injected from the p-region are not permitted to diffuse beyond the energy barrier at the p-N junction. In this way, all of the excess carriers created by current injection are injected into the narrow-gap active layer (also named depletion width. In this layer light is generated inside it as a result of electron-hole recombination) and are confined within this layer by the energy barriers of the heterojunctions on both sides of the active layer. These electrons and holes can recombine through spontaneous or stimulated emission and generate light in a semiconductor optical source. At the same time, this heterostructure provides lateral confinement of the electric field due to the higher refractive index in the central region. Such junctions are called heterojunctions, and such devices are called double heterostructures [Agrawal 2002].

The use of a heterostructure geometry for semiconductor optical source is doubly beneficial. As already mentioned, the bandgap difference between the two semiconductors helps to confine electrons and holes to the middle layer (active layer). Moreover, the active layer also has a slightly larger refractive index than those of the surrounding p-type and n-type cladding layers because its bandgap is smaller. As a result of the refractive-index difference, the active layer acts as a dielectric waveguide and supports optical modes whose number can be controlled by changing the active-layer thickness [Agrawal 2002].

When the layer between the junctions of a double heteros-

tructure is thin enough, the structure becomes a quantum well (QW) because of the quantum size effect in the thin layer. Because of the many advantages of quantum wells, many semiconductor lasers are quantum-well lasers having a single quantum well or multiple quantum wells. [Liu 2005]

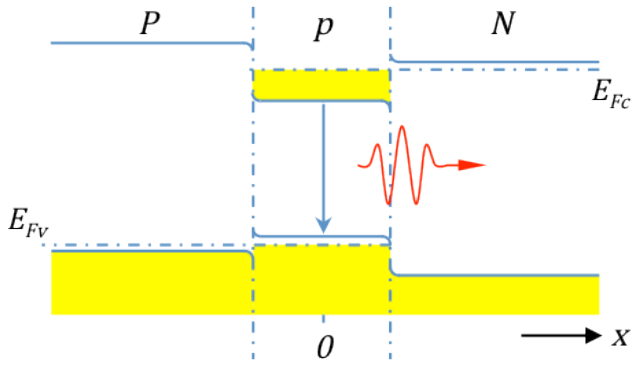

Fig. 1.1. Schematic representation of the energy level diagram of a P-p-N double heterostructure semiconductor laser under forward bias (V>0). E_c, E_{Fc}, E_{Fv}, are the Fermi energy levels.

In terms of structure, a quantum well is just a very thin double heterostructure. As the active layer of a semiconductor double heterostructure gets thinner than about 50 nm, the effect of quantum confinement for the electrons and holes in the thin active layer starts to appear in the direction perpendicular to the junction plane. This effect leads to quantization of momentum in the perpendicular direction, resulting in discrete energy levels associated with the motion of electrons and holes in this direction. In the horizontal dimensions, electrons and holes remain free and form energy bands. As a result, both conduction and valence bands are split into a number of subbands corresponding to the quantized levels.

The selection rules for optical transitions of electrons between quantized conduction subbands and quantized valence subbands establish that only are allowed transitions between a conduction subband and a valence subband with the same

quantum level.

The thickness of a typical quantum well is in the range of 5-10 nm though quantum wells as thin as 2 nm are used in some devices. To increase the total thickness of the active region for a larger gain volume while keeping the benefits of a quantum well, multiple quantum wells can be stacked together to make a multiquantum-well device. Compared to a conventional double heterostructure, a quantum well has very poor optical waveguiding ability because of its small thickness. Using multiple quantum wells helps to improve optical waveguiding [Liu 2005].

In the active region, both radiative and nonradiative electron-hole recombination process are possible. The nonradiative recombination is defined as the sum of all mechanisms removing carriers that in other situation have contributed to gain. There are two main mechanisms: Shockley-Read-Hall (SHR) recombination and Auger recombination.

The first one occurs when a defect or impurity located within the bandgap serves to trap an electron (hole) from the conduction (valence) band, before releasing it to the valence (conduction) band. The second one appears when an electron-hole recombination is transferred to an electron already in the conduction band. The excited electron relaxes down to its initial level by transferring its extra energy to the lattice with the help of phonons [Jungo 2003].

In a radiative electron-hole recombination process, a photon is generated when an electron from the conduction band relaxes and recombines with a hole in the valence band. The radiative recombination occurs through spontaneous as well as stimulated emission.

Spontaneous emission, Fig. 1.2. (a), corresponds to the process in which an electron from the conduction band relaxes and recombines with a hole in the valence band emitting a photon. The photon energy is added to the energy of the electromagnetic

field but these photons are emitted in all directions with uncorrelated phase and polarization, though their frequencies correspond to the separation between the two energy levels, making incoherent radiation. The spontaneous emission adds noise to an optical signal.

On the other hand, in the stimulated emission (see Fig. 1.2. (b)) a photon may stimulate an electron-hole recombination but the photon emitted by stimulated emission has the same frequency, phase, polarization and propagation direction as the optical radiation that induces the process. In this case, the stimulated emission results in the amplification of an optical signal.

Absorption, like stimulated emission of photons, is associated with induced transitions between the energy levels caused by interaction of an electron with the existing optical radiation. If an electron is initially in the lower level it can absorb a photon to make a transition to the upper level, as we can see in Fig. 1.2(c).

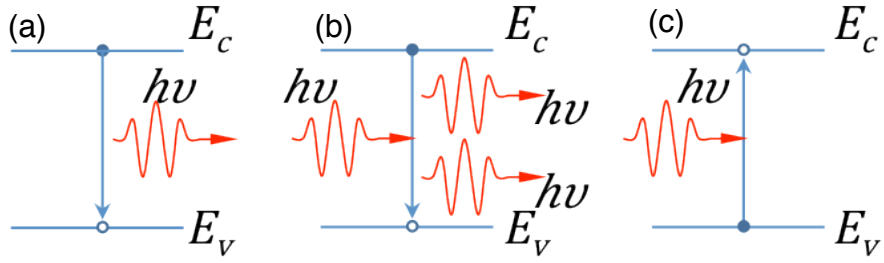

Fig.1.2. Band-to-band transitions (a) spontaneous emission of photons, (b) stimulated emission, and (c) absorption.

The principle underlying the operation of a semiconductor laser is the creation of a population inversion that provides stimulated emission more prevalent than absorption for the presence of an optical gain. For semiconductor lasers this condition is realized when the Fermi-level separation exceeds the bandgap and the photon energy at the frequency ν: $\Delta E_F = E_{Fc} - E_{Fv} > h\nu > E_g$, where E_g is the Energy band-gap of the active layer,

under forward biasing of the p-n junction. When the injected carrier density in the active layer exceeds a certain value, known as the transparency value, population inversion is realized and the active region exhibits optical gain. In the normal state of any system in thermal equilibrium, a low-energy state is always more populated than a high-energy state, hence there is no population inversion. Population inversion in a system can only be accomplished trough a process called pumping by actively exciting the atoms from a low-energy state to a high-energy state. If the system is not pumped the atoms will relax to thermal equilibrium. Therefore, population inversion is a non-equilibrium state that cannot be sustained without active pumping. To maintain a constant optical gain, continuous pumping is required to keep the population inversion at a constant level. When the population inversion is achieved, the system has a positive optical gain [Liu 2005], [Agrawal 2002].

However, the optical gain alone is not enough to operate a laser, it is necessary a mechanism to induce positive feedback. Perpendicular to the junction plane, polished facets, as we mentioned before, support the optical feedback forming a Fabry-Perot cavity. This configuration selects a favored direction for stimulated emission and also, it introduces a frequency-selective mechanism which defines the longitudinal cavity modes.

Standing waves in a Fabry-Perot cavity are only possible for a discrete number of frequencies that define the longitudinal cavity modes. The longitudinal mode frequency spacing is given by:

$$\Delta \upsilon_L = \frac{c}{2 n_g L} \tag{1.1}$$

where c the speed of the light in vacuum, n_g the group refractive index and L the cavity length.

To satisfy the lasing operation, we need that the gain overcome optical losses. The threshold gain can be derived from the unity round-trip condition, a situation in which there is a

balance between gain and losses. The condition writes:

$$G_{th} = \frac{1}{\Gamma}\left[\alpha_{abs} - \frac{\ln\left(R_1 R_2\right)}{2L}\right] \tag{1.2}$$

where Γ represents the confinement factor, α_{abs} are the optical losses, and R_1 and R_2 are the edge facet reflectivities of the mirrors of the resonator. The threshold gain provides the threshold bias current which depends strongly on the cavity layer thickness. The threshold current is the current above which lasing emission is obtained.

Depending on the geometry of the emission of light with respect to the cavity, semiconductor lasers can be classified into edge-emitting lasers (EELs) and vertical-cavity surface-emitting lasers (VCSELs).

1.2. Edge-Emitting Semiconductor Lasers (EELs)

Edge-emitting lasers are characterized by a light beam direction that is parallel to the plane of the active region. Most edge-emitting lasers are stripe-geometry lasers. The cavity of an edge-emitting laser is normally a horizontal cavity with a longitudinal axis defined by a gain-guiding or index-guiding stripe.

The Edge-Emitting Semiconductor Laser emits light from the edge of the junction region (see Fig. 1.3). The junction structure of a device determines the carrier and optical field distributions in the vertical direction perpendicular to the junction plane of a device. The carrier and optical field distributions in the transverse direction parallel to the junction plane are determined by the lateral structure [Liu 2005].

In an EEL, the light propagates in a rectangular waveguide whose longitudinal extent coincides with the active layer.

The most common types of EELs are the Fabry-Perot laser, the distributed Bragg reflector laser (DBR laser), and the distributed

feedback laser (DFB laser). In a Fabry-Perot laser the mirrors are formed by cleaving the semiconductor wafer along the crystal planes to form smooth facets. The light propagates along the resonant cavity stimulating excited electrons to decay to their ground state emitting photons that are added in a coherent way. This gain mechanism occurs along the cavity whose typical length in a Fabry-Perot laser is of the order of L~300 μm. The longitudinal mode frequency spacing, $\Delta\nu_L$, is around 100 GHz so as a consequence, a large number of longitudinal modes can participate in the laser action and hence this laser is characterized by a longitudinal multimode emission. Its long cavity gives enough single pass gain to sustain lasing action without the necessity of additional higher reflectivity mirrors. The facet reflectivities are approximately 30%.

Almost all edge-emitting semiconductor lasers have narrow stripes to ensure single-transverse-mode emission. Moreover , the strongly asymmetric geometrical structure of EELs implies that they emit a linearly polarized light. Due to the rectangular geometry of the active layer at the laser edge the shape of the beam is elliptical and highly divergent, as a consequence the coupling of the light directly from the EEL into the circular core of an optical fiber is not very efficient. These characteristics together with the multimode emission are several deficiencies of these devices.

To overcome the multi-mode emission problem, semiconductor structures have been developed such as distributed feedback lasers (DFB) and distributed Bragg reflectors (DBR) lasers between others. For instance, DFB lasers are built-in gratings for optical feedback in the light propagating direction in such a way that the oscillation wavelength is perfectly defined. Another way to select the wavelength of operation is incorporating two distributed Bragg reflectors outside the resonant cavity.

There are two types of EELs depending on the way light is confined in the structure: gain-guided and index-guided devices. Gain-guided semiconductor lasers solve the light-confinement

problem by limiting current injection over a narrow stripe. In all designs, current injection over a narrow central stripe (~5μm width)

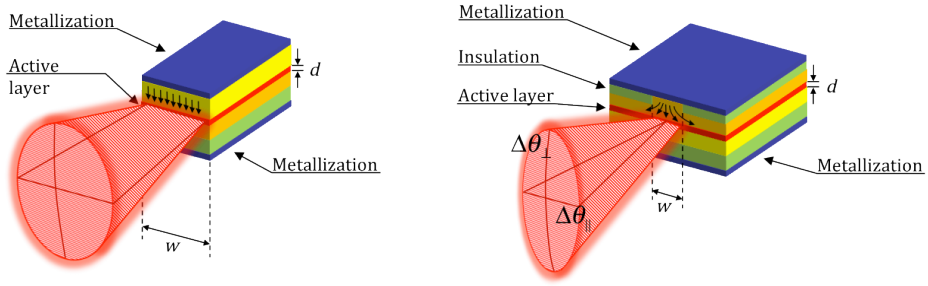

Fig.1.3. Sketch of an edge-emitting laser

leads to a spatially varying distribution of the carrier density (governed by carrier diffusion) in the lateral direction. The optical gain is maximum at the center of the stripe. Since the active layer exhibits large absorption losses in the region beyond the central stripe, light is confined to the stripe region. The lasers where the light is confined by gain are called gain-guided. The major advantage of this structure is that it is easy to fabricate but the transverse confinement of optical field and injection current density is weak so that the corresponding threshold current is high. Usually the light is emitted in the form of an elliptic spot [Agrawal 2005].

The light-confinement problem is solved in the index-guided semiconductor lasers by introducing an index step Δn_L in the lateral direction so that a waveguide is formed in a similar way to that of the waveguide formed in the transverse direction by the heterostructure design. Such lasers can be subclassified as weakly and strongly index-guided semiconductor lasers, depending on the magnitude of Δn_L. [Liu 2005]

1.3. Vertical-Cavity Surface-Emitting Lasers (VCSELs)

1.3.1 Brief history of the VCSEL

VCSEL was first proposed and fabricated by K. Iga et al. at the Tokyo Institute of Technology, Japan in the late 1970s. They successfully demonstrated the first electrically pumped InGaAsP/InP VCSEL under pulse operation at 77 K, a wavelength of 1.3 μm and a very high threshold current (900 mA) in 1979. Several years later, in 1983, they reported the achievement of an electrically pumped GaAs/AlGaAs VCSEL pulsing at room temperature emitting around 874 nm. However, further reduction of threshold current in GaInAsP/InP-based VCSELs was obstructed by the large Auger recombination and other nonradiative recombination inside such a small laser volume.

In 1987, they reported a GaAs VCSEL with threshold current of 6 mA under continuous-wave (CW) operation at 20.5°C. Two years later, they also demonstrated the first room-temperature CW GaAs VCSEL emitting at 850 nm [Yu 2003]. The rapid progress in the development of VCSELs was reached with the use of epitaxially grown distributed Bragg reflectors as highly reflectivity cavity mirrors (≈99% of reflectivity). Jewell et al. [Jewell 1989] in 1989 demonstrated a quantum-well VCSEL based on InGaAs material with 1 to 2 mA threshold and operating in pulsed regime at room temperature. The same year, Lee et al. [Lee 1989] showed the first VCSEL working at room temperature, in a continuous wave operating regime, with a relatively low threshold current (≈ 1.5 mA). With these results, an intensive research activity took place aiming at optimizing the VCSEL performance not only from a scientific point of view but also from a commercial point of view.

1.3.2 VCSEL' structure

VCSELs are a type of semiconductor lasers in which the resonant cavity is perpendicular to a thin active layer. They emit light in a direction normal to the active-layer plane. A sketch of the VCSEL is

shown in Fig. 1.4

The very thin active region (usually formed by multi-quantum well (MQW) semiconductor layers) is sandwiched between a p-doped and a n-doped DBR with high, but slightly different reflectivities (higher than 99.5%) and the carriers are injected into the active region by means of two electrical contacts.

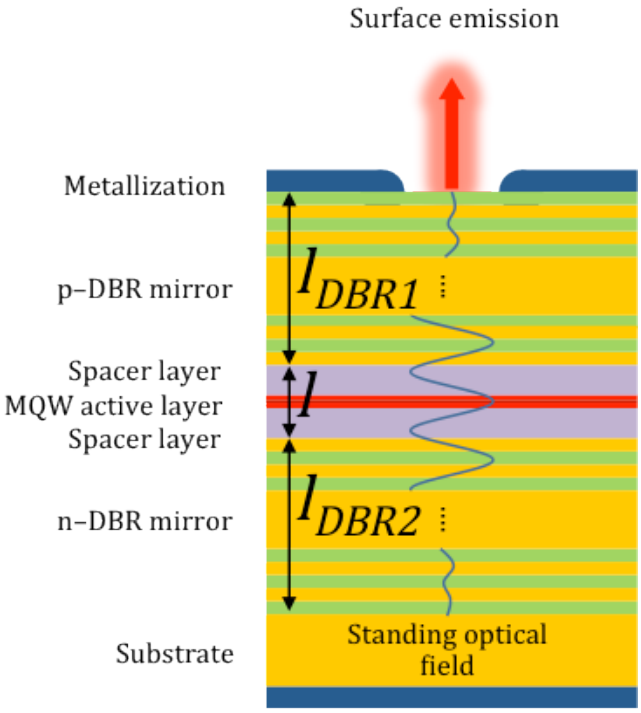

Fig. 1.4. Schematic representation of a VCSEL

The reason for doping the mirrors is to increase their conductivity and decrease ohmic losses. The main characteristic of a VCSEL is that it has a very short cavity (~1μm) made possible by its vertical orientation. Because of the short cavity of a VCSEL, it is required a thin and highly efficient gain section. For this reason, mirrors with high reflectivity are necessary. The output of the first DBR has a lower reflectivity than that of the second DBR for a better output coupling of light from the output mirror. The DBR mirrors of a VCSEL

are index-modulation gratings containing thin layers, quarter-wavelength thick, of alternating compositions, typically pairs of alternating GaAs and AlAs layers, and therefore alternating refractive indices. [Liu 2005] A number of pairs of the order of 20-40 are necessary to achieve high reflectivities.

All VCSELs have the same basic structure, the transverse optical field can be confined inside the VCSELs using gain guiding, index guiding or antiguiding mechanisms [Liu 2005].

In gain-guided VCSELs the light is confined by limiting current injection to a zone mainly determined by the electrical contacts. At high-power operation, higher-order transverse modes can be excited because of the influence of thermal lensing and spatial hole burning of carrier concentration. The main attraction of this type of VCSELs is planar configuration, which guarantees the simplification in fabrication process. [Yu 2003]

In index-guided VCSELs the light is confined by using a refractive index step in the plane orthogonal to the beam direction. Several types of index-guided VCSELs can be found in the literature such as airposted, etched mesa, regrowth buried heterostructure, and oxide aperture, which have different mechanisms to confine the optical field and injection current as well as different fabrication procedure complexities. A common problem to both, gain and index-guided devices is the electrical resistivity of the DBRs, which may increase the heat generation inside the laser cavity.

The VCSELs that we use in this work are oxide-confined VCSELs. Both current and optical confinements can be efficiently achieved in this structure. There are two types of oxide-confined VCSELs: with single oxide-aperture and with double-oxide aperture. The refractive index of the oxide aperture is lower than that of the original semiconductor layer. Hence, the induced effective index difference between the cavity and the surrounding region containing the oxide layer can be controlled through the thickness of the oxide layer and its position relative to the optical cavity. As a

result, the optical field along the transverse direction can be confined tightly by the oxide apertures. Furthermore, the oxide apertures are insulating layers forcing the injection current through the aperture, which enhances the wallplug efficiency (conversion efficiency between electrical and optical power), in consequence, remarkable improvements in terms of threshold current and power conversion efficiency are found [Liu 2005]. Ultralow threshold current is highly desirable feature, since it reduces cavity heating effects and resulting thermal crosstalk in arrays [Zakharov 2001], as well as increases the modulation bandwidth for a given electrical power.

Besides, VCSELs have a lot of advantages as reduced fabrication costs, high coupling efficiency to optical fibers due to their circular output beam, a low divergence, on-wafer testing capability which contributes to reduce the costs as we mentioned before, ease of fabrication of 2D arrays, single-mode operation, low-threshold current, compactness, etc. Finally, current devices are being manufactured with greater than 99% yield and lifetimes well above one million hours [Wipiejewski 1999]. These advantages make the VCSELs ideal candidates for use as stable sources in present and future optical telecommunication network. However, they can not emit more than a few milliwatts of power because of a small active volume. For this reason, they are mostly used in local-area and metropolitan-area networks.

Nowadays, the VCSEL technology have advanced enough that VCSELs can be designed to operate in a wide wavelength range extending from 650 to1600 nm.

CHAPTER 2

Basic principles of semiconductor laser dynamics

In this chapter we describe the basic principles of the semiconductor laser dynamics. We present a simple model based on the rate equations approach. The steady state solutions and small signal analysis are considered. Finally, the relative intensity noise is presented.

2.1. Rate equations in semiconductor lasers

A rigorous derivation of the rate equations starts from Maxwell's equations. Rate equations have been extensively used for studying the underlying phenomena governed by the interaction between photons and charge carriers.

Along the explanation we will use the term "carriers" to refer to electrons and holes, this means that there is not a difference made between both of them. The properties specific to each kind of charge carriers (mobility, effective mass, etc) are averaged, and

equal numbers of electrons and holes are assumed in the cavity. This is called "ambipolar assumption". From now on, the term "carrier" will be used in its ambipolar signification, unless otherwise stated. Another important assumption is that carriers and photons are uniformly distributed in the longitudinal and transversal directions, thus neglecting carrier diffusion and Spatial Hole Burning effect.

Assuming a single mode laser, the relationship between carrier density N and photon density S can be expressed by a set of coupled ordinary differential equations. The carrier rate equation has the basic form indicating the rates at which electrons are created or destroyed inside the active region:

$$\frac{dN}{dt} = Generation - Recombination \tag{2.1}$$

Taking into account the various carrier and photon generation and recombination processes, we have to distinguish: carrier injection, stimulated recombination, spontaneous recombination, and nonradiative recombination. Writing them together yields the formulation of the carrier rate equation or charge conservation equation given by:

$$\frac{dN}{dt} = \frac{\eta_i I}{qV_{act}} - \frac{N}{\tau_n} - v_g G(N,S)S \tag{2.2}$$

The carrier injection into the laser is given by the first term of the Eq. (2.2) where I is the drive current, q the electron charge, and V_{act} the volume of the active region. Due to possible loss mechanisms, the actual carrier density in the cavity is reduced by the factor η_i, called injection efficiency or internal efficiency [Jungo 2003]. The second term represents non-stimulated recombination. The carrier lifetime, τ_n, is the time constant of the carrier decay due to non-stimulated recombination, such as nonradiative transitions and spontaneous emission. Carrier lifetime can be considered for a qualitative description as a constant value above threshold

although actually depends on N due to nonradiative recombination and spontaneous emission process. The last term governs the rate of electron-hole recombination through stimulated emission, which consists of the difference between stimulated emission and stimulated absorption, with v_g the group velocity, $G(N,S)$, the optical gain which represents the "number of generated output photons for each input photon" and S is the photon density.

The photon density rate equation can be expressed as follows:

$$\frac{dS}{dt} = v_g \Gamma G(N,S) S - \frac{S}{\tau_p} + \frac{\beta \Gamma N}{\tau_n} \tag{2.3}$$

The first term represents the stimulated recombination contribution, the second term takes into account the loss of photons inside the cavity. Finally, the last term is the rate of spontaneous emission into the lasing mode. It is important to mention here that this term is much smaller than the total spontaneous-emission rate. The reason is that spontaneous emission occurs in all directions over a wide spectral range (30~40 nm) but only a small fraction of it, propagating along the cavity axis and emitted at the laser frequency contributes to Eq. (2.3). So, in Eq. (2.3) Γ is the confinement factor which represents the optical mode coupling to the active region, τ_p represents the photon lifetime in the cavity due to photons exiting through the mirrors or being absorbed and scattered inside the cavity, and finally, β the spontaneous emission coefficient. This coefficient represents the portion of spontaneously emitted photons that couples into the lasing mode. The parameter τ_p is related to the cavity loss α_{cav} as $\tau_p=(v_g(\alpha_{mir}+\alpha_{cav}))^{-1}$ where α_{mir} and α_{cav} are mirrors and cavity losses, respectively, with $\alpha_{mir}=(1/L)\ln(1/R_1R_2)$ where L is the cavity length and R_1, R_2 are the mirrors reflectivities.

Stimulated emission can dominate only if the condition of population inversion is satisfied. When the injected carrier density in the active layer exceeds a certain value, known as the

transparency value, population inversion is achieved and the active region exhibits optical gain as we explained in Chapter 1. In Fig. 2.1. we can see the gain spectrum of a 1.3 μm InGaAsP laser at several carrier densities N.

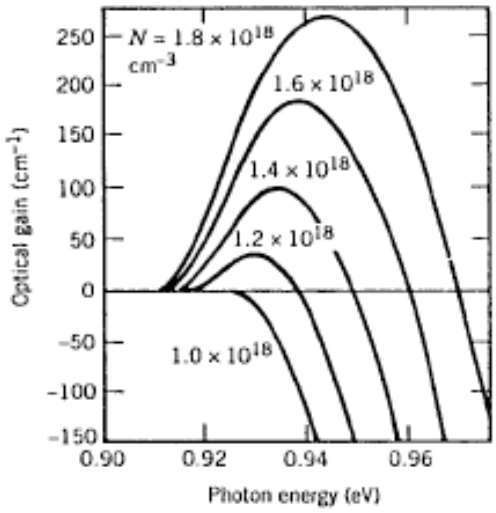

Fig. 2.1. Gain spectrum of a 1.3-μm InGaAsP laser at several carrier densities N. [Agrawal 2002]

As N increases, gain becomes positive over a spectral range that increases with N. The peak value of the gain, also increases with N, together with a shift of the peak toward higher photon energies [Agrawal 2002]. The optical gain increases rapidly once population inversion is achieved, but saturates at higher photon densities. This gain compression factor yields the general gain expression:

$$G(N,S)=\frac{\frac{dG}{dN}(N-N_{tr})}{1+\varepsilon S} \tag{2.4}$$

where ε is the gain compression factor which accounts for the gain saturation occurring at high photon densities, dG/dN represents the

differential gain and N_{tr} the transparence carrier.

2.1.1. Steady state solution

The relation between the laser output power and the pump current provides fundamental information on the operation of semiconductor laser diodes. From the rate equations we can derive analytic expressions of the power vs. current characteristic, called L-I curve or P-I curve.

Making Eqs. (2.2) and (2.3) zero and considering the threshold condition on gain the stationary solutions of these equations are obtained. Neglecting the spontaneous emission term from Eq. (2.3), gain equals losses when:

$$G_{th}(N,S) = \frac{1}{v_g \Gamma \tau_p} \tag{2.5}$$

being $G_{th}(N,S)$ the gain at threshold. Using Eqs. (2.4) and (2.5) the threshold condition on the carrier density is obtained:

$$N_{th} = N_{tr} + \frac{1}{v_g \frac{dG}{dN} \Gamma \tau_p} \tag{2.6}$$

Current and carrier densities are related through Eq. (2.2) and from now on considering η_i=1: in the steady regime, for dN/dt=0 and $I<I_{th}$, S=0 and Eq. (2.2) gives $N=\tau_n I/qV_{act}$. In this way, the threshold current I_{th} is obtained:

$$I_{th} = \frac{qV_{act}}{\tau_n} N_{th} \tag{2.7}$$

As we can see in Eq. (2.7) the threshold current of a semiconductor laser is linearly proportional to the threshold carrier density and the volume of its active region. There is a limit in decreasing the threshold carrier density to reduce the threshold current because

$N_{th}>N_{tr}$ and N_{tr} is an intrinsic property of a semiconductor gain medium. Reducing N_{th} by increasing the value of Γ does not lead to a lower value for I_{th} because both Γ and I_{th} are proportional to V_{act}. It is only practical to reduce the value of τ_p^{-1} (threshold condition) as much as possible in order to make N_{th} as close to its limit of N_{tr} as possible. For a QW VCSEL, the threshold current can be reduced by reducing its transverse dimension without changing its cavity length because $V_{act}= \mathcal{A}M_{QW}d_{QW}$ being $\mathcal{A}$ the area of the junction, M_{QW} represents the number of quantum wells and d_{QW} is the well thickness, is independent of the cavity length of the device [Liu 2005].

Solving Eq. (2.2), in the steady state above threshold and using Eqs. (2.5) and (2.7), the expression for the photon density above threshold is obtained:

$$S = \Gamma\tau_p\left(\frac{I - I_{th}}{qV_{act}}\right) \tag{2.8}$$

Then the output power of a semiconductor laser can be expressed, taking into account that $P=SV_{opt}h\nu v_g\alpha_{mir}$, where V_{opt} is the optical cavity volume, $h\nu$ is the photon energy and $v_g\alpha_{mir}$ is the rate at which photons exit the mirrors, as

$$P = \eta_d\frac{h\upsilon}{q}\left(I - I_{th}\right) \tag{2.9}$$

where η_d is the differential quantum efficiency which measures the efficiency of converting pump photons or pump electrons above threshold into laser photons at the laser.

2.1.2. Small-Signal Analysis

In order to perform a small-signal analysis, the time-domain rate equations can be transformed into frequency domain equations by taking the differential of both linearized rate equations [Coldren 1995]. A good approach consists in considering the drive current

as a superposition of an above threshold bias and an applied small-signal component modulated at the angular frequency ω. This allows writing:

$$\begin{aligned} I &= I_0 + \Delta I e^{j\omega t} \\ N &= N_0 + \Delta N e^{j\omega t} \\ S &= S_0 + \Delta S e^{j\omega t} \end{aligned} \tag{2.10}$$

where $I_0 >> \Delta I$, $N_0 >> \Delta N$ and $S_0 >> \Delta S$

The differential gain components a_N and a_S are defined as followed:

$$\begin{aligned} a_N &= \frac{\partial G}{\partial N} = \frac{g_0}{1+\varepsilon S} \\ a_S &= -\frac{\partial G}{\partial S} = \frac{\varepsilon G}{1+\varepsilon S} \end{aligned} \tag{2.11}$$

In the presence of gain compression, ε, a_N is not equal to the linear gain coefficient g_0 (sometimes also referred to as nominal differential gain). Using the equation (2.11), the gain variation can be written as:

$$\Delta G = a_N \Delta N - a_s \Delta S \tag{2.12}$$

Inserting Eq.(2.10) and Eq.(2.12) in Eq.(2.2) and Eq.(2.3) using Eq. (2.5) to substitute $1/\Gamma v_g \tau_p$ for $a_N (N-N_{tr})$, and neglecting spontaneous emission and the terms involving a_S and $e^{2j\omega t}$, simplified frequency domain rate equations can be obtained:

$$\begin{aligned} j\omega \Delta N &= -\frac{\Delta N}{\tau_n} - \frac{\Delta S}{\Gamma \tau_p} - v_g a_N \Delta N S_0 + \frac{\eta_i \Delta I}{q V_{act}} \\ j\omega \Delta S &= \Gamma v_g a_N \Delta N S_0 \end{aligned} \tag{2.13}$$

The modulation response given by $\Delta S(\omega)/\Delta I(\omega)$ is obtained from Eq.

(2.13)

$$\frac{\Delta S(\omega)}{\Delta I(\omega)} = \frac{\Gamma \eta_i}{q V_{act}} \frac{v_g a_N S_0}{v_g a_N S_0 / \tau_p - \omega^2 + j\omega\left(v_g a_N S_0 + 1/\tau_n\right)} \tag{2.14}$$

The system shown in the Eq. (2.13) is very much like an RLC oscillator whose normalized modulation transfer function (MTF) can be written as:

$$H(\omega) = \frac{1}{1 + \frac{j\omega\gamma}{\omega_R^2} - \frac{\omega^2}{\omega_R^2}} \tag{2.15}$$

In the Eq. (2.15) only the fundamental lasing processes are considered, "structural" effects such as cavity heating or electrical parasitics are neglected.

Normalizing (2.14) and identifying the terms with (2.15) yields the system's squared angular relaxation oscillation frequency (ROF)

$$\omega_R^2 = \frac{v_g a_N S_0}{\tau_p} \tag{2.16}$$

and damping coefficient

$$\gamma = v_g a_N S_0 + \frac{1}{\tau_N} \tag{2.17}$$

The two parameters ω_R and γ entirely determine the intrinsic modulation capability of the laser. Relaxation oscillation frequencies have their origin in the processes by which the carriers and photons tend to their equilibrium values [Jungo 2003]. The extremely high intrinsic relaxation oscillation frequency of VCSELs is the result of high photon density inside the small laser cavity as the ROF is proportional to the square root of the photon density [Yu 2003]. Damped relaxation oscillations derive from periodic exchange of energy between the inversion and the electric field

inside the cavity. The modulation of the carrier density in the cavity also modulates the refractive index of the active region. This is expressed through the index variation which can be related to the gain through the linewidth enhancement factor α defined as

$$\alpha = -\frac{4\pi}{\lambda a_N}\frac{dn}{dN} \tag{2.18}$$

The α-factor is responsible for the linewidth broadening with respect to the linewidth of gas lasers given by Schawlow-Townes formula, it is a source of chirp under current modulation and it has a great impact on the dynamics of laser diodes subject to optical injection.

2.2. Relative Intensity Noise

In lasers, noise can be expected to have a significant influence on the stationary values of the output variables. It is known that the noise in a single polarization state is higher than that in the total output intensity [Peeters 2003]. The optical power emitted by a laser under steady-state operation might be defined as the sum of the averaged power $< P >$ plus a fluctuation component $\delta P(t)$

$$P(t) = \langle P \rangle + \delta P(t) \tag{2.19}$$

In the time domain, the noise can be expressed by the autocorrelation function (2.20), whereas it is described in the frequency domain by spectral density of power fluctuations $S_{\delta P}(\omega)$:

$$\rho(\tau) = \langle \delta P(t)\delta P(t-\tau) \rangle \tag{2.20}$$

$$S_{\delta P}(\omega) = \left\langle \left| \Delta P(\omega) \right|^2 \right\rangle \tag{2.21}$$

where $\Delta P(\omega)$ is the Fourier transform of $\delta P(t)$.

Equations (2.20) and (2.21) are related through the Wiener-

Khintchine relations, which state that Fourier transformation of the correlation function yields the spectral density.

Using the Parseval's theorem, the mean square of the noise signal may be written as:

$$\left\langle \delta P^2(t) \right\rangle = \rho_p(0) = \int_{-\infty}^{\infty} S_{\delta P}(\omega) df \tag{2.22}$$

If the noise is passing a filter with bandwidth Δf (narrow relative to variations in the spectral density), one obtains:

$$\left\langle \delta P^2(t) \right\rangle = 2\Delta f S_{\delta P}(\omega) \tag{2.23}$$

where the factor 2 is introduced because both filter bands (positive and negative) must be taken into account.

Relative Intensity Noise (RIN) is an important characteristic of semiconductor lasers. It is defined as:

$$\frac{RIN}{\Delta f} = \frac{\left\langle \delta P(t)^2 \right\rangle}{\left\langle P \right\rangle^2} = \frac{2S_{\delta P}(\omega)}{\left\langle P \right\rangle^2} \tag{2.24}$$

The RIN decreases rapidly for increasing drive currents. It exhibits a peak near the relaxation-oscillation frequency as a consequence of the laser's intrinsic resonance [Jungo 2003].

CHAPTER 3

Characterization and emission properties of VCSELs

All VCSELs have the same basic structure which has perfect circular symmetry and also VCSELs are isotropic, this means that there is not a polarization preference yet. As we have mentioned before, the first advantage is the vertical orientation of the cavity. This allows the possibility of on-wafer testing and the growth of two dimensional arrays. A second advantage is the short cavity and as a consequence the single longitudinal mode operation. Also, the very high quality of the cavity leads to narrow linewidths, even at low powers. Another advantage is the low threshold and high efficiencies: threshold current as low as few tens of μW and efficiencies up to 80%. The last advantage is the circular output beam with a typical divergence of 12°, for this reason no specialized optics are needed to couple the light from a VCSEL into a fiber. All of these advantages come with the extra advantage of bandwidth, VCSELs with a large small signal

bandwidth of more than 20 GHz have been demonstrated [Lear 1997]. The limiting factor is mostly the parasitic capacitance inherent to the VCSEL or the packaging [Stevens, R. 2001].

But not everything is advantages, low threshold currents and small sizes also mean low power output. Their sensitivity to temperature operation also means that VCSELs temperature has to be controlled in circumstances where a stable output wavelength is required. [Peeters 2003]

3.1. Continuous wave emission properties of VCSELs

3.1.1. Light-current characteristics

The small size of the active volume and the high reflectivity of the DBRs mirrors in VCSELs gives rise to a low value of the threshold current. A typical light vs. current characteristic (L-I) is plotted in Fig. 3.1 for different temperatures. This corresponds to a 1550-nm wavelength device similar to those that will be analyzed in this Thesis. The influence of the spontaneous emission level can be seen in Fig. 3.2 where L-I curve is plotted in logarithmic scale when the temperature is 24ºC. It is clear from the Fig. 3.2. in logarithmic scale that the effect of spontaneous emission is visible only below threshold.

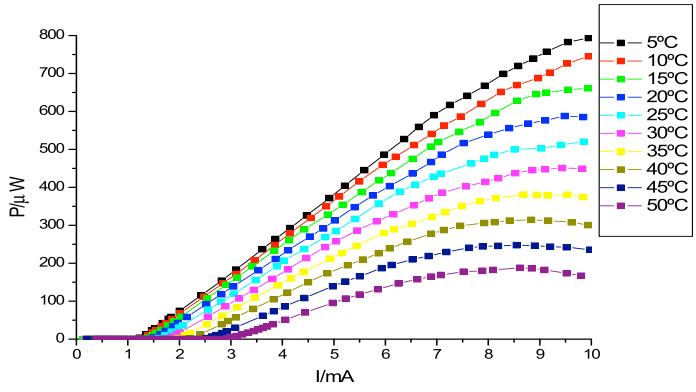

Fig. 3.1. Light-current characteristic for different temperatures.

In Fig. 3.1 we can see that the threshold current increases when the temperature increases. However, the behavior of the emitted power is the opposite, it decreases when the temperature increases. If we fix a temperature, we can see the decrease in output power at higher injection current due to the current heating of the device through the Joule effect. As temperature increases, gain red-shifts and decreases too, moreover, there is a thermal escape of carriers, which is the dominant effect, and in consequence, the emitted power is reduced (thermal roll over).

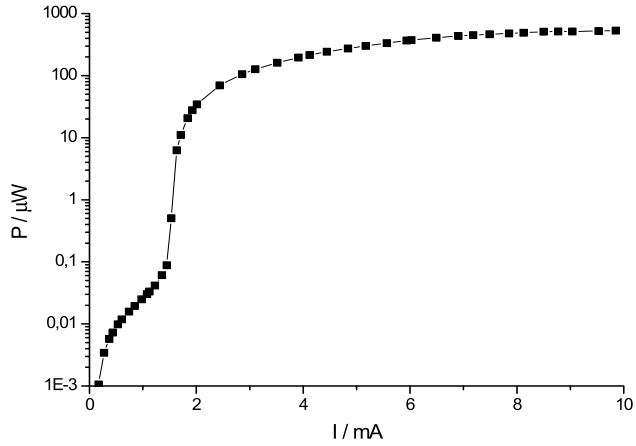

Fig. 3.2. Light-current characteristic in logarithmic scale for 24 °C. It can be seen the influence of the spontaneous emission.

3.1.2. Thermal behavior

VCSELs are extremely sensible to the temperature, affecting this to the threshold current as we can see in Fig. 3.1. The cavity is short and for this reason the longitudinal mode spacing is large and only one longitudinal mode is contained in the gain spectrum. As we mentioned before, as the temperature increases the gain red-shifts but also the resonance frequency. However, the gain profile shifts a larger rate, typically the temperature drift of the gain peak is 0.3nm/K, so that eventually, the resonance frequency is outside

the range of frequencies for which there is positive gain.

The resonance wavelength of the mode changes with the temperature T because of the dependence of the refractive index on T. Also there is a thermal expansion, as a result, the length of the cavity changes and also the resonance wavelength. The typical value is $d\lambda/dT=0.07nm/K$ depending on the composition of DBRs and the cavity. The main contribution to this value is given by the refractive index dependence on T. The minimum value of threshold current corresponds to alignment of the cavity mode with the gain peak frequencies. VCSELs usually are designed in such a way, that the minimum current threshold is reached at room temperature. As mentioned before, at higher temperatures or when the current increases the effect of thermal roll-over is stronger because of the self-heating of the device mostly as a result of the series resistance of the DBR mirrors [Miller 98].

3.1.3. Polarization and transverse mode properties of VCSELs

A peculiarity of the VCSELs is that due to their geometry, the polarization of the laser light is not well stabilized. This becomes a problem for applications which require a well stabilized polarization and it has motivated much research to fix the polarization state of the emitted light. These methods include introducing polarization sensitive DBR mirrors [Ser 1995], geometrical or stress-induced anisotropies or engineering of the semiconductor material or the growth process [Chavez-Pirson 1993] to favor the gain of one of the two independent polarization directions. Another option is to learn how to control the polarization and use this knowledge in possible applications based on the polarization state, such as optical switching [Nishikawa 1995], information processing or storage, etc. [Miller 1998].

Light emitted from VCSELs is typically linearly polarized, with the vector field randomly oriented in the transverse plane to the light

emission direction or with a preferred orientation along one of two orthogonal crystal axes in that plane. Close to threshold the VCSEL generally emits in the fundamental transverse mode. With this transverse profile fixed the polarization direction can be stable as the injection current is increased or a switch to the orthogonal polarization state can occur for some value of the injection current. Increasing the injection current a switch back can occur. The switching process can still occur in a geometry which tends to equalize the gain of the two eigen-polarizations and when the cavity resonance is always detuned to the same side of the gain peak. The polarization switching often shows hysteresis, so this means that the value of the injection current at which the switch occurs is different depending on if we increase or decrease the injected current.

Transverse modes of higher order than the fundamental begin to emit for values of the injection current that strongly depend on the dimensions of the electrical contact. Transverse modes of different order are separated in frequency by 100-200 GHz, while transverse modes of the same order are separated in frequency by birefringence. This separation can vary from smaller than 1 GHz up to tens of GHz. The origin of birefringence can be due to the electro-optic effect during laser operation with drive voltage and a random contribution due to the elasto-optic effect. Another possibility to explain the birefringence of these devices is due to the residual strain in the fabrication process or in the electrical contacts.

The emission in multiple transverse modes can be attributed to "spatial hole burning" effects [Changhasnain 1991]. We will explain this phenomenon later.

3.1.3.1 Transverse modes in VCSELs

An optical mode is a solution of the wave equation that satisfies the appropriate boundary conditions and has the property that its spatial distribution does not change with propagation. For knowing

the allowed transverse optical modes in a cylindrical waveguide is necessary resolve exactly the Maxwell's equation. Transverse mode characteristics of VCSELs can be analyzed by the cylindrical dielectric waveguide theory, because VCSELs with cylindrical geometry have transverse confinement structures similar to that of the optical fiber. [Yu 2003]

Different solutions of Maxwell's equations give different optical modes. They can be transverse modes (TE (transverse electric) and TM (transverse magnetic)) where both the electric and magnetic field do not have a longitudinal components or they can have longitudinal components, it means through the propagation direction, they are called hybrid modes: (HE and EH modes, hybrid electric and hybrid magnetic modes respectively)

In the weakly guiding approximation (the effective refraction index at the core region is slightly greater than the one at the cladding region), the modes are assumed to be nearly transverse and can have an arbitrary state of polarization. Thus, the two independent sets of modes can be assumed to be x-polarized and y-polarized, and in the weakly guiding approximation they have the same propagation constants. These linearly polarized modes are usually referred to as LP modes. These modes LP_{mn} are indexed with m=0,1,2,... and n=1,2,3...where m and n determine the number of zeros in the angular and radial direction respectively. LP_{10} is referred as the fundamental mode, LP_{11} the first-order transverse mode and the remaining as higher transverse modes [Saleh 1991].

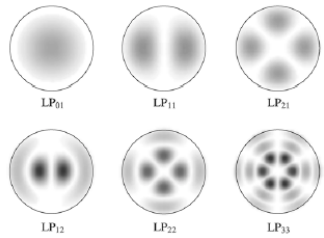

Fig. 3.3. Intensity profiles of a few LP modes [Liu 2005].

3.1.3.2 Spatial Hole Burning

Spatial Hole Burning is the main reason for multi-transverse mode emission in VCSELs. The transverse mode structure in the lasing regime is essentially determined by the relevant modal gains, which in turn, are determined both by the mode field distribution and the spatial distribution of the carriers in the device active region. The mode field distribution is largely determined by the device structure, though it is also dependent upon the carrier concentration distribution. The carrier concentration profile is clearly dependent upon the distribution of the current injected into the device active region and on carrier diffusion effects. Above the lasing threshold the carrier profile is also influenced by spatial hole burning, arising due to carrier recombination in the lasing process.

Spatial Hole Burning effects have been studied in a model of a VCSEL with two transverse modes [Valle 1995]. For currents slightly above threshold, fundamental transverse mode uses to appear since its modal gain is the highest: the intensity profile of this mode overlaps in an optimal way with the carrier density because this is usually concentrated near the center of the laser. At higher currents, the increasing stimulated recombination of carriers produces a hole in the carrier profile near the center of the device and the high order transverse mode reach threshold resulting in multimode emission. This happens because the modal gain of the high order transverse mode has increased as the transverse mode and carrier profiles have become more similar.

Transverse mode emission depends on the spatial overlap between modes. When the modes have not a strong spatial overlap they feed from carriers coming from different zones of the active region. In this way several transverse modes can reach threshold and a multi-transverse mode spectrum is observed. When the modes overlap significantly and thus, occupy essentially the same part of the device active region, then there is strong competition between the modes which may result in just one

mode dominating. Which of the two modes dominates is determined by which has the highest net modal gain. The carrier concentration distribution arising from a combination of multimode spatial hole burning and carrier diffusion will determine the modal gains of the modes.

Then, depending upon the spatial overlap between the transverse distribution of optical gain and transverse mode profile, the device may be expected to move toward either multimode operation or to a situation where one mode with higher gain is sustained [Valle 1995].

3.1.3.3 Polarization switching (PS). PS induced by optical injection

Polarization switching occurs by destabilization of the polarization mode with the higher gain-to-loss ratio in favor of the weaker mode. Close to threshold the VCSEL generally emits in the fundamental transverse mode. With this transverse profile fixed, the polarization direction can be stable or switch to the orthogonal polarization state varying the injection current.

Different physical mechanisms have been proposed to explain PS in VCSELs. Choquette et al. attributed the polarization switching at the condition of cavity resonance/gain spectral alignment. There is a spectral shift of the material gain maximum relative to the cavity resonance modes due to thermal origin (current heating) causing PS [Choquette 1995]. Alternative mechanism leading to PS was proposed by Panajotov et al. based on the effect of thermal lensing and to subsequent competition of the modal gains for the two orthogonal and linearly polarized modes [Panajotov 1998]. Another mechanism invoked in weak index-guided VCSELs to explain the polarization switching is the combined effect of birefringence and spatial holeburning [Valle 1997]. Also the effect of the photon-energy-dependent loss and gain mechanisms inside the cavity has been proposed to understand PS behavior of VCSELs [Ryvkin 1999]. Another

approach is based on a four-level model as proposed by San Miguel Feng and Moloney [Sanmiguel 1995]. In the next section we summarize the fundamentals of the Spin-Flip Model (SFM).

PS can also be induced by optical injection for a fixed value of the electrical injection current: injecting into the laser an optical signal whose polarization is orthogonal to that emitted by the laser can produce polarization switching [Pan 1993]. The polarization switching often shows hysteresis, so that the switch occurs for different values of some parameter when this is increased or decreased.

Two different situations have to be considered, switching by an optical pulse [Kawaguchi 1995a] or switching by continuous optical pump [Pan 1993]. In the first case polarization switching occurs for pulses above a certain injected energy which depends on the detuning between the injected signal and VCSEL frequencies. The fact that the VCSEL remains in the new polarization state after switching, indicates that it is operating in a bistable domain.

Switching under continuous optical injection is needed when the VCSEL operates in a domain in which only one of the polarization states is stable. In this case the laser goes back to the initial state soon after the injected signal is removed. The switching on and off occurs for different values of the injected power as this is increased and decreased. These values depend on the frequency of the injected signal, being sometimes, the switching power minimum when the injected frequency locks to the frequency of the slave laser after switching. This resonant frequency also separates a region of gradual transition from one of abrupt switching [Miller 1998].

3.2. Spin Flip Model

The Spin-Flip Model (SFM) [San Miguel 1995] is frequently used to explain polarization switching mechanism in VCSELs. The

polarization properties of VCSELs are analyzed using a four-level rate equation model. The four-level model takes into account the spin sublevels of the conduction and valence bands of the QW materials. Therefore, the lasing field of different polarizations associated with the transition between different spin sublevels can be included in the calculation.

The polarization of laser light is of a quantum nature and originates in the spin sublevels of the lasing transitions between the conduction and valence bands of the semiconductor. The polarization of light is accounted for by considering the angular momentum of the quantum states which are involved in the transitions for emission and absorption within the semiconductor material. The band structure of a quantum-well is illustrated in Fig. 3.4.

In the valence band we can see two levels of energy: one of them with high energy known as heavy-hole band and another one with low energy known as light-hole band. Near the band gap, the two valence bands are not degenerate due to quantum confinement effect present in quantum well structures. Moreover, as the energy of the light-hole band is really low, one can neglect the corresponding transitions in the radiative recombination process.

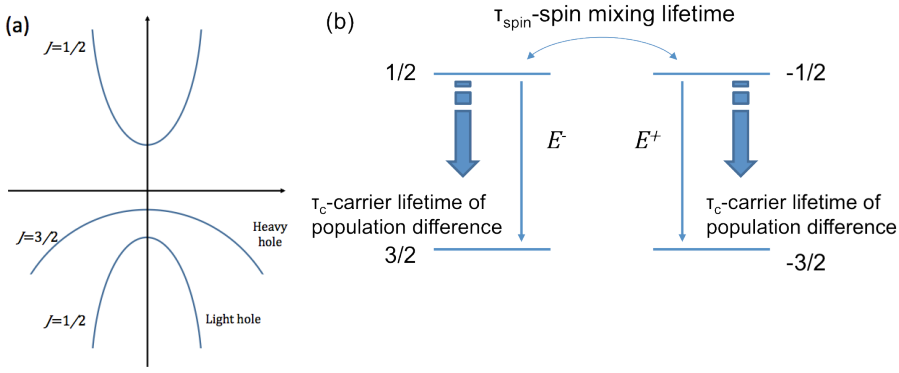

Fig. 3.4. (a) Band structure of a quantum well (b) lasing transitions associated with right (E_+) and left (E_-)circularly polarized emission.

The conduction band has a total angular moment of J_z=±1/2, while the valence band states have a total angular moment of J_z= ±1/2 and ±3/2 although the valence band associated with the state J_z=±1/2 will be disregarded because of its lower energy as we mentioned before. So, the quantum well confinement breaks the degeneracy of the J=3/2 state leading to a HH (heavy hole) state (J_z=±3/2) of higher energy than the LH (light hole) state (J_z= ±1/2). If the QW active layer is perpendicular to the direction of laser emission z, two circular polarized modes can be modeled by the transition between these spin sublevels of conduction and valence bands. Because of the quantum nature of light, the allowed electric dipole transitions that result in electron-hole recombination are those in which ΔJ_z=±1. Emission of right circularly polarized photons corresponds to ΔJ_z=-1 and left circularly polarized photons to ΔJ_z=+1. The dipole transition from J_z=1/2 to J_z=3/2 is associated with the left circularly polarized light and that from J_z=-1/2 to J_z=-3/2 is associated with the right circularly polarized light [Miller 1998].

Applying the semiclassical approach to the four-level system, one obtains the Maxwell-Bloch equations, then after a number of assumptions a simplified SFM model can be derived. We are going to consider that the VCSEL emits only in the fundamental transverse mode, so in this way, the effect of the carrier diffusion process and the diffraction of the electric field may be neglected. We can write the rate equations considering that the laser frequency is close to zero at threshold current as:

$$\frac{d\tilde{E}_{\pm}}{dt} = -\kappa(1+i\alpha)\tilde{E}_{\pm} + \tilde{P}_{\pm} \tag{3.1}$$

$$\frac{d\tilde{P}_{\pm}}{dt} = -\gamma_{\perp}(1-i\alpha)\tilde{P}_{\pm} + \gamma_{\perp} a\left(1+\alpha^2\right)\left(D - D_t \pm d\right)\tilde{E}_{\pm} \tag{3.2}$$

$$\frac{dD}{dt} = C - \gamma_e D - \left(\tilde{E}_{+}\tilde{P}_{+}^{*} + \tilde{E}_{-}\tilde{P}_{-}^{*} + c.c.\right) \tag{3.3}$$

$$\frac{dd}{dt} = -\gamma_s d - \left(\tilde{E}_{+}\tilde{P}_{+}^{*} - \tilde{E}_{-}\tilde{P}_{-}^{*} + c.c.\right) \tag{3.4}$$

where $\tilde{E}_{\pm}$ and $\tilde{P}_{\pm}$ are respectively the slowly-varying amplitudes of the left (-) and right (+) circularly-polarized components of the electric field and the dipole polarization. *D* and *d* are the carrier variables defined as:

$$D = D_{+} + D_{-} \tag{3.5}$$
$$d = D_{+} - D_{-} \tag{3.6}$$

being D_{+} and D_{-} the carrier density variables associated to the transition channel for which ΔJ_z=+1 and ΔJ_z=-1 respectively. Therefore, the variable D represents the total carrier density referred to its transparency value D_t, while d represents the difference between the two carrier populations associated with emission of $\tilde{E}_{+}$ and $\tilde{E}_{-}$.

α is the linewidth enhancement factor and it represents the phase-amplitude couplings of field and polarization, a is the differential gain at the laser frequency and C accounts for the contribution of the injection current to the total inversion population. κ is the relaxation rate of the amplitudes of the electric field, $\gamma_{\perp}$ is the decay rate of the material polarization. γ_e and γ_s are the relaxation rates of D and d respectively. γ_s takes into account the spin relaxation processes that mix the carrier populations with opposite values of J_z.

Note here, that if we consider that the polarization relaxes much faster than the other system variables we can simplify the Eq. (3.1) to (3.4). It means that $\gamma_{\perp} >> \kappa > \gamma_s > \gamma_e$ and in this way, the polarization can be adiabatically eliminated by setting the left hand of the Eq. (3.2) equal to zero. Therefore:

$$\tilde{P}_{\pm} = (1 + i\alpha) a \left(D - D_t \pm d \right) \tilde{E}_{\pm} \tag{3.7}$$

Normalizing the rate equations to become the field and carrier variables dimensionless, we can realize the following variable

change:

$$E_{\pm} = \sqrt{\frac{2a}{\gamma_e}}\tilde{E}_{\pm} \tag{3.8}$$

$$N = a\frac{D - D_t}{\kappa} \tag{3.9}$$

$$n = a\frac{d}{\kappa} \tag{3.10}$$

After the polarization variable is adiabatically eliminated from Eqs (3.1) to (3.4) and using the variable changes show above, the SFM writes:

$$\frac{dE_{\pm}}{dt} = \kappa(1+i\alpha)(N \pm n - 1)E_{\pm} \tag{3.11}$$

$$\frac{dN}{dt} = \gamma_e \mu - \gamma_e N\left(1+\left|E_+\right|^2+\left|E_-\right|^2\right) - \gamma_e n\left(\left|E_+\right|^2-\left|E_-\right|^2\right) \tag{3.12}$$

$$\frac{dn}{dt} = -\gamma_s n - \gamma_e n\left(\left|E_+\right|^2+\left|E_-\right|^2\right) - \gamma_e N\left(\left|E_+\right|^2-\left|E_-\right|^2\right) \tag{3.13}$$

where μ is the normalized injection current which takes a unit value at the lasing threshold.

The polarization state of light emitted by a laser depends on two main facts. The first is the angular momentum of the quantum states involved in the material transitions for emission or absorption. Emission of a quantum of light with right (left) circular polarization corresponds to a transition in which the projection of the total material angular momentum on the direction of propagation change by -1(+1) as we mentioned before. The second factor is associated with the intrinsic optical anisotropies, which lead to a preference for a particular polarization state of the laser light [Yu 2003].

The model described above Eqs. (3.11)-(3.13) does not take into account cavity anisotropies. If we include amplitude anisotropies and linear phase, both states orthogonal and linearly polarized exhibit different phases and losses. These anisotropies contribute to the selection of two preferential orthogonal linearly

polarized states in the transverse plane and affect also the stability as well as the polarization switching mechanism [MartinRegalado 1997a],[MartinRegalado 1997b],[Gatare 2008].

Assuming that the eigen axes of linear phase and amplitude anisotropies are parallel to the VCSEL polarization eigen axes, their contribution can be included in the SFM model as follows:

$$\frac{dE_{\pm}}{dt} = \kappa(1+i\alpha)(N \pm n - 1)E_{\pm} - (\gamma_a + i\gamma_p)E_{\mp} \tag{3.14}$$

$$\frac{dN}{dt} = \gamma_e \mu - \gamma_e N\left(1+|E_+|^2+|E_-|^2\right) - \gamma_e n\left(|E_+|^2-|E_-|^2\right) \tag{3.15}$$

$$\frac{dn}{dt} = -\gamma_s n - \gamma_e n\left(|E_+|^2+|E_-|^2\right) - \gamma_e N\left(|E_+|^2-|E_-|^2\right) \tag{3.16}$$

The intrinsic optical anisotropies are included through the linear phase anisotropy or birefringence γ_p and the linear amplitude anisotropy or dichroism γ_a.

Using transformation relations between circular and linear bases we can rewrite the Eq. from (3.14) to (3.16). The transformations are given by:

$$E_+ = \frac{E_x + iE_y}{\sqrt{2}} \tag{3.17}$$

$$E_- = \frac{E_x - iE_y}{\sqrt{2}} \tag{3.18}$$

which leads to the following formulation of the SFM model:

$$\frac{dE_x}{dt} = -(\kappa+\gamma_a)E_x - i(\kappa\alpha+\gamma_p)E_x + \kappa(1+i\alpha)(NE_x + inE_y) \tag{3.19}$$

$$\frac{dE_y}{dt} = -(\kappa-\gamma_a)E_y - i(\kappa\alpha-\gamma_p)E_y + \kappa(1+i\alpha)(NE_y - inE_x) \tag{3.20}$$

$$\frac{dN}{dt} = -\gamma_e\left[N\left(1+|E_x|^2+|E_y|^2\right) - \mu + in\left(E_yE_x^* - E_xE_y^*\right)\right] \tag{3.21}$$

$$\frac{dn}{dt} = -\gamma_s n - \gamma_e\left[n\left(|E_x|^2+|E_y|^2\right) + iN\left(E_yE_x^* - E_xE_y^*\right)\right] \tag{3.22}$$

The SFM described by Eqs. (3.14)-(3.16) or (3.19)-(3.22) describes a VCSEL operating in the fundamental transverse mode with two polarization modes with different frequencies. Further extensions of

this model to account for multiple transverse mode operation in weakly-index and gain guided devices has been done in [Valle 1998b] and [MartinRegalado 1997a].

3.3. Dynamics of VCSELs subject to orthogonal optical injection

Nonlinear dynamics arising from optical injection have been investigated with different semiconductor lasers: edge-emitting lasers [Simpson 1997], [Simpson 2003], and VCSELs [Altes 2006], [Schires 2011a], [Schires 2011b], [Gatare 2006b], [Gatare 2009].

Nonlinear dynamics of optically injected semiconductor lasers is interesting from a practical point of view because the period-one oscillation state is one of the potential candidates for carrying message in a radio-over-fiber (RoF) system [Chan 2006]. Also optical injection can be used to reduce the laser linewidth, the mode partition noise, or for enhancing the modulation bandwidth without modifying the semiconductor laser design [VanTartwijk 1995].

Because of the significant advantages of the VCSELs, such as low cost, high coupling efficiency to optical fibers, single-longitudinal mode operation, etc. VCSELs are substituting the EELs in many applications such as fiber for the home links, computer networks, optical sensing, etc. Besides, the first commercially available VCSELs operated around 850 nm or 970 nm but, nowadays, VCSELs working at 1300- and 1500-nm are available. These wavelengths represent the telecommunication wavelengths. For these reasons, combined with the potential for nonlinear laser outputs to be used in applications such as secure optical data communication, nonlinear dynamics from VCSEL systems has current priority in nonlinear laser studies [Toomey 2012].

Emission in multiple transverse modes is usually found in VCSELs and is attributed to spatial hole burning effects, this characteristic together with the lack of polarization anisotropies provide new characteristics to the rich nonlinear dynamics induced by optical

injection [Toomey 2012]. Optical injection consists on injecting light from a master laser into the slave laser. Two main types of optical injection in VCSELs have been considered: parallel and orthogonal optical injection. Early experiments and simulations were done for a polarization of the injected light that is parallel to that of the VCSEL [Li 1996], [Hong 2003], the so called "parallel optical injection". However, most of the recent work have considered the "orthogonal optical injection" in which linearly polarized external light is injected orthogonally to the linear polarization of the free-running VCSEL, [Altes 2006], [Valle 2008], [Hurtado 2008b]. Dynamic maps identifying the boundaries between different regions such as stable locking, unlocking, periodic dynamics, chaos, bistability and polarization switching have been reported in short-wavelength VCSELs [Altes 2006], [Gatare 2009], [Panajotov 2009],[Nizette 2009] and in long wavelength devices [Al-Seyab 2011]. More details on previous work on bistability and nonlinear dynamics of VCSELs subject to orthogonal optical injection will be given in the introductions of chapters 6 and 7, respectively.

CHAPTER 4

Description and characteristics of the experimental equipment

In this chapter we describe some characteristics and operation principles of the equipment used in this Thesis.

Laser Diode Mount (Thorlabs TCLDM9)

The TCLDM9 by Thorlabs is a temperature-controlled laser diode mount.

The TCLDM9 uses two thermoelectric coolers (TEC) to precisely regulate the operating temperature of the laser diode. Each TEC element is capable of up 10 W of cooling at a maximum operating current of 5 A. The two TECs are connected in series so that a single connection provides up to 20 W of cooling. Temperature sensing is done by using a temperature transducer that provides a linear temperature monitor proportional to the laser temperature in degrees Celsius. The typical temperature range (laser diode dependent) is from 5 to 70 °C.

Temperature and Laser Diode Controllers (Thorlabs TED200 and Thorlabs LDC202B)

The temperature controller Thorlabs TED200 is a precision temperature controller designed to drive thermoelectric cooler (TEC) elements with currents up to ± 2 A. The temperature is displayed with a resolution of 0.01 °C. The temperature stability is less than 0.002 °C. The operating temperature is from 0 to 40 °C.

The Thorlabs LDC202B laser diode controller has a current range from 0 to 20 mA with a precision of 0.001 mA. Using this controller, laser diodes can be driven in constant current (CC) or constant power (CP) mode. In CC mode, the current to the laser is held precisely at the desired set level. This mode is used when the lowest noise and highest response speed are required. Most applications in this mode require a stable temperature as well. This is the mode that has been used in this wok.

Fiber-optic power meter (Thorlabs PM20)

The Thorlabs PM20 fiber-optic power meter is a fiber-optic power measurement system with built-in optical sensor with FC-PC fiber-connector. The optical power meter has an InGaAs sensor with a size of the diameter of 2 mm. The optical power range that the power meter can measured varies from -60 dBm to 20 dBm. It covers a width range of wavelengths from 400 to 1700 nm. The measurements can be done in dBm or in W. The desired wavelength must be fixed for measuring. The measurement uncertainty is ± 0.25 dB. It can operate between 5 and 40 °C. Optical damage threshold is 50W/cm^2.

Optical Spectrum Analyzer (Anritsu MS9710B)

An optical spectrum analyzer is a device capable of measuring power spectral density for a given range in the optical frequency domain.

Our Anritsu MS9710B optical spectrum analyzer (OSA) is a diffraction-grating spectrum analyzer for analyzing optical spectra. A diffraction grating is an optical quality mirror with thousands of

narrow, closely spaced, depending on the wavelengths of interest, parallel slits. When a collimated light beam attains the diffraction grating, the light is reflected over an angle range given by the grating surface curvature. There are selected directions at which the light waves from the different slits interfere in phase and in these directions the maximums of the light intensity are observed producing an constructive interference. Also it is possible a destructive interference depending on the path difference of rays. This effect will thus be a function of the reflection angle and the wavelength of the light.

Normally, the position of the entrance and exit slits is fixed but the diffraction-grating can be tuned along the wavelength range, the optical power passing through the filter is measured with a photodetector.

The resolution of the analyzer is given by the full width at half maximum (FWHM) of the resultant analysis filter. So this parameter represents the ability of the device to resolve components with similar power and separated a certain wavelength distance.

Another important characteristic of an OSA is the dynamic range defined as the difference between the highest and lowest power that the analyzer can measure simultaneously. A high dynamic range is not capable to resolve the low power components if the spectral components are close.

The sensitivity is another interesting parameter because it represents the minimum power of an input signal to be correctly measured, is defined as six times the rms (root mean square) noise level of the instrument.

The most relevant characteristics of our OSA can be found in Appendix A. Table 1.

Tunable laser (Anritsu tunable laser Tunics Plus)

Our tunable laser is an external cavity semiconductor laser. This device provides the ability to tune the wavelength to any desired value with a continuous characteristic between the actual value

and the target value. Elements characteristics of an external cavity laser are a laser diode chip which anti-reflection coated on its rear facet, a collimating lens, and finally a diffraction grating.

The tilted grating acts alone as an angle-tuned wavelength selective mirror, but the selected wavelength peak, which is fedback in the diode, is rather wide. The laser cavity itself selects all wavelengths for which the optical cavity length is an integral multiple of half-wavelengths, the cavity longitudinal modes. Working with the tilted grating and the laser cavity length, they cause the laser cavity oscillate on a single narrow peak, whose wavelength is determined by the grating angle and cavity length. So, the laser is tuned simply by rotating the grating.

It is known that, working with a constant cavity length, the grating provides a coarse selectivity and the output wavelength does not change until an adjacent cavity mode exhibits a higher gain because the grating feedback has moved far enough, in this case, the wavelength undergoes a sudden change called mode hop. Its magnitude is the cavity mode-spacing, which is determined by the cavity length.

The principle of a continuously tunable source is to compensate mechanically for cavity length in order to stay on the same mode of the cavity over a wide wavelength range. This is achieved by keeping the cavity length/wavelength ratio constant when changing the wavelength.

The external cavity laser consists of a diode laser, a dihedral reflector and a diffraction grating. Continuous wavelength tunability is obtained by rotating the dihedral reflector around of a center of rotation changing only the diffraction angle in such a way the cavity length/wavelength ratio is constant. It ensures a mode-hop-free tunability over a wide wavelength range. Anyway, this design alone does not provide for an absence of mode-hop over the whole range of wavelength, temperature and measurement duration.

To obtain a mode-hope free operation, simultaneous control of the wavelength of the mode and adjustment of the grating feedback response relative to the mode are necessary. A piezoelectric actuator provides a pure rotation on the dihedral reflector. The dihedral reflector changes the location of the feedback response and the mode is performed through a dithering of the dihedral reflector combined with a measurement of the emitted power.

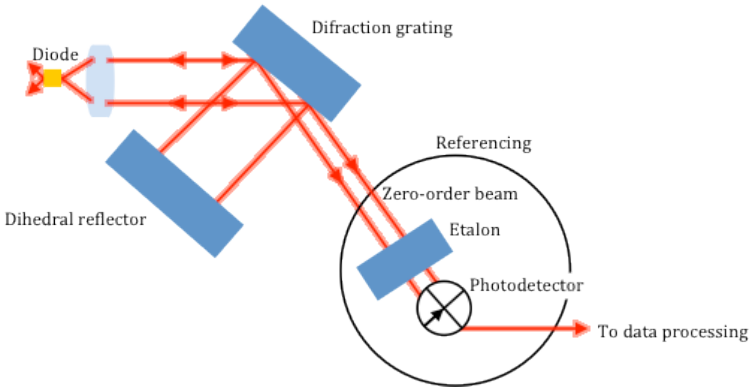

Fig. 4.1. Optical referencing scheme of tunable laser.

The Tunics Plus is a benchtop tunable laser, with a tuning range from 1500 to 1625 nm and with a resolution of 1pm. The output power is up to +8 dBm (6 mW) with a resolution of 0.01mW providing high-dynamic range measurements. Our tunable laser features continuous tunability (without a mode-hop) over a spectral range of more than 30 nm, and accurate wavelength sweep over its entire tuning range. Unfortunately, it is not possible with only the attainable precision and stability of mechanical machining to fully suppress the mode hops, and the wavelength at which a mode hop occurs also depends on temperature and the aging of the system. Therefore, when mode-hop free operation over the full spectral range is needed, a method to automatically compensate for the minute imperfections of the mechanical system is needed. Tunics Plus incorporates this automatic active cavity control in order to obtain a mode-hop free range covering

the full spectrum. The sweeping mode delivers a continuous variation of the wavelength at a constant rate to enable a fast and uninterrupted measurement. The most relevant characteristics of our tunable laser can be found in Appendix A. Table 2.

Oscilloscope (Agilent Technologies 54855A DSO Infiniium Oscilloscope)

The Agilent Technologies 54855A DSO Infiniium Oscilloscope provides full real-time bandwidth of up to 6 GHz and is supported on every channel by the 20 GSa/s sample rate. The most relevant characteristics of our oscilloscope can be found in Appendix A. Table 3.

High resolution optical spectrum analyzer (Aragon Photonics BOSA 210)

Stimulated Brillouin Scattering (SBS) is a nonlinear effect with a very narrow interaction bandwidth that, pumped with a tunable light source, can be used to select a narrow slice of the optical spectrum of a signal, and thus be used for optical spectrum analysis.

SBS is generated when an optical wave with enough power and narrow spectrum travels through a nonlinear medium as a optical fiber producing acoustic waves, caused by thermal effects in the core of the fiber. This acoustic wave generates a modulation of the refractive index of the medium. This is equivalent to an index grating, whose Bragg's frequency corresponds in principle, with the input optical signal which is partially reflected in the backward direction. Actually, the acoustic wave moves through the core of the fiber with an acoustic velocity v_A. This originates a Doppler shifted frequency ν_D of the Bragg's frequency which is reflected (to lowest frequency).

Physically, SBS can be considered as a process in which participate three waves, the input optical signal (or pump wave), with a frequency ν_0, the acoustic wave with a frequency ν_D and the third one, the Stokes's wave $\nu_S=\nu_0-\nu_D$, originated by the movement of the grating, which moves in the opposite direction of

the pump wave. So, the movement of the grating moving at the speed of the acoustic wave, produces a frequency downshift due to Doppler effect which is maximum for the backward direction and given by $\nu_D=2n\upsilon_A/\lambda_p$ where λ_p is the wavelength of the wave causing the backscattering, referred to as pump wave and *n* is the refraction index.

The High Resolution Optical Spectrum Analyzer (BOSA) uses the narrow Brillouin amplification window to obtain the optical spectrum of a signal with a resolution of 0.08 pm (10 MHz). The measurement process consists in a tunable laser (TL) which continuously changes its wavelength along the spectral range of interest, and the simultaneous detection of the Brillouin backscattered light.

Since the TL is changing in wavelength, different spectral components of the signal under test are backscattered and amplified. In other words, the Brillouin effect generates an active tunable optical filter of 0.08 pm width. By modifying the wavelength of the pump it is possible to amplify selected spectral components of the signal. All the filtering process takes place in the optical domain and the spectral information of the signal under test is directly reaching the detection stage. An acquisition set up synchronized with the TL sweep stores and process the data. The TL sweep speed can be set at high values to obtain almost real time measurements.

The interferential nature of the Brillouin interaction between measured and pump beams implies the need for a proper alignment of the polarization states of both beams in order to get the greatest efficiency in the generation of the measured signal. Specific mechanism and algorithms are internally used by the BOSA to compensate and calibrate these variations by actively controlling the polarization state of the pump beam.

The nonlinear power amplification found in the backscattered signal allows the detection of spectral components at very low power levels. Spectral components with power density of -70 dBm/

0.08 pm can be detected.

The finesse of the optical filter provided by SBS is not achievable by the diffraction gratings technique used in conventional OSA. Moreover, the Brillouin effect does not impose any incompatibility between resolution and dynamic range, so it is possible to keep the highest values on those parameters for any measurement span. The most relevant characteristics of our BOSA can be found in Appendix A, Table 4.

Fiber Fabry-Perot Tunable Filter (Micron Optics FFP-TF2)

The Fabry-Perot interferometer, generates the interference pattern that is characteristic of the spectral features of the laser under test. A simple device that relies on the interference of multiple beams, the Fabry-Perot interferometer consists of two partially transmitting mirrors precisely aligned to from a reflectivity cavity. Incident light enters the Fabry-Perot cavity and undergoes multiple reflections between the mirrors so that the light interferes with itself many times.

Free Spectral Range (FSR) and finesse can be considered two of the most important characteristics of a Fabry-Perot interferometer-based laser spectrum analyzer. FSR is the interferometer's spectral measurement window of the frequency bandwidth over which it is possible to measure without overlapping different interference orders. Therefore, to obtain meaningful measurements, the FSR must be greater than the spectral bandwidth of the laser under test. The general rule is that the FSR should be at least twice the laser's spectral bandwidth. At the same time, for the highest resolution measurements, the FSR should be as small as possible.

Finesse is a dimensionless value used to quantify the performance of a Fabry-Perot interferometer. A higher finesse value indicates a greater number of interfering beams, resulting in a more complete interference process and therefore higher resolution measurements. The relationship between finesse, the

laser spectrum analyzer's spectral resolution (FWHM) and the minimum resolvable bandwidth is represented by equation:

$$FWHM = FSR/Finesse$$

The FSR must be large enough to have only one resonant wavelength in the spectral range of the interest, but this also causes the FWHM to increase in the same proportion creating a compromise that must be considered for each applications. In Fig. 4.2. we can see this parameters graphically.

For spectral analysis, a scanning Fabry-Perot can be easily obtained by displacing one of both parts of the resonator to change the path length and thus the resonant wavelengths.

The Micron Optics FFP-TF2 Fiber Fabry Perot (FFP) Tunable Filter is a specialized filter based on the all-fiber Fabry-Perot etalon technology. The FFP tunable filter passes wavelengths that are equal to integer fractions of the cavity (etalon) length; all other wavelengths are attenuated according to the Airy function.

The key to the design on the FFP tunable filter is the lensless fiber construction. There are no collimating optics or lenses, thus the FFP tunable filter achieves high finesse and maintains a low loss transmission profile.

In Fig. 4.3. we can see the design of the fiber Fabry-Perot tunable filter of Micron Optics. Increasing the voltage to the PZT (piezoelectric element) decreases the cavity length. Changes in cavity length by modulation of PZT drive voltage yield corresponding changes to the FP resonance frequency. The cavity is comprised mostly of glass with only a small air-gap comprising the remainder. This small air-gap allows, for the compression or expansion of the cavity length which results in the filters ability to be tuned. The most relevant characteristics of our Fabry-Perot can be found in Appendix A, Table 5.

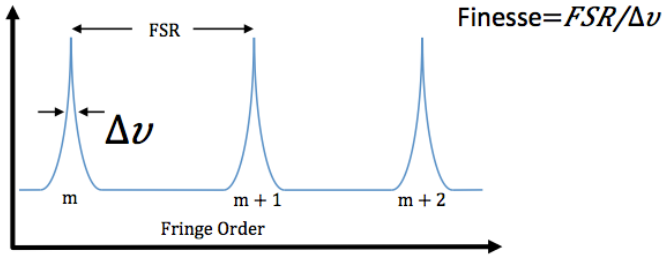

Fig. 4.2. Typical transmission pattern of Fabry-Perot Interferometer.

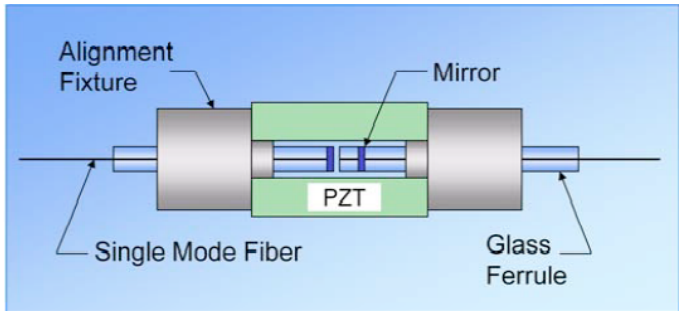

Fig. 4.3. Structure of the fiber Fabry-Perot Tunable Filter (Micron Optics FFP-TF2)

To control the PZT in the FFP tunable filter we use a tunable filter controller (Micron Optics FFP-C). The Micron Optics FFP-Controller is an electronic piezoelectric actuator driver and optical signal processor specially designed for the FFP Tunable Filter or Scanning Interferometer. The most relevant characteristics of our tunable filter can be found in Appendix A, Table 6.

Microwave Spectrum Analyzer (Anritsu MP1800A)

The Anritsu Microwave Spectrum Analyzer is a synthesizer-based spectrum analyzer that provides quick and accurate measurement results. Measurements can be made using the main instrument functions: frequency, span, amplitude, and bandwidth. The analyzer is designed for monitoring, measuring, and analyzing signal environments. The instrument can display the spectral

components of a signal. It measures the optical power in dBm of the signal which proceeds of the photodetector versus the frequency. Resolution bandwidth is determined by the intermediate frequency (IF) filter bandwidth. The Spectrum Analyzer traces the shape of the IF filter as it tunes past a signal. If more than one filter is used in a Spectrum Analyzer, then the narrowest one dominates and is considered the resolution bandwidth.

The choice of resolution bandwidth will depend on the signal being measured. If two closely-spaced signals are to be measured individually, then a narrow bandwidth is required. If a wider bandwidth is used, then the energy of both signals will be included in the measurement.

Some amount of noise is always present in a measurement. Noise is often broadband in nature; that is, it exists at a broad range of frequencies. With a wide bandwidth, more noise is included in the measurement. With a narrow bandwidth, less noise enters the resolution bandwidth filter, and the measurement is more accurate. This is because the IF filter of the analyzer has been made narrower in bandwidth, which lets in less noise.

Spectrums Analyzers typically use another type of filtering after the detector called video filtering. This filter also affects the noise on the display but in a different manner than the resolution bandwidth. In video filtering, the average level of the noise remains the same but the variation in the noise is reduced. Hence, the effect of video filtering is a "smoothing" of the signal noise. The resultant effect on the analyzer's display is that the noise floor compresses into a thinner trace, while the position of the trace remains the same.

Changing the video bandwidth (VBW) does not improve sensitivity, but it does improve repeatability when making low-level measurements.

The sweep rate is not usually chosen by the user but is determined by the frequency range swept divided by the sweep

time. The limitation on sweep rate comes from the settling or response time of the resolution and video bandwidth filters. If an analyzer is swept too quickly, then the filters do not have time to respond, and the measurement is inaccurate. Under such conditions, the analyzer display tends to have a "smeared" look to it, with the spectral lines being wider than normal and shifted to the right. The most relevant characteristics of our analyzer can be found in Appendix A, Table 7.

Fiber Optical Isolator (ISC-1550 Newport)

Isolators are used to reduce or eliminate the effects of optical feedback-reflections of the laser's energy back into itself. These effects include noise, amplitude fluctuations, and even laser damage. Isolators protect the laser and provide maximum forward transmission and reverse isolation.

An isolator consists of a Faraday rotator, two polarizers and a housing. The Faraday rotator consists of a magneto-optic material within a magnetic field. In the forward mode the laser lights enters the isolator via the input polarizer and is linearly polarized. It then enters the rotator, which rotates its plane of polarization 45º. It then exits via the output polarizer, whose axis is 45º from the input plane of polarization. In the reverse mode some random beam reflections will be reflected back towards the laser. This feedback re-enters the isolator via the output polarizer and is polarized at 45º. It continues into the rotator and is rotated by another 45º. The feedback, now polarized at 90º relative to input polarizer, is extinguished. The laser is now isolated from its own reflections. The most relevant characteristics of our isolator can be found in Appendix A, Table 8.

Polarization Beam Combiner/Splitters (Newport F-PBC-15-SM-FA)

Our polarization Beam Combiner/Splitters can be used to combine light from two SM-28 input fibers into a single output fiber, or to separate the orthogonal polarization components of an input signal between two output fibers. Light from an input fiber is first collimated, then sent through a beam splitting optic to divide it

into two. The resultant output beams are then focused back into the output fibers. These rugged bulkhead devices use FC/APC connectors and have a wide operation bandwidth and high power handling capability. The most relevant characteristics of our beam splitter can be found in Appendix A, Table 9.

Fiber U-Bench Polarization controller (Thorlabs FBR05)

The polarization controller Thorlabs FBR05 utilizes three miniature waveplates placed between two prealigned fiber collimators. Using this approach to polarization control with fiber optic systems is significantly more stable than the looped fiber (paddle) controllers.

The Fiber U-bench polarization controllers is extremely stable, insensitive to both temperature variations & mechanical disturbances. It contains three rotating wave plates (1/4-wave: 1/2-wave: 1/4-wave) configuration for total polarization control. The retarders have precise continuous rotation through 360° and can produce any possible polarization state. The plates are rotated manually until you achieved the desired polarization. It is used on a trial and error method. The most relevant characteristics of our polarization controller can be found in Appendix A, Table 10.

Fiber Optic Circulators

Fiber Optic Circulators are non-reciprocating, one directional, three-port devices that are used in a wide range of optical setups and for numerous applications.

An optical circulator is a three-port device that allows light to travel in only one direction. A signal entered to Port 1 will exit Port 2, while a signal entering Port 2 will exit Port 3 all with minimal loss. Light entering Port 2 experiences large amount of loss at port 1,and light entering port 3 experiences a large amount of loss at ports 2 and 1. Optical circulators are non-reciprocal optics. This means that any change in the properties of the light caused by passing through the device are not reversed by traveling in the opposite

direction.

Fiber Optic circulators can be polarization maintaining or non-polarization maintaining. In our work, we use both of them, the first one is a polarization maintaining optical circulator by Opto-Link Corporation Ltd and the second one is a non-polarization maintaining optical circulator by Newport.

The first one, consists of polarization-maintaining fibers. This type of fibers have strong birefringence so that the polarization of light launched into the fiber is aligned with one of the birefringent axes, this polarization state will be preserved even if the fiber is bent. The method more efficient to introduce a high birefringence in an optical fiber is to generate asymmetric internal stresses over the core. It is achieved doping areas with a coefficient of thermal expansion different, in such a way that when they are cooled, they created strengths over the core in the symmetry axis of the fiber. The most relevant characteristics of our optical circulators can be found in Appendix A, Tables 11 and 12.

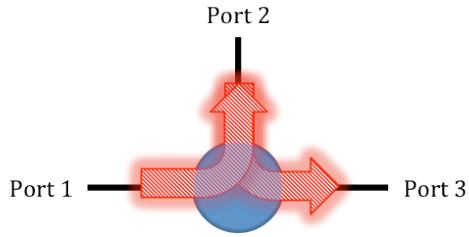

Fig. 4.4. Optical circulator

Tunable Bandpass Fiber Optic Filter (Newport TBF-1550-1.0)

In many fiber-optic applications we need to use light with a specific frequency or wavelength. Bandpass filters provide an effective means of transmitting a well-defined band of light while blocking unwanted wavelengths emanating from a broadband source.

The tunable filter consist of a collimating optical assembly, an adjustable narrow bandpass filter, and a focusing optical assembly to collect the light again. Our filter is used to adjust the center wavelength of a narrow passband within a 30 nm range around 1550 nm with a 1 nm bandwidth. The filter features high isolation, low insertion loss, low-back reflection and low polarization sensitivity.

A thin film coating interference filter, located between two angled fiber optic collimators, is used to select the wavelength of interest, by adjusting the tilt angle of the filter with a high-precision micrometer having 0.05 nm resolution (See Fig. 4.5). The most relevant characteristics of our tunable filter can be found in Appendix A, Table 13.

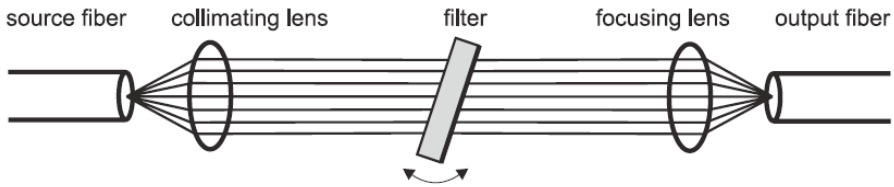

Fig. 4.5. Conceptual design of a tunable filter.

Amplified Fiber Optic Photo Detector (PDA8GS by Thorlabs)

When measurements are performed in the electrical domain, the signal must be detected using a photodiode. The photodiode gives a current proportional to the squared modulus of the opto-electric field with a conversion efficiency given by its responsivity.

Our PDA8GS is a high-speed, amplified photodetector designed to perform in a wide range of test and measurement applications involving fast optical signals. The unit incorporates a high-performance InGaAs PIN photodiode coupled with a transimpedance amplifier that has a gain of 450 V/A into 50Ω. It has a 8 GHz bandwidth. Our photodetector exhibits linear performance across the input range, yielding low analog distortion. The most relevant characteristics of our detector can be

found in Appendix A, Table 14.

Single Mode, Variable Fiber Optical Attenuators: Inline (VOA50-APC Optical Attenuator by Thorlabs)

We have used this manually adjustable, inline variable optical attenuator (VOA)to precisely balance the signal strengths in fiber circuits. Variable attenuators consist of two baseplates with lenses which are aligned to achieve the maximum coupling efficiency. The attenuation is adjusted using a screw on the side of the attenuator housing. Rotate the screw block the collimated beam between the two lenses because it changes the position of the collimated beam and for this reason the power level coupled into the receiver fiber. These in-line VOAs include SMF-28 single mode fiber. The connectors are FC/APC. The most relevant characteristics of our variable optical attenuator can be found in Appendix A. Table 15.

Optical Fiber 50/50 Coupler (Newport F-CPL-F12155)

A coupler consists of two fibers which are closer during a stretch of its length so that some of the light which enters through the input fiber is transferred to the other fiber due to the coupling of the evanescent wave. The more distance they are together, the more light is coupled. The coupling ratio depend on the length in which both fibers are parallel and close to each other. The optical fiber couplers allow bidirectional coupling and can be used to either split or combine signals. This 1x2 coupler has a 50/50 (3 dB)coupling ratio. The most relevant characteristics of our 50/50 coupler can be found in Appendix A, Table 16.

90/10 Coupler (Thorlabs 10202A-90-FC)

Thorlabs 10202A-90-FC single mode 2x2 fiber coupler has a center wavelength of 1550 nm and a split ratio of 90:10. Additionally, the coupler is bidirectional, allowing anyone of the ports to be used as an input port. The coupler has FC/PC connectors. The most relevant characteristics of our 90/10 coupler can be found in Appendix A, Table 17.

Multimode and singlemode quantum-well 1550 nm-VCSELs (Raycan)

In most experiments performed in this work we have used commercial multimode and single-mode quantum-well 1550 nm-VCSELs by Raycan.

They are fabricated on a substrate of InP. The active region, which has a thickness of 0.5λ, consists in multiples quantum wells. The active medium is localized between two plates of n-InP. These plates are used to spread with high efficiency hot and decrease the device's resistance. The part of the top and bottom DBR's mirrors is constituted for alternating layers of InAlAs/InAlGaAs. Figure 4.6 shows the structure of the 1550 nm VCSEL.

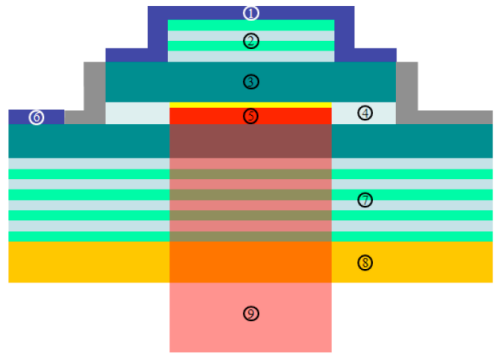

Fig. 4.6. Structure of the 1550nm VCSEL where 1 is the top contact, 2 the top DBR, 3 represents the InP spacer, 4 the current confinement, 5 the active MQW, 6 is the bottom contact, 7 the bottom DBR, 8 is the InP substrate and 9 the light emitted by the VCSEL.

CHAPTER 5

Experimental study of relative intensity noise of multimode vertical-cavity surface-emitting lasers

We have performed an experimental investigation of the relative intensity noise (RIN) spectra of multimode 1550 nm VCSELs. Several types of multi-transverse mode VCSELs have been considered. The first one emits in two transverse modes for large values of the bias current. Both modes are linearly polarized and have parallel polarizations. Two resonance peaks appear in the noise spectra of the individual modes and total power of the VCSEL in agreement with previous theoretical studies [Valle 2004]. We have measured the frequencies corresponding to both peaks as a function of the bias current. We have obtained a similar dependence to the one found in the previous work. The second VCSEL type corresponds to a laser emitting at three different transverse modes for large values of the bias current. Similar behaviors are found while the bias current is small. Emission in three transverse modes with different

polarizations is accompanied by the appearance of additional peaks in the noise spectra. It is suggested that the VCSEL polarization plays an important role in determining the multi-peaked structure of noise spectra. That is confirmed by measuring with another two-transverse mode VCSEL showing polarization instabilities in both transverse modes. It is shown that large values of the bias current applied to this VCSEL result in a complex dynamics characterized by the appearance of many additional peaks in the noise spectra.

5.1. Introduction

Multimode 850-nm vertical-cavity surface-emitting lasers (VCSELs) are the emitters of choice for high-capacity applications in short-distance fiber communication systems [Iga 2000], [Koyama 2006], [Freund 2010], [Gholami 2006]. Simultaneous emission in multiple transverse modes ensures low source coherence, greatly minimizing interference effects like the modal noise-induced bit error rate in multimode fiber systems [Hahn 1993]. Long-wavelength VCSELs emitting in several transverse modes are also of interest for use in the fiber metropolitan area network because of their low cost [Parekh 2008]. Emission in multiple transverse modes is usually found in VCSELs and is attributed to spatial hole burning effects [Changhasnain 1991], [Valle 1995], [Buccafusca 1996]. Also the VCSEL polarization is not well fixed and small changes of the injection current or the device temperature may result in polarization switching between the two linearly polarized modes [Choquette 1995], [MartinRegalado 1997b], [Valle 1997], [Ryvkin 1999]. Several experimental studies show that the emission in several transverse and polarization modes affects quantities like the relative intensity noise (RIN) [Hahn 1994], [Raddatz 1994], [Kuchta 1993], [Mahon 1993], [Vey 1999], [Zei 2001], [Hermier 2001], [Principato 2006],[Molitor 2010] and the small-signal modulation response [Satuby 1998], [Satuby 1999] of VCSELs. The understanding of those quantities is important for a variety of applications as for instance in optical communications systems [Zei

2001], optical interconnects [Principato 2006] and in biomedicine [Thrush 2004], [Lee 2008].

Theoretical investigations of RIN in linearly polarized multimode VCSELs have shown that the RIN spectra of individual transverse modes [Zei 2001], [Law 1997a], [Valle 2001], [Valle 2004] and of the total power [Valle 2001], [Valle 2004] have several maxima. Experiments have demonstrated that filtered RIN spectra have multiple resonance peaks [Zei 2001]. Also experimental RIN spectra of the total power have displayed several peaks [Kuchta 1993]. Localized increases of RIN at low frequencies as a function of the bias current have also been experimentally observed [Molitor 2010], [Raddatz 1994], [Kuchta 1993] in good agreement with the theory [Valle 2001], [Valle 2004]. Theoretical modeling of RIN in parallel polarized multimode VCSELs has been performed by using spatially independent [Zei 2001] and spatially dependent [Law 1997a], [Valle 2001], [Valle 2004] stochastic rate equations. Analytical expressions of the RIN obtained with the previous spatially dependent models show that there are two resonance peaks in the noise spectra of the individual modes and total power of a two transverse mode VCSEL [Valle 2004]. Those peaks appear at frequencies that correspond to the relaxation oscillation frequencies of the multimode laser [Valle 2004]. The dependence of the frequencies at which RIN peaks appear on the bias current applied to the VCSEL has also been obtained theoretically [Valle 2004]. Although some experimental results show multiple-resonance peaks in the RIN of individual modes [Zei 2001] and of the total power [Kuchta 1993] there are no systematic experimental investigations of the dependence of RIN spectra of multimode VCSELs on their applied bias current.

5.2. Experimental setup

The measurements were performed on two different quantum-well commercial VCSELs that emit around 1560 nm. The bias current and temperature were controlled by a laser driver and a

temperature controller, respectively. Temperature was held constant at 297K during the experiments. Spectral measurements were performed by using an Optical Spectrum Analyzer, a Fabry-Perot (FP) Optical Spectrum Analyzer and a RF-spectrum analyzer. The output of the VCSEL was coupled into an optical isolator after which a 50/50 coupler split the light in two detection arms. In the first arm an amplified photodetector and the RF-spectrum analyzer were used to obtain the noise spectra. In the second arm the optical spectra were measured by using the OSA or the FP analyzer.

Fig. 5.1 shows the optical spectrum of the first VCSEL (VCSEL 1) obtained by the OSA at two different bias currents, I_{VCSEL}. The aperture diameter of the VCSEL is around 12μm. For small values of the bias current the VCSEL emits in a single transverse mode with a wavelength near 1560 nm, as it is shown in Fig. 5.1 (a). The two peaks that appear at longer wavelengths correspond to the two orthogonal linear polarizations of the fundamental transverse mode. We have checked that both peaks correspond to orthogonal linear polarizations by using a polarization beam splitter. The reason of the polarization splitting of the transverse modes is the strong birefringence due to the strain of the material introduced during manufacturing of the VCSEL. The lowest of those peaks (1560.5 nm) corresponds to the depressed polarization (the so-called orthogonal polarization) of the fundamental transverse mode. The dominant linear polarization (the so-called parallel polarization) of the fundamental mode appear at a shorter wavelength (1559.95 nm). This VCSEL is characterized by a large value of the birefringence parameter because the frequency difference between both linear polarizations is 68.8 GHz. The peaks that appears at shorter wavelengths correspond to non-lasing higher-order transverse modes. For larger values of the bias current the VCSEL emits also in a higher-order transverse mode as it can be seen in Fig. 5.1 (b).

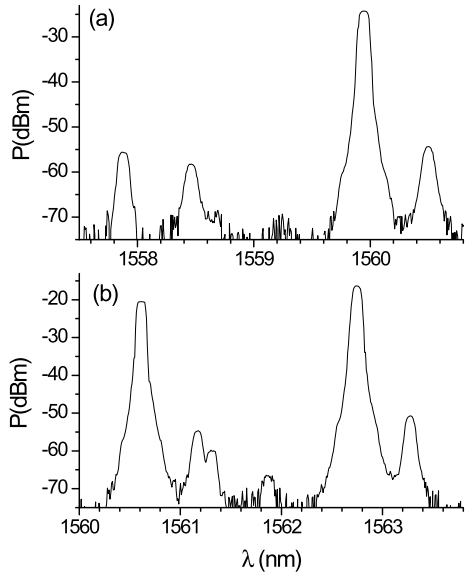

Fig. 5.1. Optical spectrum of VCSEL 1 when the applied bias current is (a) 3.51 mA and (b) 9.80 mA.

The higher-order mode appears at a wavelength of 1560.61 nm with a linear polarization that is parallel to that of the fundamental mode. We have checked that the polarizations of both transverse modes are parallel by using a polarization beam splitter. The frequency difference between the parallel polarized fundamental and higher-order transverse mode is around 267.5 GHz. That frequency separation is large enough to separate the contributions of each transverse mode to the total power with a bandpass tunable filter. In this way the transverse-mode resolved Light-current characteristics of the VCSEL 1 can be obtained.

Fig.5.2 shows the power of the transverse modes and the total power as a function of the bias current. Only two transverse modes contribute to the total power in an appreciable way. Both modes have the parallel polarization over the whole bias current range. In this way the VCSEL 1 is an example of a linearly polarized two-transverse mode VCSEL whose behavior was described in a theoretical work [Valle 2004]. We also observe in Fig. 5.2 that the

power of each transverse mode depends linearly on the bias current. The slopes of these straight lines change when the new transverse mode appears at 3.9 mA. That value correspond to 1.38 times the threshold current, I_{th} (I_{th}=2.83 mA). For bias currents smaller than 7.5 mA those observations are in agreement with a previous theoretical work that described analytically the transverse mode resolved L-I characteristics of weakly-index guided multimode VCSELs [Valle 2002]. The disagreement with the theoretical predictions when the bias current is larger than 7.5 mA could be attributed to the fact that the theoretical hypothesis of fixed transverse modal profiles is no longer fulfilled at those large values of the current.

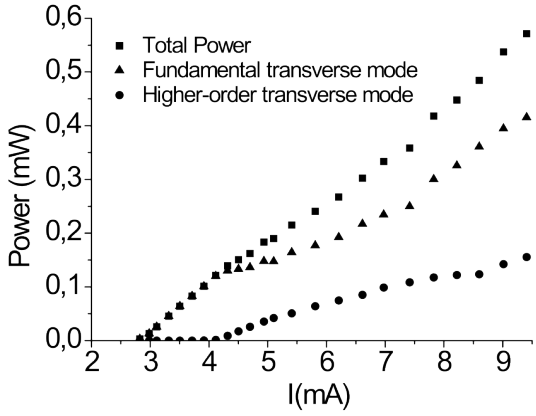

Fig. 5.2. Power of the transverse modes and total power of VCSEL 1 as a function of the bias current.

5.3. Intensity noise spectra of parallel polarized two-mode VCSEL

In this section we analyze the intensity noise spectra of the individual modes and total power as a function of the bias current applied to the parallel polarized two mode VCSEL 1. Fig. 5.3 shows the spectra (thin lines) of the total power, obtained in the RF

spectrum analyzer, for six different values of the bias current, I. There are many peaks separated by a constant frequency difference of around 100 MHz in all the spectra. That frequency difference corresponds to the reflections that occur at the end of the one meter fiber that is pigtailed to the VCSEL. The underlying structures of those peaks have been obtained by performing the Savitzky-Golay smoothing algorithm. The smoothed spectra are also plotted in Fig. 5.3 with thick red lines. Fig. 5.3 (a) shows that when the VCSEL emits in the fundamental transverse mode there is only one clear peak in the smoothed spectra at 0.9 GHz (a much weaker harmonic peak appears at 1.8 GHz). The frequency at which the peak appears increases as the bias current increases as it can be seen in Fig. 5.3 (b). Harmonics of the main peak appear because the power fluctuations have an underlying periodic structure. Fig. 5.3 (c) shows that the excitation with significant power of the higher-order transverse mode (see also Fig. 5.2) is accompanied by the emergence of a second peak at a lower frequency (0.75 GHz). The bump that appears at 1.5 GHz corresponds to the first harmonic of that peak. In a similar way Fig. 5.3 (d)-(f) show that two clear peaks appear in the smoothed spectrum for larger values of I for which only two transverse modes are excited. Further small peaks also appear at larger frequencies in Fig. 5.3 (d)-(f) that correspond to sum-frequency of the lower frequency peaks. Fig. 5.3 then shows that two resonance peaks appear in the spectra of the total power of a VCSEL that emits in two parallel transverse modes in agreement with previous theoretical studies [Valle 2004].

The intensity noise spectra that correspond to individual transverse modes were also measured by inserting the tunable bandpass filter before the RF-spectrum analyzer. Fig. 5.4 shows the intensity noise spectrum of the fundamental, higher order transverse mode and of the total power for different values of the bias current. As in Fig. 5.3 the non smoothed and smoothed data are plotted with thin and thick solid lines, respectively. Fig. 5.4

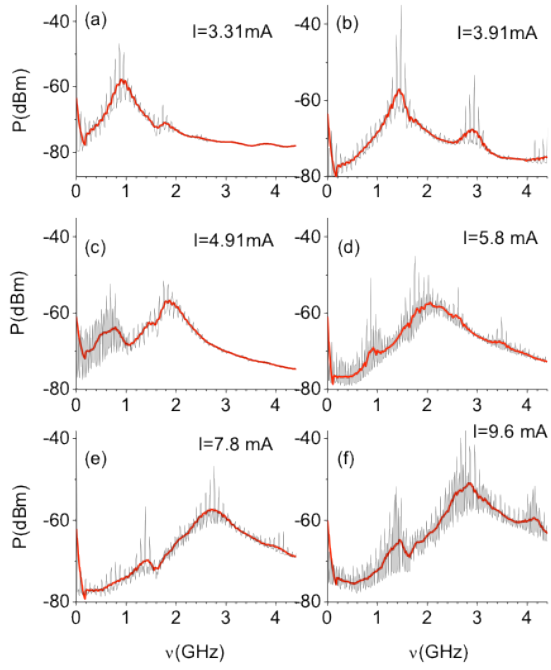

Fig. 5.3. RF spectra of the total power of the two-transverse mode VCSEL at different values of the bias current. The smoothed spectra are plotted with thick (red) lines.

shows that in the two-transverse mode regime the spectra of the individual transverse modes have also two peaks that appear at the same frequencies than those corresponding to both peaks of the spectrum of the total power. This result is also in agreement with previous theoretical analysis [Valle 2004]. RIN spectra of individual modes are usually higher than that of the total power [Valle 2001], [Valle 2004]. However, Fig. 5.4 shows that RF spectra of individual modes are smaller than that of the total power. This can be explained by the way of measuring our RF spectra. A tunable filter is placed before the RF-spectrum analyzer to measure RF spectra of individual modes in contrast to the measurement of the RF spectra of the total power in which no filter is used. The tunable filter produces a significant loss of power that lowers RF spectra of individual modes below that of the total power. We also note that

the RIN is obtained from the RF spectra by normalizing with the square of the averaged power [Valle 2001], [Valle 2004] and therefore they are not the same quantities.

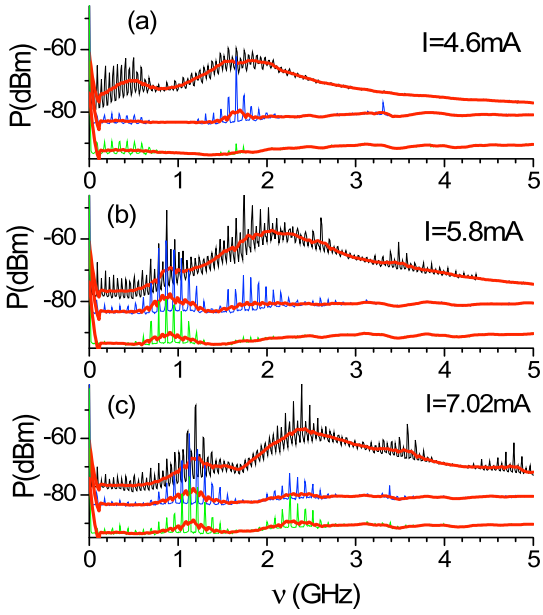

Fig. 5.4. RF spectra of the individual transverse modes and of the total power of the two-transverse mode VCSEL at different values of the bias current. Upper (black), middle (blue) and lower (green) curves correspond to the spectrum of the total power, fundamental and higher order mode, respectively. The spectrum of the higher-order mode is shifted in -10 dBm for the sake of clarity. The smoothed spectra are plotted with thick(red) lines.

We showed in Fig. 5.3 that the frequencies at which the spectrum of the total power has a maximum increase as the bias current is increased. We show in Fig. 5.5 (a) the detailed dependence of those frequencies on the bias current. We have plotted the frequencies obtained with the smoothed spectra. For currents smaller than 3.9 mA the VCSEL is single transverse mode and the noise spectrum has only one maximum. The typical linear relationship between the square of that frequency and $I-I_{th}$ is

obtained in the single mode regime as illustrated in Fig. 5.5 (b). When the laser begins to emit in the two transverse modes the spectra develops two maxima as it is shown in Fig. 5.5 (a). This situation is maintained for larger values of the bias current. Both frequencies at which the noise spectra has a maximum increase when increasing the current until saturating when I>7.5 mA. The theoretical results of Ref. [Valle 2004] show similar trends to the observed in our experiment while I<7.5 mA. We have performed a detailed analysis of the frequency versus current dependence. The dependence of the frequency of the second peak on the current is such that $\nu \sim (I-I_{th,h})^{0.6}$ where $I_{th,h}$ is the threshold current of the high-order mode.

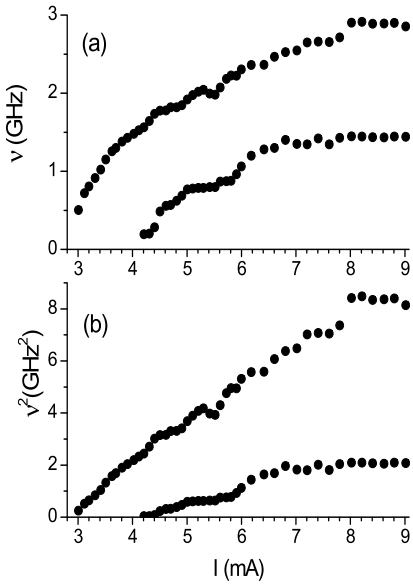

Fig. 5.5. (a) Frequencies and (b) Frequencies squared at which the noise spectrum of the total power is maximum versus the bias current obtained with VCSEL 1.

The theoretical results of Fig. 6 of Ref. [Valle 2004], obtained for a VCSEL with half the diameter of our VCSEL, are such that

$\nu \sim (I-I_{th,h})^{0.52}$. We note that the range of bias currents at which the theoretical predictions fail (I>7.5 mA) is similar, in particular for the current-dependence of the power of individual transverse modes and that of the frequencies at which the spectrum has a maximum. We believe that in this bias current range the failure of the theory for describing the experimental results can be related to the theoretical assumption of fixed transverse modal profiles that could not be the case for large values of I as it was already discussed in relation to Fig. 5.2.

5.4. Intensity noise spectra of a three-mode VCSEL with polarization instabilities

We now analyze the current-dependence of the noise spectrum of another VCSEL (VCSEL 2) that is characterized by the appearance of a third transverse mode at large values of the bias current. While the VCSEL is emitting in the three transverse mode regime we find changes in the polarization of the modes as the current is changed. Our three-mode VCSEL has a threshold current of 3.65 mA. Above that current value the VCSEL emits in the fundamental transverse mode (mode 1) until a higher order transverse mode (mode 2) begins to appear at I=7.5 mA. The third transverse mode (mode 3) appears with significant power at I=11.5 mA. Intensity noise spectra similar to those of the previous section are observed while the VCSEL is emitting in one or two transverse modes (I<11.5 mA). Moreover the current-dependence of the frequencies at which the spectrum of the total power is maximum is similar to that presented in the previous section if I<8 mA. That similar behavior is shown in Fig. 5.6 in which those frequencies are plotted as a function the bias current. As in Fig. 5.5 two clear peaks appear at the bias current (slightly below 8 mA) at which the VCSEL begins to emit in two transverse modes. Both frequencies increase when increasing the current until saturation is reached. The dependence of the frequency of the second peak on the current is such that $\nu \sim (I-I_{th,h})^{0.99}$. This exponent is clearly different to that obtained for

VCSEL1. This difference can be explained in the following way. The threshold current of the high-order mode VCSEL2 is much larger than that of VCSEL 1. Then the high-order mode is excited at values of the bias current at which saturation has been reached, as it can be seen in Fig. 5.6. As discussed in the previous section that situation corresponds to the range of bias currents at which the theoretical predictions fail.

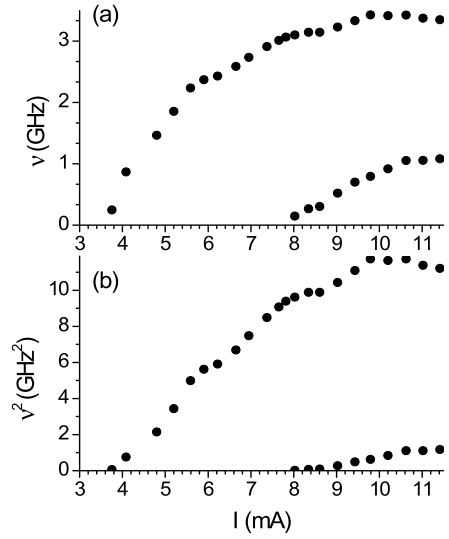

Fig. 5.6. (a) Frequencies and (b) Frequencies squared at which the noise spectrum of the total power is maximum versus the bias current obtained with VCSEL 2.

We also note that the theory of Ref. [Valle 2004] describes RIN spectra for arbitrary spatial coupling between two transverse modes. The theoretical results of Ref. [Valle 2004] show that an 0.5 exponent is obtained if non coupled modes are considered. The consideration of strongly coupled modes can change the exponent although it has not been studied in detail in [Valle 2004].

The optical spectrum of VCSEL 2 obtained with the F-P spectrum analyzer is shown in Fig. 5.7 for several values of the bias current. All the frequencies in this figure are measured with respect

to the frequency of the parallel polarized fundamental transverse mode (referred as mode $1_{\parallel}$). Single fundamental mode emission in the linear parallel polarization is illustrated in Fig. 5.7 (a). An example of the optical spectrum in the two-mode regime is shown in Fig. 5.7 (b) where the parallel polarized higher order mode (referred as mode $2_{\parallel}$) appears at a frequency of 123. 7 GHz when I=10.88 mA. A parallel polarized third transverse mode (mode $3_{\parallel}$)emits with significant power (SMSR with respect to mode $2_{\parallel}$ smaller than 10 dB) when I>11.5 mA. The mode $3_{\parallel}$ is the mode that appears at a 107.1 GHz frequency in Fig. 5.7 (c). The corresponding optical spectrum at the OSA show that each of those three modes has an associated peak that appears shifted around -40 GHz with respect to their frequency. Those peaks correspond to the orthogonal polarizations of the transverse modes (referred from now on with the $\perp$ subindex).

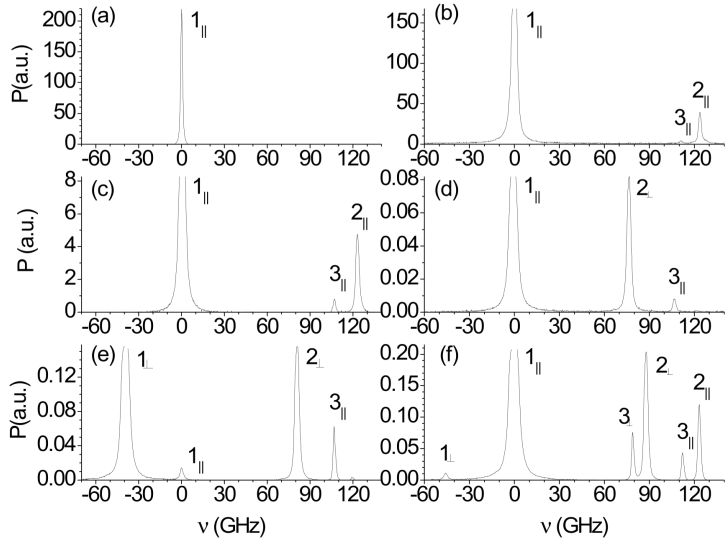

Fig. 5.7. Optical spectrum of the three-mode VCSEL (VCSEL 2) for several values of the bias current: (a) 7.2 mA (b) 10.88 mA, (c) 12.36 mA (d) 12.46 mA (e) 12.76 mA, and (f) 13.01 mA.

Fig. 5.7 (d) illustrates how one of those orthogonal modes (mode $2_{\perp}$) is excited while the corresponding parallel mode is suppressed. Then a polarization switching (PS) of the mode 2 has occurred at that value of the current (I=12.46 mA). Further PS of the mode 2 appear at I=12.49 and 12.54 mA. Fig. 5.7 (e) illustrates a different PS: when I=12.76 mA the polarization of the fundamental mode switches to the orthogonal one. The mode 1 remains in the orthogonal polarization only in a narrow current range because it switches back again at I=12.85 mA. Fig. 5.7 (f) shows that the optical spectrum becomes more complex at larger values of the current because there is an excitation of both polarizations of the higher order transverse modes.

Noise spectra of the total power obtained with this VCSEL are shown in Fig. 5.8 for several values of the bias current. In contrast with the experimental setup of the previous section, we have now used index-matching gel at different fiber FC/PC connectors in order to minimize the reflections in those connections. The reflection peaks that appear in the noise spectra of Fig. 5.8 are much less pronounced than in Fig. 5.3 (we note that the graphs shown in Fig. 5.8 correspond to the direct data obtained in the RF-spectrum analyzer: no smoothing is applied). A similar behavior to the one obtained with VCSEL 1 is shown in Figs. 5.8 (a)-(c). In Fig. 5.8 (a) the laser emits in a single mode and only one clear peak appears in the spectrum. In Figs. 5.8 (b)-(c) only two parallel polarized transverse modes have significative power and a couple of broad peaks are apparent in those spectra. The situation described above changes as the bias current increases to values where PS of transverse modes begin to occur. Fig. 5.7 (d) and Fig. 5.8 (d) show that when the mode 2 switches its polarization a couple of additional peaks appear at 11.1 and 13.5 GHz while the structure of the spectrum at frequencies smaller than 6 GHz remains similar. As the bias current increases three additional peaks begin to emerge. The first two appear at 8.4 and 2.5 GHz while the third one develops gradually from frequencies near zero to around 145 MHz. That situation is illustrated in Fig.5.8 (e). The value of 2.5

GHz corresponds to the frequency difference between the two peaks that appear at the largest frequencies. These peaks have increased and broadened when compared to the corresponding in Fig. 5.8 (d)

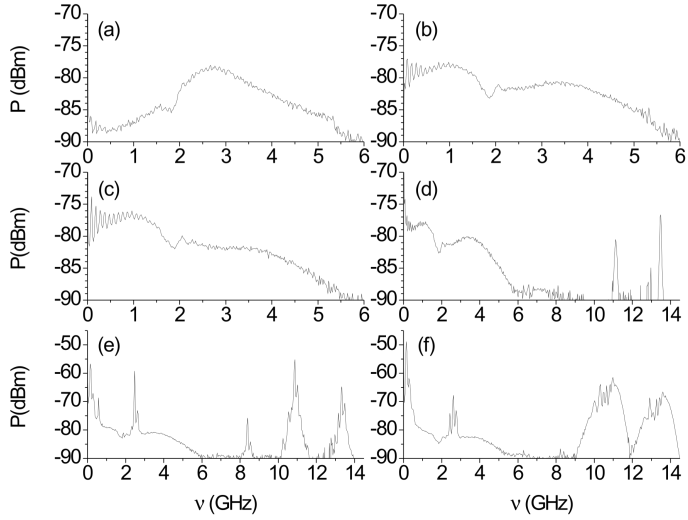

Fig. 5.8. RF spectrum of the three-mode VCSEL (VCSEL 2) for several values of the bias current: (a) 6.95 mA, (b) 10.62 mA, (c) 12.36 mA, (d) 12.46 mA (e) 12.76 mA, and (f) 13.2 mA.

The position of those peaks do not change significatively as the current increases and only the strength and width of those peaks change as it can be seen in Fig. 5.8 (f). Fig. 5.7 (f) shows that the frequency difference between the orthogonally polarized 2 and 3 modes is near 10 GHz while the difference between the parallel polarized 2 and 3 modes is around 11.2 GHz. This suggests that a possible origin for the additional peaks appearing in Fig. 5.8 (f) could correspond to the beating between the orthogonally polarized 2 and 3 modes, and the parallel polarized 2 and 3 modes, respectively.

Measurements on another three-mode VCSEL (VCSEL 3) have been performed in order to confirm the hypothesis of beating between modes 2 and 3. Optical and RF spectrum are shown in Fig. 5.9 for a bias current value of 11.5 mA. Fig. 5.9 (a) shows that

there is excitation of three parallel polarized transverse modes ($1_{\parallel}$, $2_{\parallel}$ and $3_{\parallel}$ modes) and a possible excitation of two orthogonal modes (marked as $2_{\perp}$ and $3_{\perp}$) that can not be resolved with our Fabry-Perot analyzer of 1 GHz resolution. This means that the frequency separation between $2_{\perp}$ and $3_{\perp}$ modes is smaller than between $2_{\parallel}$ and $3_{\parallel}$ modes, like in VCSEL 2. Beating between $2_{\parallel}$ and $3_{\parallel}$ modes could explain the large amplitude peak observed in Fig. 5.9 (b) at 3.7 GHz because the frequency difference between these modes in Fig. 5.9 (a) is 3.9 GHz. Beating between $2_{\perp}$ and $3_{\perp}$ modes could also explain the large amplitude peak that appears at 1.42 GHz.

A reminiscence of the broad peaks obtained at lower currents (similar to those in Fig. 5.8 (b)) is still visible in the pedestal between 3 and 5 GHz of Fig. 5.9 (b). Separations between $2_{\parallel}$ and $3_{\parallel}$ modes and between $2_{\perp}$ and $3_{\perp}$ modes are smaller than those found in VCSEL 2. In this way the large amplitude peaks in the RF spectrum due to mode beating appear superimposed to the broad peaks obtained at lower currents. A low frequency peak, similar to those observed in Figs. 5.8 (e)-(f), also appears around 0.3 MHz.

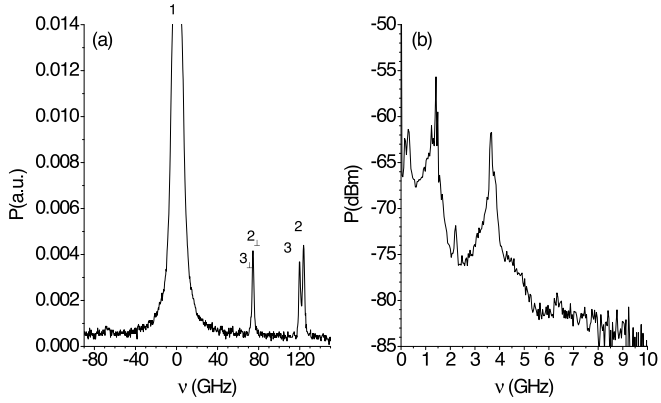

Fig. 5.9. (a) Optical and (b) RF spectrum of a three-mode VCSEL (VCSEL 3) for a bias current of 11.5 mA.

5.5. Discussion and summary

We have done spectrum calculations using the model of Ref. [Valle 1998b] in order to clarify the origin of the high-frequency peaks. First we have assumed that modes 1, 2 and 3 correspond to LP_{mn} modes with different values of m and n. We have considered waveguide parameters in such a way that the VCSEL emits with a wavelength near 1.56 μm and with a frequency separation between the fundamental (LP_{01}, $1_{\parallel}$ in the experiment) and the first high-order transverse mode (LP_{11}, that would be $3_{\parallel}$ in the experiment) similar to that obtained experimentally (110 GHz). With these parameters the next high-order mode (LP_{21}, that would be $2_{\parallel}$ in the experiment) appears at a frequency 150 GHz larger than that of LP_{11}. This value is much larger than the experimental frequency difference between $2_{\parallel}$ and $3_{\parallel}$. This means that the assignment of LP_{11} to $3_{\parallel}$, and of LP_{21} to $2_{\parallel}$ modes has not sense. A more reasonable hypothesis is to consider that modes 2 and 3 are LP_{11}'s modes with different azimuthal distributions (LP_{11}^{c} and LP_{11}^{s} with the notation of [Valle 1998a]). A possible reason for the splitting of LP_{11}-mode could be an oblong aperture shape. Measurements of near and far fields would be desirable to determine whether modes 2 and 3 corresponded to LP_{11}'s with different azimuthal distributions. We plan to do these measurements in the future.

In this work we have shown how the noise behavior obtained when the VCSEL is emitting in two parallel polarized transverse modes is well described with the simple theory developed in Ref. [Valle 2004]. This result has been shown with the results of VCSEL 1 and VCSEL 2 with small enough values of the applied bias current. However, the measurements performed for VCSEL 2 and VCSEL 3 at large values of the current suggest that the polarization and the azimuthal dependence of transverse modes can also play an important role in determining the new structures that appear in the noise spectra. As the model of Ref.[Valle 2004] fails to describe our results for VCSELs 2 and 3 at large bias currents an extension of that

model to consider both linear polarizations of azimuthally-dependent transverse modes would be desirable. The important role that the emission in both linear polarizations has on the RIN spectra was theoretically studied by Mulet et al. in a VCSEL emitting in the fundamental transverse mode [Mulet 2001]. Extensions of that model taking into account the spatial degree of freedom for considering the spatial hole burning effects that lead to emission in multiple transverse modes have already appeared in the literature [Valle 2007], [Mulet 2002b] although they were not used to calculate RIN spectra. Further calculations using those models would be desirable to explain our experimental results.

To summarize, we have studied the intensity noise spectra of two types of multimode long wavelength VCSELs with different transverse and polarization modes characteristics. The first type corresponds to a VCSEL that emits in two transverse modes for large values of the bias current. Both modes are linearly polarized and have parallel polarizations. Two resonance peaks appear in the noise spectra of the individual modes and total power of the VCSEL in agreement with previous theoretical studies [Valle 2004]. The frequencies at which both peaks appear have been measured as a function of the bias current. We have obtained a similar dependence to the one found in [Valle 2004]. With the second type of VCSEL an emission in three different transverse modes for large values of the bias current is obtained. Both types of VCSELs have similar behavior while the bias current is small. However, additional peaks appear in the noise spectra as the bias current increases in such a way that emission in three transverse modes with different polarizations appears. We believe that the polarization and the higher-order transverse mode rotational instabilities can play an important role in determining the structure of noise spectra. Further theoretical and experimental work is needed to elucidate the role played by the previous mechanisms on the noise spectra of VCSELs emitting in multiple transverse modes.

CHAPTER 6

Bistability properties of the polarization switching in a single-mode 1550nm-VCSEL subject to orthogonal optical injection

In the first part of this chapter we experimentally study the polarization switching (PS) obtained in single-mode long-wavelength VCSELs subject to orthogonal optical injection and its bistability properties.

The injected power required to achieve PS is measured as a function of the frequency detuning between the injected light and the orthogonal linear polarization of the VCSEL. We show that for a wide range of bias currents applied to the device, the injected power required for the occurrence of PS exhibited a minimum and a plateau with respect to the frequency detuning. The minimum (plateau) was found at negative (positive) frequency detuning.

We have also studied the bistability properties of the PS obtained when changing the injected wavelength for a fixed injected power, the so called " frequency-induced polarization bistability". We have obtained three different types of bistability. Two of them are studied when the injected power is around a few hundred μW. In this case, we find that one of the bistable regions appears at short wavelengths and the other one appears at longer wavelengths. The widths of both bistable regions are similar and nearly independent of the injected power. The width of the region where PS takes place is shown to increase as the injected power is increased. When the injected power is increased up to a few mW, a third region appears at longer wavelengths and the hysteresis width increases as the injected power or the VCSEL current increases. Very large hysteresis widths are obtained. These widths are more than seven times larger than previously reported widths.

Later on we study the bistability properties of the PS obtained when changing the injected power for a fixed injected wavelength, the so called "power-induced polarization bistability". We report the experimental observation of three different shapes of polarization bistability, anticlockwise, clockwise and X-Shape bistability, all of them with wide hysteresis cycles. The relationship between power and wavelength-induced bistabilities is also discussed.

In the second part of this chapter we make a theoretical study of some of the above mentioned results on PS and its associated bistability. We use the spin-flip model [Sanmiguel 1995], [MartinRegalado 1997a] extended to account for orthogonal optical injection as in [Sciamanna 2006]. A good overall qualitative agreement is found between our theoretical and experimental results.

6.1. Introduction

VCSELs are intrinsically single-longitudinal mode devices but they usually show complex polarization characteristics [Changhasnain 1991], [Sanmiguel 1995], [Choquette 1995], [Valle 1996], [MartinRegalado 1997b], [Ryvkin 1999]and multi-transverse mode dynamics [Changhasnain 1991], [Vakhshoori 1993], [Valle 95], [Buccafusca 1996], [Mulet 2002a], [Zhang 2004]. While emission in several transverse modes is usually attributed to spatial hole burning effects, the polarization behavior can be influenced by different physical mechanisms. The light emitted by a VCSEL is commonly linearly polarized along one of two orthogonal directions, and PS between the two linearly polarized modes is often observed when the injection current or temperature is varied. Understanding and controlling the VCSEL polarization is crucial for their use in polarization-sensitive applications such as magnetooptical disks and coherent detection systems.

The effect of optical injection in VCSELs has been studied since 1993 [Pan 1993]. When the VCSEL is emitting in the fundamental transverse mode, stable injection locking has been observed when both the VCSEL and the externally injected light have parallel polarizations [Li 1996]. A different configuration, usually called "orthogonal optical injection," was used by Pan et al. [Pan 1993] to inject light into a single transverse mode VCSEL. In that configuration, linearly polarized light from a tunable laser source is injected orthogonally to the linear polarization of the free-running VCSEL. Switching from that polarization to the orthogonal polarization mode has been observed as the injected power increases [Sciamanna 2006], [Altes 2006], [Mori 2006], [Gatare 2007a], [Gatare 2007b], [Hurtado 2008b], [Valle 2008], [Hurtado 2009c], [Pan 1993], [Hong 2000b], [Hong 2001], [Ryvkin 2004], [Gatare 2006], [Jeong 2008]. Optical bistability associated with the PS has also been reported theoretically [Altes 2006], [Gatare 2007a], [Gatare 2007b] and experimentally [Altes 2006], [Hurtado 2008b], [Valle 2008], [Hurtado 2009b], [Pan 1993], [Hong 2000b],

[Hong 2001], [Ryvkin 2004], [Gatare 2006], [Jeong 2008], [Hurtado 2009c], [Boiko 1999], [Kawaguchi 1995b].

In the seminal work by Pan et al., intensity polarization bistability was observed where hysteresis appeared in the polarization of the slave laser as the optically injected power was varied [Pan 1993]. Less attention has been paid to the "wavelength-induced polarization bistability," which is the bistability found in VCSELs when changing the Master Laser (ML) wavelength with a fixed ML power. That bistability has been first found in experiments using 850 nm wavelength VCSELs [Hong 2000a], [Hong 2001]. It was shown that the change in the ML wavelength leads to two successive PSs in such a way that only the PS appearing in the longer wavelength regime exhibited bistable behavior [Hong 2000a], [Hong 2001]. In these experiments the excitation of another perpendicular polarized higher-order transverse mode played a relevant role. Theoretical work on a single-transverse mode VCSEL has shown that both PSs can exhibit bistable regions [Gatare 2007a]. The dependency of hysteresis widths on ML power has also been analyzed from experimental [Hong 2000a], [Hong 2001] and theoretical [Gatare 2007a] points of view. Recent experimental investigations [Hurtado 2009b], [Valle 2008], [Hurtado 2009c] have shown that long-wavelength (1550nm) single-transverse and polarization mode VCSELs also exhibit wavelength-induced polarization bistability when subject to orthogonal optical injection. As the ML wavelength λ_{ML} is scanned near the resonance wavelength of the depressed linearly polarized mode, and for a fixed injected power P_{inj}, the VCSEL exhibits two successive PSs. Bistable regions are found for both short-wavelength (SW) and long-wavelength (LW) PSs when the VCSEL is biased well above threshold [Valle 2008]. When the VCSEL is biased slightly above threshold, bistability is only observed in the LW PS. Recent theoretical analysis showed that the transition from one LW bistable regions is obtained as the bias current is increased [Gatare 2007a]. Experiments with 1550 nm VCSELs seem interesting due to the potential of these devices for their use in optical interconnects,

optical switching, and optical signal processing at that important telecommunication wavelength.

"Power-induced optical bistability" have undergone considerable research in short-wavelength [Pan 1993], and in long-wavelength VCSELs [Hurtado 2009b], [Hurtado 2009c], [Marki 2008], [Katayama 2008b]. Different shapes of power-induced PS and bistability (anticlockwise and clockwise) have been observed in 1550-nm VCSELs subject to orthogonal optical injection [Hurtado 2009b], (as well as to different polarized optical injection [Hurtado 2009c]) into the orthogonal polarization of the fundamental mode of the device. Experimental and theoretical research in this subject is of interest since different practical applications, including logic gates [Marki 2008], flip-flop operation [Katayama 2008b] and buffer memories [Katayama 2008a] have been recently reported.

6.2. Experimental Setup

Orthogonal optical injection is achieved using the experimental setup shown in Fig. 6.1. An all-fibre system has been used to inject the light from a tunable laser source (ML) into the 1550nm-VCSEL used in the experiments. The bias current and the temperature of the device were controlled with a laser driver and temperature controller respectively. The temperature of the VCSEL was held constant at 298 K for all the experiments. In order to minimize the reflections at different FC/PC connectors, we have used index-matching gel in those connections. A variable attenuator is included for the control of the optical power of the externally injected signal. The output of the ML is then injected into the VCSEL via a three-port optical circulator. The control of the polarization of the externally injected signal is performed by using a fibre polarization controller. A 98/2 fibre directional coupler divides the optical path in two branches; the 2% output of the coupler is connected to a power meter for the monitoring of the optical input power whereas the 98% coupler's output is directly connected to the 1550nm-VCSEL. Finally, an Optical Spectrum

Analyzer (OSA) is connected to the third port of the optical circulator for the analysis of the reflective output of the VCSEL. Note that the power measured at the OSA includes the power emitted by the VCSEL plus the reflection of the input light.

The device used in the experiments was a commercially available quantum-well 1550nm-VCSEL (Raycan) [Park 2006]. Figure 6.2 (a) plots the experimentally measured L-I curve of the VCSEL at the temperature of 298K, showing a threshold current (I_{th}) of 2.05 mA. The VCSEL emits in a linear polarization which we will call the "parallel" (or "y") polarization. Figure 6.2 (b) shows the measured spectrum of the VCSEL when biased with a current of 2.50 mA also at 298 K. Fig. 6.2 (b) shows that the lasing mode of the device with parallel polarization is located at the wavelength of 1543 nm when a bias current of 2.50 mA (I_{bias}=1.22 I_{th}) is applied to the VCSEL. The emission in that polarization is stable and no PS is observed for any bias current above threshold. The second subsidiary mode has orthogonal (or "x") polarization and is shifted approximately 0.5 nm to the long-wavelength side of the lasing mode.

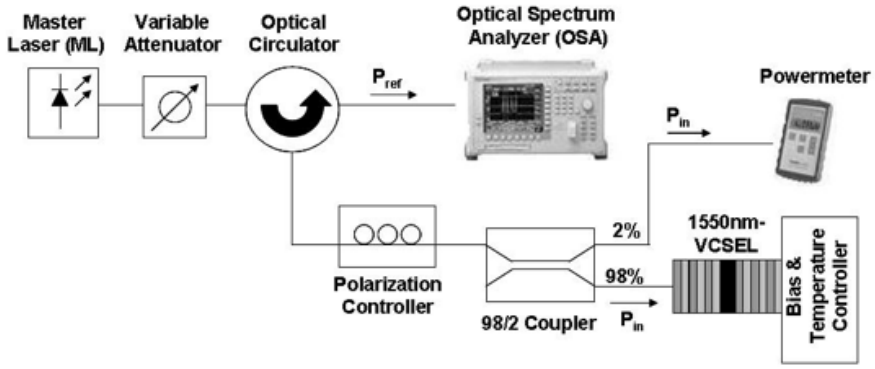

Fig. 6.1. Experimental setup used for the orthogonal optical injection in a 1550-nm VCSEL.

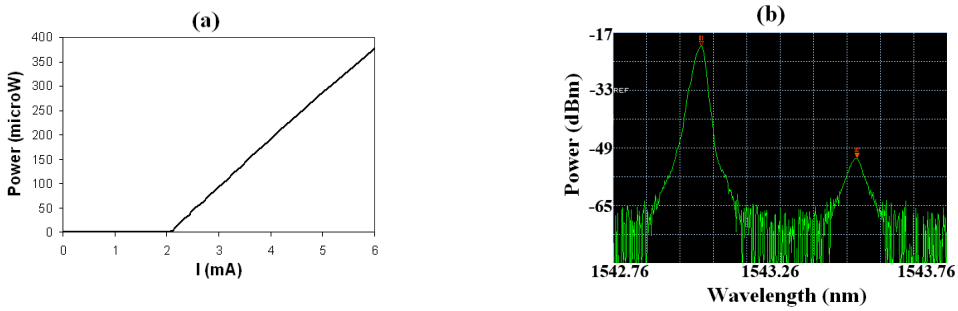

Fig. 6.2. (a) L-I Curve of the 1550-nm VCSEL. (b) Spectrum of the device biased with a current of 2.50 mA.

6.3. Experimental results for polarization switching as a function of the injected wavelength

We have measured the injected power for PS as a function of the frequency detuning between the externally injected signal and the orthogonal polarization mode of the VCSEL, $\Delta\nu=\nu_{inj}-\nu_x$. These measurements are performed for several values of bias current applied to the device. Hurtado et al. [Hurtado 2009a] have studied the injection-locking properties of 1550-nm VCSELs subject to orthogonal optical injection. Theoretical and experimental injection locking diagrams in the plane of frequency detuning vs. optical input power have been obtained for a single value of current, I_{VCSEL} [Hurtado 2009a]. Injection locking has been obtained when the side mode suppression ratio (SMSR, ratio between the power of the orthogonal and parallel polarizations) is higher than 30 dB [Hurtado 2009a] . The injected optical power P_{inj} required for PS has displayed an almost symmetric behavior with frequency and has shown a minimum near $\Delta\nu$=-1 GHz when the VCSEL is biased slightly above threshold (I_{VCSEL}=3mA) [Hurtado 2009a]. In our experiments, we also consider that the orthogonal optical injection induces a PS when SMSR>30dB.

Fig. 6.3. shows the injected power required for PS as a function of $\Delta\nu$ for different values of I_{VCSEL}. When I_{VCSEL} is small (3mA) the results reported in [Hurtado 2009a] are recovered. Results obtained

for I_{VCSEL}=5mA show that a plateau is being formed at positive $\Delta\nu$, while the minimum still appears at small negative values of $\Delta\nu$. As I_{VCSEL} is further increased (see the results for I_{VCSEL}=7,8, and 9 mA in Fig. 6.3), a wide plateau appears at positive values of $\Delta\nu$. A shallow local minimum appears at $\Delta\nu$=2GHz, close to the center of the previously described plateau. Therefore, for a wide range of I_{VCSEL}, the P_{inj} required for PS shows a clear minimum and a wide plateau for negative and positive values of $\Delta\nu$, respectively. These results confirm the theoretical predictions of [Sciamanna 2006]. The frequency location of the absolute minimum does not follow a clear trend: a fluctuation between $\Delta\nu$=-1 and -0.2 GHz is observed as I_{VCSEL} is increased. However, the optical power value of the absolute minimum grows as I_{VCSEL} increases (the minimum P_{inj} increases from 11.25 to 26.25 μW as I_{VCSEL} changes from 3 to 11 mA, as seen in Fig. 6.3.) although some fluctuations are still clearly visible. On the other hand, the values of the optical power at the plateau increase as higher bias current are applied to the VCSEL. In addition, the results obtained for the largest applied value of I_{VCSEL} (11mA) show new qualitative features. For positive frequency detunings, the plateau begins to disappear because P_{inj} becomes again an increasing function of $\Delta\nu$. More interestingly, P_{inj} required for PS has an "S" shape for small negative values of $\Delta\nu$. This shape implies a novel behavior of the polarization in a detuning range spanning from -0.75 to -0.5 GHz. A new region appears in that detuning range, marked as region B in Fig. 6.3. In that region, PS to the orthogonal polarization is not observed. A vertical dotted arrow has been included in Fig. 6.3 to indicate the three different regions of distinct behavior of the polarization appearing as the injected power is increased when the device is biased with 11 mA. This three different regions are marked as regions A, B, and C in Fig 6.3. In region A, PS from parallel to orthogonal polarization is obtained. Consequently, the orthogonal polarization dominates throughout this region. In region B, PS is no longer observed and the SMSR becomes smaller than 30 dB, reducing to levels of only around 10 dB. Nonetheless, throughout this region the orthogonal

polarization is still dominant and no reverse polarization switching to the parallel polarization mode is observed. Finally, in region C, PS is observed and the orthogonal polarization becomes again the dominant one with SMSR> 30 dB.

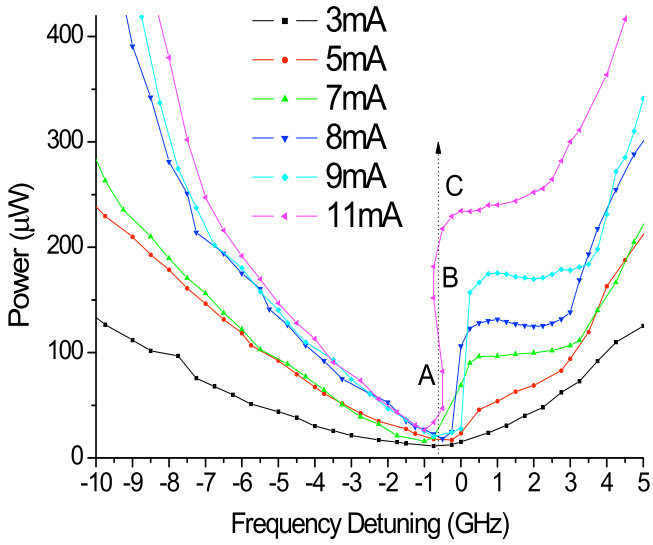

Fig. 6.3. Measured minimum injected power required for PS as a function of the frequency detuning for several values of the VCSEL current.

Figs. 6.4 shows the injected power required for PS vs. detuning when increasing and decreasing the injected power. We find a bistable behavior of the polarization with wide hysteresis cycles. There is a non-monotonous dependency of the hysteresis width vs. the detuning, which is in agreement with the theoretical predictions of [Sciamanna 2006]. The hysteresis width increases as the frequency detuning becomes more negative, also in agreement with [Sciamanna 2006]. We have also obtained that for positive values of frequency detuning, $0<\Delta\nu<15$ GHz, no hysteresis was observed. The condition $0<\Delta\nu$ corresponds to $\Delta\omega>\gamma_p$ in [Sciamanna 2006], where γ_p is the linear birefringence parameter and $\Delta\omega$ is the frequency detuning with respect to a frequency intermediate between that of the parallel and the

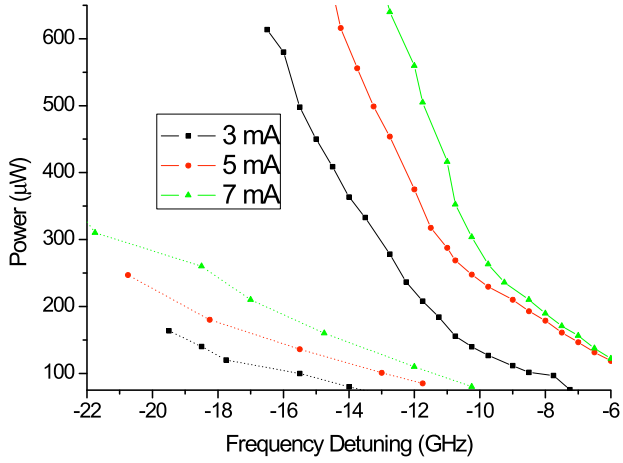

Fig. 6.4. Measured injected power required for PS as a function of the frequency detuning for several values of the VCSEL current. Results corresponding to increasing and decreasing the injected power are plotted with solid and dotted lines, respectively.

orthogonal polarizations. This results is in agreement with [Sciamanna 2006, FIg.11], if $\Delta\omega$<45 rad/s . That figure also shows that the hysteresis width increases with $\Delta\omega$ when $\Delta\omega$>45 rad/s. That value approximately corresponds to the maximum detuning that has been reached in our experiments. In [Sciamanna 2006] (in our experiments) it corresponds to an injected frequency that is larger than the frequency of the orthogonal polarization for a value given by 0.27 (0.24) times the frequency difference between both polarizations. Further experimental work at larger frequency detunings would be interesting to fully check the theoretical predictions of [Sciamanna 2006]. A deeper insight of the bistable behavior of the single-mode device will be given in the remainder of this chapter.

6.4. Wavelength-induced polarization bistability

6.4.1 Low injected power

In this subsection we study experimentally the wavelength-induced polarization bistability in a 1550-nm VCSEL biased well above threshold and subject to orthogonally-polarised optical injection with low power into the subsidiary orthogonal polarization mode of the device.

As the ML wavelength λ_{ML} is scanned near the resonance wavelength of the depressed linearly polarized mode, and for a fixed injected power P_{inj}, the VCSEL exhibits two successive PSs. Bistable regions are found for both SW and LW PSs when the VCSEL is biased well above threshold [Valle 2008]. When the VCSEL is biased slightly above threshold, bistability is only observed in the LW PS. Recent theoretical analysis showed that the transition from one LW bistable region to two bistable regions is obtained as the bias current is increased [Gatare 2007a].

Figure 6.5 shows the widths of both bistable regions measured as a function of the injected power when I_{VCSEL}=4mA (around $2.5I_{th}$). Hysteresis widths fluctuate around a constant level of 2 GHz. The behavior of the hysteresis widths is similar for the SW and LW bistable regions. Figure 6.6 shows the width of the region where the PS takes place as a function of P_{inj} when I_{VCSEL}=4mA. The PS width increases as P_{inj} increases like in [Valle 2008]. We have considered the width obtained when increasing λ_{ML} because the results obtained when decreasing λ_{ML} are similar [Valle 2008]. The widths of the bistable and PS regions have been calculated like in [Valle 2008]. Also the same automatic control of the measurements described in [Valle 2008] has been used to obtain Figs. 6.5 and 6.6.

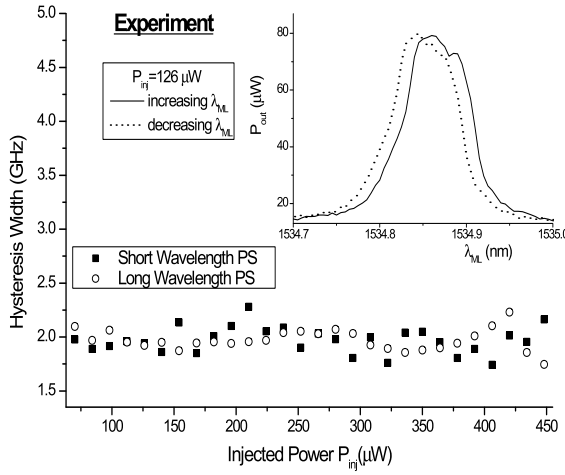

Fig. 6.5. Frequency widths of the bistable regions as a function of the injected power. Results corresponding to the SW and LW bistable regions are plotted with squares and circles, respectively. The inset shows the output power as a function of the wavelength of the injected light when P_{inj}=126μW. Results corresponding to increasing and decreasing the wavelength are plotted with solid and dashed lines, respectively. In this figure I_{VCSEL}=4mA=2.47I_{th}.

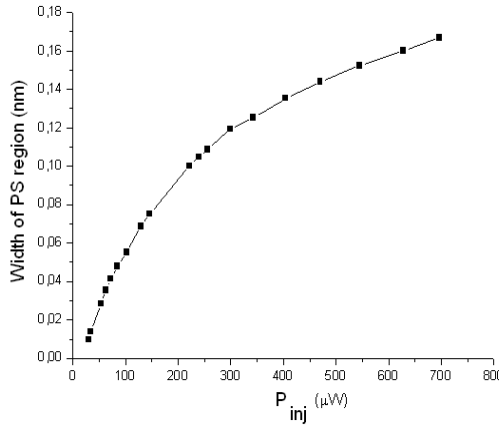

Fig. 6.6. Width of the PS region as a function of P_{inj} when I_{VCSEL}=4mA.

6.4.2 High injected power

In this subsection, we perform an experimental study of the bistable behavior of a 1550-nm wavelength single-mode linearly polarized VCSEL when subject to high power orthogonal optical injection. In our experiment, the injected power is increased well above the values considered in the previous subsection. Our results show, that the hysteresis width of one of those bistable regions significatively increases as the injected power or the applied bias current increase. Measured values of that hysteresis width can go beyond 37 GHz. Those values are much larger than previously reported widths [Hong 2000a], [Valle 2008], [Hurtado 2009b].

In the previous subsection (Fig.6.5) we showed that as λ_{ML} is scanned near the orthogonal polarization wavelength $\lambda_{\perp}$ with fixed injection power P_{inj}, the VCSEL exhibits two successive PS with two bistable regions in such a way that pure frequency-induced polarization bistabilities were found. The same result can be found in [Hong 2000a], [Valle 2008]. Now, we have been able to significatively increase P_{inj} by using all elements with the same type of fiber connectors/angled polished connector (FC/APC). The consideration of larger values of P_{inj} changes the behavior obtained in [Valle 2008] as it can be seen in Fig 6.7, where the output power of the orthogonal polarization $P_{\perp}$ is plotted as a function of the wavelength detuning $\Delta\lambda=\lambda_{ML}-\lambda_{\perp}$. Two bistable regions are found [corresponding to PS from the parallel to the orthogonal polarization and vice versa, marked with I and II in Fig. 6.7 (a), respectively] similar to those obtained in [Valle 2008, Fig.2 (a)]. Both bistable regions can be described in a theoretical way by using a model that takes into account the lasing transitions between the spin sublevels of the conduction and valance bands of a quantum-well semiconductor [Gatare 2007a].

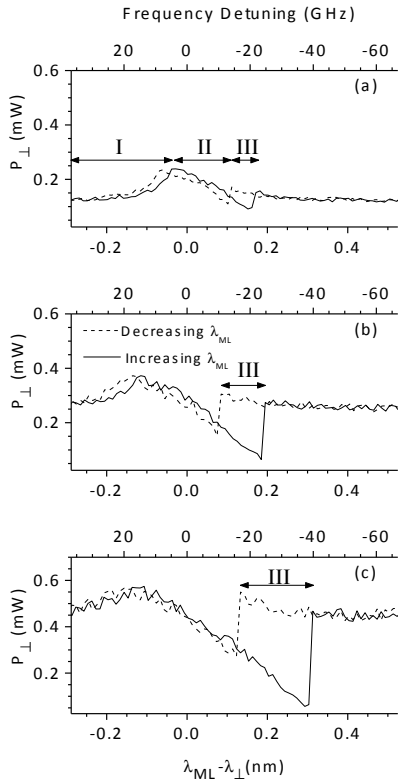

Fig. 6.7. Output power in the orthogonal polarization versus the wavelength detuning when increasing (solid lines) and decreasing (dashed lines) λ_{ML} for injection power (a) P_{inj}= 0.75 mW; (b) P_{inj}=1.5 mW; and (c) P_{inj}=2.7 mW. In this figure, I_{VCSEL}=4mA and $\lambda_{\perp}$=1534. 74nm.

In fact we will see in subsection 6.7.2 that the experimental dependence of the width of both hysteresis cycles on P_{inj} is similar to the obtained theoretically with the model of [Gatare 2007a]. We also observe that a new third bistable region appears at longer $\Delta\lambda$. That third bistable region is the one marked with III in Fig. 6.7. That bistable region was also found in [Hurtado 2009b], but no observation of the simultaneous presence of those three bistable regions was done in that work. For the first time to our knowledge, we measure the width and depth of that third bistable region as a function of P_{inj} and of the bias current I_{VCSEL}. Fig. 6.7 shows that both the width and depth increase as P_{inj} increases.

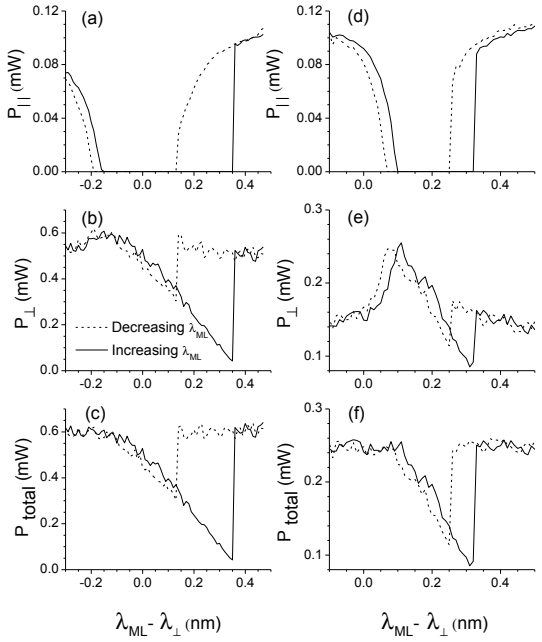

Fig 6.8. Output power in (a), (d) parallel polarization; (b), (e) orthogonal polarization; and (c), (f) total power versus wavelength detuning when increasing (solid lines) and decreasing (dashed lines) λ_{ML}. Parts (a)-(c) and (d)-(f) correspond to P_{inj}=3.7 and 0.75 mW, respectively.

Anticlockwise, clockwise, and anticlockwise responses are obtained as the wavelength detuning increases, as shown in. 6.7 (a) and (b). However, Fig. 6.7(c) shows that the first two bistable regions that appear at lower λ_{ML} are not well defined when P_{inj} is large. In this situation the power of the VCSEL becomes a small fraction of the injected power. These bistable regions are then hidden due to the larger influence of the fluctuating character of the power reflected by the VCSEL cavity.

Measurements of the output powers in the orthogonal and parallel $P_{\parallel}$ polarizations and of the total reflected power in both polarizations P_{total} as a function of the wavelength detuning have also been performed. These measurements were obtained by substituting the optical circulator by another circulator that does

not maintain the polarization. Fig. 6.8 shows the results for I_{VCSEL}=4mA, and two different values of P_{inj}. Measurements of $P_{\parallel}$ and $P_{\perp}$ show qualitative behaviors similar to the one observed in [Hurtado 2009b], but with a much wider hysteresis cycle in the long wavelength bistable region due to our larger value of I_{VCSEL}. For instance, the 0.22-nm wide hysteresis cycle shown in Fig. 6.8 (b) is more than 15 times wider than the widest cycle reported in [Hurtado 2009b]. Fig. 6.8 (a) shows that $P_{\parallel}$ displays clockwise and anticlockwise responses as λ_{ML} increases. The ratio between $P_{\parallel}$ when decreasing and increasing λ_{ML} can be very large [around 40 dB at $\Delta\lambda$=0.45 nm in Fig. 6.8 (a)]. We show in Fig. 6.8 (d)-(f) that the same responses are obtained when decreasing P_{inj}, situation in which the three bistable cycles in $P_{\perp}$ are clearly defined. A wide bistable region at the same $\Delta\lambda$ also appear for P_{total}. The decrease of $P_{\parallel}$ as λ_{ML} increases compensates the maximum observed in $P_{\perp}$, in such a way that P_{total} has no longer a maximum at negative wavelength detunings, as shown in Fig.6.8.

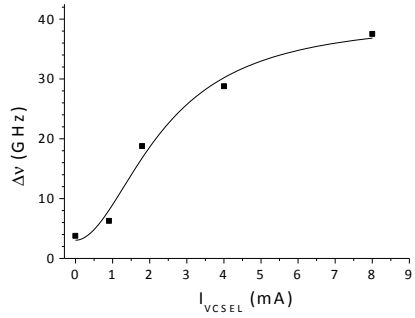

Fig 6.9. Frequency width of the hysteresis cycle as a function of I_{VCSEL} when P_{inj}=3,7mW. Squares represent experimental data.

The third bistable region becomes wider as the VCSEL current increases, as shown in Fig. 6.9, where the frequency width of that region has been plotted as a function of I_{VCSEL}. Hysteresis cycles are very wide: their width is larger than 20 GHz when I_{VCSEL}>1.3 I_{th} and P_{inj}=3.7mW. We note that a qualitatively similar hysteresis cycles appears when no current is applied to the VCSEL. That means that

the origin of this third bistability lies in the passive cavity although Fig. 6.9 shows that the width is largely affected by the active operation of the device. We think that the aspect of the passive cavity that is responsible for the third form of bistability is the dispersive nonlinearity [Hurtado 2008b]. These frequency widths can go beyond 37 GHz, that is a value more than seven times larger than previously measured values [Hong 2000a], [Valle 2008], [Hurtado 2009a].

6.5 Optical power polarization bistability

In this subsection we experimentally analyze the power-induced polarization bistability, that is the bistability observed when the injected power is changed for a fixed injected wavelength. We measure the output powers of the emitting parallel polarization mode and the subsidiary orthogonal polarization mode of the 1550nm-VCSEL and we obtain different shapes of PB in a 1550nm-VCSEL, including anticlockwise, clockwise and X-Shape or butterfly bistability. We observe wide hysteresis cycles up to four times wider with respect to previously reported results [Hurtado 2008b]. This diversity of behavior at 1550 nm, the most commonly used wavelength in optical telecommunication networks, offers promise for the use of VCSELs in optical signal processing and optical switching applications.

Figures 6.10 (a) and (b) show the input/output power characteristics for the parallel and the orthogonal polarization modes of the VCSEL for different levels of applied bias current to the device, namely 3mA ($1.83I_{th}$), 4mA ($2.44I_{th}$), 5mA ($3.05I_{th}$), and 7mA ($4.27I_{th}$).

The initial wavelength detuning between the externally injected signal and the orthogonal polarization mode of the device was kept constant and equal in all cases to 0.15 nm. As we have seen, PS can be observed in the VCSEL under orthogonal optical injection when the optically injected power is high enough

to lock the orthogonal polarization mode of the VCSEL to the wavelength of the externally injected signal. At that point PS is produced and the output of the parallel polarized mode of the VCSEL is suppressed whereas the output of the orthogonal polarized signal switches between two stable output states [Pan 1993], [Gatare 2006], [Hurtado 2008b], [Valle 2008]. As has been previously reported in short-[Pan 1993], [Gatare 2006] and long-wavelength [Hurtado 2008b], VCSELs, the results in Fig. 6.10(a) show that the output of the parallel polarized mode of the VCSEL exhibits clockwise optical bistability for all cases of applied bias current. At the same time, as can be seen in Fig. 6.10(b) the I/O characteristic of the orthogonal polarization mode of the VCSEL also shows clockwise bistability for all the biasing cases considered.

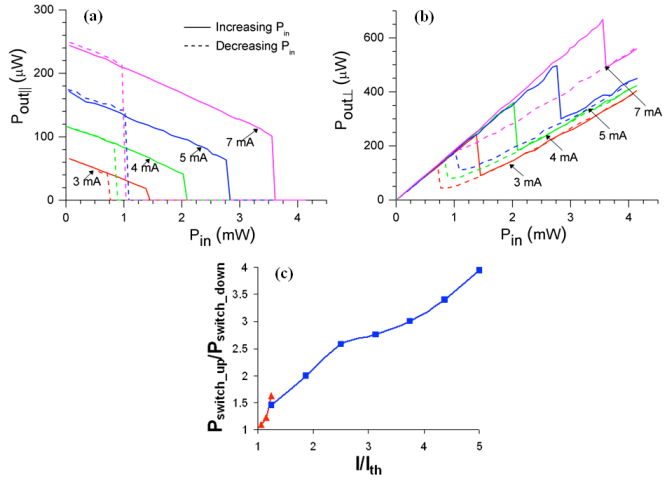

Fig 6.10. I/O power characteristic for different levels of applied bias current and constant initial wavelength detuning of 0.15 nm for the (a) parallel and the (b) orthogonal polarization mode. (c) Width of the hysteresis cycle vs. applied bias current.

The latter had only been recently reported in 1550nm-VCSEL [Hurtado 2008b] for cases of high enough initial wavelength detuning (in particular, 0.15 nm in [Hurtado 2008b]). It is important to note here that prior to the onset of PB, the external optical

injection produced slight shifts in the wavelength of the two polarization modes of the VCSEL and we believe that this may be due to frequency pulling effects.

Figures 6.10 (a) and 6.10 (b) show that for both polarization modes of the device, as the applied bias current is increased well above threshold the more power is needed for the obtaining of optical bistability and also the width of the associated hysteresis cycles widen considerably. This behavior is the same as that observed for dispersive bistability in Vertical-Cavity Semiconductor Optical Amplifiers [Hurtado 2007] and also in planar devices, including Fabry-Perot [Pakdeevanich 2000] and distributed feedback semiconductor laser amplifiers [Hurtado 2006]. We believe therefore that the dispersive nonlinearity is also the physical phenomenon that explains the widening of the hysteresis cycles associated with the occurrence of PB as the bias current is increased well above threshold. Figure 6.10 (c) summarizes the measured widths of the hysteresis cycles for the VCSEL used here (blue squares) in comparison to previously reported results [Hurtado 2008b] (red triangles) showing the increase in the width of hysteresis as a result of biasing the device with levels of current well above threshold. In particular, the measured widths of the hysteresis cycles are up to four times larger than those reported previously. This result is of importance for the potential development of low-cost, low-power, high speed all-optical bistable flip-flops as well as all-optical bistable memory elements with 1550-nm VCSELs for all-optical signal processing applications in optical communications networks. These functions can be easily obtained when large hysteresis widths are achieved for optical bistability, as has been reported in vertical-cavity [Kaplan 2009], [Zhang 2009b] as well as in edge-emitting devices [Inoue 1987], [Maywar 2001].

Figures 6.10 (a) and 6.10 (b) also show that the simultaneous occurrence of clockwise bistability for both polarization modes of the VCSEL produces a drop in the total reflected output power

(defined as the sum of the parallel and orthogonally polarized modes). This phenomenon is observed for high enough levels of initial wavelength detuning between the externally injected signal and the orthogonal polarized mode of the device [Hurtado 2008b]. The explanation for this drop in the total output power lies in the delicate balance between the different optical intensities in the device: the input, the reflected, the transmitted and the average intensity within the cavity [Pakdeevanich 1999], [Hurtado 2006]. The higher the initial wavelength detuning, the more power needs to be injected in order to obtain switching between the two output states. This produces a higher drop in the gain associated with switching, which in turn favours the transmitted output of the device whereas the reflective output experiences a reduction of the on-off contrast ratio between output states. As a consequence, the shape of the nonlinear transition changes from anticlockwise bistability (for lower values of detuning) to the clockwise bistability appearing for higher values of detuning, as can be seen in Fig. 6.10 (b).

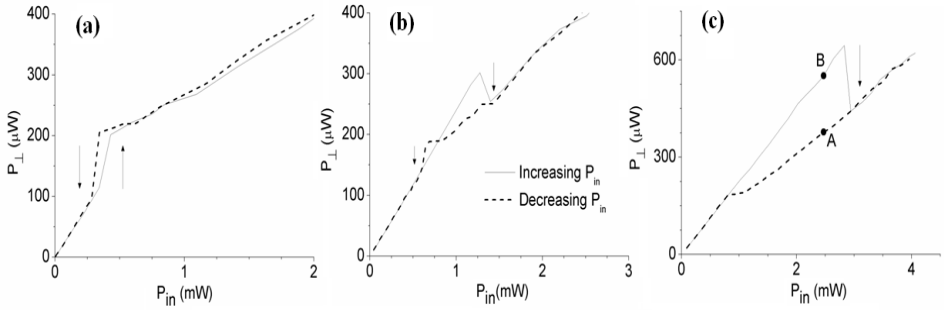

Fig. 6.11. I/O power characteristic for the output of the orthogonal polarization mode for three different levels of initial wavelength detuning of (a) 0.07nm, (b) 0.118nm and (c) 0.15nm and with constant bias current of 6mA ($3.66I_{th}$).

The latter effect can be better seen in the influence of the initial wavelength detuning on the measured characteristics of the optical power PB. Figures 6.11 (a-c) show the input/output power

relationships of the orthogonal polarization mode of the VCSEL for three different levels of initial wavelength detuning. Three different shapes of bistability, namely anticlockwise, X-shape (or butterfly) and clockwise, appear as the initial wavelength detuning is increased, all of them with wide hysteresis cycles in comparison to previously reported results [Hurtado 2007]. Therefore changes in the initial wavelength detuning modify the balance between the input, the transmitted, the reflected, and the averaged intensities leading to these three different types of bistable loops in the reflected transfer function of the VCSEL.

6.6 Relationship between power-induced and wavelength-induced polarization bistability

As we have seen the wavelength-induced polarization bistability is observed when the wavelength of the externally injected signal, λ_{ML}, is modified whilst the optical injected power is kept constant. Figures 6.12 (a) and 6.12 (b) show the output power of the parallel and the orthogonal polarization modes of the VCSEL as a function of the wavelength detuning. The results in Figs. 6.12(a) and 6.12(b) have been measured for increasing and decreasing λ_{ML}. Three different regions of bistability can be observed in Fig. 6.12(b) (marked from I to III) similar to those obtained in Fig.6.8. In section 6.4 we have seen that the width of the hysteresis cycle of region III can be very large (up to 37 GHz wide) when high levels of input power or bias current are applied to the device (see Fig. 6.9). Also, as seen in Fig. 6.12(b), region III is characterized by two stable states, A and B, which can be reached by increasing or decreasing λ_{ML}, respectively. Spectral measurements show that the A(B) state is characterized by the locking (unlocking) of the orthogonal polarization mode of the VCSEL to the wavelength of the externally injected signal. The upper (lower) limit of the III region corresponds therefore to the transition from locked to unlocked (unlocked to locked) output of the VCSEL when λ_{ML} is increased (decreased). These two stable states, A and B, are also marked in Fig. 6.11 (c). The unlocked B state is reached by

increasing P_{inj} from small values. Further increase of P_{inj} produces injection locking slightly below 3mW. The locked A state can then be reached by decreasing P_{inj}. The very large hysteresis width obtained for large wavelength detuning (see Fig. 6.11 (c)) is a direct consequence of the large hysteresis width of region III.

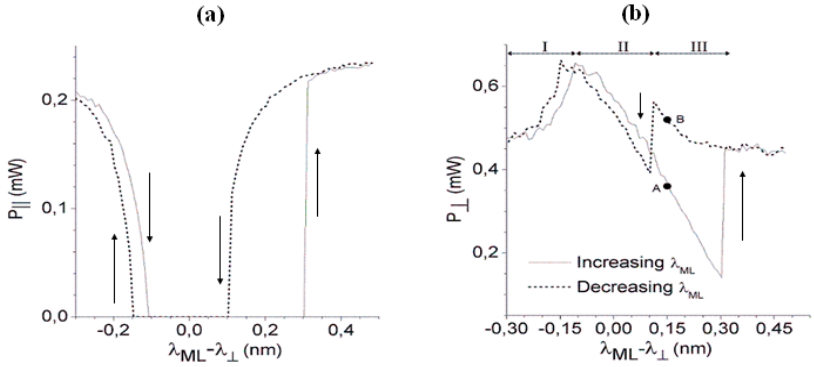

Fig. 6.12. Output power of (a) the parallel and (b) the orthogonal polarization mode of the VCSEL as a function of the initial wavelength detuning when increasing (solid lines) and decreasing (dashed lines) λ_{ML}, with P_{inj}=2.5mW and applied bias current of 6 mA.

6.7 Theoretical model

Our rate equation model for the optically injected VCSEL is based on the model reported by San Miguel, Feng, and Moloney, also called spin-flip model (SFM) [Sanmiguel 1995], [MartinRegalado 1997b]. In our simulations, the parameters have been chosen such that the free-running VCSEL exhibits a stable and stationary *y* (or parallel) linearly polarized state. With these parameters, the frequency of the *y* polarized mode is higher than that of the x (or orthogonal) linear polarization ($\nu_y > \nu_x$). This is exactly the same situation measured for the VCSEL used in the experiments. We therefore choose to inject optically along the x direction in order to obtain PS from the *y* to the *x* linear polarizations. We have integrated by using the same numerical method for stochastic differential equations used in [Mulet 2001] with an integration time

step of 0.1 ps. The rate equation model written in the frequency reference frame of the master is given by:

$$\frac{dE_x}{dt} = \kappa(1+i\alpha)\left(NE_x + inE_y - E_x\right) - i\left(\gamma_p + \Delta\omega\right)E_x - \gamma_a E_x + \kappa_{inj}E_{inj} + \sqrt{\beta_{sp}}\xi_x \tag{6.1}$$

$$\frac{dE_y}{dt} = \kappa(1+i\alpha)\left(NE_y - inE_x - E_y\right) + i\left(\gamma_p - \Delta\omega\right)E_y + \gamma_a E_y + \sqrt{\beta_{sp}}\xi_y \tag{6.2}$$

The equation for *N* and *n* are given by equations (3.21) and (3.22). In this chapter we consider the case where the coupling coefficient coincides with the field decay rate ($\kappa_{inj}=\kappa$) for the ideal case of an effectively mode-matched injected input beam [MartinRegalado 1997b]. The $\Delta\omega$ parameter is defined as the difference between the angular frequency of the injected light ω_{inj} and the reference angular frequency ω_{ref}, intermediate between those of the *x* and *y* linear polarizations, i.e., $\Delta\omega=\omega_{inj}-\omega_{ref}$, where $\omega_{ref}=(\omega_x+\omega_y)/2$. The VCSEL parameters chosen for the simulations are: γ_e=1 ns^{-1}, γ_p=192.1 ns^{-1}, γ_a=1 ns^{-1}, γ_s=1000 ns^{-1}, κ=300 ns^{-1}, and α=3. With this parameter choice, the free-running VCSEL emits in the *y* linear polarization and does not show PS over the injected current range studied here. Also, the calculated value for the frequency difference between the *y* and *x* polarization modes (γ_p/π=61.1 GHz) is close to the experimental value of 63 GHz.

6.7.1 Theoretical results about polarization switching as a function of the injected wavelength

In this subsection we will analyze the minimum injection power needed to obtain PS in order to compare to results of Section 6.3. We consider that PS occurs when the SMSR≥ 30 dB (the same criterion used in the experiments). Fig. 6.13. shows, for different values of bias current μ, the minimum values of $P_{inj}=|E_{inj}|^2$ needed to obtain PS as a function of the frequency detuning $\Delta\nu$ [calculated as the difference between ν_{inj} and ν_x, i.e., $\Delta\nu=(\omega_{inj}-\omega_x)/2\pi$]. This frequency detuning is similar to that obtained experimentally. We note a parabola-like dependence of the minimum P_{inj} required for PS as a function of $\Delta\nu$ for a normalized current of μ=1.6. The value

of μ gives an approximate idea of the value of the current relative to the threshold current (the exact relationship between both quantities is given in [Homayounfar 2007]). The minimum P_{inj} appears at a negative value of detuning. For all analyzed bias currents, the injected power needed for PS exhibits an absolute minimum value P_{inj} appearing at a frequency detuning of $\Delta\nu_{min}$=-3 GHz ($\Delta\nu_{min}$ does not depend on the bias current). The theoretical value of P_{inj} increases as μ increases.

When μ≥3, a plateau with some fluctuations begins to develop for positive values of the frequency detuning. The values of the optical power at those plateaus grow as μ increases. Fig. 6.13 also shows that a second minimum value of injected power for the occurrence of PS also appears at larger positive frequency detuning. The value of this second minimum as well as the frequency detuning at which it appears grows as μ increases. For the largest value of the bias current, our experimental results indicated that the P_{inj} required for PS had an "S" shape for small negative values of $\Delta\nu$. In order to compare our theoretical results with the experimental measurements, we will not only focus on the minimum value of P_{inj} required for PS had an "S" shape for small negative values of $\Delta\nu$ as in Fig. 6.13 but also consider numerous values filling the P_{inj}-$\Delta\nu$ plane to theoretically evaluate whether windows exist where PS is not observed.

For a current of μ=1.6 [Fig. 6.14 (a)], the minimum values of P_{inj} needed for PS show the same parabolic dependence observed in Fig. 6.3. The uniform filling above the parabolic curve means that, once PS is obtained, increasing P_{inj} does not produce any further PS. The situation is different when larger values of bias current are considered. Fig 6.14 (b) shows calculated results for μ=5. A small window appears in the P_{inj}-$\Delta\nu$ plane at around $\Delta\nu$=6 GHz, P_{inj}=0.017, in which no PS is observed. The existence of windows where PS is no longer observed is much more obvious when even higher values of μ are considered. Fig. 6.14 (c) shows that, for small negative values of $\Delta\nu$, the P_{inj} required for PS exhibits an "S" shape with a window appearing centered at P_{inj}=0.022 for -1.4 GHz ≤ $\Delta\nu$ ≤

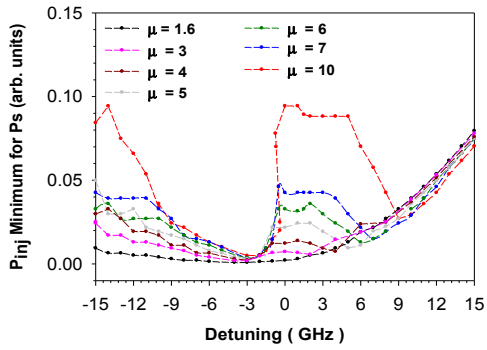

Fig. 6.13. Calculated minimum value of P_{inj} necessary to obtain PS as a function of the detuning $\Delta\nu$ for different values of injected current μ.

-1GHz, where PS is no longer observed. The "S" shape is clearer when the current increases, as can be seen in Fig. 6.14 (d) because of the range of P_{inj} values in which there are no PS increases: it is 0.05 (0.015) at $\Delta\nu$=-0.5 GHz ($\Delta\nu$=-1GHz) when μ=10 (μ=6). This is exactly the same behavior observed in the experiments (see Fig. 6.3) for the case of an applied bias current of 11 mA. Fig. 6.14 (c) and (d) also shows that the window that appeared in Fig. 6.14 (b) around 6 GHz has evolved to an "island" (surrounded by dots where PS occurs) located at larger values of $\Delta\nu$. Therefore, for large enough values of μ, two different windows appear in the P_{inj}-$\Delta\nu$ plane (at negative and positive frequency detuning) where PS is not found. The evolution of both windows can be better understood with the help of Fig. 6.15. The black dots in the E_{inj}-μ plane in Fig. 6.15 indicate for a given value of μ the E_{inj} value for PS occur. The first region without PS, appearing at $\Delta\nu$=-1GHz, is shown in Fig. 6.15 (a) as the tilted white band beginning at μ=6. The level of E_{inj} needed for the appearance of this region increases as μ grows. However, the width of this region does not depend on μ. This is consistent with the increase of the injected power range as the current increases observed in Fig. 6.14 second region without PS, as illustrated in Fig.

6.15(b) for Δν=11 GHz. Fig. 6.15 (a) and (b) also show the coexistence of both regions when μ>8.

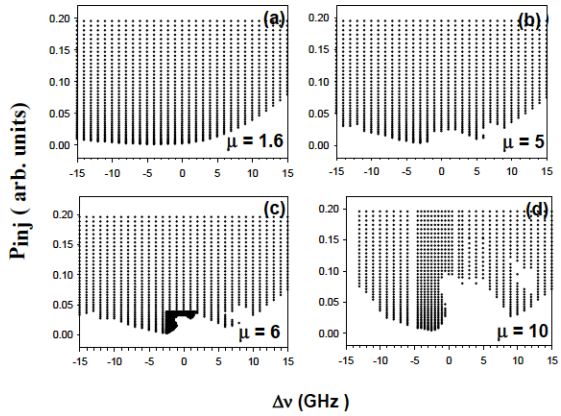

Fig. 6.14. Calculated injected optical power vs. detuning (P_{inj}-Δν plane). A black point indicates the occurrence of PS for (a) μ=1.6, (b)μ=5, (c) μ=6,and (d) μ=10.

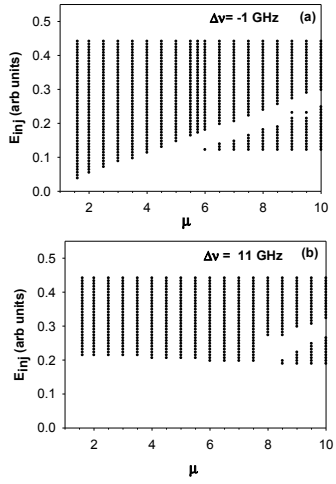

Fig. 6.15. Calculated injected electric field vs. normalized current (E_{inj}-μ plane). A black point indicates the occurrence of PS for (a) Δν=-1 GHz, and (b) Δν=11 GHz.

6.7.2 Wavelength-induced polarization bistability. Theoretical results for low injected power.

In this subsection we will analyze the wavelength-induced polarization bistability obtained when changing λ_{ML} for a fixed P_{inj}. The scale of the injected power is taken to match the experimental minimum value of P_{inj} required to obtain PS induced by the orthogonal optical injection. In the experiment the minimum P_{inj} to achieve PS is 24 μW for a $2.6I_{th}$ bias current, while in our theoretical simulations the minimum E_{inj} required for PS at the current is 0.0384. Then in our calculations we consider that $P_{inj}=c|E_{inj}|^2$, where $c=1.628\cdot10^4$ μW.

We show in Fig. 6.16 (a) the output power corresponding to the x and y polarizations (I_x and I_y, respectively) as a function of the ML wavelength for fixed values of P_{inj} and I_{VCSEL}. We have considered the temporal variation of λ_{ML} illustrated in the inset of Fig. 6.16 (a). λ_{ML} decreases from a value above the wavelength corresponding to the orthogonal mode [λ_x, shown in the inset of Fig. 6.16 (a) with the upper horizontal line] until reaching an intermediate value between λ_x and λ_y (λ_y is also shown in that inset with the lower horizontal line). From that time a symmetric increasing dependence of λ_{ML} is considered. The variation of λ_{ML} is performed in discrete steps of height $\Delta\lambda_{step}$ and duration τ_{step} to approach the experimental conditions. The output power in both polarizations is averaged on the interval of time τ_{step} using a standard moving average. In Fig. 6.16 (a) we show the results that correspond to decreasing λ_{ML}. As λ_{ML} decreases below 1534.90 nm I_x begins to increase in such a way that, when λ_{ML} is getting near the resonance wavelength of the orthogonal polarization of the VCSEL, all the power is transferred to the orthogonal polarization. This switching corresponds to the previously described LW PS in Fig. 6.5. As λ_{ML} decreases below the value λ_x, the output power I_x drops and the total output power is transferred to the y polarization. Then there is a new PS that is similar to the SW PS shown in Fig 6.5. Figure 6.16(b) shows the total output power in the orthogonal polarization

as a function of λ_{ML} when decreasing and increasing λ_{ML}. The bistability behavior is shown clearly in this figure. The curve obtained when increasing λ_{ML} is shifted toward longer wavelengths in agreement with the experimental results shown in Fig. 6.5.

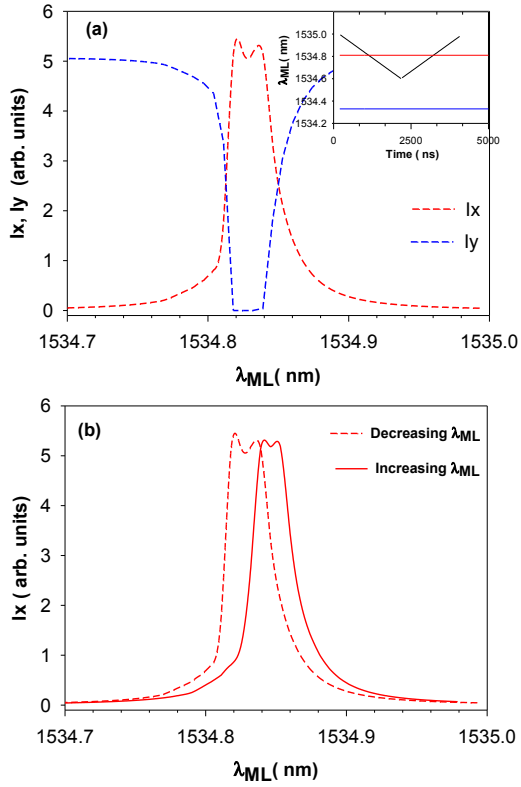

Fig. 6.16. (a) Orthogonal (dashed line) and parallel (dotted line) polarization intensities, I_x, I_y, as functions of a decreasing ML wavelength, λ_{ML} . (b) Orthogonal polarization intensity, I_x, as a function of increasing (solid lines) and decreasing (dashed line) ML wavelengths. In this figure $I=2{,}47I_{th}$, $P_{inj}=100\mu W$, $\Delta\lambda_{step}=0.007nm$, and $\tau_{step}=35$ ns. The inset shows the considered temporal variation of λ_{ML}.

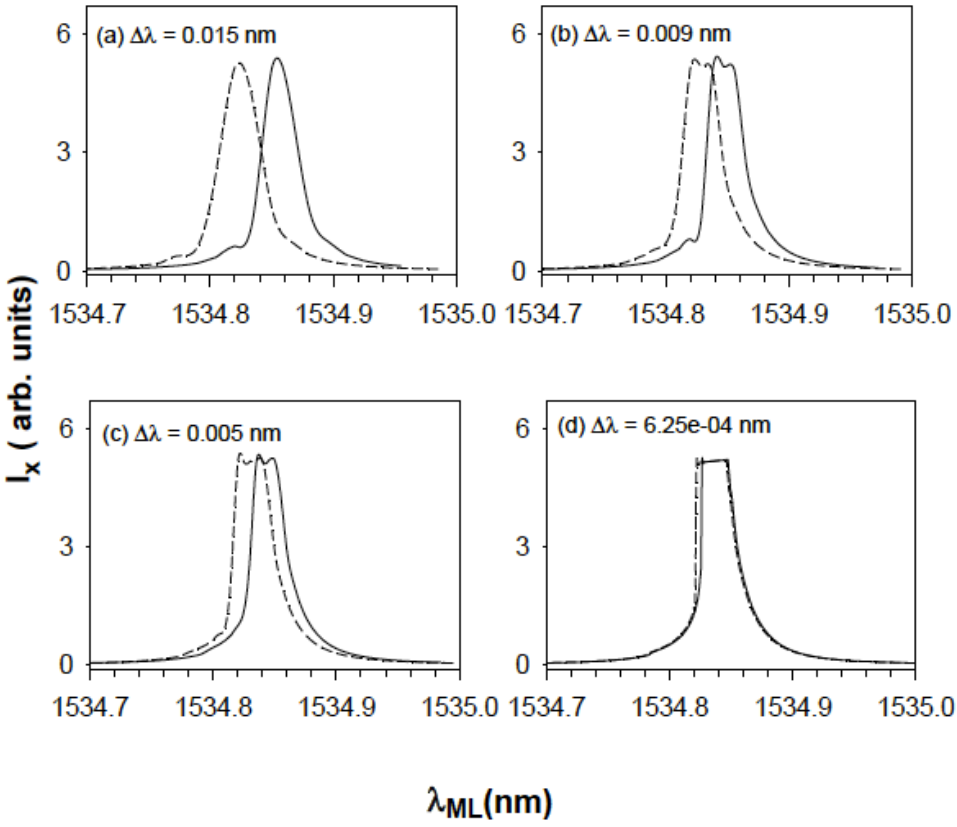

Fig. 6.17. Orthogonal polarization intensity, I_x, as a function of the ML wavelength when decreasing (dashed line) and increasing (solid line) λ_{ML} for different $\Delta\lambda_{step}$ values: (a) $\Delta\lambda_{step}$=0.015 nm, (b) $\Delta\lambda_{step}$=0.009 nm, (c) $\Delta\lambda_{step}$=0.005 nm, (d) $\Delta\lambda_{step}$=6.25·10^{-4} nm.

The results reported in Fig. 6.16 (b) change when considering different values of the height of the steps, $\Delta\lambda_{step}$. We show in Fig. 6.17 the dependence of I_x on λ_{ML} when increasing and decreasing λ_{ML} for different values of $\Delta\lambda_{step}$. We find that the hysteresis width diminishes when $\Delta\lambda_{step}$ decreases. This result is in agreement with our experimental results when using different values of $\Delta\lambda_{step}$. For very small $\Delta\lambda_{step}$ (smaller than the values shown in Fig. 6.17), that is, modeling the variation of λ_{ML} in a continuous form, the positions of

the maximum of I_x for increasing and decreasing λ_{ML} are exchanged. Then the direction of the hysteresis cycles is inverted in agreement with the results reported in [Gatare 2007a].

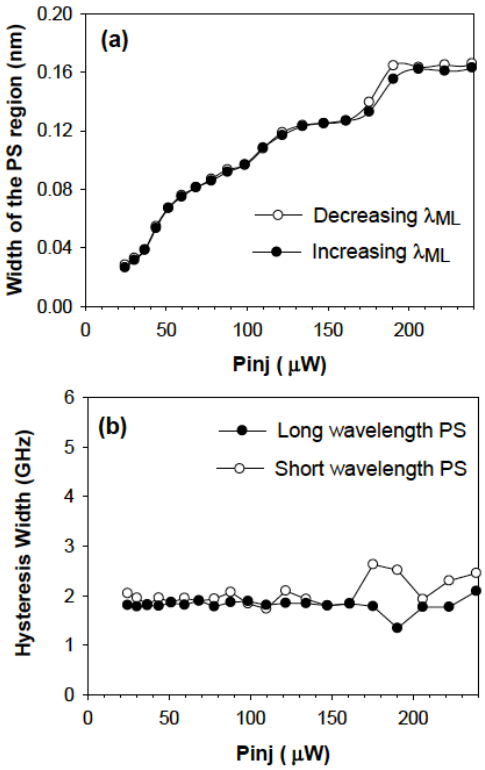

Fig. 6.18. (a) Widths of the PS regions as a function of the injected power for decreasing (white circles) and increasing (black circles) λ_{ML}. (b) hysteresis width of the bistable regions as a function of the injected power. Results correspond to the LW (black circles) and SW (white circles) bistable regions. In both cases I_{VCSEL}= 2.58 I_{th}, $\Delta\lambda_{step}$=0.007 nm, and τ_{step}= 35ns.

We now analyze the theoretical dependence of the width of the PS region on the injected power. The width of the PS region is calculated by using the I_x versus λ_{ML} curves. This width is calculated by averaging over five values obtained around a level at 50% of

the maximum value of I_x. This kind of average was also used in [Valle 2008] to minimize the effect of some experimental fluctuations obtained in the PS zones of the I_x versus λ_{ML} curves. In Fig. 6.18 (a) we show the width of the regions where the PS to the orthogonal polarization takes place as a function of the injected power when $I_{VCSEL}=2.85I_{th}$. Results for decreasing and increasing λ_{ML} are shown with open and filled circles, respectively. Similar widths are obtained when increasing and decreasing the ML wavelength in agreement with [Valle 2008]. The PS width increases as P_{inj} increases in agreement with the results reported in Fig. 6.8. We have also found that the width of the PS region does not change for different values of $\Delta\lambda_{step}$. In Fig. 6.18 (b) we show the width of both bistable regions as a function of the injected power P_{inj} when I_{VCSEL}= 2.85 I_{th}, and λ_{ML} is varied in 50 steps with $\Delta\lambda_{step}$=0.007 nm and τ_{step}= 35 ns. The value of $\Delta\lambda_{step}$ is near the experimental one (0.005 nm), while the theoretical duration of the pulse is much smaller than the experimental one (several seconds). The theoretical value of $\Delta\lambda_{step}$ has been chosen to get the best agreement with the experimental results of Fig. 6.5 for the hysteresis width. The theoretical value of τ_{step} has been chosen as long as possible while maintaining a reasonable computing time. The results reported in Fig. 6.18 (b) show that the hysteresis widths of both bistable regions are similar and are nearly independent of the injected power, in agreement with Fig. 6.5. Also the directions of the hysteresis cycles are in agreement with the experimental results contained in Fig. 6.5 and in [Valle 2008].

6.8. Discussion and conclusions

In summary, we have studied experimentally the PS appearing in 1550-nm VCSELs subject to orthogonal optical injection. Our VCSELs are characterized by a large value of their birefringence parameter and by a linearly polarized emission over the whole current range. We have investigated the injected power P_{inj} required for PS as a function of the frequency detuning, $\Delta\nu$. For a

certain range of VCSEL current, the injected power for PS exhibits a minimum and a plateau with respect to frequency detuning. The minimum appears at negative frequency detuning, whereas the plateau appears at positive detuning. For the highest current applied to the VCSEL, we have described the existence of regions in which an increase of the injected power produces the disappearance and further appearance of PS. We have found these regions, when the frequency detuning is negative and small, in agreement with previous studies [Altes 2006], [Gatare 2007b]. Bistable behavior of the polarization is found experimentally.

In previous work [Valle 2008] under orthogonal optical injection, was shown that as λ_{ML} is scanned near $\lambda_{\perp}$ with fixed injection power P_{inj}, the VCSEL exhibits two successive polarization switching with two bistable regions in such a way that pure frequency-induced polarization bistabilities were found. Now, we have been able to significatively increase P_{inj} and it changes the behavior obtained in [Valle 2008]. We have observed three different regions of bistability. The origin of the first two regions lies in the physical processes that determine the polarization of the VCSEL as an active device. A third bistability region, with a different physical origin to the one of the first two regions, appears at longer wavelength detunings. We have shown that the frequency width of the third bistable region significatively increases as the injected power or the VCSEL current increase. These frequency widths can go beyond 37 GHz, that is a value more than seven times larger than previously measured values [Hong 2000], [Valle 2008], [Hurtado 2009b].

Besides, we have also studied optical power polarization bistability in the same VCSELs under orthogonally-polarized optical injection. Three different shapes of polarization bistability, including anticlockwise, X-shape and clockwise have been experimentally observed. In all cases, wide hysteresis cycles have been experimentally measured, up to four times higher than previously reported results. This diversity of behavior in a VCSEL at the

important telecom wavelength of 1550nm offers promise for the development of low-cost, low-power, high-speed all-optical bistable flip-flops, memory elements and logic gates for use in optical signal processing and optical switching applications in present and future optical telecommunication networks.

Finally, we have also studied theoretically the PS appearing in 1550-nm VCSELs subject to orthogonal optical injection. In general, a good qualitative agreement has been found between theory and experiments on the conditions for the occurrence of PS. In agreement with our experimental measurements, the theoretical value of P_{min} increases as I_{VCSEL} grows. Additionally, both the experimental and theoretical values of $\Delta\nu_{min}$ are negative. However, the experimentally measured of $\Delta\nu_{min}$ does not follow a clear trend with I_{VCSEL}, whereas the theory predicts a constant value for $\Delta\nu_{min}$. This theoretical result may be consistent with our experimental observations since the measured fluctuations could be due to the thermal effects. Both experimental and theoretical results show that plateaus appear at positive values of $\Delta\nu$. In both cases, the value of the optical power at the plateau increases as a higher bias current is applied to the VCSEL. However, the experimental results show that a shallow minimum can appear at the center of the plateau, while a plateau with some fluctuations and a more defined minimum are obtained by using our theory. We have also found in theory, the existence of windows where the PS disappears in agreement with the experiments. The latter has been observed for the highest current considered and for small negative values of $\Delta\nu$. However, the experimental results have not confirmed the theoretical predictions of the existence of similar windows also for positive values of $\Delta\nu$. Furthermore, we have studied theoretically the wavelength-induced polarization bistability for low injected power. Two bistable regions are found for both SW and LW PSs. The directions of theoretical hysteresis cycles are in agreement with the experimental results. We find that the widths of both bistable regions are similar and nearly independent of the injected power. In our simulations, the spontaneous emission

rate is quite small. Spontaneous emission noise in this problem acts as a seed to trigger the dynamical evolution that is basically deterministic above a low power level. We have checked that larger and more realistic values of the spontaneous emission rate (around 10^{-5}-10^{-4}) do not change in a significant way our results.

We also note that the change in τ_{step} at a single wavelength step changes the hysteresis width. Experimental values of τ_{step} are of the order of several seconds. We can not consider those values in the theory due to the prohibitive calculation times in the computer. Our approach to obtain the theoretical results has been the following. Given a wavelength step similar to the experimental one, we have then chosen a value of τ_{step} as long as possible while maintaining a reasonable computing time. This is the best strategy that we could devise in order to compare our theoretical and experimental results.

The locking region in Figs. 6.16 and 6.17 is more symmetric than those observed in [Hong 2001], [Gatare 2007a]. Our solitary VCSEL emits in a linearly polarized single-transverse mode over the whole bias current range. Solitary VCSELs in [Hong 2001], [Gatare 2007a] have different qualitative behaviors because emission in two transverse modes is found in [Hong 2001], while a PS of the fundamental transverse mode was observed in [Gatare 2007a]. This indicates that a possible reason for the symmetric locking region observed in our work could be the single mode behavior of our solitary device.

The main novelty of our simulations is the obtaining of constant hysteresis widths of the bistable regions (Fig. 6.18(b)) that are similar to our experimental results (Fig. 6.5). These results are qualitatively different to those obtained in [Gatare 2007a] (Figs. 6.17 and 6.18) in which different maxima of the hysteresis widths are obtained for several values of the injected power. The theoretical models used in our work and in [Gatare 2007a] are similar. Then the reason behind this different behavior is the consideration of very different device parameters in both works. The main difference in the values

of the parameters corresponds to the birefringence value (our birefringence value is 6.4 times larger than in [Gatare 2007a]). Our birefringence value was large in order to obtain a theoretical wavelength splitting between the two linear polarizations similar to that measured in our device (0.5 nm).

The value of the spin-flip relaxation rate that we have used (γ_s=1000 ns^{-1}) is very large. We chose that value in order to have a stable polarization in the solitary laser because of the very large value of the birefringence parameter. An alternative that produces also a mono-stable behavior is the use of the SFM with a more realistic value of γ_s (250ns^{-1}) and a larger value of the linear anisotropy parameter (γ_a=2ns^{-1}). A better agreement would be expected if the working parameters of our VCSELs are extracted.

CHAPTER 7

Study of the nonlinear dynamics in single-mode VCSELs subject to optical injection.

In this chapter, we report an experimental study of the nonlinear dynamics appearing in a 1550 nm single-mode VCSEL subject to parallel and to orthogonal optical injection. For the first time to our knowledge we report experimentally measured stability maps of that system identifying the boundaries between regions of different nonlinear dynamics for both cases of polarized optical injection. A rich variety of nonlinear behaviors, including periodic (limit cycle, period doubling) and chaotic dynamics have been experimentally observed. For the orthogonal optical injection we present an experimental and a theoretical study of the polarization and time-resolved nonlinear dynamics. Special attention is paid to the correlation properties of both linear polarizations emitted by the VCSEL. We measure simultaneous time traces of both linearly polarized output signals for several values of the bias current, the

strength of the optical injection, and the frequency detuning between master and the free-running VCSEL. For positive frequency detuning we usually find that the orthogonal polarization is the only polarization that contributes to the dynamics of the total power. Only for large values of the bias current and for small values of the optical injection strength, near the border of the periodic region, we have found correlated periodic dynamics in both linear polarizations. For negative frequency detuning we find anticorrelated dynamics in both linear polarizations. The average and dispersion of the time between consecutive pulses that appear in the anticorrelated regime increase with the injected power. The irregular dynamics, characterized by broadened power spectra, is related to large values of the dispersion of the time between pulses. A good overall qualitative agreement is found between our theoretical and experimental results.

7.1. Introduction

Nonlinear dynamics of VCSELs under orthogonal optical injection has been experimentally and theoretically analyzed for 850 nm[Hong 2003], [Altes 2006], [Gatare 2007b], [Panajotov 2009], [Nizette 2009], [Boiko 1999] and 1550 nm, [Al-Seyab 2011] wavelength devices. Rich nonlinear dynamics, including period doubling, quasiperiodicity, injection locking, bistability and chaos, have been found in short-wavelength VCSELs [Hong 2003], [Altes 2006], [Gatare 2007b], [Panajotov 2009], [Nizette 2009], [Boiko 1999]. These devices were characterized by small values of birefringence and showed PS in absence of optical injection. Analysis of 1550 nm wavelength single transverse mode VCSELs subject to orthogonal optical injection have also shown limit cycle and period doubling dynamics, injection locking, irregular behavior [Al-Seyab 2011] and bistability [Hurtado 2006],[Valle 2008], [Torre 2010]. These long-wavelength devices were characterized by very large values of the birefringence parameter and by emission in a single linear polarization over the whole bias

current range in absence of optical injection. In this chapter we make a more systematic study of the nonlinear dynamics found in these systems.

7.2. Experimental Setup

We now describe the experimental setup used for the study of the nonlinear dynamics of a 1550 nm-VCSEL subject to parallel and to orthogonal optical injection. In contrast with previous experiments with 845nm-VCSELs [Altes 2006] our device is single transverse mode with a preferred polarization for the whole bias current range. Moreover the frequency of the parallel polarization is higher than that of the orthogonal one with a much larger frequency difference between both polarizations as it's showed in Fig. 6.2 (b). Figure 6.2 (a) shows the L-I curve and Figure 6.2 (b) shows the optical spectrum of the VCSEL when the current is 2.50 mA.

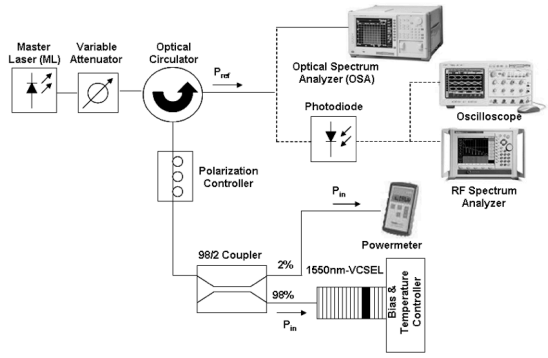

Fig. 7.1. Experimental Setup.

Figure 7.1 shows the all-fiber Setup that has been developed to inject the light emitted by a tunable laser into the 1550 nm-VCSEL. The Setup is similar to the Setup shown in Fig. 6.1, the difference is that now we have a 50/50 fibre directional coupler connected to the third port of the optical circulator. This coupler divides the optical path in two branches. One of the 50% branch is connected to the photodiode which is connected to the oscilloscope or to the RF Analyzer and the other one is connected to the OSA.

7.3. Experimental results for parallel and orthogonal optical injection

7.3.1 Parallel polarized optical injection

In most of the studies of injection locking and nonlinear dynamics in semiconductor lasers, the polarization of the ML has been traditionally chosen to match that of the light emitted by the slave laser. Therefore, initially we have analyzed the case of parallel polarized injection into the parallel polarized lasing mode of the 1550 nm-VCSEL and Fig. 7.2 (a) shows the experimental stability map for parallel optical injection measured with the device biased with an applied current of 4 mA (I_{bias}=2.44*I_{th}). The frequency of the externally injected signal, ν, was swept around the resonant frequency of the parallel polarization mode,$\nu_{\parallel}$, the frequency detuning being ν-$\nu_{\parallel}$. Regions of different behavior were observed, including periodic dynamics such as limit cycle (period 1, P1) and period doubling (period 2, P2) and regions of chaos. When measuring these maps we consider P1 dynamics when the peak in the RF spectrum of the total power measured in the RF analyzer was 10 dB above the noise floor. The latter were observed for both positive and negative frequency detuning. It is important to note here that the measured stability map (Fig. 7.2 (a)) exhibits strong similarities with those reported in edge-emitting devices [see Fig. 7.3 [Wieczorek 2005]]. Similarities appear since we are matching the polarization of the external signal to that of the lasing mode. This conforms to the convention with edge-emitting lasers, where the polarizations of the ML and the slave laser are matched. The RF spectra shown in this chapter have been obtained by subtracting the RF spectra in the absence of light to the RF spectra with optical injection. We have done it in order to subtract the noise floor in the photodetector and RF analyzer.

Figures 7.2 (b-e) show the experimental RF spectra for the points marked in Fig. 7.2 (a). Figure 7.2 (b) shows a broadened RF spectrum characteristic of a chaotic dynamics situation. Figure 7.2

(c) shows the RF spectrum signature of a limit cycle (Period 1, P1) dynamics; with a strong peak at 3.8 GHz, frequency at which the VCSEL output oscillates. Figure 7.2(d) shows an RF spectrum indicating period doubling dynamics (Period 2, P2). Finally, Fig. 7.2 (e) shows again a limit cycle (Period 1, P1) dynamics situation.

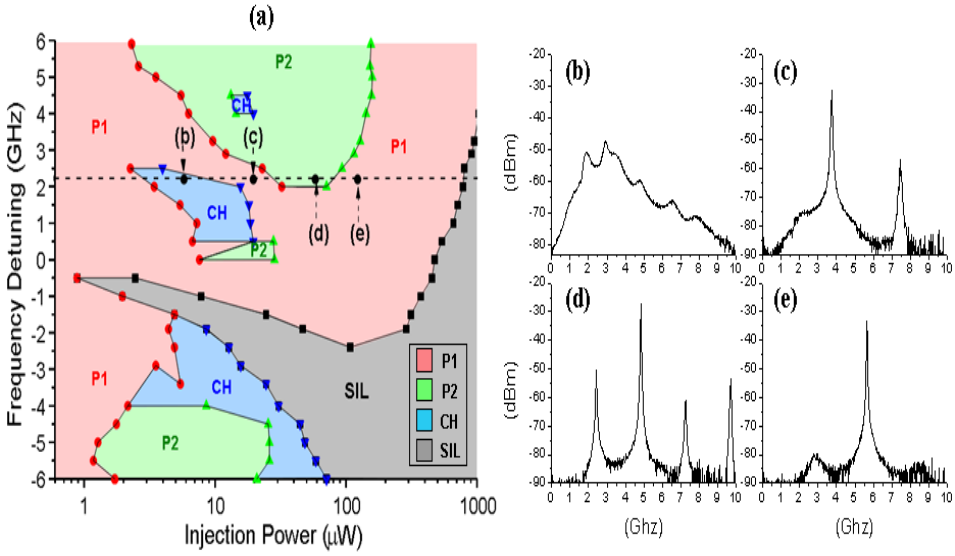

Fig. 7.2. (a) Experimental stability map of the 1550nm-VCSEL subject to parallel polarized injection: Different regions are observed: SIL(stable injection locking), P1 (Period 1), P2 (period 2) and CH (chaos); (b-e) RF spectra measured for the situations indicated in the stability map corresponding to a frequency detuning of 2.2 GHz and various levels of input power: (b) 5.8 μW (chaos, CH), (c) 19.6 μW (Period 1, P1), (d) 58.31 μW (Period 2,P2) and (e) 122.5 μW (Period 1,P1). Applied bias current of 4mA (I_{bias}=2.44*I_{th}).

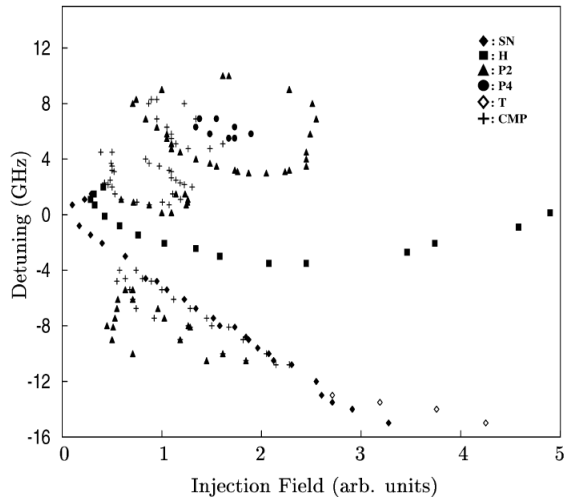

Fig. 7.3. Experimental bifurcation diagram. Squares denote the appearance of the relaxation oscillation. Period-two operation is shown by triangles and a further doubling by circles confine regions of period-four oscillation. Full diamonds correspond to the transition from stable, locked operation to unlocked operation while the open diamonds at large negative offset frequencies correspond to the transition from unlocked to stable locked operation. Crosses bound regions of more complicates spectral and dynamic characteristics where the spectral characteristics change rapidly as the operating point is changed. [Wieczorek 2005].

7.3.2 Orthogonally polarized optical injection

Figure 7.4(a) shows the experimental stability map of the 1550nm-VCSEL subject to orthogonally polarized optical injection into the subsidiary orthogonal polarization mode of the device. A bias current of 4 mA (I_{bias}=2.44 I_{th}) was applied to the VCSEL. The nonlinear dynamics have been mapped when the frequency of the externally injected signal is swept around the frequency of the orthogonal polarization of the fundamental transverse mode, $\nu_{\perp}$, the frequency detuning being $\Delta\nu=\nu-\nu_{\perp}$. Different regions corresponding to different dynamical regimes appear in the

stability map. Region SL represents the stable injection locking range, while region P1 show periodic dynamics (limit cycle or Period 1) and finally region CH corresponds to irregular and possibly chaotic dynamics. The SL region exhibits now an almost symmetric shape [Hurtado 2008a]. We believe that this could be perhaps related to the significant difference in the power emitted by the two orthogonal polarizations of the solitary VCSEL. The ratio of injected power to power emitted by the mode under injection would be much higher now than in the case of parallel polarized injection. Here, the asymmetry of the Hopf bifurcation [Mogensen 1985], [Wieczorek 2005] is not observed and an almost symmetric behavior is found for the SL region. Other factors that could be behind this behavior would include the gain anisotropy and the large frequency splitting between the two orthogonal polarizations of the fundamental mode of the VCSEL. Additionally, Fig. 7.4 (a) also shows the optical power required to obtain polarization Switching (PS))[Hurtado 2008b], [Valle 2008], [Hurtado 2009b]. PS refers to the situation where the output is switched from parallel to orthogonal polarization under orthogonally polarized optical injection [Pan 1993], [Gatare 2006], [Jeong 2008], [Hurtado 2008b], [Valle 2008], [Hurtado 2009b]. This can be better understood with Figs. 7.4 (b) and 7.4 (c), which show the optical spectrum of the free-running VCSEL lasing in the parallel polarized mode, and the optical spectrum of the device subject to orthogonal optical injection respectively. In Fig. 7.4 (c) the parallel polarized mode is suppressed, PS is attained and the output of the device changes to orthogonal polarization. It is found that PS is always accompanied with stable locking for negative frequency detuning (see Fig. 7.4 (a)). However, PS can be also observed together with a periodic dynamical regime for certain values of positive frequency detuning, in particular with Period 1 dynamics (limit cycle) as shown in Fig. 7.4 (a). The latter had only been reported previously in short-wavelength VCSELs [Altes 2006], but had not been observed in long-wavelength devices.

Furthermore, we have measured another stability map for applied bias current of 8 mA and orthogonal optical injection (see Fig. 7.5). As in the previous map, the region P1 shows periodic (period 1) behavior, region IR corresponds to irregular dynamic, region SL represents the stable locking regime and P2 represents period doubling dynamics. The injected power required for PS to the orthogonal polarization of the VCSEL is also shown in Fig. 7.5.

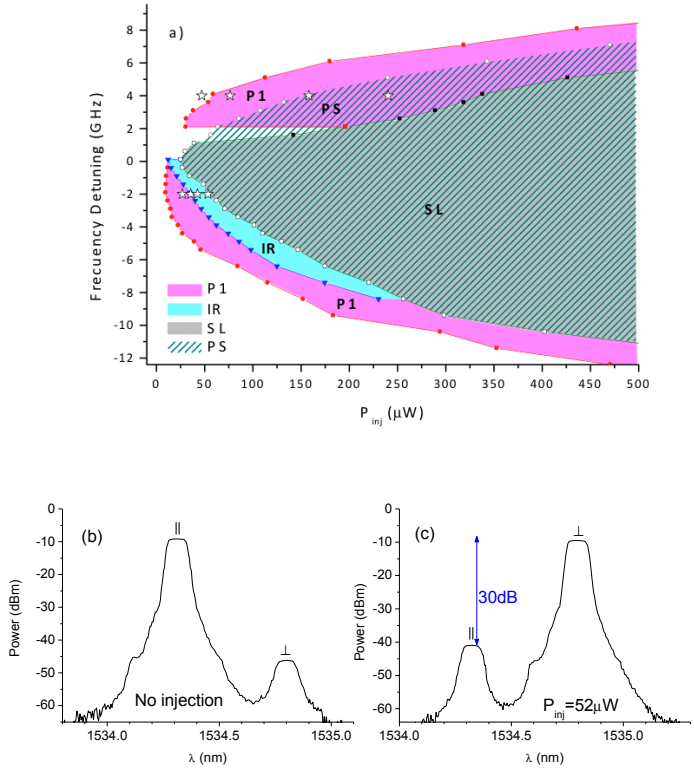

Fig. 7.4. (a) Stability map of the 1550nm-VCSEL subject to orthogonal injection. Different regions are observed: SIL (stable injection locking), PS (polarization switching), P1 (period 1) and CH (chaos); the white stars included in the map mark the dynamic situations analyzed with detail in Figs. 7.6 and 7.7. (b) Optical spectrum of the free-running VCSEL. (c) Optical spectrum of the VCSEL subject to orthogonal injection with input power of 52 μW and $\Delta\nu$=-0.9 GHz. Polarization switching is produced. Applied bias current of 4 mA (I_{bias}=2.44*I_{th}) in all cases.

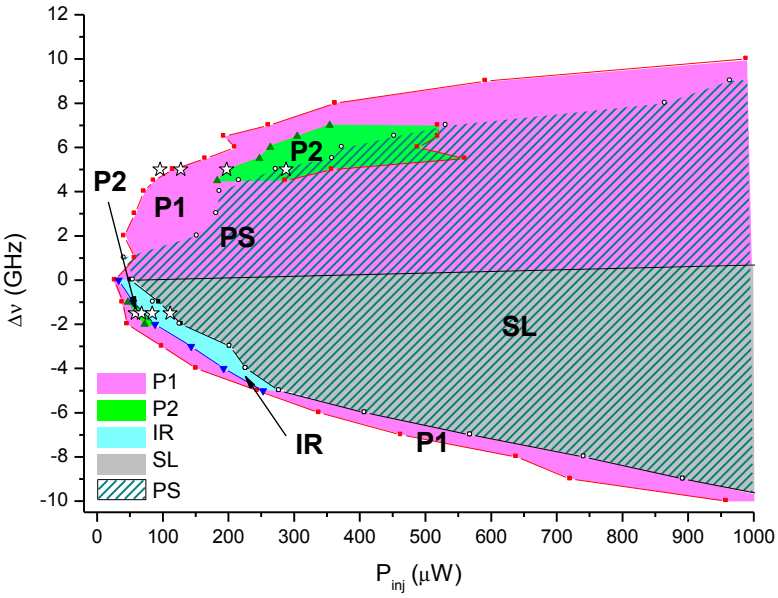

Fig. 7.5. Stability map of the 1550nm-VCSEL subject to orthogonal injection for applied bias current of 8mA. Different regions are observed: SL, stable locking; P1, period 1; P2, period 2; IR, irregular dynamics; PS, polarization switching. The stars mark the situations analyzed in Figs. 7.8 and 7.9

7.3.2.1 Simultaneous measurements of linearly polarized temporal traces. Correlation properties between polarizations.

We now present in Figs. 7.6 and 7.7 the results relative to the simultaneous measurement of linearly polarized power temporal traces for positive and negative frequency detunings, respectively. The simultaneous time traces of the power of both linear polarizations are shown in the left column of Fig. 7.6. for a fixed frequency detuning of 4 Ghz, bias current of 4 mA and increasing values of P_{inj}. In all the time traces presented here, we also include the sum of both powers (total power). Direct measurements of time traces of the total power show a similar behavior to that

shown in the figures. RF spectra for the two polarizations and for the total power are shown in the central column. In the right column we present the optical spectra for the total power measured with a high-resolution optical spectrum analyzer BOSA. Showing results for the total power is enough to describe the optical spectra of both linear polarizations. We have checked that optical spectra of the orthogonal (parallel) polarization correspond to the optical spectra of the total emitted light below (above) 0 GHz. The zero value of the frequency has been chosen to correspond to $\nu_{th}=(\nu_{\perp}+\nu_{\parallel})/2$, that is the intermediate value between the frequencies of both linear polarizations.

The cases considered in Fig. 7.6 are identified in Fig. 7.4 (a) with the upper row of white stars. We first analyze the transition to P1 dynamics that appears at low values of P_{inj}. Fig.7.6 (a) shows that oscillations of small amplitude around the steady state characterize both linear polarizations and the total power. This behavior corresponds to a point near the period 1 (P1) region in the stability map Fig. 7.4 (a). Figure 7.6 (b) shows that a peak in the RF spectrum of the total power begins to appear near the frequency detuning. A similar peak appears in the RF spectrum of the orthogonal polarization power, while the spectrum corresponding to the parallel polarization is much flatter. Several peaks appear in the optical spectrum Fig. 7.6 (c): the first one at -31 GHz, corresponds to the orthogonal polarization, the second one, at 4.4 GHz to the right, corresponds to the optical injection, and the last one, at 31.5 GHz corresponds to the parallel polarization. A clear P1 dynamics in the total and orthogonal polarized powers is obtained when increasing P_{inj} as it is shown in Fig. 7.6 (d) and 7.6 (e). The power of the parallel polarization is still appreciable; however, the amplitude of their oscillations is very small without contributing to the periodic dynamics of the total power. This is also seen in Fig. 7.6 (e) in which its RF spectrum is weak and flat. This periodic dynamic is caused by beating between the optical injection and the orthogonal mode of the VCSEL. Fig. 7.6 (f) shows that the optical spectrum of the

orthogonal and parallel polarizations have more peaks than in Fig. 7.6 (c). They are equally spaced around a value of 4.6 GHz. This value also corresponds to the frequency at which the RF spectra of the orthogonal and total power have a well defined peak (see Fig. 7.6 (e)). The separation between consecutive peaks in the optical spectrum increases as P_{inj} increases. This can be explained in terms of the "frequency pushing" effect. Effect that appears due to the positive value of α: when $\Delta\nu>0$ the resonance wavelength of the orthogonal mode moves away the injected wavelength as P_{inj} increases. This also means that optical injection is less effective in creating nonlinear effects. P1 dynamics is caused by beating between the optical injection and the orthogonal mode of the VCSEL. Further increase of P_{inj} produces PS: the peak corresponding to the parallel polarization is no longer observed in Fig. 7.6 (i). Fig. 7.6 (g) shows that the orthogonal polarization power is oscillating at a frequency around 5.3 GHz. Figure 7.6 (g) shows that the frequencies of the times traces of the total and orthogonal polarized powers have increased to the values at which RF spectra have their peaks (see Fig. 7.6 (h)). Further increase of P_{inj} produces a decrease of the amplitude of the oscillations of the time traces (see Fig. 7.6 (j)). This is also shown by the decrease of the peaks in the RF spectrum (see Fig. 7.6 (k)). Figures 7.6 (j) and 7.6 (k) also illustrate the situation in which PS and P1 dynamics are obtained. The optical spectrum of the total power in Fig. 7.6 (l) shows that PS has occurred. Operation in the stable locking (SL) regime is illustrated in the lower part of Fig. 7.6. The amplitude of the oscillations in the time traces is very small (see Fig. 7.6 (m)) and the orthogonal polarization mode of the VCSEL is stably locked to the optical injection as it can be seen in Fig. 7.6 (o). The RF spectrum of the total power and of the power of both linear polarizations become flat (see Fig. 7.6 (n)).

The correlation properties between the power of the parallel, $P_{\parallel}(t)$, and the orthogonal, $P_{\perp}(t)$, linear polarizations can be discussed in terms of their cross-correlation function, defined as

$$C(\tau)=\frac{\overline{\left(P_{\parallel}(t+\tau)-\overline{P}_{\parallel}\right)\left(P_{\perp}(t)-\overline{P}_{\perp}\right)}}{\sigma_{\parallel}\sigma_{\perp}} \tag{7.1}$$

where the bar means time averaging operation and $\sigma_i^2=\overline{\left(P_i(t)-\overline{P}_i\right)^2}, i=\parallel,\perp$

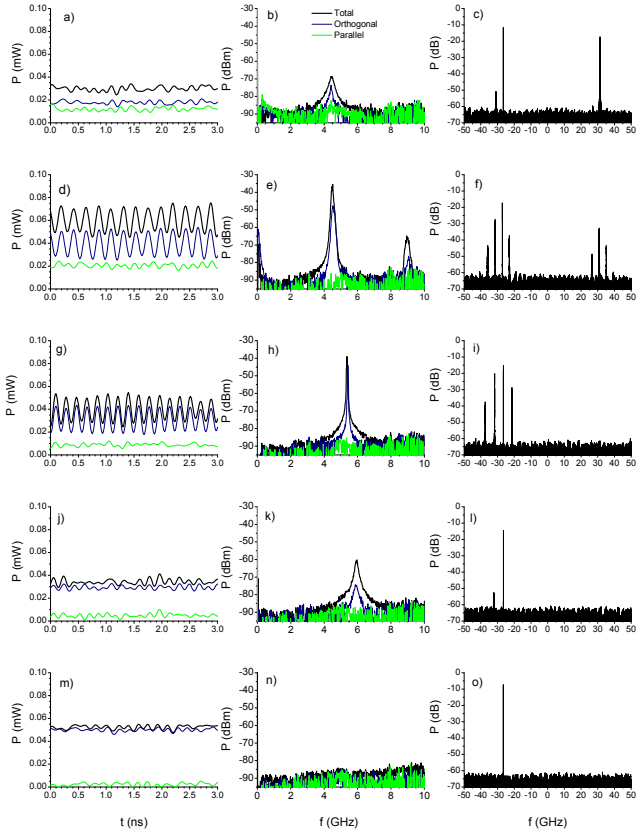

Fig. 7.6. (Left) Time traces of the total power and of the power of both linear polarizations. (Central) RF spectra of the total and polarized powers. (Right) Optical spectra of the total power. Several values of injected power are considered: (a), (b), (c) P_{inj}= 47 μW, (d), (e), (f) P_{inj}=76.4 μW, (g), (h), (i) P_{inj}=158 μW, (j), (k), (l) P_{inj}=240.3 μW, and (m), (n),(o) P_{inj}=1275.5 μW. The frequency detuning is $\Delta\nu$=4 GHz, and the bias current is 4mA.

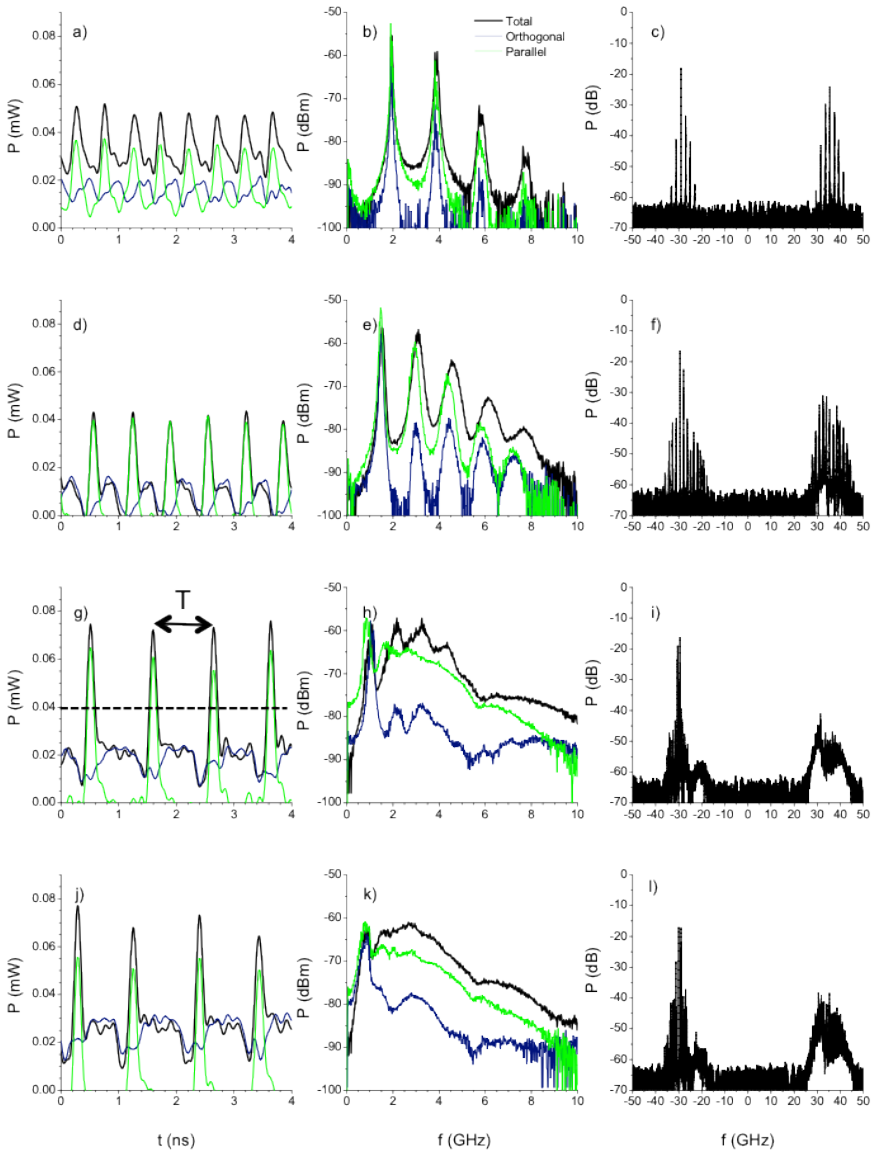

Fig. 7.7. (Left) Time traces of the total power and of the power of both linear polarizations. (Central) RF spectra of the total and polarized powers. (Right) Optical spectra of the total power. Several values of injected power are considered: (a), (b), (c) P_{inj}= 26.9 μW, (d), (e), (f) P_{inj}=35.5 μW, (g), (h), (i) P_{inj}=42.4 μW and (j), (k), (l) P_{inj}=53.6 μW. The frequency detuning is $\Delta\nu$=-2 GHz, and the bias current is 4mA.

Temporal averages have been performed by using time series of 500 ns duration. The correlation between the power of the parallel and orthogonal linear polarizations is very weak for all the cases analyzed in Fig. 7.6. The absolute value of the cross-correlation functions obtained for the different cases considered in Fig. 7.6 is always below 0.08.

We now analyze in Fig. 7.7. the case of a negative frequency detuning, $\Delta\nu$=-2 GHz, with the same value of the applied bias current (4 mA). The cases analyzed in Fig. 7.7 are marked in Fig. 7.4 (a) with the lower row of white stars. Fig. 7.7 shows the time traces, the RF spectra and optical spectra for a negative value of the frequency detuning, $\Delta\nu$=-2 GHz. Figs. 7.7 (a)-(c) illustrate the behavior obtained for small values of P_{inj}, in such a way that the system is in the P1 regime. Non-sinusoidal periodic dynamics are obtained for both periodic dynamics, in contrast with the positive $\Delta\nu$ case. The non sinusoidal shape of the temporal traces (see Fig. 7.7 (a)) is related to the large amplitude of the harmonic peaks in the RF spectrum (see Fig. 7.7 (b)). RF spectra of both polarizations and total power have peaks at a fundamental frequency (1.9 GHz) and their harmonics that corresponds to the frequency detuning observed in the optical spectrum in Fig. 7.7 (c). The optical spectrum of the orthogonal and parallel polarizations have multiple peaks. The separation between consecutive peaks is around 1.9 GHz, that it is the value at which the RF spectra have their fundamental frequency. Fig. 7.7 (a) shows that the power of the parallel polarization consists of a train of large amplitude pulses that are responsible for the large amplitude pulses of the total power. The shoulder that appears in the total power after those pulses is due to the contribution of the orthogonally polarized mode. Fig 7.7 (a) shows that, after the decrease of $P_{\perp}$, a pulse of $P_{\parallel}$ is fired with a certain delay. That delay is small enough for the pulse of $P_{\parallel}$ to still coincide with the valley of the orthogonal power. Also the maximum of $P_{\perp}$ coincides with the absence of a pulse of $P_{\parallel}$. In this way the orthogonal and parallel polarized powers are anticorrelated. Fig. 7.7 (e) shows that, for increasing P_{inj} values,

peaks of the RF spectra of both polarizations and total power appear at smaller value of frequency. This is a "frequency pulling" effect due to the change of refractive index induced by the increase of P_{inj}. The qualitative behavior of $P_{\parallel}$ and $P_{\perp}$ shown in Fig. 7.7 (d) is similar to that described in Fig. 7.7 (a), although now the contributions of the pulses of $P_{\parallel}$ and $P_{\perp}$ to the amplitude peaks and shoulders of the total power, respectively, are better defined. Comparison between Figs. 7.7 (a) and 7.7 (d) shows that the time between consecutive large amplitude peaks (larger than a chosen reference level plotted in Fig. 7.7 (g) with a dotted line) increases as P_{inj} increased. That time is usually called the interpulse time, T. Broadening of the optical and RF spectra is related to a large increase of the interpulse time dispersion,σ_T. The average of the interpulse time corresponding to the total power, $\langle T \rangle$, is 0.52 and 0.66 ns for Figs. 7.7 (a) and 7.7 (d), respectively. The fundamental frequency in the RF spectra in Figs. 7.7 (b) and 7.7 (e) corresponds approximately to the inverse of $\langle T \rangle$. Comparison between Fig. 7.7 (c) and 7.7 (f) shows that the number of peaks in the optical spectra of both linear polarizations increases as P_{inj} increased. Also, the separation between consecutive peaks decreases to 1.5 GHz in Fig. 7.7 (f). Figs. 7.7 (g)-(i) show the irregular dynamical behavior that is obtained when increasing P_{inj}. This dynamics is characterized by broad RF spectra in which the peaks tend to disappear (Fig. 7.7 (h) and 7.7 (k)). A better defined peak appears near 1 GHz frequency that approximately corresponds to the inverse of $\langle T \rangle$ in Fig. 7.7 (h) ($\langle T \rangle$=0.93 ns) Figs. 7.7 (i) and 7.7 (l) show the corresponding optical spectra. Irregular dynamics is characterized by optical spectra for both linear polarizations with wide pedestals and much less defined peaks with smaller separation between them. Broadening of the RF spectra as P_{inj} increases is related to a large increase of the interpulse time dispersion, σ_T. In fact, σ_T is 12, 40, and 96 ps (see Table 7.1) for Figs. 7.7 (d), 7.7 (g) and 7.7 (j), respectively. The shoulder that appears after the large pulse of the total power changes its shape toward a plateau with small oscillations as P_{inj} increases (see Figs. 7.7 (g) and 7.7 (j)). The main

contribution to the plateau is given by the orthogonal polarization. This means that, as the PS region is approached, the VCSEL is orthogonally polarized with a constant power during a longer time. In fact PS is obtained, simultaneously to SL, by increasing slightly P_{inj} to 65 μW.

Anticorrelation between both linear polarizations is clear from the time traces of Fig. 7.7. This anticorrelation is confirmed by using the cross-correlation coefficient at τ=0, C(0) that takes the values -0.54, -0.51, -0.48, -0.50 (see Table 7.1) for Figs. 7.7 (a), 7.7 (d), 7.7 (g) and 7.7 (j), respectively. Information about the relative phase between the time traces of both polarizations can be obtained from the time at which $C(\tau)$ takes its minimum value. $C(\tau)$ have minimum values of -0.85, -0.76, -0.64, -0.66, at τ_{min}=0.075, 0.1, 0.175, 0.187 ns (see Table 7.1) for Figs. 7.7 (a), 7.7 (d), 7.7 (g) and 7.7 (j), respectively. τ_{min} increases when increasing P_{inj} in such a way that the relative phase $(1-2\tau_{min}/\langle T\rangle)\pi$ is approximately constant (0.71π, 0.69π, 0.62π, 0.67π rads for Figs. 7.7 (a), 7.7 (d), 7.7 (g) and 7.7 (j), respectively). This relative phase is not exactly π (antiphase) due to the delay of the emission of the parallel polarization pulse with respect to the decrease of the orthogonal one. Antiphase dynamics has been observed experimentally in multimode edge-emitting lasers with optical injection but at positive values of the frequency detuning [Osborne 2009]. Theoretical calculations in VCSELs subject to orthogonal optical injection predicted that the two linearly polarized modes are anticorrelated at the time scale of slow oscillations while they exhibit an in-phase dynamics at the fast time scale of the relaxation oscillations [Sciamanna 2006]. Very recently, excitability and self-pulsating dynamics has been analyzed in optically injected quantum-dot and quantum-well laser diodes [Kelleher 2011], [Olejniczak 2010]. Time traces of the total power shown in Figs. 7.7 (g) and 7.7 (j) resemble the traces showing single-pulse excitability or self-pulsating behavior observed in [Kelleher 2011], [Olejniczak 2010].

$\Delta\nu$/GHz	$P_{inj}/\mu W$	$\langle T\rangle$/ns	σ_T/ps	C(0)	$C(\tau_m)$	τ_m/ns
4	47.0	0.22	60	6	0.006	0
	76.4	0.22	8	-0.12	-0.21	0.0375
	158.0	0.19	6	0.014	0.036	0-0.0375
	240.3	0.18	40	0.002	0.019	-0.05
-2	26.9	0.52	17	-0.54	-0.85	0.075
	35.5	0.66	12	-0.51	-0.76	0.1
	42.4	0.93	40	-0.48	-0.64	0.175
	53.6	1.04	96	-0.50	-0.66	0.187

Table 7.1: Averaged interpulse time ($\langle T\rangle$), standard deviation (σ_T), and correlation coefficient (C(0)), first minimum of the cross-correlation function ($C(\tau_m)$) and time at which it appears (τ_m). The applied bias current is 4mA.

We now discuss the experimental results corresponding to a large value of the bias current, I=8 mA. We show in Fig. 7.8 the results corresponding to a fixed frequency detuning of $\Delta\nu$=5 GHz and different values of P_{inj}. The cases considered in Fig. 7.8 are identified in Fig. 7.5 with the upper row of white stars. In Fig.7.8 (a) sinusoidal time traces are found for the power of both linear polarizations. These time traces have a correlated behavior as it can also be seen in Table 7.2. The optical spectrum of each linear polarization consists in several peaks as it can be seen in Fig. 7.8 (c). The peak that corresponds to the optical injection is the one appearing near the -25 GHz frequency. Consecutive peaks are separated by an averaged value of 5.4 GHz. This value is very similar to the value at which RF spectra have a well defined peak (5.5 GHz) as it is shown in Fig. 7.8 (b). P1 dynamics is more clear when increasing P_{inj} as it can be seen in Fig. 7.8 (d), 7.8 (e), and 7.8 (f) because the total power has more regular oscillations with larger amplitudes. Positive correlation between linear polarizations is also confirmed by using C(0) that takes the values 0.75 and 0.65 for Figs. 7.8 (a) and 7.8 (d), respectively. Information about the relative phase between the time traces of both polarizations can

be obtained from the time at which C(τ) takes its maximum value. These times are τ_{max}= -0.012, 0 ns, for Figs. 7.8 (a) and 7.8 (d), respectively. The relative phase is given by 0.13π, 0 rads for Figs. 7.8 (a) and 7.8 (d), respectively. This corresponds to a slight delay of the appearance of the maximum value of the orthogonal polarization with respect to the parallel one for Fig. 7.8 (a). Only in the region near the border of P1 have we been able to observe correlated periodic dynamics in both linear polarizations (see Fig. 7.8 (d)). As we move further inside the P1 region, the RF peak corresponding to the parallel polarization disappears, while those corresponding to the orthogonal polarization and total power are maintained. This situation, in which only the orthogonal polarization contributes to the dynamics of the total power, is found for all the values of P_{inj} before SL is reached. It can be seen in Figs. 7.8 (h) and 7.8 (k). Fig. 7.8 (f) and 7.8 (i) show that the number of peaks in the optical spectrum of the orthogonal polarization is larger as P_{inj} increased. The separation between consecutive peaks in Fig. 7.8(i) is around 6.2 GHz. The magnitude of the peaks in the spectrum of the parallel polarization decreases because of the PS is approached. Figures 7.8 (g)-(l) are two examples that illustrate this behavior. In the situation illustrated in Figs. 7.8 (g), 7.8 (h), 7.8 (i), the power of the parallel polarization is still not negligible since the polarization of the VCSEL has not switched yet, as can be seen in Fig. 7.5. A weak positive correlation is found in Fig. 7.8 (g): C(τ) has a maximum value of 0.24 at τ_{max}=0 ns. In-phase behavior of both polarizations is observed. Figs. 7.8 (g)-(i) show weak period doubling dynamics that we were not able to appreciate in the optical spectrum although we can see this period doubling dynamics in the RF spectra (see Fig. 7.8 (h)). Figs. 7.8 (j)-(l), in which PS has already occurred, no correlation is observed (the maximum value of C(τ) is 0.05). Fig. 7.8 (l) shows that PS has been achieved when P_{inj}=278.8 μW. Further increase of P_{inj} leads to SL dynamics, as it is shown in Figs. 7.8 (m)-(o).

We know analyze the dynamics obtained for the case of a negative $\Delta\nu$ value. Figure 7.9 shows RF and optical spectra and

time traces for $\Delta\nu$=-1.5 GHz. The cases considered in Fig. 7.9 are identified in Fig. 7.5 with the lower row of white stars.

$\Delta\nu$/GHz	$P_{inj}/\mu W$	$\langle T\rangle$/ns	σ_T/ps	C(0)	$C(\tau_m)$	τ_m/ns
5	96.1	0.19	7	0.75	0.87	-0.0125
	127.6	0.187	6	0.65	0.65	0
	197.3	0.168	6	0.24	0.24	0
	287.8	0.155	6	-0.013	-0.05	0.0375
-1.5	58.5	0.326	7	-0.37	-0.94	0.0625
	67.6	0.404	10	-0.47	-0.93	0.0625
	84.0	0.38	200	-0.67	-0.77	0.075

Table 7.2: Averaged interpulse time ($\langle T\rangle$), standard deviation (σ_T), and correlation coefficient (C(0)), first minimum of the cross-correlation function ($C(\tau m)$) and time at which it appears (τ_m). The applied bias current is 8mA.

Figures 7.9 (a), 7.9 (b) and 7.9 (c) illustrate the P1 dynamics obtained at low values of P_{inj}. The qualitative behavior of both polarizations is similar to that shown in Figs. 7.7 (a)-(c): maxima (shoulders) of the total power are due to the large amplitude peaks (maxima) of the parallel (orthogonal) polarization. Fig. 7.9 (c) shows that there are several peaks in the optical spectra of the parallel and orthogonal polarization. They are separated by 3.3 GHz, a value that is similar to that found for the frequency of the fundamental peak (3 GHz) in the RF spectrum (see Fig. 7.9 (b)).

Comparison between Fig. 7.9 (c) and Fig. 7.9 (f) shows that the number of peaks in the optical spectra of both linear polarizations increases as P_{inj} increased. This behavior is similar to that found in Fig. 7.7 (c) and 7.7 (f). However, the approach to the SL dynamics as P_{inj} is increased is different to that found for small bias currents. Figure 7.9 (e) shows that the P2 dynamics is obtained for both linear polarizations and for the total power when increasing P_{inj}. In fact, one of the main differences with respect to the small bias current case is the presence of P2 regions for positive and negative $\Delta\nu$ values (see Fig. 7.5). The optical spectrum

corresponding to this case is shown in Fig. 7.9 (f). P2 dynamics is barely visible from the peak appearing near 29 GHz frequency.

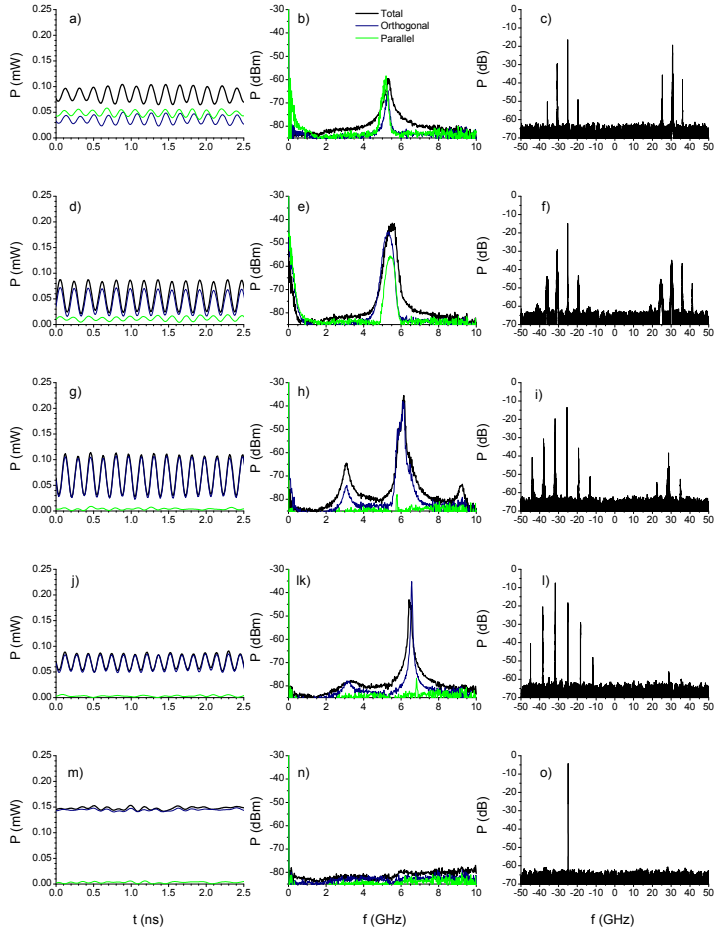

Fig. 7.8. (Left) Time traces of the total power and of the power of both linear polarizations. (Central) RF spectra of the total and polarized powers. (Right) Optical spectra of the total power. Several values of injected power are considered: (a), (b), (c) P_{inj}= 96.1 μW, (d), (e), (f) P_{inj}=127.6 μW, (g), (h), (i) P_{inj}=197.3 μW and (j), (k), (l) P_{inj}=287.8 μW and (m), (n), (o) P_{inj}=3301.8 μW. The frequency detuning is $\Delta\nu$=5 GHz, and the bias current is 8mA.

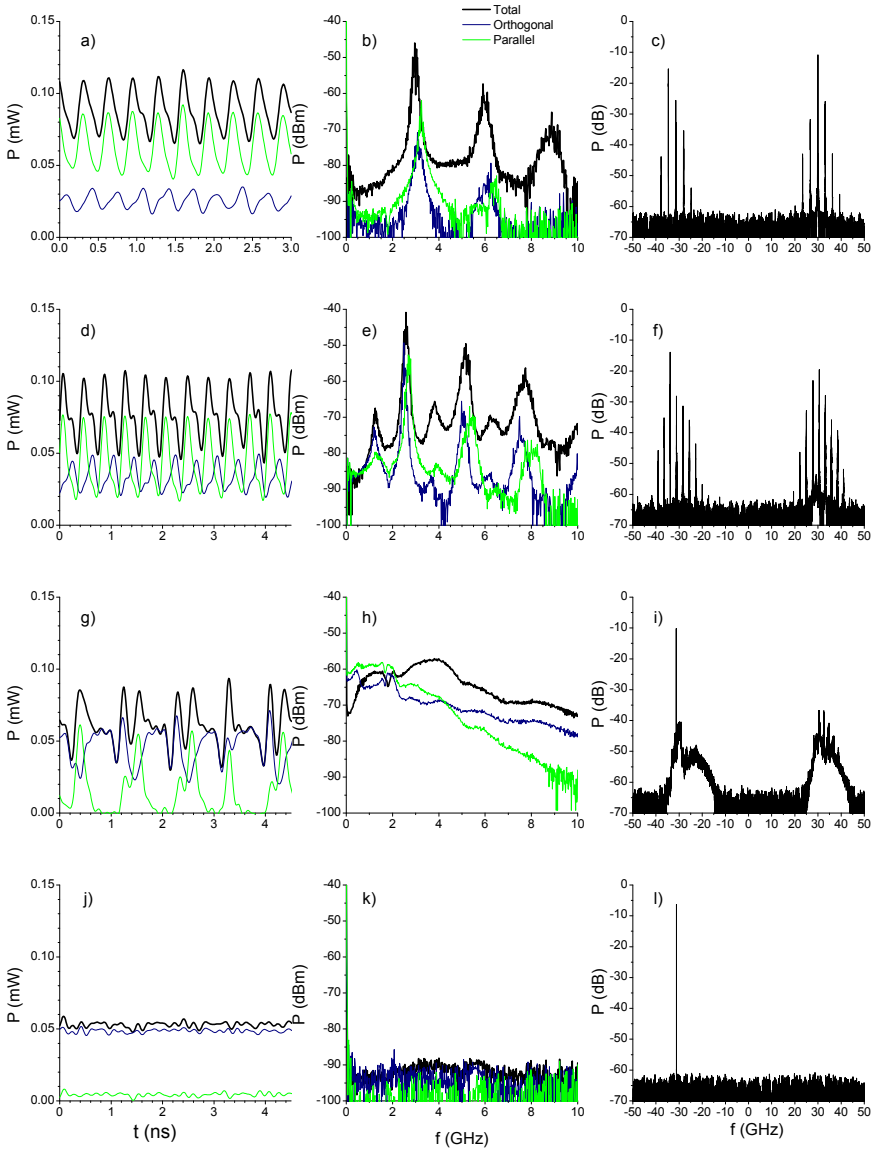

Fig. 7.9. (Left) Time traces of the total power and of the power of both linear polarizations. (Central) RF spectra of the total and polarized powers. (Right) Optical spectra of the total power. Several values of injected power are considered: (a), (b), (c) P_{inj}= 58.5 μW, (d), (e), (f) P_{inj}=67.6 μW, (g), (h), (i) P_{inj}=84μW and (j), (k), (l) P_{inj}=111.2 μW. The frequency detuning is $\Delta\nu$=-1.5 GHz, and the bias current is 8mA.

Second, further increase of P_{inj} leads to irregular behavior in both linear polarizations that is qualitatively different to that shown in Figs. 7.7 (j)-(l). Figure 7.9 (g) shows that, before the SL region, time traces are much more irregular than those observed for smaller bias currents (see Fig. 7.7 (j)). Two large amplitude consecutive pulses are occasionally obtained in the total power (see Fig. 7.9 (g) between 1 and 2 ns, between 2 and 3 ns, and after 4 ns). The first (second) large amplitude pulse is due to a pulse of the orthogonal (parallel) polarized mode. Other parts of the time series resemble the results shown in Fig. 7.7 (j): for instance, sometimes a single pulse is fired in the total power. This pulse is due to a large pulse of parallel polarized light (see Fig. 7.9 (g) between 0 and 1 ns and between 3 and 4 ns). The more irregular behavior obtained for large values of the bias current is also observed in RF spectra: peaks of Fig. 7.9 (h) are more smeared than those of Fig. 7.7 (h), especially those corresponding to the RF spectrum of the orthogonal polarization. The value of the interpulse time dispersion increases as P_{inj} increased (σ_T=7, 10, 200 ps for Figs. 7.9 (a), (d), (g), respectively). The large value of σ_T in Fig. 7.9 (g) is caused by the simultaneous presence of single-pulse and two-pulse packages. The corresponding optical spectra are shown in Fig. 7.9 (i). The optical spectrum corresponding to the orthogonal polarization consists in a very intense peak at the frequency of the optical injection and a very wide pedestal characterized by two maxima that appear near -30 and -24 GHz. The parallel polarization is also characterized by a wide optical spectrum with some peaks still visible between 30 and 35 GHz. Finally, dynamics illustrating simultaneous achievement of SL and PS are also illustrated in Figs. 7.9 (j)-(l). Some other similarities are observed with respect to the case of small bias current. First, the irregular behavior is also obtained only for negative values of $\Delta\nu$. Second, the orthogonal and parallel polarized powers are anticorrelated.

This anticorrelation is confirmed by using the cross-correlation coefficient at τ=0, C(0) that takes the values -0.37, -0.47, -0.67 for Figs. 7.9 (a), (d) and (g), respectively. C(τ) have minimum values of

-0.94, -0.93, -0.77 at τ_{min}=0.062, 0.062, 0.075 ns for Figs. 7.9 (a), (d) and (g), respectively. τ_{min} increases when increasing P_{inj} in such a way that the relative phase $(1-2\tau_{min}/\langle T\rangle)\pi$ is approximately constant (0.64π, 0.69π, and 0.74π rads for Figs. 7.9 (a), (d) and (g), respectively). Both signals are not exactly in antiphase due to the delay of the emission of the parallel polarization pulse with respect to the decrease of the orthogonal one. As it is illustrated in Fig. 7.9 (l) in the SL regime, only the optical spectrum corresponding to the orthogonal polarization has a very narrow peak that appears at the frequency of the optical injection.

7.4. Theoretical results

In this section we are going to analyze from a theoretical point of view the correlation properties corresponding to the two linearly polarized modes emitted by the VCSEL subject to orthogonal optical injection. Our rate equation model for the polarization of a VCSEL is based on the SFM [MartinRegalado 1997b]. If the parameters are chosen such that the free-running VCSEL emits in the y polarization, orthogonal optical injection is obtained by considering an external field along the x direction. The SFM model equations are given by

$$\frac{dE_x}{dt} = \kappa(1+i\alpha)\left(NE_x + inE_y - E_x\right) - i\gamma_p E_x - \gamma_a E_x + \kappa E_{inj} e^{i\Delta\omega t} + \\ + \sqrt{\beta_{sp}\gamma_e/2}\left(\sqrt{N+n}\xi_+(t) + \sqrt{N-n}\xi_-(t)\right) \tag{7.2}$$

$$\frac{dE_y}{dt} = \kappa(1+i\alpha)\left(NE_y + inE_x - E_y\right) + i\gamma_p E_y + \gamma_a E_y + \\ + \sqrt{\beta_{sp}\gamma_e/2}\left(\sqrt{N+n}\xi_+(t) + \sqrt{N-n}\xi_-(t)\right) \tag{7.3}$$

$$\frac{dN}{dt} = -\gamma_e\left(N\left(1+|E_x|^2+|E_y|^2\right)\right) + \gamma_e\mu - i\gamma_e n\left(E_y E_x^* - E_x E_y^*\right) \tag{7.4}$$

$$\frac{dn}{dt} = -\gamma_s n - \gamma_e n\left(|E_x|^2+|E_y|^2\right) - i\gamma_e N\left(E_y E_x^* - E_x E_y^*\right) \tag{7.5}$$

where $E_{x,y}$ are the two linearly polarized slowly varying components of the field and N and n are two carrier variables. N accounts for

the total population inversion between conduction and valence bands, while *n* is the difference between the population inversions for the spin-up and spin-down radiation channels. The internal VCSEL parameters are as follows: κ (=125 ns^{-1}) is the field decay rate, γ_e (=0.67 ns) is the decay rate of *N*, γ_s (=1000 ns^{-1}) is the spin-flip relaxation rate, α (=2.2) is the linewidth enhancement factor, μ is the normalized injection current, γ_a (=2 ns^{-1}) is the linear dichroism, and γ_p (=192 ns^{-1}) is the linear birefringence. The fluctuating nature of the spontaneous emission (with a fraction of spontaneous emission photons that goes into the laser mode of β_{sp} =10^{-4}) is included in our calculations since $\xi_+(t)$ and $\xi_-(t)$ are complex Gaussian noise terms of zero mean and time correlation given by $\langle\xi_i(t)\xi_j^*(t')\rangle=\delta_{ij}\delta(t-t')$. The optical injection parameters are E_{inj} and $\Delta\omega=\omega_{inj}-(\omega_x+\omega_y)/2$. We have integrated Eqs. (7.2)-(7.5) by using the same numerical method for stochastic differential equations used in [Mulet 2001] with an integration time step of 0.01 ps. The evolution of E_x is such that the $\kappa E_{inj}\exp(i\Delta\omega t)$ term appears in the equation for dE_x/dt. However, no injection term appears in the equation for dE_y/dt. In this way the increase of the optical injection strength (given by κE_{inj}) only affects directly to E_x, producing the PS to the x-polarized mode that has been usually observed in VCSELs since the pioneering work of Pan *et al*.[Pan 1993].

We have chosen parameters based on those reported by Al-Seyab et al. [Al-Seyab 2011] for a long wavelength VCSEL similar to our device. With our parameters, the free-running VCSEL is emitting in the parallel polarized mode (y mode) for all the bias current values, as in the experimental situation. Also, the frequency of the parallel polarized mode is higher than that of the orthogonal linear polarization (x mode): $\nu_y>\nu_x$, like for the VCSEL used in our experiments. The main change with respect to the parameters of [Al-Seyab 2011] is the value of the linear dichroism since we have checked that the value reported in [Al-Seyab 2011] leads to light-current characteristics in which multiple PSs occur as the bias

current is increased. Multiple PS appear because both polarizations are stable with the parameters chosen in that work [Al-Seyab 2011].

Our first theoretical results illustrate the case in which positive correlation is found between both linear polarizations. Figure 7.10 (a) shows time traces of the total power and of the power of both polarizations when the bias current is five times the threshold value (μ=5) and $\Delta\nu=\nu_{inj}-\nu_x$=5 GHz (similar to Fig. 7.8) and E_{inj}=0.29. Qualitative behavior is similar to that shown in Fig. 7.8 (a): both linearly polarized powers oscillate in a correlated way in such a way that both contribute to the almost sinusoidal time trace of the total power. Figure 7.10 (b) shows the time evolution of the total population inversion. *N* is characterized by a sinusoidal evolution of small amplitude. The decrease of *N* is related to the increase of the power in both polarizations. The frequency of the oscillations is around 6 GHz, larger than the value of $\Delta\nu$. This is due to the frequency pushing effect.

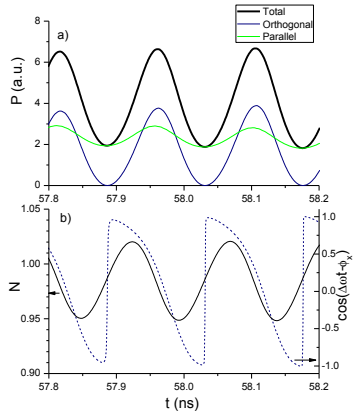

Fig. 7.10. Theoretical time traces of the (a) total power and power of both linear polarizations and (b) total population inversion (solid line) and $\kappa E_{inj}\cos(\Delta\omega t-\phi_x(t))$ term (dashed line). The frequency detuning is $\Delta\nu$=5 GHz, μ=5, and E_{inj}=0.29.

The time evolution of the quantities shown in Fig. 7.10 is nearly sinusoidal. A positive correlation between linear polarizations of C(0)=0.87 is obtained. C(τ) takes its maximum value at τ_{max}=0 ns. The relative phase is given by 0.12π rads. This corresponds to a slight delay of the appearance of the maximum value of the orthogonal polarization with respect to the parallel one, in agreement with our experimental results shown in Fig. 7.8 (a).

Figure 7.11 shows the time evolution of the total power, the power of both polarizations and *N*, and the RF spectra when μ=2.44 and $\Delta\nu$=-2 GHz (similar to Fig. 7.7) for two different values of the injected power, E_{inj}=0.0445 and 0.047. Qualitative behavior is similar to that shown in Figs. 7.7 (a) and 7.7 (g), respectively. Anticorrelated periodic dynamics are obtained for both polarization modes. Increasing the value of E_{inj} to 0.0495 produces simultaneous PS and SL, similar to our experimental results. Nonlinear effects are stronger than those obtained for $\Delta\nu$>0 because an increase of P_{inj} makes the resonant wavelength of the orthogonal mode approach the injected wavelength. In fact, nonlinear oscillations of all the variables appear in Fig. 7.11, in contrast to the sinusoidal evolution shown in Fig. 7.10.

The strength of nonlinear oscillations increase as P_{inj} is increased (see for instance figures 7.11 (c) and (d)). Figures 7.11 (c) and (d) also show that faster decrease of *N* is related to the excitation of the parallel polarized pulse, while the low recovery of *N* is accompanied by the emission of the wider orthogonally polarized pulse. The presence of these two different evolution stages of *N* is related to the observed anticorrelated behavior between both polarizations. We have performed calculations of C(τ) by using theoretical time series of the total power of 819.2 ns duration. C(0) takes the values -0.96 and -0.51 for Figs. 7.11 (a) and 7.11 (b), respectively. C(τ) have minimum values of -0.96, -0.71 at τ_{min}=0.01,0.12 ns for Figs. 7.11 (a) and 7.11 (b), respectively. τ_{min} increases when increasing P_{inj} in such a way that the relative phase (1-2τ_{min}/$\langle T \rangle$)π is approximately constant (0.99π, 0.92π rads for Figs.

7.11 (a) and 7.11 (b), respectively), in qualitatively agreement with the experimental results reported in Fig. 7.7.

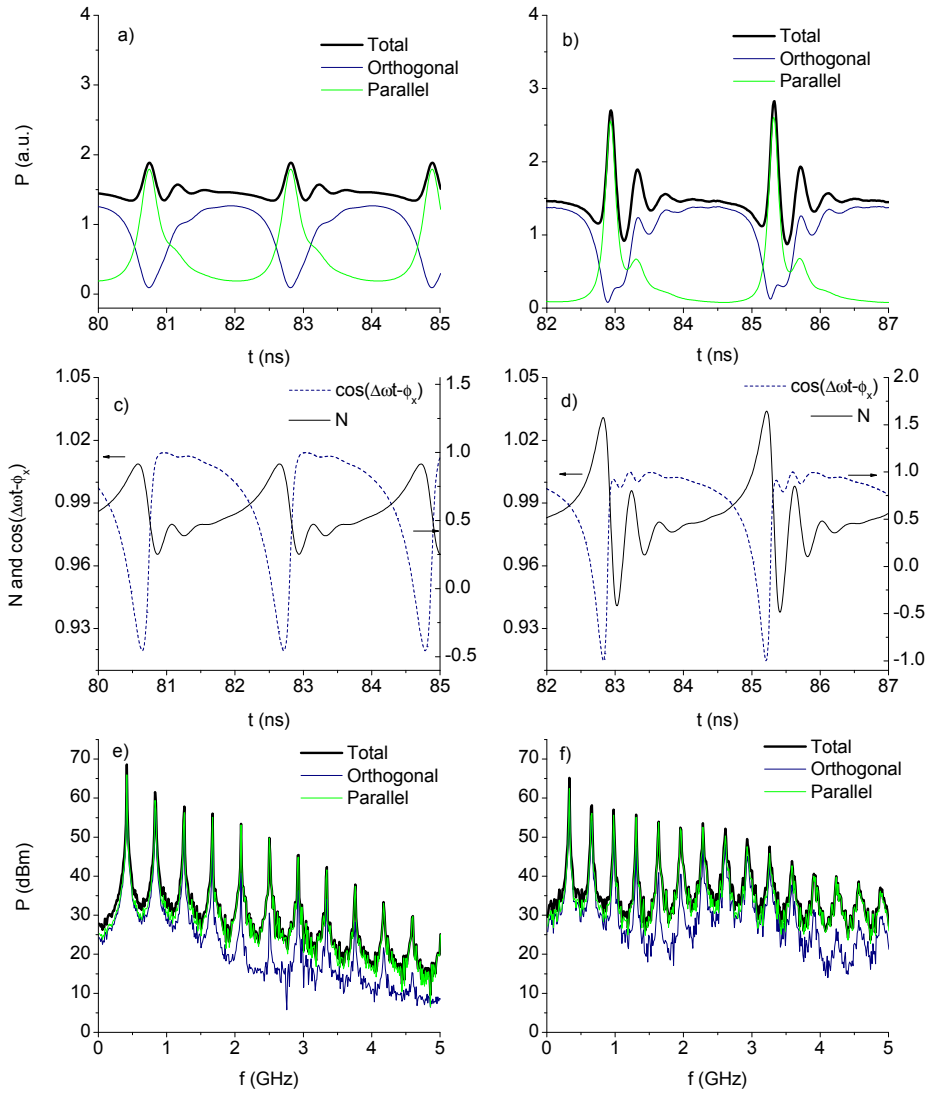

Fig. 7.11. Theoretical time traces of the (a), (b) total power and power of both linear polarizations, (c), (d) total population inversion and $\kappa E_{inj}\cos(\Delta\omega t-\phi_x(t))$ term, and (e), (f) RF spectra. The frequency detuning is $\Delta\nu$=-2 GHz, μ=2.44, (left) E_{inj}= 0.0445, and (right) E_{inj}=0.047.

The interpulse time increases as P_{inj} is increased as can be seen in Figs. 7.11 (a) and 7.11 (b). Theoretical values of $\langle T \rangle$ are 2.4, 3.06 ns for Figs. 7.11 (a) and 7.11 (b), respectively. The interpulse time dispersion, σ_T, also increases from 25 to 40.9 ps when going from Fig. 7.11 (a) to 7.11 (b). The behavior of both $\langle T \rangle$ and σ_T as a function of P_{inj} is in qualitative agreement with the corresponding experimental results reported in the previous section. The lower row of Fig. 7.11 shows the RF spectrum of the total power and of the power of both linear polarizations for E_{inj}=0.0445 and 0.047. A similar spectra broadening to that reported in Figs. 7.7 (e) and 7.7 (k) is obtained when E_{inj} is increased. This broadening is related to the observed increase of σ_T: decreasing the strength of spontaneous emission noise leads to the decrease of σ_T and narrower spectra. Comparison with experimental data also shows that simulations show stronger RF modes than in the experiment. There are several reasons that can contribute for this difference. First, experimental time traces (See Fig. 7.7) have more dispersion in the peaks height than that found theoretically (see Fig. 7.11). Second, although we have used angled polished ferrule connectors in our Setup to minimize the optical feedback in the VCSEL, this effect can be still present and degrade the signal to noise in our experimental RF spectra. Third, and more importantly, we do not know for sure the parameters of our VCSEL. In this way extraction of the laser parameters would be desirable for obtaining a better agreement with the experiments.

7.5. Discussion and conclusions

For negative (positive) frequency detunings, we have obtained anticorrelated (correlated) operating regimes. We explain this behavior because there is a dynamics of competence between polarizations for $\Delta\nu<0$ while that dynamics disappears when $\Delta\nu>0$. For $\Delta\nu<0$, anticorrelated dynamics appears when the system is approaching the injection locking regime. In this approach (see Figs. 7.11 (a) and 7.11 (b)), the orthogonal polarization tries to

reach the constant values of amplitude and phase that characterize the injection locked regime, but it is not able to do it because of the effect of the phase of the injected field. Figure 7.11 also shows that the average power of the orthogonal (x) polarization is larger that of the parallel (y) polarization. As discussed in Section 7.3, optical injection produces a frequency pulling effect such that the powers of both polarizations oscillate at a frequency that is smaller than the frequency detuning observed in the optical spectrum that we will call "effective frequency detuning." Optical phase of the orthogonal polarization is also oscillating at the effective frequency detuning. The orthogonal polarization cannot reach the stable locked behavior because the optical injection becomes out of phase with respect to that polarization.

In order to clarify this point, we have made further calculations analyzing the amplitude, $A_i(t)$, and the phase, $\phi_i(t)$, of the electrical fields of both linear polarizations, $E_i(t)=A_i(t)\exp(i\phi_i(t))$. When writing Eqs. (7.2)-(7.5) using the new variables, the evolution of the amplitude of the x polarization is such that a $\kappa E_{inj}\cos(\Delta\omega t-\phi_x(t))$ term appears in the equation for dA_x/dt. We plot in Figs. 7.11(c) and 7.11 (d) that term together with N. When the optical injection becomes out of phase with respect to the x polarization, the cosinus term decreases, causing the fall of A_x, (see Fig. 7.11 (a) and 7.11 (b)). Simultaneously, N increases until it decreases sharply with the fire of a large amplitude y pulse. In this way one of the two polarizations states exhibit large amplitude pulses, while the other exhibits the shoulders. This is the explanation of the anticorrelation observed between orthogonal and parallel polarizations, which is typical of a dynamics of competence between polarizations.

For positive frequency detunings, the system is far from the injection locking regime in such a way that the average powers of the both polarizations are similar (see Fig. 7.10 (a)). The optical phase of the x polarization is oscillating at the effective frequency detuning that is larger than the frequency detuning due to the

frequency pushing effect. Again, the optical injection can be out of phase with respect to the orthogonal polarization as seen in Fig. 7.10 (b) in which the $\kappa E_{inj}\cos(\Delta\omega t-\phi_x(t))$ term has been plotted. The phase term induces a modulation of the amplitude of the x-polarization power. That modulation causes a small amplitude sinusoidal dependence of N, in which A_x has the typical $\pi/2$ delay with respect to N. In this way correlation between orthogonal and parallel polarization is obtained.

Summarizing, in this chapter, we have made a theoretical and experimental study of the polarization-resolved nonlinear dynamics of a 1550 nm single-mode VCSEL subject to parallel and orthogonal optical injection. For this last case simultaneous measurements of the time traces of the power of both linear polarizations have permitted us to evaluate their contribution to the dynamics of the total power. We have characterized the periodic, period doubling, and irregular dynamics that appear for both polarizations in terms of time traces and power spectra. We have obtained that the correlation properties of both linear polarizations depend on the frequency detuning between the injected frequency and the frequency of the suppressed orthogonal mode of the solitary laser. For positive frequency detuning values, we have usually found that orthogonal polarization is the only polarization that contributes to the dynamics of the total power. Only correlated periodic dynamics in both linear polarizations has been found near the border of the periodic region, when the bias current is large and optical injection strength is small. For negative frequency detuning values, the correlation properties change because we find anticorrelated dynamics in both linear polarizations. This dynamical regime is characterized by a larger influence of nonlinear effects that produce anticorrelated trains of pulses in both linear polarizations. These trains of pulses have been characterized by the average and dispersion of the interpulse time increase as the injected power is increased. We have also shown that the appearance of broad power spectra that characterizes the irregular dynamics is

related to large values of the dispersion of the interpulse time. We have also analyzed the relative phase between the oscillations observed in the time traces of the optical power of both polarizations. Good qualitative agreement has been demonstrated between theory and experiment.

CHAPTER 8

Dynamic characteristics of an all-optical inverter based on polarization switching in long-wavelength VCSELs

An all-optical inverter using PS of a long-wavelength single-mode VCSEL is experimentally demonstrated. PS appears when linearly polarized light is injected orthogonally to the linear polarization of the solitary VCSEL. The dynamic behavior of the all-optical inverter under different pulsed optical inputs is analyzed. We consider low and high-frequency pulsed optical injection to describe the dynamic behavior of the all-optical inverter. Power time traces, rise and fall times of the linearly polarized output signals are reported. The dependence of these quantities on the bias current and injected optical power is investigated. This analysis permits us to identify proper operation conditions for all-optical inversion. The PS-based all-optical inverter is demonstrated with a 2.5 Gb/s non-return-to-zero (NRZ) input signal. These results offer exciting prospects for the use of PS in VCSELs in novel high-speed optical signal processing applications in present and future optical

networks.

8.1. Introduction

All-optical processing of high-speed signals is expected to be a key technology in future photonic networks. Of the range of candidate technological options semiconductor lasers have been shown to offer great promise [Kawaguchi 1994], [Kawaguchi 1997], [Adams 2010]. Recently, the unique features of a special type of semiconductor laser, the VCSEL, has led to extensive research for its use in all-optical switching and signal processing [Koyama 2006], [Onishi 2005], [Onishi 2004a], [Onishi 2004c], [Mori 2008], [Mori 2006], [Sakaguchi 2010a], [Sakaguchi 2010b], [Lee 2010b], [Pan 1993]. VCSELs are promising devices for these applications because of the characteristics mentioned in the previous chapters: small size, low power consumption, reduced fabrication costs, circular output beam, wafer level testing, easy of fabrication of 2D arrays,etc [Koyama 2006].

Optical injection in VCSELs has been a usual method to obtain nonlinear transfer functions useful for all-optical signal processing using those devices [Koyama 2006]. Those functions are obtained because optical injection strongly affects the transverse mode and polarization characteristics of VCSELs. On one hand optical injection can induce transverse mode switching in VCSELs. All-optical inversion [Onishi 2005], [Onishi 2004c] and signal regeneration [Onishi 2005] using transverse mode switching of a 1.55 μm VCSEL have been demonstrated. On the other hand optical injection can be used to obtain polarization switching (PS) and polarization bistability in single transverse mode VCSELs as we have seen in chapters 6 and 7 in which VCSELs were subject to orthogonal optical injection. PS and bistability have been observed in VCSEL devices [Mori 2008], [Mori 2006], [Sakaguchi 2010a], [Sakaguchi 2010b], [Lee 2010b], [Lee 2010a], [Pan 1993], [Boiko 1999], [Hong 2000], [Ryvkin 2004],[Sciamanna 2006], [Altes 2006], [Hurtado 2007], [Valle 2008], [Jeong 2008], [Marki 2008].

PS by optical injection is expected to be fast and thus suitable for application in all-optical signal-processing systems. Based on this mechanism high-speed all-optical signal regeneration [Mori 2008] and all-optical flip-flop memories [Mori 2006], [Sakaguchi 2010a], [Sakaguchi 2010b], [Lee 2010b], [Lee 2010a] have been reported.

8.2. Experimental Setup

All-optical inversion operation is achieved using the experimental Setup shown in Fig. 8.1. As in previous chapters an all-fiber system has been developed in order to inject the light from a tunable laser into a quantum-well commercially available 1550nm-VCSEL. As always, the bias current and the temperature of the device were controlled with a laser driver and temperature controller, respectively. The temperature of the VCSEL was held constant at 298K for all the experiments. The polarization of the externally injected signal was controlled using fibre polarization controllers (PC). The injection of light into the VCSEL was obtained via a three-port optical circulator as in previous chapters. A polarization controller (PC2) was used in order to inject linearly polarized light orthogonally to the linear polarization of the free-running VCSEL. An 85/15 fiber directional coupler was included in the setup to divide the optical signal from the tunable laser into two branches. The first branch was directly launched into the VCSEL, whilst the second one was connected to a Power Meter (PM) to monitor the optical input power. The reflective output of the VCSEL was measured by connecting the third port of the optical circulator to an oscilloscope for the measurement of the time traces. A polarization controller (PC3) and a polarization beam splitter (PBS) were included before the oscilloscope for the measurement of the time traces corresponding to each of the two linear polarizations of the VCSEL. An erbium doped fibre amplifier (EDFA) was also included in the final part of the setup to adjust the level of the reflective signal of the VCSEL for a proper measurement. Pulsed optical injection was obtained by using a Mach-Zender intensity

modulator (MZM). The polarization of the light entering the MZM was controlled by a polarization controller (PC1). Electrical pulses generated by a 12.5 GHz pulse pattern generator (PPG) were amplified in the high-frequency amplifier and applied to the MZM for the modulation of the light coming from the tunable laser source.

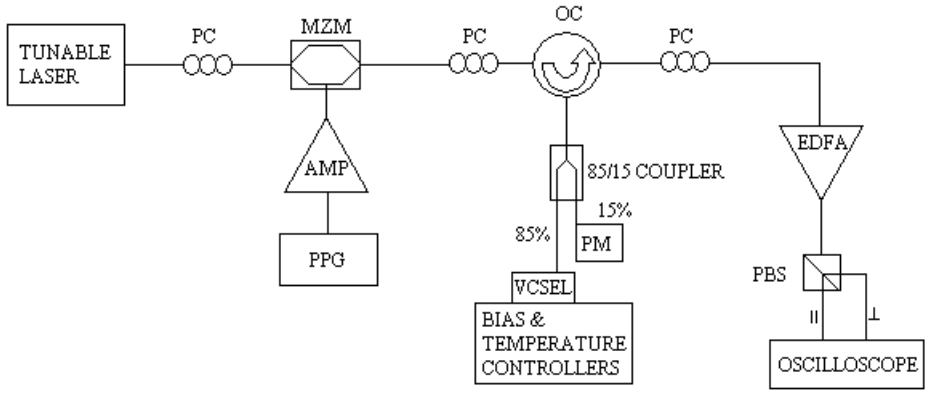

Fig. 8.1. Experimental Setup of all-optical inversion using the polarization switching in a VCSEL.

In the continuous wave (CW) regime the solitary VCSEL emits in the fundamental transverse mode with parallel polarization as it can be seen in the spectrum of Fig. 6.2 (b). The emission in that polarization is stable and no PS is observed for any bias current above the threshold.

8.3. Dynamics under low-frequency periodic modulation: effect of the bias current

The CW input-output power characteristics of the single-mode long-wavelength VCSEL subject to orthogonal optical injection have been recently measured in [Hurtado 2007]. These characteristics are also presented in chapter 6 of this thesis. In these experiments the optical injection wavelength was near the wavelength of the orthogonal linear polarization. The output power of the parallel polarized optical signal as a function of the

input power of the orthogonally polarized injected signal is illustrated in Fig. 5(d) of [Hurtado 2007] and in Fig. 6.10 (a) of chapter 6. Both figures show the typical characteristics of all-optical inverters. When no external optical power is injected the output power of the parallel polarized mode is at a high or ON output state. If the power of the orthogonal optical injection is increased, the parallel polarized output power gradually decreases until PS is obtained. At the PS point the power of the parallel polarized mode decreases abruptly from an ON to an OFF state. In this way an all-optical inverter based on PS in a VCSEL is obtained when considering the output power in the linear parallel polarization mode.

We have measured the dynamical response of this all-optical inverter using a pulsed optical input. Figs. 8.2 and 8.3 show the output power of the orthogonal and parallel polarized modes of the VCSEL when a squared-wave orthogonally polarized optical input is applied to the device. Results for two different values of bias current (3 and 5 mA) have been included in these figures. The wavelength detuning between the externally injected signal and the orthogonal polarization mode of the VCSEL, $\Delta\lambda$, is 0.05 nm. A low frequency (50 MHz) periodic modulation has been used. The injected power arriving at the VCSEL under modulation conditions is P_{inj}=50μW.

Fig. 8.2 only shows the waveforms during the rise of the orthogonally polarized square-wave signal. Figs. 8.2 (a) y 8.2 (c) show the rise of the orthogonally polarized output of the VCSEL for applied bias currents of 3 and 5 mA, respectively. For the orthogonal polarized output, the squared shape of the optical input is reproduced with the exception of some small damped oscillations. Comparison between Figs. 8.2 (a) and 8.2 (c) shows that there is a small increase in the amplitude and frequency of the oscillations for larger bias currents.

The corresponding analysis for the parallel polarized output power is shown in Figs. 8.2 (b), (d) for the two different applied bias

currents. Figs. 8.2 (b), (d) show a squared-shape response of the parallel polarized power during the rise of the orthogonally polarized input pulse. The parallel polarization output provides an inverted copy of the input signal. The abrupt decrease of the parallel polarized power coincides with the sharp increase of the

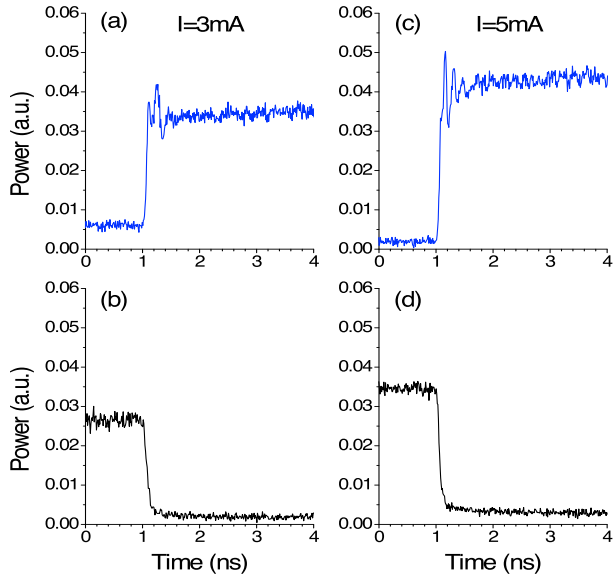

Fig. 8.2. Waveforms of the (a), (c), orthogonal and (b), (d) parallel polarizations during the rise of the optical input for two different bias currents: (a), (b) 3 mA, and (c), (d) 5 mA. in this figure P_{inj}=50μW.

orthogonally polarized power. No relaxation oscillation are observed during the decay of the parallel polarized power. Comparison between Figs. 8.2 (a) and 8.2 (c) (Figs. 8.2 (b) and (d)) show that the rise time of the orthogonal (fall time of the parallel) polarized output pulses is rather similar for different bias currents. The dynamical response of both linearly polarized modes during the fall of the orthogonally polarized input pulse is shown in Fig. 8.3. A large amplitude pulse appears in the orthogonally polarized output just after the fall of the optical input. Figs. 8.3 (a), (c) show that the amplitude and width of this peak substantially increases with the bias current. The difference between the times at which that pulse appears and it which the orthogonal polarization begins

to fall decreases as the bias current increases.

The approach of the parallel polarized power to its steady state is characterized by damped oscillations as can be seen in Figs. 8.3 (b), (d). The amplitude of the oscillations decreases as the

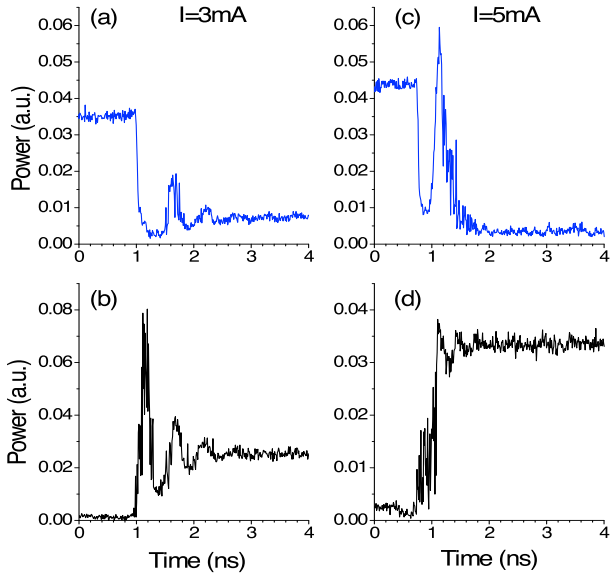

Fig. 8.3. Waveforms of the (a), (c), orthogonal and (b), (d) parallel polarizations during the fall of the optical input for two different bias currents: (a), (b) 3 mA, and (c), (d) 5 mA. in this figure P_{inj}=50μW.

bias current is increased. Figs. 8.3 (a), (b) show that the frequencies of the oscillations of both linear polarizations are similar. As the bias current is increased the frequency of oscillations in the parallel polarization also increases. We have checked that this frequency corresponds to the relaxation oscillation frequency of the solitary VCSEL. However, we have only observed several oscillations in the power of the orthogonal polarization when the bias current is 3 mA. For larger values of the current only one peak is observed, as shown in Fig. 8.3 (c). Figs. 8.3 (b), (d) also show that the shape of the parallel polarized output approaches that of a step of increasing height as the bias current is increased. The height of the step increases linearly with the bias current as expected from the linear behavior of the L-I characteristics of the solitary VCSEL.

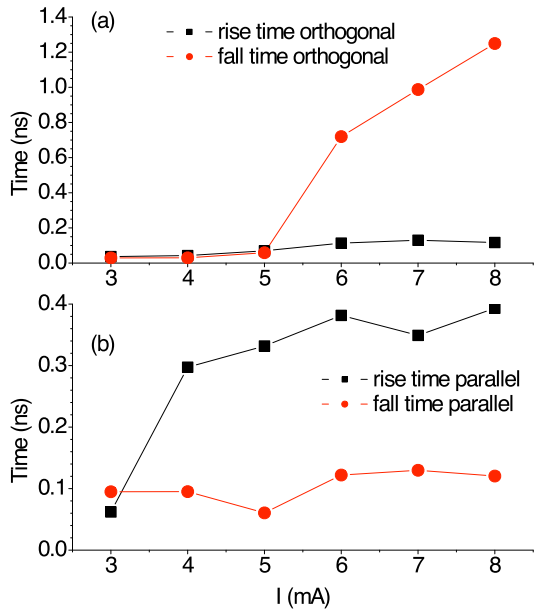

Fig. 8.4. Rise and fall times of the linear polarizations as a function of the bias current applied to the VCSEL: (a) Rise and fall times of the orthogonal polarization. (b) Rise and fall times of the parallel polarization. In this figure P_{inj}=50μW.

An analysis of the rise and fall times is desirable to complement the information given by Figs. 8.2 and 8.3. Fig. 8.4 shows the rise and fall times of both linearly polarized powers as a function of the applied bias current. We have measured the rise (fall) time as the time required for the power to change from a low to a high (high to low) value near the steady-state. We have considered values of 20% and 80% of the step height. Fig. 8.4 shows that the rise time of the orthogonal polarization and the fall time of the parallel polarization are very small. The rise time of the orthogonal polarization increases from 40 (I=3 mA) to 120 ps (I=8mA). The fall time of the parallel polarization fluctuates at around 100 ps.

Fig. 8.4 also shows that the transition associated with the rise of the optical input (see Fig. 8.2) is faster than the associated with the fall of the optical input (see Fig. 8.2). The fall time of the orthogonal

polarization increases to very large values due to the appearance of the large amplitude pulses of Figs. 8.3 (a), (c). The rise time of the parallel polarization is very small (around 60 ps) for I=3mA. For larger bias currents that rise time increases to values between 300 and 400 ps. The fall time of the orthogonal polarization output is longer than the rise time of the parallel polarization only when I⩾6mA. When I is smaller (equal or larger) than 6 mA the 20% level used to calculate the fall time of the orthogonal polarization is above (below) the first minimum that appears after switching-off this polarization. Then the longest time that is used to calculate the fall-time of the orthogonal polarization appears after the large spike when I⩾6mA. In this case the fall-time of the orthogonal polarization is much longer than the rise time of the parallel polarization because of the large value of the width of that spike.

8.4. Dynamics under low-frequency periodic modulation: effect of the injected power

In this section we measure the dynamical response of our system as a function of the injected optical power. A periodic modulation similar to that considered in the previous section is applied to the VCSEL. Figs. 8.5 and 8.6 show the output power of the orthogonal and parallel polarized modes when a 50 MHz squared-wave orthogonally polarized optical input is applied to the VCSEL. Results for two different values of P_{inj} (20 and 70 μW) have been included in those figures. A bias current of 5 mA has been chosen. In this way the cases analyzed in Figs. 8.2 (c), (d) and Fig. 8.3(c), (d) are intermediate to those considered in Figs. 8.5 and 8.6, respectively.

Fig. 8.5 shows the waveforms during the rise of the orthogonally polarized input signal. The amplitude and frequency of the oscillations of the orthogonal polarized power increase when P_{inj} increases. The squared shape and the absence of relaxation oscillations during the fall of the parallel polarized power is maintained throughout the whole P_{inj} range considered in this chapter.

Waveforms of both linearly polarized modes during the fall of the orthogonally polarized input pulse are shown in Fig. 8.6. Figs. 8.6 (a), (c) show that the amplitude and width of the orthogonally polarized pulses slightly decrease as P_{inj} increases. Figs. 8.6(b), (d) and Fig. 8.3 (d) show that the qualitative shape of the rise of parallel polarized power does not change significantly as P_{inj} in changed.

The dependence of rise and fall times on P_{inj} is illustrated in Fig. 8.7. A slight decrease is observed for the rise and fall times as P_{inj} is increased. Due to our bias current choice (I=5 mA) the numerical values for these times are small with the exception of the rise time of the parallel polarization (around 350 ps). In any case, these times are rather independent of the value of P_{inj}, at least for the range considered in this work. The measured values of rise and fall times for the parallel polarization indicate the potential of the PS-based all-optical inverter for operating at several Gb/s as will be shown in the next section.

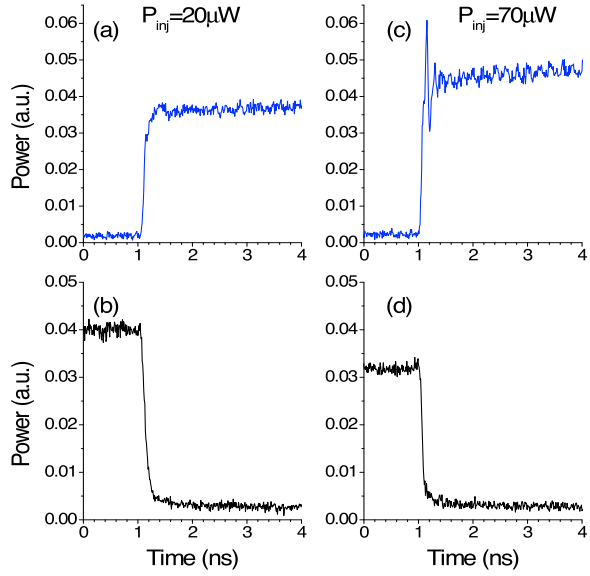

Fig. 8.5. Waveforms of the (a), (c) orthogonal and (b),(d) parallel polarizations during the rise of the optical input for two injected optical powers: (a), (b), 20 μW, and (c), (d) 70 μW. In this figure I=5 mA.

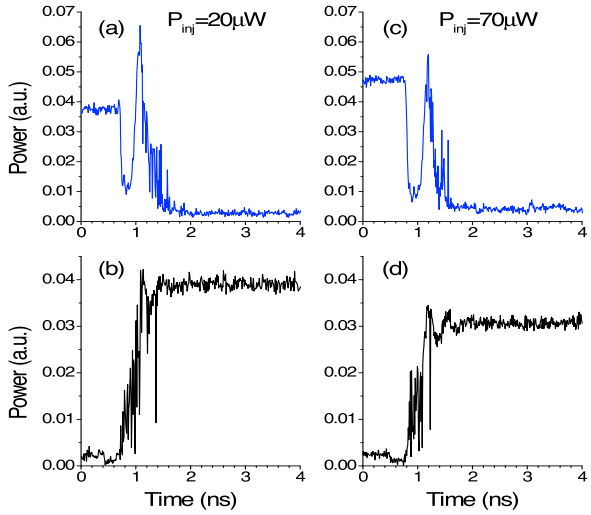

Fig. 8.6. Waveforms of the (a), (c) orthogonal and (b), (d) parallel polarizations during the fall of the optical input for two injected optical powers: (a), (b) 20μW, and (c), (d) 70μW. In this figure I=5mA.

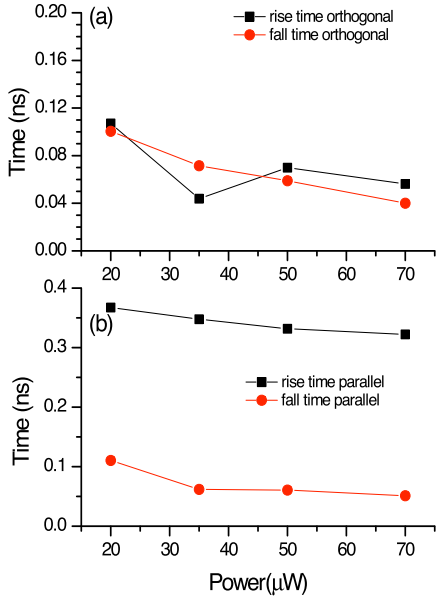

Fig. 8.7. Rise and fall times of the linear polarizations as a function of the injected optical power: (a) Rise and fall times of the orthogonal polarization. (b) Rise and fall times of the parallel polarization. In this figure I=5mA.

8.5. Dynamic behavior under high-frequency modulation

In this section we analyze the dynamic behavior of the all-optical inverter when subject to an optical input signal modulated at high-frequency. Fig. 8.8 shows results when a 2.5 Gbps NRZ optical signal with the following bit pattern "1011 1000 0111 0001 1110 1101 1010 0111" (a 32-bit word) is injected into the device. The wavelength detuning and optical input power are similar to those considered in the previous sections, $\Delta\lambda$=0.05 nm and P_{inj}= 50μW. Typical rise and fall times (20-80%) of the optical injection signal are 27 and 30 ps, respectively. The bias current applied to the VCSEL is 4mA. Fig. 8.8 (a) shows the input data arriving at the VCSEL's input. Fig. 8.8 (b) shows the time response of the parallel polarized power, which is the output signal of the all-optical inverter. The comparison of Figs. 8.8 (a) and 8.8 (b) shows that good waveform inversion is experimentally demonstrated at 2.5 Gbps.

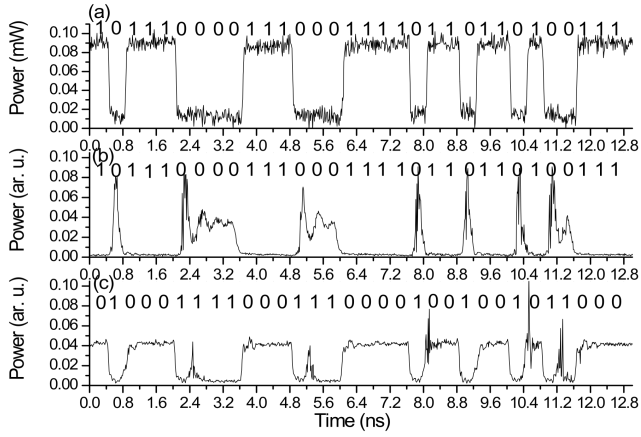

Fig. 8.8. Waveform inversion of a 2.5 Gb/s NRZ input signal. (a) Input light. (b) Power of the parallel polarization. (c) Power of the orthogonal polarization. The VCSEL is biased at 4 mA.

The power of the orthogonal polarization, shown in Fig. 8.8 (c), presents some of the qualitative features already discussed in the

previous sections. First, small damped oscillations appear during he build-up of the pulse. Second, large amplitude peaks, similar to those shown in Fig. 8.3 and Fig. 8.6, appear after the fall of the power of the orthogonal polarization. These unwanted spikes occur in the last "0" bit of "100" output bit sequences. These results suggest that use of the orthogonal polarization to obtain the all-optical gating functionality would suffer from patter-dependent error-rate degradation.

8.6. Discussion and Conclusions

The detailed polarization properties of VCSELs varies from chip to chip even though they are all single-mode VCSELs made from the same wafer. We have repeated the same measurements with another VCSEL of the same type, (the one that has been used in the previous chapter (see Fig. 7.4 (b)) to see whether the strong pulse spike that appears in the orthogonal polarization direction after turn-off of the injection pulse is observed or not. Results are shown in Fig. 8.9. Fig. 8.9 (a) and Fig. 8.9 (b) show the waveforms of the orthogonal polarization during the fall of the optical input for two different bias currents.

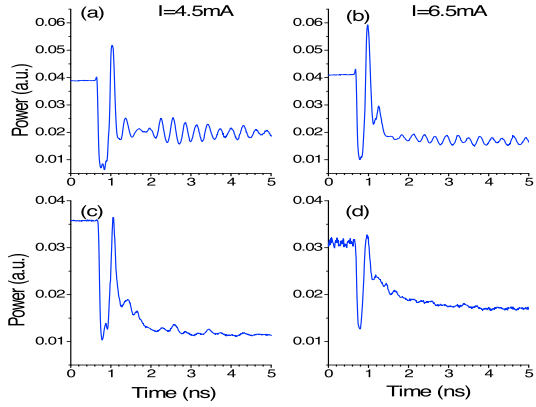

Fig. 8.9. Waveforms of the orthogonal polarizations during the fall of the optical input for a different VCSEL. (a) $\Delta\lambda$=0.05 nm, I=4.5 mA; (b) $\Delta\lambda$=0.05 nm, I=6.5 mA; (c) $\Delta\lambda$=0 nm, I=4.5 mA; (d) $\Delta\lambda$=0 nm, I=6.5 mA. In this figure P_{inj}= 50μW.

The same phenomenon is observed: a strong spike appears just after the fall of the optical input. The amplitude of the spike increases with the bias current as shown by comparing Fig. 8.9 (a) and Fig. 8.9 (b). Using this VCSEL we have made also measurements for a different detuned wavelength. Fig. 8.9 (c) and Fig. 8.9 (d) shows the results for $\Delta\lambda$=0 nm and two different bias currents. Strong spikes keep on appearing. The width of spike increases with the bias current. The amplitude of the spikes is smaller than those obtained for $\Delta\lambda$=0.05nm.

Optical inversion of the same type of VCSEL has also been reported in [Marki 2008]. In their experiment two injected beams are required for optical inversion: first, a CW light is injected into the orthogonal polarization, then another parallel polarized pulsed optical injection is injected near the wavelength corresponding to the parallel polarization. The injection locked orthogonal polarization mode acts as the output of the inverter. Our experiment is different because only one injected beam is required for optical inversion: an orthogonal polarized pulsed optical injection is injected near the wavelength corresponding to the orthogonal polarization. In this way the parallel polarization mode is the one acting as the output of the inverter.

The relevant quantity for the evaluation of the dynamic characteristics of the PS-based all-optical inverter is the corresponding time dependence of the parallel polarized output. Experimental results of Fig. 8.4 and Fig. 8.7 show that the rise time of the parallel polarized power is much larger than the fall time of that polarization: typical values of that rise (fall) time are between 0.3 and 0.4 ns (around 0.1 ns). This suggests that the operation speed of the all-optical inverter is limited by the rising edges of parallel polarized pulses. A possibility to avoid that limitation is to consider small bias current values: Fig. 8.4 shows that the rise time of the parallel polarization is an increasing function of the bias current. In fact, values of that rise time can be much smaller than 0.1 ns for a 3 mA bias current. However, the advantages of a small rise time are overshadowed by the small extinction ratio for the

parallel polarized power obtained in that case. An increase of the injected optical power does not seem to solve this problem either because Fig. 8.7 shows that the rise time decreases very slowly with P_{inj}. Nevertheless, our results show that all-optical inversion can be obtained with a 2.5 Gb/s NRZ input signal with a particular 32-bit word modulation. It would be interesting to extend our analysis to a high-frequency pseudorandom word modulation in order to know the impact of different words on the BER of the system.

The orthogonal polarization output shows unwanted spikes that degrade the response of the system for all optical gating operation. These spikes keep on appearing when a 2.5 Gbs NRZ input signal is considered. These results suggest that the use of orthogonal polarization to obtain all-optical gating would suffer from pattern-dependent error-rate degradation. These findings require further investigation to determine under which conditions all-optical gating could be successfully obtained with a VCSEL in conjunction with all-optical inversion operation.

Our experiments show that all-optical inversion is obtained at an operation speed of 2.5 Gbps with a commercially available device without any further device design optimization. A big advantage of all-optical switching operation is the speed which cannot be matched by electrical modulation. The resonant injection field can perturb the cavity field directly. The switching speed is mostly limited by the injection pulse speed. Finally, we should also note that our experiments were carried out with a device emitting at 1550 nm, the most used wavelength in long-haul optical networks, offering promise for novel uses of VCSELs in present and future optical telecommunication networks.

Summarizing, we have experimentally demonstrated all-optical inversion using PS of a long-wavelength single-mode VCSEL. The dynamic behavior of the all-optical inverter under low and high-frequency optical inputs has been analyzed. Time traces, rise and fall times of the linearly polarized output signals have been measured. The dependence of these quantities on the bias current

applied to the VCSEL and on the injected optical power has been investigated. The PS-based all-optical inverter has been demonstrated with a 2.5 Gb/s NRZ input signal. These results show that polarization switching in VCSELs can be a useful mechanism for high-speed optical signal processing applications.

CHAPTER 9

Experimental study of transverse mode selection in VCSELs induced by parallel polarized optical injection

Modal selection induced by parallel polarized optical injection is studied experimentally in a VCSEL with emission in two transverse modes that are linearly polarized in a direction referred as parallel. We show that the selection of the fundamental transverse mode can be achieved in this multimode VCSEL. The selection of the fundamental mode is accompanied by locking of that mode to the optically injected signal for large enough values of the wavelength detuning between the fundamental mode and the externally injected signal. The injected power needed to induce modal selection grows as the VCSEL bias current is increased and exhibits a minimum with respect to the injection wavelength at a value λ_{min} that is slightly longer than the wavelength of the fundamental mode of the solitary VCSEL. We also report that the selection process exhibits a bistable behavior when the

wavelength of optical injection increases beyond λ_{min}. The width of the observed bistable region grows linearly with the wavelength of the optically injected signal. The minimum injected power to achieve the modal selection of the fundamental mode and the wavelength detuning at which it appears increase with the VCSEL bias current. Selection of the higher order transverse mode is achieved when the optical injection wavelength is close to that of the higher order transverse mode. The qualitative behavior associated with the selection of the higher order mode is similar to that of the fundamental mode.

9.1. Introduction

Injection locking in VCSELs has been proven to reduce the frequency chirp [Chang 2003] and the laser noise, and to increase the dynamic range [Chrostowski 2011] and the resonance frequency beyond 100 GHz [Lau 2008]. An injection-locked VCSEL has been used as a duplex transmitter/receiver [Gu 2008] and also as a multifunctional device for performing format conversion and NRZ data clock recovery [Zhang 2009a]. Rich nonlinear dynamics can also be experimentally found in VCSELs subject to external optical injection as we have seen in the chapter 7. Moreover, all-optical signal processing functions such as signal regeneration, inversion, buffer memory etc can be performed with VCSELs subject to appropriate optical injection as we have already mentioned in previous chapters. We have also seen how optical injection can induce polarization switching as we mentioned in chapter 6. Polarization switching and transverse mode selection in VCSELs induced by the external optical injection [Koyama 2006], [Onishi 2004a], [Onishi 2004b], [Onishi 2004c],[Onishi 2005] make these devices suitable for all-optical flip-flop and buffer memory operation [Kawaguchi et al 2006],[Mori 2006] finding then applications in all-optical signal processing and optical computing.

Emission in different polarization and transverse modes is usually

found in solitary VCSELs. While the multitransverse mode emission is attributed to Spatial Hole Burning (SHB) effects [Changhasnain 1991], [Vakhshoori 1993], [Valle 1995], the polarization behavior of VCSELs can be influenced by a number of physical mechanisms [Choquette 1995], [MartinRegalado 1997b], [Valle 1997], [Ryvkin 1999]. The selection process under parallel optical injection depends on the polarization of the transverse modes of the solitary VCSEL. Selection of the fundamental transverse mode has been reported when both modes are orthogonally polarized [Hong 2002], [Onishi 2004b], [Law 1997b], [Torre 2004], [Torre 2006], [Torre 2010]. However, different experimental results have been obtained when the free-running VCSEL has two parallel-polarized modes. In particular, in [Onishi 2004b], the selection of the fundamental mode was achieved, whereas in [Hong 2002] that selection was not possible. Recent theoretical work [Torre 2010] has shed some light on this discrepancy. In general, transverse mode selection can be attained when the two modes have parallel polarizations [Torre 2010]. In that case, the minimum injected power needed to select a transverse mode increases as the injection current is increased [Torre 2010]. Theoretical simulations also show that the modal selection is favored as the frequency of the injected light becomes smaller than the frequency of the mode to be selected [Torre 2010].

9.2. Experimental Setup

Experimentally, parallel optical injection is achieved by using the setup presented in chapter 6 (see Fig. 6.1.). The main difference with respect the setup showed in Fig. 6.1. is that now we use a three-port polarization-maintaining optical circulator and an OSA with a resolution of 0.01 nm. The temperature was held constant at 297 K during the experiments.

We have first characterized the free-running VCSEL measuring its Light-Current (L-I) characteristics and the optical spectra for

several values of bias current. Fig. 9.1. shows the L-I curve of our device, showing an experimentally measured threshold current (I_{th}) of 2.83 mA at 297 K. Optical spectra show that the VCSEL first emits in the fundamental mode until its current reaches a value of I_{VCSEL}=3.9 mA. Exceeding that level the VCSEL also emits in a higher order transverse mode. This is illustrated in Fig 9.2 (a) which shows the optical spectrum of the VCSEL with an applied bias current of I_{VCSEL}=4.9 mA. The two main peaks appearing in the spectrum correspond to the fundamental transverse mode (located at the wavelength of λ_f =1560.59 nm) and to a higher order transverse mode (at the wavelength of λ_h= 1558.5 nm). We have checked that both modes are linearly polarized and have parallel polarizations for the values of current considered in this chapter. The two mode-emission is maintained over the whole VCSEL current range.

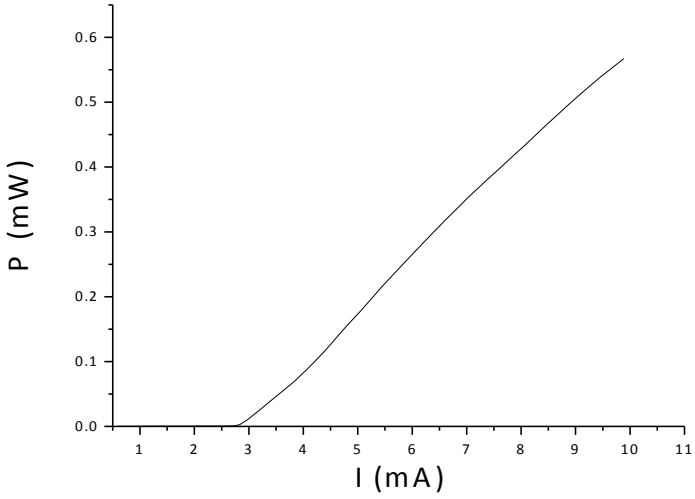

Fig. 9.1. Light-current characteristics of the multitransverse mode VCSEL.

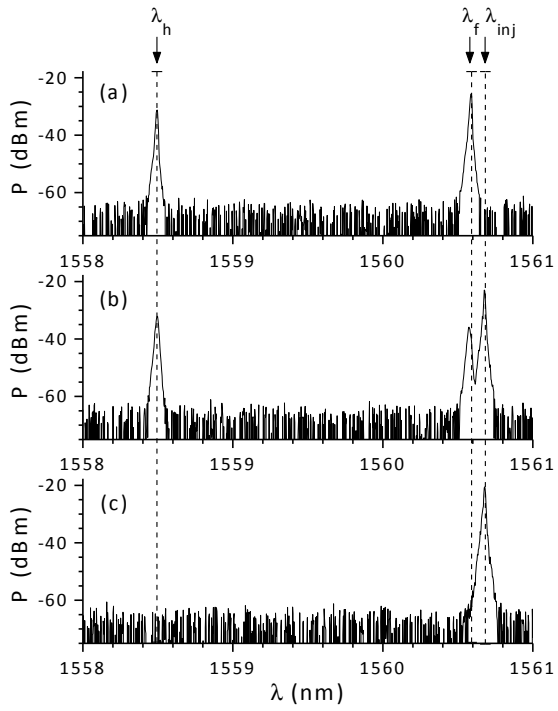

Fig. 9.2. Optical spectrum when P_{inj} is (a) 0, (b) 1.32 mW, and (c) 1.49 mW. In this figure, $\Delta\lambda$=0.09 nm and I_{VCSEL}= 4.9 mA.

9.3. Transverse mode selection

To obtain modal selection, an optical signal is injected close to the wavelength of the fundamental transverse mode, λ_f. The polarization controller is adjusted to assure the parallel optical injection configuration. We characterize the optical injection by its strength, given by the value of the power entering into the VCSEL, P_{inj}, and by its wavelength, λ_{inj}. P_{inj} is obtained by multiplying the power measured at the power meter by 49. When the optical injection is applied, a new peak appears at λ_{inj} in the optical spectrum. The magnitude of that peak increases as P_{inj} increases whereas the peaks appearing at λ_f and λ_h, corresponding to the fundamental and higher order transverse mode, respectively,

remain unchanged. This fact indicates that the peak appearing at λ_{inj} is due to the tunable laser light that is reflected at the VCSEL cavity. The situation changes for larger values of P_{inj} that are slightly below the value in which injection locking occurs. This is shown in Fig. 9.2(b) where the optical spectrum is plotted when P_{inj}=1.32 mW and λ_{inj} =1560.68 nm, corresponding to an initial wavelength detuning of 0.09 nm ($\Delta\lambda=\lambda_{inj}-\lambda_f$=0.09 nm) with respect to the fundamental mode. Two light sources contribute to the peak appearing at λ_{inj}: the tunable laser light that is reflected at the VCSEL and the fundamental mode of the VCSEL. This mode is contributing because the peak appearing at λ_f has clearly decreased its level with respect to the free-running case [please compare Figs. 9.2 (a) and (b)]. Injection locking is obtained for a slightly larger value of P_{inj} as shown in Fig. 9.2 (c), where both peaks, located at λ_f and λ_h, disappear and the measured optical spectrum exhibits a single peak at the optical injection wavelength. Fig. 9.2 (c) shows that the injection locking of the VCSEL's fundamental mode is accompanied by a suppression of the higher order transverse mode of more than 40 dB. For the detuning conditions considered in Fig. 9.2 both phenomena, the locking and the selection of the fundamental mode occur simultaneously within the resolution of our variable attenuator.

We have measured the injected power needed to obtain the selection of the fundamental mode as a function of the bias current applied to the VCSEL, I_{VCSEL}. The results are presented in Fig. 9.3. for two different values of initial wavelength detuning, $\Delta\lambda$. We consider that the selection of the fundamental mode is achieved if the power of the higher order mode becomes smaller than the 5% of the total power without injection. The injected power, given in dBs, corresponds to the ratio between P_{inj} and the solitary VCSEL power.

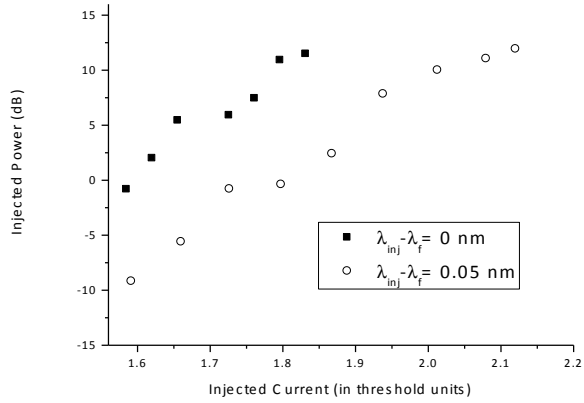

Fig. 9.3. Injected power required to achieve the fundamental transverse mode selection as a function of I_{VCSEL}. The selection is achieved above the squares and circles for $\Delta\lambda$=0 and $\Delta\lambda$=0.05 nm, respectively.

For the two cases of detuning considered, $\Delta\lambda$=0 and $\Delta\lambda$=0.05 nm, the selection of the fundamental mode is attained for values of injected power higher than those represented respectively by the squares and circles included in Fig. 9.3. This indicates, in agreement with the theoretical results reported in [Torre 2010] that for small values of current the selection of the fundamental mode by optical injection is possible. Also as predicted in [Torre 2010], the minimum injected power needed to select the fundamental transverse mode increases as the VCSEL injection current increases. However, [Torre 2010] also predicts that if P_{inj} is then further increased the VCSEL again would emit in two transverse modes. Our experimental results do not confirm this theoretical prediction. We believe that this is due to the high levels of optically injected power necessary to obtain again emission in two modes. These levels of input power could not be obtained in our experiments due to the equipment limitation (in our setup the maximum available P_{inj} was around 4 mW).

In [Hong 2002], it is experimentally reported that in the case of two parallel-polarized transverse modes, the VCSEL single-mode

operation cannot be obtained via optical injection. These observations are quite different from our results and those of [Onishi 2004b]. A possible reason behind such discrepancies could be the different injection rates in the i-transverse mode, κ_i (i=f,h for fundamental and higher order transverse mode, respectively) achieved in both experiments. In the Ref. [Torre 2010], the authors have theoretically shown that when $\kappa_f=\kappa_h$ the selection of the fundamental mode can be achieved by selecting a small enough VCSEL bias current. That is the situation that we have found in our experiment. However, [Torre 2004] and [Torre 2010] also show that when the injection rate in the higher order transverse mode is larger than that of the fundamental mode ($\kappa_h=2\kappa_f$) there are no values of injected power nor VCSEL bias current in which the fundamental mode is selected. This situation can be obtained if the injected beam has a larger spacial overlap with the higher order transverse mode and could be the reason behind the results of [Hong 2002].

Fig. 9.3 also shows that the value of P_{inj} required to obtain the selection of the fundamental mode decreases as the detuning, $\Delta\lambda$, is increased from 0 to 0.05 nm. In principle, this result is in agreement with [Torre 2010] since the modal selection is favoured as the wavelength of the injected light becomes longer than the wavelength of the mode to be selected [Torre 2010]. However a more detailed analysis of this dependence over a wider range of detuning, $\Delta\lambda$, would be desirable to fully check the previous agreement. This analysis is performed in the following section.

9.4. Bistable behavior of the transverse mode selection

In this section, we measure the injected power required to obtain the fundamental mode selection as a function of the detuning, $\Delta\lambda$, for a fixed value of the VCSEL current. Two sets of results are presented in Fig. 9.4. The first set, shown with a dotted line, correspond to the case of increasing the injected optical power,

P_{inj}, from 0 until the maximum level is reached (P_{inj}= 3.92mW). Subsequently P_{inj} is decreased from that maximum until the zero level is reached again. Results corresponding to the selection when decreasing P_{inj} are plotted with a solid line in Fig. 9.4. We can observe that for $\Delta\lambda<\Delta\lambda_{min}$ =0.045 nm, the P_{inj} required to achieve selection decreases as $\Delta\lambda$ increases. If the detuning is further increased above that value the power required for selection increases again. The existence of a wavelength (λ_{min}) for which the power required for the fundamental mode selection is minimum can be explained by the fact that the selection is associated with injection locking. As the wavelength of the injected signal is moved towards longer values of detuning with respect to the resonant wavelength of the VCSEL, the locking, and, hence, the selection of the fundamental mode will require and increasing amount of injection power. The comparison between the dotted and the solid lines in Fig. 9.4 also shows that the process of transverse mode selection exhibits a bistable behavior. A similar kind of bistability was obtained by Koyama [Koyama 2006] although in that case, in contrast to most of the results reported in this chapter, the optical injection was performed in the vicinity of the higher order transverse mode in order to select that mode. Fig. 9.4 also shows the existence of three distinct regions in the plane of injected power versus initial wavelength detuning: regions of stable locking, unstable locking, and no locking. In the unstable locking region, for a fixed value of detuning, the VCSEL will only be locked to the externally injected signal if the injected power, P_{inj} is decreased from values inside the stable locking region. The bistable behavior is much clearer when $\lambda>\lambda_{min}$ since the width of the hysteresis region increases significantly. Very wide hysteresis cycles can be obtained for larger values of wavelength detuning. Fig. 9.5 shows the width of the measured hysteresis cycles, ΔP_{inj}, as a function of the detuning. When $\lambda>\lambda_{min}$ a linear increase of the hysteresis width with the wavelength detuning is observed. However, when $\lambda<\lambda_{min}$, no bistable region is observed and hysteresis width vanishes.

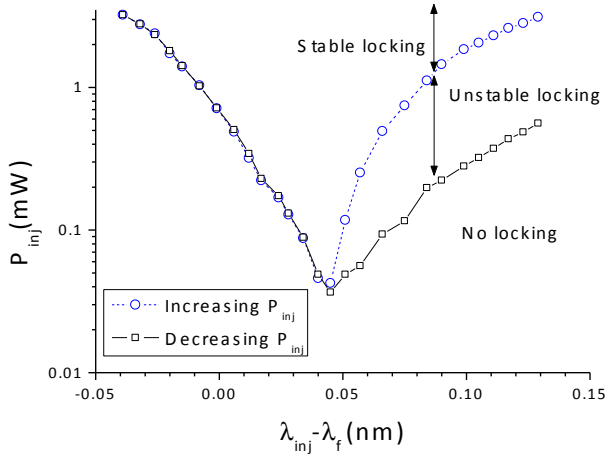

Fig. 9.4. Injected power required to achieve the fundamental transverse mode selection as a function of $\Delta\lambda$ when I_{VCSEL}=4.9 mA. Results corresponding to increasing and decreasing P_{inj} are plotted with dotted and solid lines, respectively.

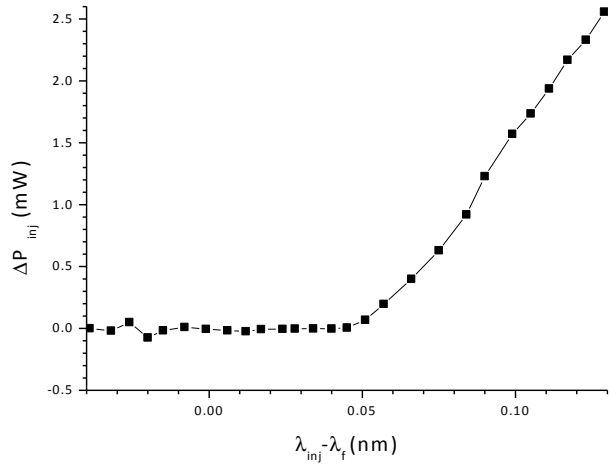

Fig. 9.5. Hysteresis width as a function of $\Delta\lambda$ when I_{VCSEL} is 4.9 mA.

Fig. 9.6 shows the dependence of P_{min}, the absolute minimum of the injected power required for modal selection, and $\Delta\lambda_{min}$ on I_{VCSEL}. Both quantities increase when increasing the bias current. A linear increase of $\Delta\lambda_{min}$ with the current was obtained in theory [Salvide 2011]. This means that if the fundamental mode has to be selected with the minimum injected power, an increase of the injected current must be accompanied by a linear increase of the wavelength of the optical injection [Salvide 2011]. A linear fit of our results is included in Fig. 9.6(b). The slop of the fit is $\Delta\lambda_{min}/\Delta I_{VCSEL}$ is 0.032 nm/m and its regression coefficient is 0.94. The low regression coefficient can be due to the large uncertainty in the determination of $\Delta\lambda_{min}$ for I_{VCSEL}=4.2 mA due to the wide plateau around the minimum value. Measurements for more values of I_{VCSEL} are desirable to fully check the previous linear relationship.

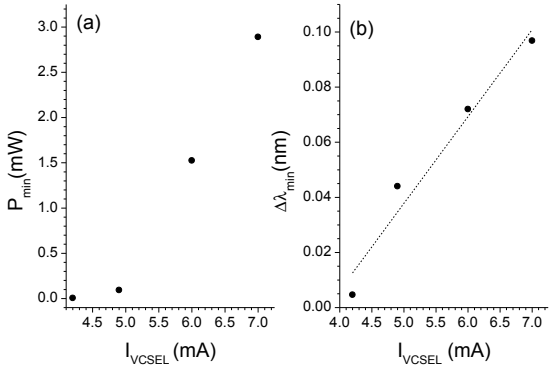

Fig. 9.6. (a) P_{min} and (b) $\Delta\lambda_{min}$ values as a function of the bias current.

9.5. Selection of the higher order transverse mode

In this section, we extend our study to the selection mechanism of the higher order transverse mode, i.e., when the optical injection wavelength is close to that of the higher order transverse mode. We now consider a wavelength detuning, $\Delta\lambda_h$, with respect to the higher order transverse mode, $\Delta\lambda_h=\lambda_{inj}-\lambda_h$. Our results follow similar trends to those described in the previous sections. The selection of

the higher order transverse mode is achieved when λ_{inj} is near λ_h. We have checked that the selection is accompanied by locking of the higher order mode to the optically injected signal for the same conditions of Fig.9.2 (I_{VCSEL}=4.9mA, and large enough positive detuning, $\Delta\lambda_h$=0.09 nm). The qualitative evolution of the optical spectrum as P_{inj} is increased is very similar to that shown in Fig. 9.2.

We also find that the injection locking and the higher order transverse mode selection occur simultaneously. Fig. 9.7. shows the injected power required to obtain the higher order mode selection as a function of $\Delta\lambda_h$. A comparison with Fig. 9.4 shows that the selection of the higher order mode is obtained for larger values of the injected power. Similarly to Fig. 9.4, results corresponding to increasing and decreasing P_{inj} are shown. The qualitative trends associated with the selection of the higher order mode are similar to those of the fundamental mode.

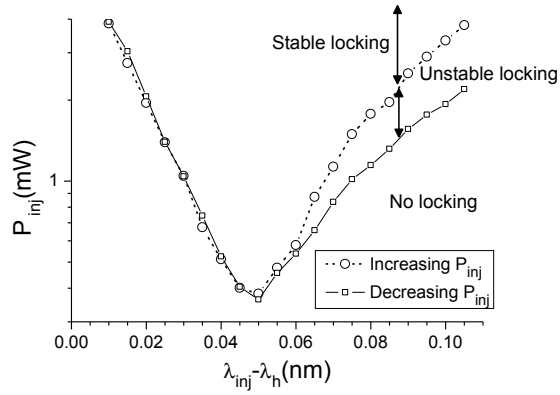

Fig. 9.7. Injected power required to achieve the higher order transverse mode selection as a function of $\Delta\lambda_h$ when I_{VCSEL}=4.9 mA. Results corresponding to increasing and decreasing P_{inj} are plotted with dotted and solid lines, respectively.

The injected power required for modal selection exhibits a minimum with respect to the injection wavelength at a value that is slightly longer than λ_h. The minimum appears at a wavelength detuning $\Delta\lambda_h$=0.05 nm, very near to that found in Fig. 9.4. Fig. 9.7

also shows that the selection process exhibits a bistable behavior when $\Delta\lambda_h$ increases beyond 0.05 nm.The width of the bistable region increases with the wavelength of the optically injected signal. This is more clearly shown in Fig. 9.8 where the hysteresis width has been plotted as a function of $\Delta\lambda_h$.

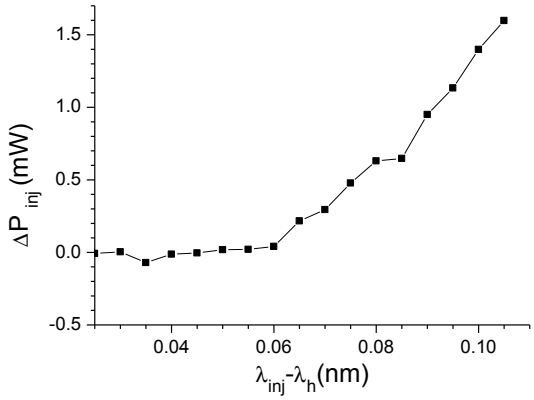

Fig. 9.8. Hysteresis width as a function of $\Delta\lambda_h$ when I_{VCSEL}=4.9 mA.

Also, a linear increase of the hysteresis width with the wavelength detuning is observed when $\Delta\lambda_h$>0.05 nm. The comparison between Figs. 9.5 and 9.8 also shows that the hysteresis width is larger when considering the fundamental mode selection.

9.6. Summary and conclusions

In this chapter we have experimentally studied, for the first time to our knowledge, the selection of the fundamental transverse mode of a 1550-nm VCSEL induced by parallel optical injection. We have demonstrated that this selection is obtained for the VCSEL used in our experiments which is characterized by a free-running emission in two transverse modes both with parallel polarizations. In general, the modal selection can be achieved in most classes of multimode VCSELs providing that the VCSEL bias current is small enough. However, the selection process does not only depend on the class of VCSEL but also on the injection conditions, for instance on the spatial overlap between the injected beam and the transverse

modes profiles. In fact, it has been shown theoretically in [Torre 2004] and [Torre 2010] that the selection is not possible when the fundamental mode has a lower injection rate than that of the higher order transverse mode, a situation that could be found for a larger spatial overlap between the injected beam and the higher order transverse mode profile. For large enough positive wavelength detuning, the selection of the fundamental mode is accompanied by locking of that mode to the optically injected signal. Future work will be devoted to the simultaneous measurement of the selection and locking processes for different wavelength detunings and bias currents. In this way, the parameter regions in which selection and locking coincide will be determined. Preliminary theoretical results using the model of [Torre 2010] show that for wavelength detunings and VCSEL bias current similar to those considered in Fig. 9.2 the selection and injection locking occur simultaneously. We have measured the injected power needed to select the fundamental mode as a function of the VCSEL current. In agreement with previous theoretical results [Torre 2010], we have experimentally demonstrated that the selection of the fundamental mode by optical injection is possible for small enough values of bias current. We have also shown, again in agreement with the predictions of [Torre 2010], that the injected power needed for modal selection grows monotonically as the VCSEL current is increased. However, some of the theoretical predictions contained in that work, namely i) once the injected mode has been selected an increase of the injected power leads again to multimode operation, and ii) the selection of the mode is no longer possible if the current surpasses a certain value, could not be fully confirmed because they would require larger values of injection power that were available in our experimental setup. The injected power needed for fundamental mode selection shows a minimum when measured as a function of the optical injection wavelength. The value of the wavelength, λ_{min}, at which the minimum occurs, is 0.045 nm longer than the wavelength of the free-running fundamental mode of the VCSEL. The modal selection

process induced by optical injection exhibits a bistable behavior. The minimum injected power and the wavelength detuning at which the selection of the fundamental mode is achieved increase with the bias current. Wide hysteresis cycles are attained when the wavelength of the optically injected signal is longer than λ_{min} and the width of the bistable region grows linearly as the wavelength of the injected signal is increased. Selection of the higher order transverse mode is also achieved by using an optical injection of wavelength close to that of the higher order transverse mode. The selection process shows similar trends to those observed in the fundamental mode selection.

CHAPTER 10

Polarization bistability induced by orthogonal optical injection in 1550-nm multimode VCSELs

In this chapter, we have analyzed experimentally the power induced polarization bistability found in a long-wavelength multi-transverse mode VCSEL under orthogonal optical injection. Bistability with very wide hysteresis cycles is measured for both the fundamental and the high-order transverse mode of the device. The shape of the associated hysteresis cycle is different for each of the two transverse modes. The power of the parallel polarized high-order (fundamental) transverse mode remains constant (gradually decreases) as the injected power is increased. Both powers suddenly drop to low levels at large values of the injected power. The squared shape measured for the input/output characteristic of the high-order transverse mode is of particular interest for obtaining good quality all-optical inversion and all-optical regeneration for use in optical telecommunication

networks.

10.1. Introduction

Polarization switching in VCSELs using orthogonal optical injection has been mainly analyzed in devices that emit only in the fundamental transverse mode (see Chapter 6). Recent interest has also appeared in the transverse mode switching induced by optical injection (see Chapter 9). This interest has been mainly motivated by the all-optical signal processing functionalities associated with the switching of a high-order transverse mode induced by optical injection [Koyama 2006], [Onishi 2005], [Onishi 2004a], [Onishi 2004c], [Hasebe 2006]. Polarization bistability phenomena associated with PS have been reported in 850 nm [Pan 1993], [Altes 2006] and 1550 nm (see Chapter 6) wavelength VCSELs. Analyses of the polarization bistability in multi-transverse mode VCSELs induced by orthogonal optical injection are scarce and only refer to 850 nm devices [Valle 2007]. The corresponding analysis in 1550 nm-VCSELs is of interest for exploiting the multi-transverse mode character of these devices in all-optical signal processing and optical switching/routing applications in long-haul optical networks applications were 1550 nm technology is dominant.

10.2. Experimental setup

Experimentally, orthogonal optical injection is attained with the setup presented in Fig. 6.1. Fig. 9.1 shows the experimentally measured L-I curve of the free-running VCSEL. Figure 10.1 shows the optical spectrum of the VCSEL when I_{bias}=5.5 mA. The two main peaks correspond to the parallel polarized fundamental and high-order transverse modes, located at the wavelengths of $\lambda_{f\parallel}$=1560.77 nm and $\lambda_{h\parallel}$=1558.69 nm, respectively. The orthogonal polarizations of the fundamental and high-order transverse modes are located at the wavelength of $\lambda_{f\perp}$ and $\lambda_{h\perp}$, respectively. Orthogonally-polarized transverse modes are shifted 0.56 nm to the long

wavelength side of the corresponding parallel modes. Parallel polarized emission in the two transverse modes is maintained over the whole bias current range.

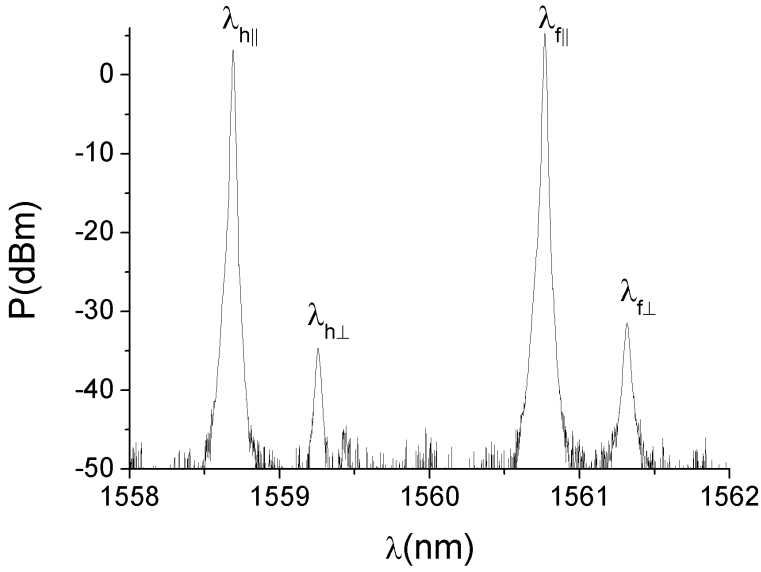

Fig. 10.1. Spectrum of the free-running VCSEL (I_{bias}=5.5 mA).

10.3. Experimental results

Fig. 10.2 shows experimental optical spectra when the VCSEL is subject to the orthogonal optical injection. Several values of injected power, P_{inj}, and frequency detuning between the externally injected signal and the orthogonal polarized fundamental mode, $\Delta\nu=\nu_{inj}-\nu_{f\perp}$, were considered. The injected light that is reflected at the VCSEL cavity contributes to the peaks appearing at the wavelength λ_{inj}. For large and negative values of $\Delta\nu$ (see Fig. 10.2. (a)), the power of the parallel polarized fundamental transverse mode, $P_{f||}$, decreases as the value of P_{inj} increases. However, the behavior of the high-order mode is different because the power of the parallel polarized high-order transverse mode, $P_{h||}$, remains constant as P_{inj} is increased.

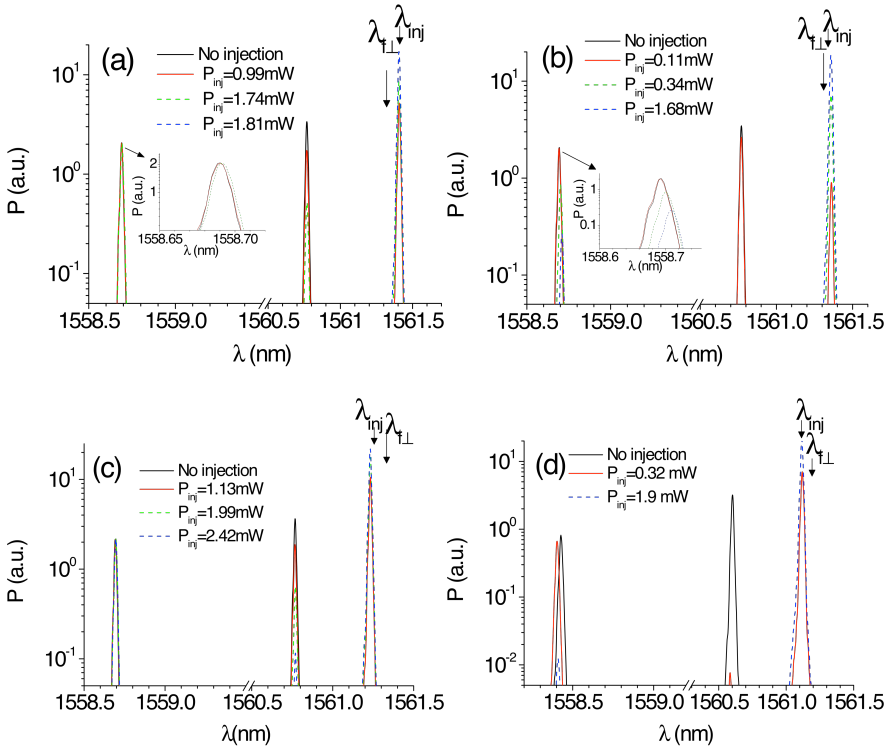

Fig 10.2. Optical spectra for several values of injected power when (a) I_{bias}=5.5 mA, $\Delta\nu$=-10.75 GHz, (b) I_{bias}=5.5 mA, $\Delta\nu$=-4GHz, (c) I_{bias}= 5.5 mA, $\Delta\nu$=11.25 GHz, and (d) I_{bias}= 4.6 mA, $\Delta\nu$=5.5 GHz.

The situation changes when P_{inj}=1.81 mW because both, $P_{f\parallel}$ and $P_{h\parallel}$, suddenly drop to very low power levels. In this case, PS occurs together with injection locking and the VCSEL emits now all the power at the wavelength of the external signal and with orthogonal polarization. This evolution is also illustrated in Fig. 10.3 (a-b) in which the values of $P_{f\parallel}$ and $P_{h\parallel}$ are plotted as a function of P_{inj}. The powers of the fundamental and first-order modes have been measured by finding the local maxima of their corresponding peaks in the optical spectra. These maxima are the values plotted in Fig. 10.3. $P_{f\parallel}$ decreases gradually whereas $P_{h\parallel}$ remains constant until a value of P_{inj}=1.75 mW is reached. When P_{inj}> 1.75 mW, $P_{f\parallel}$ and $P_{h\parallel}$ decrease to very low power levels. PS and injection locking are then simultaneously obtained at P_{inj}=1.75 mW.

The insensitivity of the higher-order mode amplitude with respect to the injected power in the fundamental mode was already observed in a 850 nm VCSEL [Hong 2002]. However the injected power was not enough to suppress the higher-order mode [Hong 2002]. Fig. 10.3 (a-b) illustrates the bistable character of the measured PS arising from the different behavior attained when P_{inj} is alternatively increased or decreased. Very wide hysteresis cycles are observed for both transverse modes as Fig. 10.3 (a-b) shows. The hysteresis cycle observed for the input/output (I/O) power relationship of the parallel polarization of the fundamental mode (Fig. 10.3 (a)) is similar to that observed in single transverse-mode VCSELs [Hurtado 2009b]. Nevertheless, the multitransverse mode behavior of the VCSEL adds new funcionalities to our system. The squared shape with very high associated on-off contrast ratio between output states measured for the I/O power relationship of the parallel polarization of the high-order transverse mode ($P_{h\parallel}$ vs P_{inj}) is of interest as it offers promise for obtaining good quality all-optical inversion and all-optical signal regeneration. The previous qualitative behavior changes when λ_{inj} approaches $\lambda_{f\perp}$ as shown in Figs. 10.2 (b) and 10.3 (c-d). A gradual decrease of $P_{f\parallel}$ is also observed as P_{inj} increases until it suddenly drops to very low power levels at P_{inj}=170μW. In the other hand, $P_{h\parallel}$ shows two different behaviors: if P_{inj} is smaller (larger) than 170μW, $P_{h\parallel}$ does not change (gradually decreases) with P_{inj}. No bistable behavior is observed for this case. Additionally, optical spectra for a large and positive value of $\Delta\nu$ are shown in Fig. 10.2 (c). In this case, $P_{f\parallel}$ gradually decreases as P_{inj} increases while $P_{h\parallel}$ remains constant and does not drop to low power levels when P_{inj} is further increased due to injected power limitations of our setup.

Fig. 10.3 (e-f) shows respectively the I/O power characteristic when I_{bias}= 4.6 mA and $\Delta\nu$=-10.75 GHz. The current-dependence of the behavior is analyzed by comparing Fig. 10.3 (e-f) with Fig. 10.3 (a-b). In the former, PS with injection locking of both modes is observed at P_{inj}=1.03 mW whereas in the latter a higher level of injected power P_{inj}=1.80 mW is needed to obtain analogous

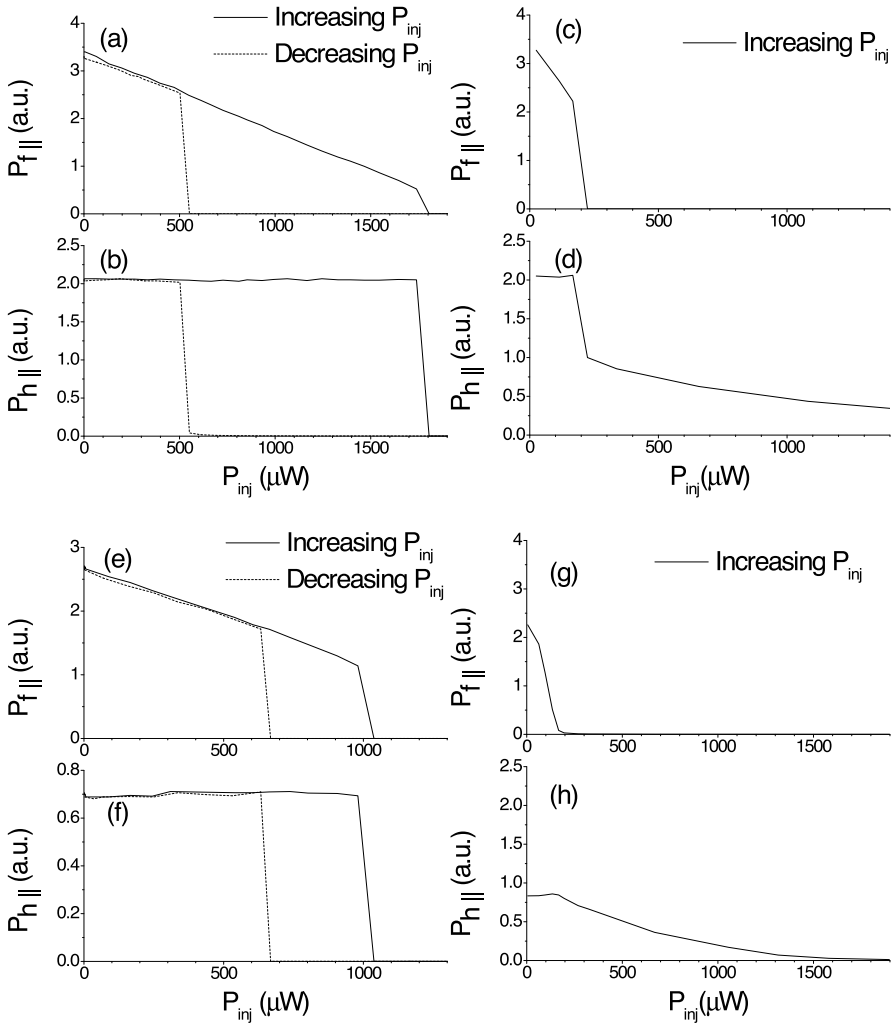

Fig.10.3. I/O power characteristic for the output of the parallel polarized fundamental (upper row) and high-order (lower row) transverse modes. (a-b) I_{bias}=5.5 mA, $\Delta\nu$=-10.75 GHz, (c-d) I_{bias}=5.5 mA, $\Delta\nu$=-4GHz, (e-f) I_{bias}=4.6 mA, $\Delta\nu$=-10.75 GHz, and (g-h) I_{bias}=4.6 mA, $\Delta\nu$=5.5 GHz.

behavior. Furthermore, the change of the bias current also affects the width of the bistable regions obtained for both transverse modes. The comparison of Fig. 10.3 (e-f) with Fig.10.3 (a-b) shows

that the width of the hysteresis cycle is larger at 5.5 mA than it is at 4.6 mA.

The situation found when $\Delta\nu$ is small and positive is illustrated in Fig. 10.2 (d) and Figs. 10.3 (g-h). These figures show that for this case the behavior is similar to that observed when small and negative $\Delta\nu$ values are considered (see Fig. 10.2 (b) and Figs. 10.3 (c-d)). No bistability has been found for the conditions of Figs. 10.3 (g-h) either. Fig. 10.2 (d) also shows that the fundamental and first order modes do not undergo polarization switching at the same injected power. When the injected power is 0.32 mW the fundamental mode exhibits polarization switching whilst the first order mode does not. The injected power must be increased significantly (see Fig. 10.2 (d), P_{inj}=1.9 mW) for the first order mode to undergo polarization switching.

Frequency pulling/pushing phenomena can be observed in Fig. 10.2. A slight frequency pulling is observed in Fig. 10.2 (a) as the injected power is increased. Insets with zooms of some peaks have been included in Figs. 10.2 (a-b) for a better visualization of the phenomenon. A clearer frequency pulling is observed in the zoom of Fig. 10.2 (b). Frequency pushing phenomenon is observed in the left part of Fig. 10.2 (d) when $\Delta\nu$ is positive. However, similarly to what is observed in Figs. 10.2 (a-b), a much smaller frequency shift appears in Fig. 10.2 (c) when $|\Delta\nu|$ increases.

We illustrate in Fig. 10.4 (a-b) for different values of applied bias current, the frequency detuning dependence of the injected power required for the suppression of the parallel polarized fundamental and high-order transverse modes, $P_{inj,f}$ and $P_{inj,h}$ respectively. We consider that $P_{f\parallel}$ and $P_{h\parallel}$ are suppressed when the Side Mode Suppression Ratio (with respect to the power emitted in the orthogonal polarization) is higher than 20 dB. Fig. 10.4 (a-b) shows that, for large and negative frequency detuning, $P_{f\parallel}$ and $P_{h\parallel}$ drop at similar values of P_{inj} , and therefore $P_{inj,f} \sim P_{inj,h}$.

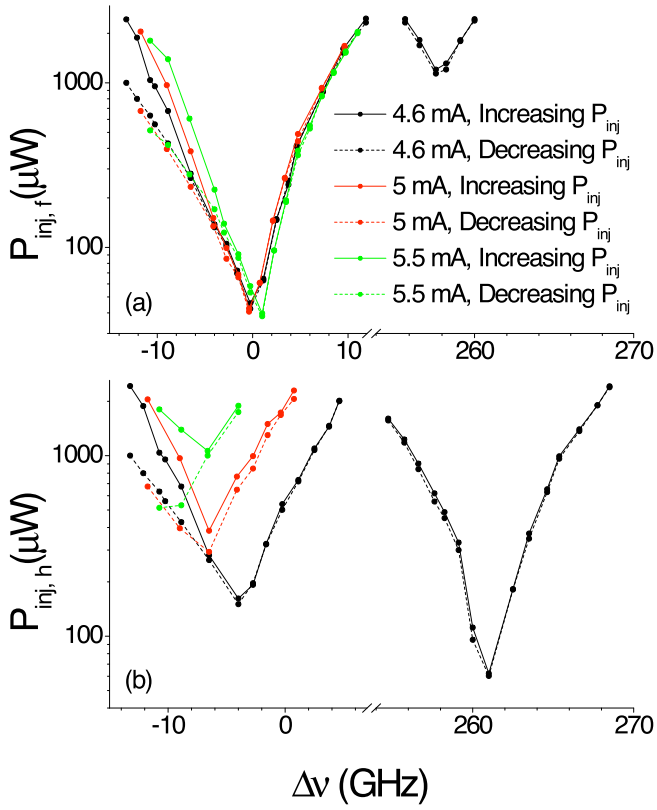

Fig. 10.4. Injected power required for suppressing the parallel polarized (a) fundamental and (b) high-order transverse mode versus the frequency detuning for three different levels of bias current. Results corresponding to increasing and decreasing the injected power are plotted with solid and dotted lines.

Those values correspond to the injected power at which the transition in the optical inversion characteristics occurs. As $\Delta\nu$ approaches to zero, $P_{inj,f}$ decreases until it reaches a minimum value at $\Delta\nu_f \sim 0$. Both $\Delta\nu_f$ and the minimum value of $P_{inj,f}$ change only slightly with I_{bias}. $P_{inj,h}$ also reaches a minimum value at $\Delta\nu_h < 0$. However, the behavior of $P_{inj,h}$ is different since both $|\Delta\nu_h|$ and the minimum value of $P_{inj,h}$ increase as higher bias currents are applied to the VCSEL. Fig. 10.4 (a-b)also shows that $P_{inj,f} \sim P_{inj,h}$ if $\Delta\nu < \Delta\nu_h$ and

$P_{inj,f}<P_{inj,h}$ if $\Delta\nu>\Delta\nu_h$: the injected power required to suppress the parallel polarized fundamental mode is smaller (similar) than that needed to suppress the parallel polarized high-order mode when the frequency detuning is larger (smaller) than $\Delta\nu_h$.

The results measured when P_{inj} is increased or decreased are also included in Fig. 10.4 (a-b). Both the fundamental and the high-order transverse mode powers exhibit bistable behavior for large and negative values of $\Delta\nu$. Fig. 10.5 (a-b) plots the measured hysteresis width, ΔP,as a function of $\Delta\nu$ corresponding to the curves included in Fig. 10.4 (a-b). For large enough negative values of $\Delta\nu$, i) ΔP increases as $|\Delta\nu|$ increases, and ii) ΔP increases as I_{bias} increases (with a fixed $\Delta\nu$). However, only three different values of bias current have been considered in Fig. 10.5. Measurements for more values of bias current would be desirable to fully check the dependence on this magnitude.

Fig. 10.4 (a-b) also describes the situation obtained for very large values of $\Delta\nu$, at which the wavelength of the optically-injected signal is close to the orthogonal polarized high-order transverse mode wavelength. Results are only plotted when I_{bias}=4.6 mA. $P_{inj,f}$ and $P_{inj,h}$ exhibit minimum values when $\Delta\nu$ is near 260 GHz which is the frequency separation between the parallel polarized fundamental and high-order transverse modes. Finally, Fig. 10.4 (a-b) also states that i) $P_{inj,h}<P_{inj,f}$ and ii) the width of the hysteresis regions is very small. Our experimental results are in agreement with previous theoretical results contained in [Sciamanna 2006], and [Valle 2007]. Two minimum values of injected power needed to obtain polarization switching of the total power have also been found in [Valle 2007] for two different values of the frequency detuning: the first one corresponding to an optical injection wavelength near the orthogonally polarized fundamental mode resonant wavelength; and the second one appearing close to the frequency difference between the high-order and the fundamental transverse modes of the solitary VCSEL [Valle 2007]. Our experimental results support that theoretical

prediction. Also polarization switching and injection locking are attained with the same value of the injected power when the frequency detuning is negative [Valle 2007]. In this way the experimental results shown in Figs. 10.2 and 10.3 support the theoretical model of Ref. [Valle 2007].

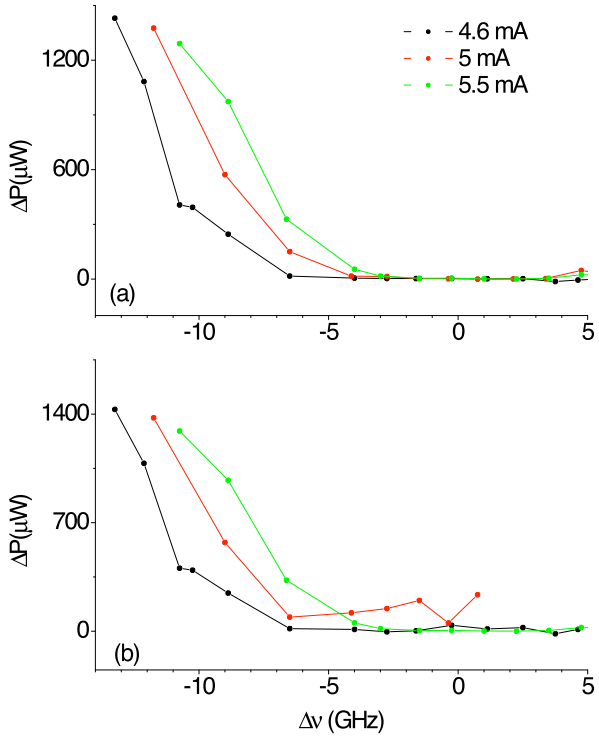

Fig. 10.5. (a-b) Hysteresis width corresponding to the data of Fig. 10.4 (a-b), respectively.

10.4. Discussion and Conclusions

The potential of VCSELs for all-optical signal processing in future photonic networks has been recently demonstrated [Koyama 2006]. All-optical regeneration and all-optical inversion have been reported using optical injection to excite a high-order transverse mode of a VCSEL which in the absence of optical injection emits in the fundamental mode [Koyama 2006], [Onishi 2005]. The step-like

transfer function useful for all-optical regeneration/inversion was obtained in those studies plotting the output power of the fundamental mode versus the injected power. In contrast with that work, our approach is to use optical injection for the suppression of the high-order transverse mode of a solitary multimode VCSEL. Our step-like transfer function is thus different as it is obtained considering the output power of the parallel polarized high-order transverse mode as a function of the injected power. Fig. 10.6 shows $P_{f\parallel}$, $P_{f\perp}$, $P_{h\parallel}$ and $P_{h\perp}$ as a function of P_{inj}. An example of our transfer function ($P_{h\parallel}$ vs P_{inj}) is shown in Fig. 10.6 (b). Furthermore, we have used a vertical logarithmic scale for a better comparison with the results reported in Ref [Koyama 2006]. Our results are also obtained for similar frequency detuning values to that used in Fig. 15 of Ref. [Koyama 2006].

The nonlinearity of our transfer function improves previous results since its step-character is better defined: $Ph_{\parallel}$ in Fig. 10.6 (b) is constant if P_{inj}<1.75 mW, whereas in the results shown in Fig. 15 of Ref. [Koyama 2006] the output power decreased approximately 2 dB when the fibre input power was smaller than 3.4 mW. The width of the bistability window can be estimated by the ratio between the injected powers at which the downward and upward transitions occur, P_{down}/P_{up}. This ratio is 3.5 in our work (see Fig. 10.6) while in [Koyama 2006] (see Fig. 9.15 in that work) reduces to approximately 1.15). This result can be of interest for potential applications of our work in all-optical memories.

Similar switching powers (of the order of some mW) and extinction ratios (around 30 dBs) are found in our work and in Ref. [Koyama 2006]. Figure 10.6 (b) shows that the values of $P_{h\perp}$ are always very small. However, the values of $P_{f\perp}$ in Fig. 10.6 (a) are large as they include the power emitted by the fundamental mode in the orthogonal polarization plus the reflection of the injected light at the VCSEL mirror, like in Chapter 6 [Hurtado 2009b].

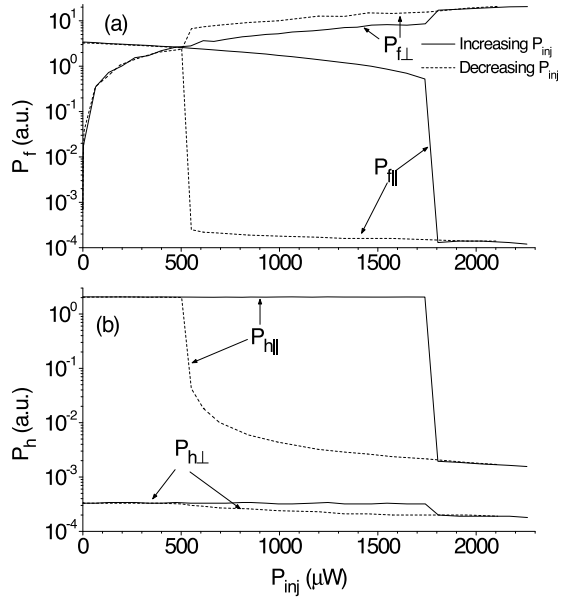

Fig. 10.6. Polarization-resolved I/O power characteristic for the output of the (a) fundamental and (b) high-order transverse mode. I_{bias}=5.5 mA, $\Delta\nu$=-10.75 GHz.

Fig. 10.6 (a) also shows that another step-like transfer function is obtained when considering $P_{f\parallel}$ vs P_{inj}. This transfer function has the advantage of a larger extinction ratio (more than 40 dB) but the disadvantage of having a gradual decrease (8 dB) when transiting from P_{inj}=0 to 1.75 mW. The width of the hysteresis region associated to $P_{f\parallel}$ is larger than that found when considering single-transverse mode VCSELs subject to orthogonal optical injection [Hurtado 2009b] (P_{down}/P_{up}=2 when I_{bias}=2 I_{th} and $\Delta\nu$=-19 GHz).

The bias current has been chosen large enough to assure multimode operation of the solitary VCSEL. The injected wavelength has been selected close to the resonant wavelengths corresponding to the orthogonal polarizations of the fundamental and high-order transverse modes of the device. In Figs. 10.4 and 10.5 we have considered a variety of values of bias current and injected wavelengths to identify the optimal operating conditions for all-optical inversion and bistability. Fig. 10.4 shows that the

minimum injected power required for suppressing the parallel polarization appears near the zero frequency detuning. This means that the optimum injected power to achieve all-optical inversion is obtained when the injected wavelength is near the wavelength of the orthogonal polarization of the fundamental mode, as in Ref. [Valle 2007]. Fig. 10.5 shows that, for a fixed negative frequency detuning, the hysteresis width increases as the bias current is increased, as in Ref. [Hurtado 2009b], which means that increasing the bias current is therefore suitable to achieve optimum all-optical memory operation.

We have reported the experimental observation of polarization bistability in each of the transverse modes of a 1550 nm multimode VCSEL when subject to orthogonal optical injection. We have studied in detail the injected power requirements for polarization bistability. We have also characterized the width of the associated hysteresis cycles as a function of the frequency detuning for three different values of bias current. In particular very wide hysteresis cycles have been obtained for both transverse modes when the frequency detuning has large and negative values. The multi-mode emission property of the VCSEL adds new functionalities to the system in comparison to previous studies in single transverse mode devices. A squared shape with very high on-off contrast ratio and very wide associated hysteresis cycle has been measured for the I/O power characteristic of the parallel polarized high-order transverse mode. This promising result offers potential for the use of multimode VCSELs operating at the very important telecom wavelength of 1550 nm as low-cost and low-power consuming components for all-optical signal processing applications, such as all-optical inversion and all-optical signal regeneration, in long-haul optical networks.

CHAPTER 11

Polarization dynamics of a multimode vertical-cavity surface-emitting laser subject to orthogonal optical injection

In this chapter we study the effect of orthogonal optical injection coming from a similar VCSEL on the dynamics of a multi-transverse mode VCSEL. Short-wavelength VCSELs emitting in four transverse modes are considered in contrast to the long-wavelength two-mode VCSEL studied in the previous chapter. Also the birefringence parameter value is much smaller than that of the VCSEL of chapter 10. Near field profiles of transverse modes are measured in this chapter. Our results reveal that when the receiver operates with several strong transverse modes of parallel polarization, optical injection can induce polarization switching in all of them while only one mode is locked to the external frequency. The induced switching can occur for a very weak (a few microwatts) injected beam. Periodic oscillations and low-frequency irregular pulsations are observed as well.

11.1. Introduction

As we know, the interest in effects of optical injection on VCSELs arise from both potential applications and intellectual curiosity for mechanisms underlying the phenomena. For example, control of polarization is an important issue in telecommunication applications because coupling of a VCSEL to an optical fiber may result in different loss for the two polarizing modes and lead to an increase of the intensity noise at the fiber output [Altes 2006]. On the other hand, a well-controlled polarization switching and polarization bistability may be useful for all-optical signal processing functionalities [Onishi 2004c]. From the point of view of fundamental sciences, the interplay of polarization and transverse modes in optically injected VCSELs still needs investigations.

In the previous studies [Hong 2002], it was shown that transverse modes of parallel polarization behave independently of each other for both parallel and orthogonal optical injection. On contrary, in this chapter we observe simultaneous polarization switching of several linearly polarized transverse modes when one of the modes is frequency locked to the injected beam even when the injection power is only a few microwatts. This opens possibility of controlling the polarization of the VCSEL in the multi-transverse-mode regime. Most experiments use a tunable semiconductor laser as the transmitter, however, our transmitter is a VCSEL that is very similar to the receiver: they are from the same manufacturer, of the same model number, and came in the same package. Given the recent efforts in studying VCSEL-by-VCSEL optically injection-locked systems [Hayat 2009], it is necessary to understand polarization dynamics in such a system.

11.2. Experimental setup

In our experiment, a proton-implanted VCSEL, V_1 (receiver), emitting at 850 nm receives a single or two-frequency injected signal provided by another VCSEL, V_2 (transmitter), of the same model, as shown in Fig. 11.1. The temperatures of the two VCSELs

are stabilized at 24.01 °C and 32.02 °C separately by temperature controllers of same model (Thorlabs TEC2000). Their bias currents are controlled by current drivers (Thorlabs LDC200C). The dominant polarization of both VCSELs is parallel to the optical table, which is termed X polarization. The polarization perpendicular to the optical table is termed Y polarization. In this chapter the X(Y) polarization is the parallel (orthogonal) polarization. The X polarization of the transmitter is selected by a polarizing beam splitter (PBS) and sent through an optical isolator (ISO). Since the isolator makes the polarization rotated by 45°, a half-wave plate (HWP) is placed behind the isolator to rotate the polarization of the transmitted light by another 45°, becoming perpendicular to the optical table. Now the polarization of the injected light is orthogonal to the dominant polarization of the receiver. The injection is sent into the receiver by mirror M_2 and a nonpolarizing plate beamsplitter M_1. We obtain the optimal alignment when the injection power necessary to induce polarization switching is minimized at the boundary of the PS region.

For the purpose of observation and measurement, the output of V_1 is split at M_1: the transmitted part is sent to a Fabry-Perot (F-P) spectrum analyzer (FSR 150 GHz) and a charge coupled device (CCD) camera, the reflected light is sent to a one-meter spectrometer (Jobin Yvon 1000m) and a fast detector (Newport 1580B, 12 GHz) which can be connected to an RF spectrum analyzer (Agilent EXA N9010A, 9 kHz to 26.5 GHz) or a digital oscilloscope (Tektronix DPO 7254, 2.5 GHz). With the aid of another PBS and a half-wave plate, we can detect spectrum and dynamics of each polarization of V_1 as well as its power. The power of each polarization is measured with a power meter. We can also set up two fast detectors to observe temporal behaviors of the X and Y polarizations simultaneously. Half of the beam from the transmitter V_2 can be sent to the spectrometer or to the F-P spectrum analyzer and the CCD camera. In order to send the light of V_2 to the F-P spectrum analyzer, we use a mirror, M_3, installed on a translational stage. M_3 and the PBS that reflects the output of V_2

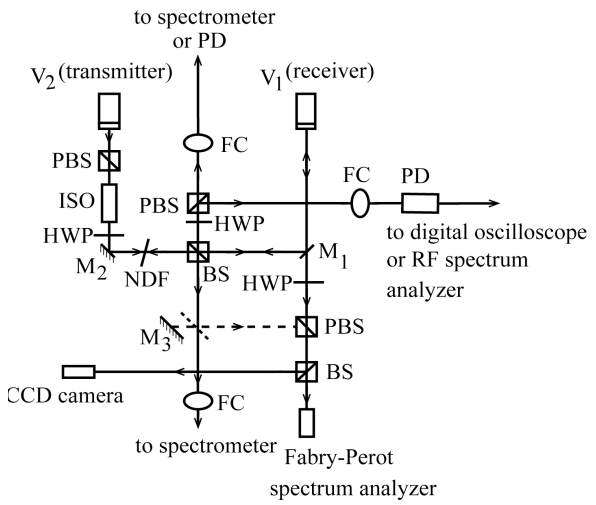

Fig.11.1. Experimental setup, where PBS stands for polarizing beamsplitter, BS for nonpolarizing beamsplitter, HWP for half-wave plate, ISO for optical isolator, FC for fiber coupler, and PD for fast photodetector. M_1 is a plate beamsplitter, M_2 and M_3 are mirrors.

are carefully aligned to get the frequency structure of V_2 at the F-P spectrum analyzer. The frequency (wavelength) detuning is obtained form the F-P spectrum analyzer (spectrometer). The neutral density filter is used to adjust the injection power. The power of the injected signal is measured in front of the collimating lens of V_1.

As shown in Fig. 11.2 (a), the solitary V_1 is dominantly polarized in the X direction and no polarization switch occurs. From threshold to 3.33 mA, the VCSEL operates in fundamental mode (TEM_{00} mode). The second mode, a higher-order transverse mode, starts lasing from 3.33 mA. Its beam profile indicates that it can be described as a TEM_{01} mode. From 3.65 mA to 4.75 mA, the VCSEL operates with three transverse modes. The third mode is a TEM_{10} mode. The fourth transverse mode can be described as a TEM_{02} mode. It is on from 4.75 mA and is essentially Y polarized. In our study, we focused on the bias current between 4.8 mA and 5.6 mA, where the receiver operates with four transverse modes.

The polarization feature of V_1 and the spatial profile of each transverse mode are shown in Fig. 11.2 (b). The fundamental mode and the TEM_{10} mode are X polarized; however, each has a nonlasing Y mode with a higher frequency. The fourth mode (TEM_{02}) is Y polarized. The TEM_{01} mode has two polarized states: an elliptically polarized state and a nonlasing Y polarized state. The frequency of the Y polarization is 8 GHz higher. As illustrated, the X component of the elliptical polarization is much stronger than its Y component, therefore this polarization can be regarded as X polarization essentially. The frequency difference is 45 GHz between the TEM_{00} and TEM_{10} mode and 60 GHz between the TEM_{00} and essentially X-polarized TEM_{01} mode. The frequency of the Y-polarized TEM_{02} mode is 124 GHz higher than the TEM_{00} mode.

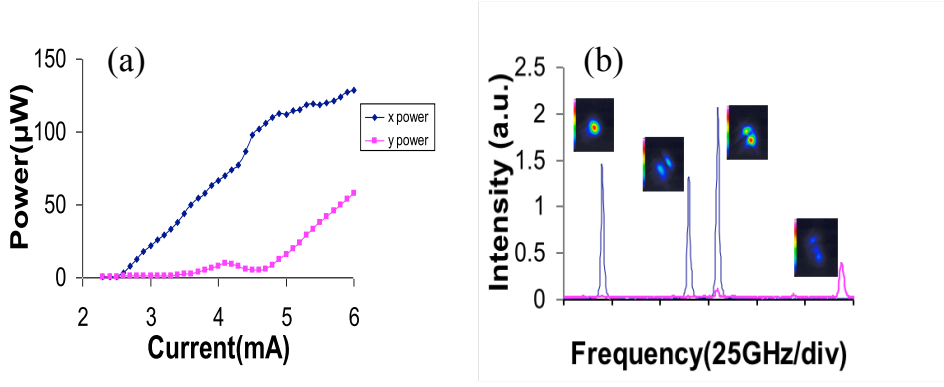

Fig.11.2. Polarization resolved (a) L-I curves and (b) optical spectra of the solitary V_1. The bias current of V_1 is 5.219 mA. (Blue: X polarization; pink: Y polarization.)

11.3. Experimental results

In our experiment, the bias current of V_2, I_2, is 3.1 mA. The output from V_2 is single frequency with the beam profile of the fundamental mode. We tune I_1, the bias current of the receiver, to change the frequency detuning, $\Delta\nu$, between V_1 and V_2. We define $\Delta\nu$ as the frequency difference between the injected light, ν_2, and the nonlasing Y-polarized TEM_{01} mode of the solitary V_1, ν_{1Y}.

The frequency detuning is read from the optical spectra obtained from the F-P spectrum analyzer. The reading uncertainty is ~ 0.6 GHz. Another control parameter is the injection power, P_{inj}. The injection power is measured in front of the collimating lens of V_1. Its value is adjusted by using a neutral density filter (NDF). The maximum injection power is 19.6 μW.

Fig. 11.3 demonstrates polarization switching in the total output power when the injection power is varied and frequency detuning is relatively small. In Fig. 11.3 (a), dominantly X-polarized total power switches to Y-polarized power when P_{inj} is greater than 10 μW. The corresponding frequency detuning is $\Delta\nu$=-2.0 GHz. When $\Delta\nu$=-1.4 GHz, polarization switching occurs for even lower injection power. This is similar to [Altes 2006], [Valle 2007], in which a minimum injection power induces PS for appropriate detuning. However, the power of Y (X) polarization is lower (higher) than that in Fig. 11.3 (a) by approximate 15 μW. This is because the transverse modes do not always have PS together.

As shown in Fig. 11.4, though the three X-polarized modes start to drop simultaneously, they do not reach their lowest intensity together. Among the three modes, the TEM_{01} mode undergoes polarization switching in a detuning range of ~3 GHz. The other two, the X-polarized fundamental mode and TEM_{10} mode, stay at their lowest intensity for a very narrow range of detuning and then begin to increase.

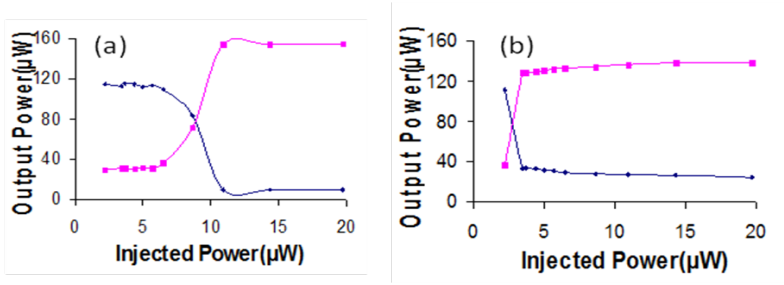

Fig. 11.3. Polarization resolved total power versus P_{inj} for (a) $\Delta\nu$=-2.0 GHz and (b) $\Delta\nu$=-1.4 GHz. (Blue diamond: X polarization; pink square: Y polarization.)

Therefore, though the total power still undergoes polarization switching in Fig. 11.3 (b), the switching is not as complete as in Fig. 11. 3 (a). The modal intensity also shows that the influence of the injection on the fourth transverse mode is minimal: its Y-polarized state only has a slight decrease and the X polarization increases slightly when the detuning is changed from -3 GHz to 0 GHz.

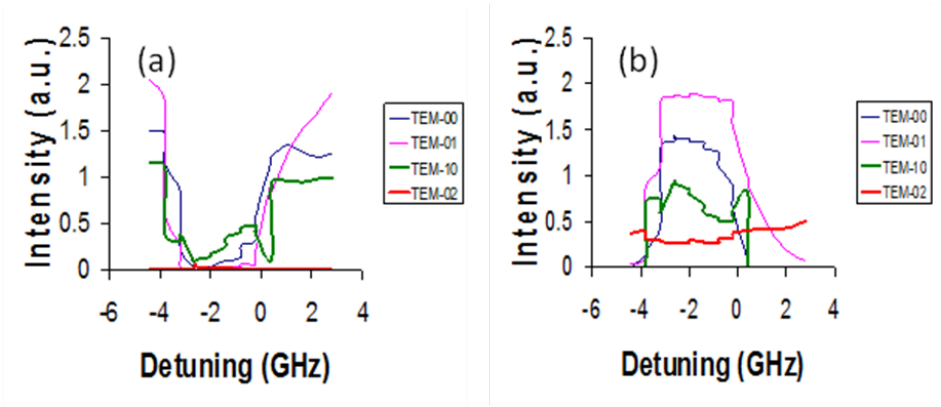

Fig. 11.4. (a) X-polarized and (b) Y-polarized modal intensities versus frequency detuning, where the injection power is 19.6 μW.

The polarized optical spectra of V_1 in the PS region are given in Fig. 11.5. It is obvious that frequency locking is achieved between the Y-polarized TEM_{01} mode and the injected beam. Frequencies of the Y-polarized fundamental mode and TEM_{10} mode are~7 GHz higher than their X-polarized counterparts, indicating that their nonlasing Y polarizations start oscillation now. Their frequencies, however, are far from that of the injection. Thus it is reasonable to say that the underlying physical mechanism is not frequency locking for the fundamental mode and TEM_{10} mode. Note that the Y(X) polarization of the TEM_{02} mode has a slight decrease (increase). This agrees with what is shown in Fig. 11.4.

As a comparison, we give the polarized optical spectra of V_1 when the injected signal has frequency locking with the fundamental mode and the TEM_{10} mode, respectively. Figs. 11.6 (a) and 11.6 (b) show injection-induced polarization switching in

the TEM_{00} mode for I_1 to be 3.408 mA. For this bias current, the TEM_{01} mode has started oscillation but is much weaker than the fundamental mode. The frequency detuning in Figs. 11.6 (a) and 11.6 (b) is -67 GHz. It is obvious that the fundamental mode becomes Y polarized and frequency locking is achieved between the injected signal and the Y-polarized fundamental mode. The TEM_{01} (the weak peak in Fig. 11.6 (a)) is not affected by the injection. This is somewhat similar to the behavior of the TEM_{02} mode in Fig. 11.5, in which the three strong X-polarized modes undergo polarization switching whereas the TEM_{02} mode only has a slight change in its intensity. When the injection gets close to the TEM_{10} mode, it causes polarization switching in the X-polarized TEM_{10} mode but does not affect polarization of the other modes, as shown in Figs. 11.6 (c) and 11.6 (d) for detuning to be -16 GHz.

When the frequency detuning and injection power are varied separately, the output of the receiver demonstrates polarization switching and various instabilities. The dynamics of V_1 is mapped in Fig. 11.7.

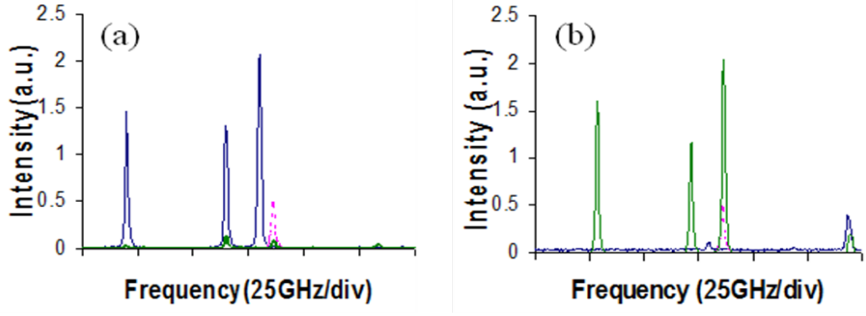

Fig. 11.5. Polarization resolved optical spectra of V_1 for $\Delta\nu$ to be -2GHz and P_{inj} to be 19.5μW. (a) X polarization (blue: solitary V_1; green: V_1 with injection) and (b) Y polarization (blue: solitary V_1; green: V_1 with injection). The pink, dashed curve represents injected signal in both polarized spectra.

Experimentally, we consider that the mode switches from X to Y polarization when its X-polarized modal intensity drops to one tenth of its original. Similarly, the mode is considered switching back

when its X-polarized modal intensity rises to one-tenth of its original. The modal polarization switching, however, is complex. As shown in FIg. 11.4, the TEM_{10} mode switches twice as detuning is varied from ~-3GHz to 1 GHz. Therefore we define a modal polarization switching regime instead of illustrating switching/switching back boundary for each mode. The modal polarization switching refers to the regime where there are one or more transverse modes switching from X-polarized state to Y-polarized state. As for slight discrepancy between Fig. 11.4 and Fig. 11.7 (in Fig. 11.4, modal switching regime is from ~-3 GHz to ~0.5 GHz for maximum injection power; in Fig. 11.7, the modal switching regime is from ~-2 GHz to ~1.5 GHz for maximum injection power), it is probably caused by uncertainties in reading and alignment of the F-P spectrum analyzer. The overall dynamics, however, repeats the same pattern as the detuning is tuned from negative value to positive. In the modal PS regime, when all the X-polarized modes have PS, the output is stable. Otherwise, a low frequency (<0.2 GHz) shoulder is

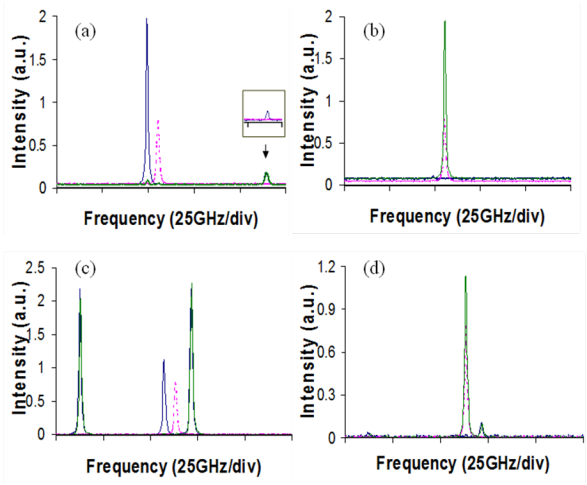

Fig. 11.6. Polarization resolved optical spectra of V_1 for (a,b) I_1=3.408 mA, $\Delta\nu$=-67 GHz and (c,d) I_1=4.799 mA, $\Delta\nu$=-16 GHz. P_{inj} is 19.5μW. (a) and (c) give X polarization (blue: solitary V_1; green: V_1 with injection; pink: injected signal). (b) and (d) are Y polarization (blue: solitary V_1; green: V_1 with injection; pink dashed: injected signal). An inset is included in (a) to illustrate with clarity the TEM_{01} mode of the solitary V_1.

observed in the RF power spectrum of the receiver, as shown in Fig. 11.8 (a). The corresponding time series manifest antiphase, irregular fluctuations (Fig. 11.8 (b)). This is because modal polarization switch and switching back do not always occur simultaneously for all transverse modes in the modal polarization regime. When some modes switch whereas others do not, polarization competition will happen and results in irregular antiphase fluctuations of relatively low frequencies.

We analyzed the RF power spectrum of V_1 and categorized the instabilities into three types. In the analysis, we take a distinguishable peak in the power spectrum into account when the magnitude of the peak is equal or greater than 3 dBm. Among the three types of instabilities, type 1 and type 2 are also observed

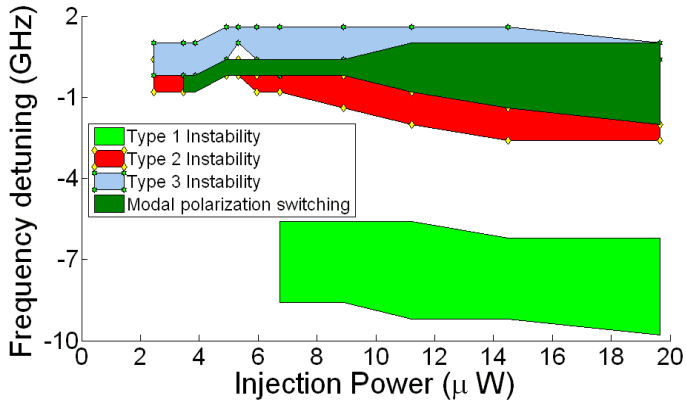

Fig. 11.7. Dynamics map of V_1 in the parameter plane of detuning versus injection power, in which regions of modal polarization switching and three types of instabilities are illustrated respectively.

when the VCSEL is subject to a two-frequency optical injection, as we will see in the next chapter. When the detuning is greater than -10 GHz, a sharp peak is observed in the power spectrum and its frequency changes with the detuning. We term this type of oscillation as type 1 instability.

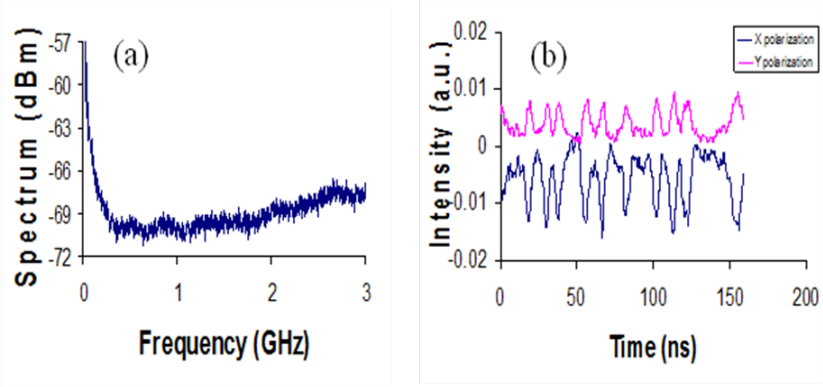

Fig. 11.8. (a) Power spectrum of the Y-polarization and (b) polarization-resolved time series (blue: X; pink: Y) for $\Delta\nu$=-0.2 GHz and P_{inj}=19.5μW. The receiver is in the modal PS regime. The time series of X polarization is shifted downward for visual convenience.

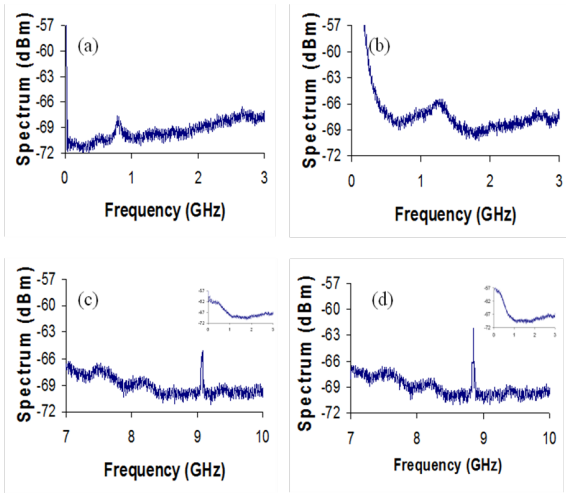

Fig. 11.9. Power spectrum of the Y-polarization of V_1. (a) Type 1 instability for $\Delta\nu$=-7.4 GHz, (b) type 2 instability for $\Delta\nu$=-2 GHz, (c) type 3 instability for $\Delta\nu$=0.4 GHz. The injection power is 19.5 μW. The inset shows the low-frequency shoulder in the power spectrum. (d) Type 3 instability for P_{inj}=8.6 μW.

As shown in Fig. 11.9 (a), there is a sharp peak of ~0.8 GHz in the RF power spectrum of V_1 for detuning to be -7.4 GHz. For this specific

detuning, the frequency difference between the injection and the elliptically polarized TEM_{01} mode is 0.6 GHz. These two frequencies are the same by taking the reading uncertainty into account. On contrary, type 1 instability is not observed when the external signal is injected to the TEM_{00} or TEM_{10} mode of the receiver because these two modes are X-polarized in solitary operation. Therefore the oscillation is probably the beating of the injected beam and the y-component of the TEM_{01} mode. The second type of instability is represented by a peak ~1 to 2 GHz in the power spectrum and a low frequency enhancement of the power spectrum of the Y-polarization, as shown in Fig. 11.9 (b). It occurs immediately before a mode switches from X to Y polarization and the bandwidth of the frequency peak in the power spectrum is wider than that in type 1 instability. The origin of this instability is likely due to noise-induced mode hopping that typically accompanies polarization switching. Polarization mode hopping in QW VCSELs is only observed when the laser is biased in the vicinity of the current of an abrupt PS [Willemsen 1999], [Nagler 2003], [Giacomelli 1998], [Kaiser 2002]. Type 2 instability only occurs when the parameters are close to the PS boundary, as shown in Fig. 11.7. Also the RF spectrum of Fig. 11.9 (b) shows an enhancement of low frequency component similar to that observed in VCSELs showing polarization mode hopping [Giacomelli 1998]. It also occurs as the signal from the transmitter is injected on the TEM_{10} mode. The third type of instability includes a low-frequency shoulder (<1 GHz) and a sharp peak at ~9 GHz (Fig. 11.9 (c)). The low-frequency shoulder represents polarization competition between X and Y polarizations and is wider than that in type 2 instability. The magnitude of the 9 GHz peak is affected by injection power. When the injection power is decreased but not too weak, the magnitude of the peak increases, as shown in Fig. 11.9 (d). Since the low-frequency shoulder is wide and there is a ~9 GHz peak in the power spectrum, it may indicate a transition to chaos via undamped relaxation oscillation. However, we did not obtain such a frequency of relaxation oscillation experimentally. Therefore the origin of this

instability needs further investigation. Our theoretical modeling and numerical simulation are under way.

We also investigated whether there is any bistability for the observed PS since detunig-induced PS is typically accompanied by hysteresis regions in VCSELs [Gatare 2007a]. When the frequency detuning is decreased, we observed a very narrow region of hysteresis. However, since the width of the region is similar to the level of reading uncertainty, we do not think that this is solid evidence of bistability. This may be related to the low power of the injected signal.

11.4. Discussion and conclusions

It was reported that when the VCSEL operates with two transverse modes-a fundamental mode and a first-order mode-with parallel polarization, the behaviors of the two modes are independent for both parallel and orthogonal optical injection. That is, optical injection only affects one mode while the only mode is unperturbed [Hong 2003]. In our study, this modal independence was observed in Fig. 11.6 when the external signal is injected to the fundamental mode and the TEM_{10} mode, respectively. However, a strong modal correlation evidenced by PS in three modes was demonstrated when the TEM_{01} mode received the injection. The fourth mode, orthogonally polarized to the first three, is quite independent of the PS that occurs in the other modes. This implies that both spatial profile overlapping and modal strength play roles in the observed PS. When the external beam is injected into the TEM_{01} mode, the bias current of V_1 is more than two times the threshold. For this relatively high current, all the X-polarized transverse modes are strong, and the TEM_{01} mode is the strongest one among them, as shown in Fig. 11.5. Therefore, it is possible that the spatial coupling between the TEM_{01} mode and the other two modes (the TEM_{00} and TEM_{10} modes) are significantly stronger than their couplings for lower bias current (Fig. 11.6), and this stronger coupling leads to the PS in all the three modes. The fourth

transverse mode is much weaker than the first three modes, so its behavior is more independent. Our results also show that PS can be achieved with a very low injection power (a few μW), which is lower than most injected power used in previous studies [Hong 2002], [Valle 2007]. This indicates a possible way to control the polarization of a multimode VCSEL via a weak signal.

The dynamics underlying the transition to polarization switching has been discussed for single [Sciamanna 2006], [Gatare 2007b] and multimode [Altes 2006], [Valle 2007] VCSELs subject to orthogonal optical injection. Physics and bifurcations have been studied by doing a detailed analysis of the changes in optical spectra observed when changing the injected power for a fixed value of the frequency detuning. A better insight into the dynamics obtained in our experiment can be gained by comparing with results for multimode VCSELs [Altes 2006], [Valle 2007]. Switching from the X to the Y-polarized fundamental transverse mode is also obtained in the previous chapter and in [Valle 2007] when the frequency of the optical injection is near to that of the high-order transverse mode. The transition to locked high-order transverse mode observed in chapter 10 and in [Valle 2007] is not obtained in our experiment, possibly due the limited injected power in our set-up. However, a direct comparison with the results of chapter 10 and [Altes 2006], [Valle 2007] has its limitations because in our free-running VCSEL four different modes have appreciable power whereas in chapter 10 only two modes of the free-running VCSEL were excited and in [Altes 2006], [Valle 2007] only the fundamental mode of the solitary VCSEL was lasing. This difference suggests that an analysis of the dynamics, similar to that performed in [Altes 2006], [Valle 2007], [Sciamanna 2006], [Gatare 2007b], would be desirable in our system for a better understanding of the physics and bifurcations. But this analysis is beyond the scope of this work.

In conclusion, we have studied experimentally the effect of a single-frequency orthogonal optical injection on a VCSEL

operating with four transverse modes. Our results reveal that when the strongest mode, the TEM_{01} mode, is frequency-locked to the injection, polarization switching is achieved in the TEM_{01} mode as well as the other strong modes. This leads to polarization switching in the total output power of the receiver. The results imply that spatial overlapping and modal intensities play roles in the modal polarization switching in the fundamental mode and the TEM_{10} mode. We have identified three types of instabilities outside the modal polarization switching regime and proposed physical mechanisms for some of them.

CHAPTER 12

Two-frequency optical injection on a multimode vertical-cavity surface-emitting laser

We study experimentally effects of two-frequency orthogonal optical injection on a short-wavelength multimode VCSEL. The injected signal comes from another multi-transverse mode VCSEL. Thus, we consider partially coherent optical injection. Polarization switching (PS) with and without frequency locking occurs for relatively small frequency detuning. Double injection locking involving two transverse modes is obtained in VCSELs subject to two-frequency orthogonal optical injection. Outside the regime of polarization switching, the VCSEL demonstrates two types of instabilities. The instability regions and boundaries of PS of each transverse mode are mapped in the parameter plane of frequency detuning versus injected power.

12.1. Introduction

Single-mode VCSEL-by-VCSEL optical injection locking has been recently studied as a first step for obtaining integrated low-cost high-speed communications modules [Hayat 2009]. As seen in previous chapters, in most studies on optical injection, the injected signal comes from an external laser (named transmitter or master laser) that operates with a single frequency. Much less attention has been paid to the injection of more than one frequency. Since optical injection changes the coupling characteristics between the electric field in the laser cavity and the charge carriers, the dynamics of a laser subject to more than one injected frequency is expected to be more complicated. Recently, some theoretical and experimental studies have been extended to optical injection of more than one frequency on EELs [Li 1994], [Troger 1999], [Al-Hosiny 2006], [Qi 2011b], [Juan 2011]. From the applications point of view, dual-beam optical injection is of special interest since photonic generation of broadly tunable microwave signals has been obtained by using a DFB laser [Juan 2011]. Optical injection of more than one frequency, however, has not been applied to VCSELs yet.

12.2. Experimental setup

In this chapter the experimental setup is the same than that considered in the previous chapter (see Fig. 11.1). We call V_1 to the receiver VCSEL and V_2 to the transmitter VCSEL. The polarization resolved L-I curve of V_1 is shown in Fig. 11.2 (a), the solitary V_1 is dominantly polarized in the X direction. For this case, from threshold I_1=2.51 mA to 3.35 mA, the VCSEL operates in fundamental mode (TEM_{00} mode). The second mode, a higher-order transverse mode, starts lasing from 3.35 mA. Its beam profile indicates that it can be described as a TEM_{01} mode. The frequency difference between the TEM_{01} mode and the fundamental mode is 63 GHz. From 3.50 mA to 4.75 mA, the VCSEL operates with three

transverse modes. The third mode is a TEM_{10} mode. The frequency of its X polarization is 15 GHz less than that of the TEM_{01} mode. The fourth transverse mode is on from 4.75 mA. In our experiment, the VCSEL operates in the three-transverse-mode regime. No polarization switching (PS) is observed in the solitary VCSEL within the current range we have used. The injected light includes two lasing modes: a fundamental mode and a first-order mode. Their frequency difference is 61 GHz. The spectrum and beam profile of each transverse mode of both receiver (V_1) and transmitter (V_2) are given in Figs. 12.1 (a) and 12.1 (b) respectively.

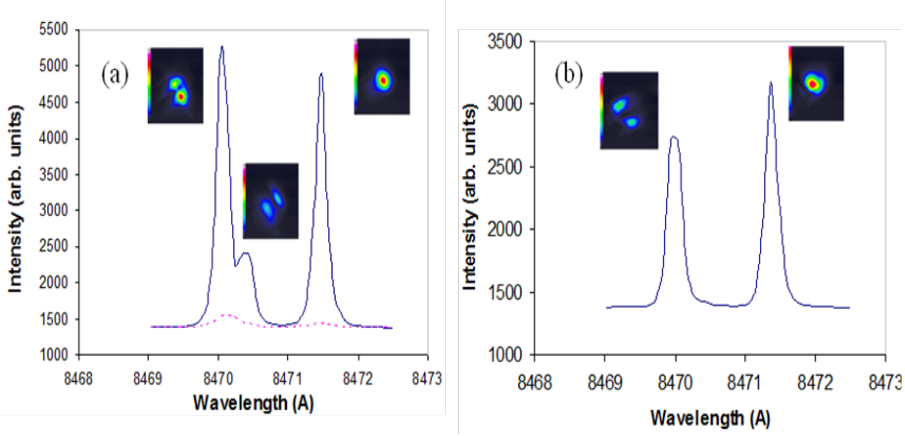

Fig. 12.1. (a) Polarization resolved optical spectrum and spatial profile of each transverse mode of V_1 for I_1=4.513mA (blue solid: X polarization; pink dashed: Y polarization). (b) Optical spectrum and spatial profile of each mode of V_2, for which I_2=4.115 mA.

Fig. 12.2 illustrates frequency difference between the X and Y components of each transverse mode in the three-mode regime of V_1. Fig. 12.2 (b) reveals that the Y component of the fundamental mode has two frequencies, one of the same frequency as the X component, the other is 9 GHz higher. The polarization feature of the TEM_{01} is similar. It includes an essentially X polarized mode and a non-lasing Y polarized mode that is ~7GHz away. For the TEM_{10} profile, the difference between X and Y polarized modes is 7 GHz. For both first-order profiles the Y

polarized mode has the higher frequency.

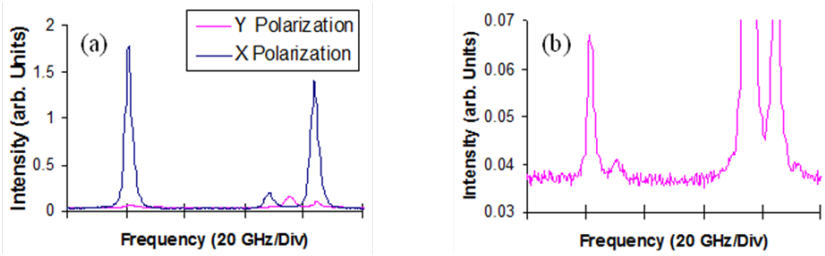

Fig. 12.2. (a) Polarization resolved optical spectra of V_1 for I_1=4.2 mA. (b) The spectrum of the corresponding Y polarization plotted in a more sensitive scale. (Blue: X; pink: Y)

12.3. Experimental results

We define frequency detuning, $\Delta\nu$, as the frequency difference between the fundamental mode of the injected light, ν_{2f}, and the Y polarization of the fundamental mode of the solitary V_1, ν_{1fY}. We change $\Delta\nu$ by varying I_1, the bias current of the receiver. Another control parameter is the injected power. For the results presented below, the bias current of V_2 is 4.2 mA. When $\Delta\nu$ is changed, the injection power, P_{inj}, is kept constant. The injection power is adjusted by using a neutral density filter (NDF).

We have observed PS in each transverse mode for a certain range of the frequency detuning and injected power. Figure 12.3 illustrates modal intensities versus frequency detuning, in which the three transverse modes switch simultaneously for $\Delta\nu$ to be ~-2 GHz. However, they do not switch back together as the detuning is increased. As shown in Fig. 12.3, the fundamental mode switches back when the detuning is increased beyond -0.5 GHz, the TEM_{01} mode switches back for 0.5 GHz, and the TEM_{10} mode is the last to switch back, at around 2 GHz. Therefore, we have observed that the polarized total power has an abrupt change on one side of the PS regime and a gradual variation on the other side. The similar way of switching and switching back is observed for other values of injection power, except that the detuning range in which PS

occurs becomes narrower when the injection power is weaker.

For a fixed frequency detuning, PS may occur when the injection power is strong enough. The minimum power to induce PS varies with the value of detuning. Fig. 12.4 shows how the total power of each polarization varies with the injection power when the frequency detuning is set at -1.8 GHz. The total power has PS when the injection power is greater than 38 μW. Fig. 12.5 shows the optical spectrum of each polarization at different values of frequency detuning, where the left column is for X polarization and the right column for Y polarization. Fig. 12.5 (a) is for $\Delta\nu$=-1.8 GHz, at

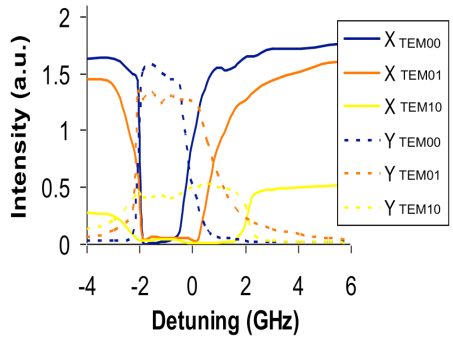

Fig. 12.3. Polarization resolved modal intensities versus frequency detuning. The injection power is 52.5 μW.

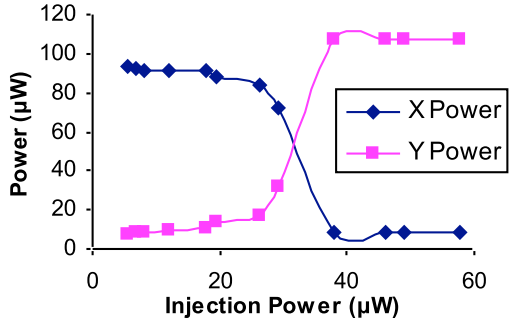

Fig. 12.4. Polarization resolved total power versus injected power for frequency detuning to be -1.8 GHz.

which the three modes undergo PS together. Both the fundamental mode and TEM_{01} mode are wavelength locked to the corresponding modes in the injected signal whereas their X components are minimized. The PS in the TEM_{10} mode, however, is not due to wavelength locking; it is likely due to polarization competition. Results of Fig. 12.5 (a)-(b) show that double injection locking involving two transverse modes can be obtained in VCSELs subject to two-frequency orthogonal optical injection. For $\Delta\nu$=0 GHz (Fig. 12.5 (c)-(d)), the fundamental mode is partially X polarized with the same frequency as its counterpart of the solitary V_1, whereas its Y component remains locked to the fundamental mode of the injected signal. The other two higher order modes are still in PS state. Now the X polarization of V_1 is operating with single transverse mode.

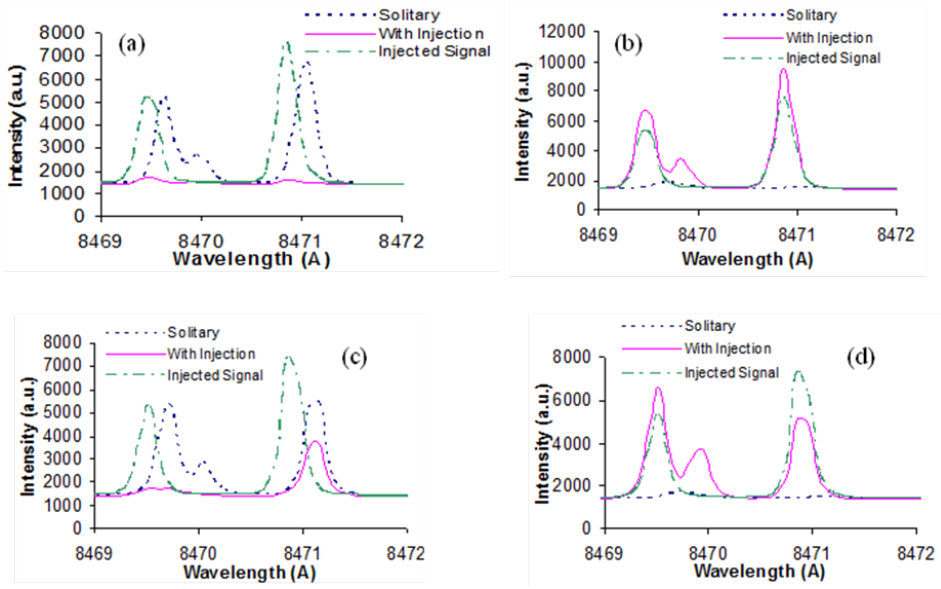

Fig. 12.5. Spectrum of X polarization (left column) and Y polarization (right column) of the receiver VCSEL. (a)-(b) $\Delta\nu$=-1.8 GHz, and (c)-(d) $\Delta\nu$=0 GHz. The injection power is 57.9 μW.

The dynamics of the VCSEL subject to the two-frequency injection is mapped in Fig. 12.6. It shows that in a wide range of the injected power, the three transverse modes have PS simultaneously but switch back for different values of detuning. We consider the mode's polarization as switching back when its Y component drops to 90% of its value in the PS state. Switching occurs in the fundamental mode for negative detuning in most cases, whereas the detuning can be both positive and negative for the first order modes. Typically, the stronger the injection power, the wider range of detuning for which PS can occur. When $\Delta\nu$ is about 0 GHz, both the fundamental mode and the TEM_{01} mode have PS with minimum injected power. That is, the minimum power for switching is obtained when the X polarization of the fundamental mode is about 9 GHz less than the fundamental mode of the injected signal. This frequency difference is the splitting between the X and Y polarization of the fundamental mode of the receiver. This is similar to [Altes 2006] in which the minimum switching power is obtained for a detuning corresponding to the frequency splitting between the two components of the fundamental mode. The optical spectra (not shown) manifest that for both the TEM_{00} mode and the TEM_{01} mode, their wavelengths are locked to the corresponding injected modes. The switching in the TEM_{10} mode is not related to wavelength locking. It is probably caused by polarization competition. In the regime where the three modes undergo PS simultaneously, the output power is stable. When one or two modes switch back while the other is still in PS, the output is unstable. For a chosen value of P_{inj}, as the detuning is increased from -12 GHz toward the PS regime, the VCSEL demonstrates fluctuations which we classify as type 1 and type 2 instabilities. Type 1 instability includes a sharp peak and a low frequency shoulder in the RF power spectrum (Fig. 12.7 (a)) of both polarizations of the VCSEL. Its frequency is close to the frequency difference (0.4 GHz) between the X polarization of the fundamental mode and the ν_{2f} injected frequency. We measured the frequency of the first type of instability versus ν_{2f}-ν_{1fX}. The result

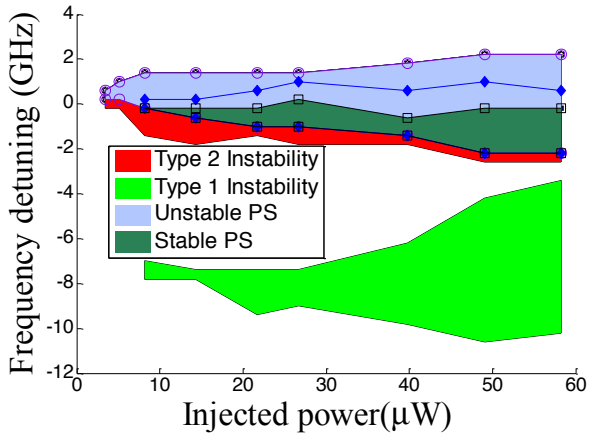

Fig. 12.6. Stability map in the $\Delta\nu$-P_{inj} parameter plane, where the square symbol indicates the boundary of the PS regime of the fundamental mode, the diamond symbol represents the boundary of the PS regime of the TEM_{01} mode, and the circle symbol is for the TEM_{10} mode.

shows a good linear relation and the slope of the best fitting line is very close to 1. Therefore, the peak in the first type of instability has probably the same origin than the type 1 instability discussed in the previous chapter, that is the beating of the injected beam and the Y component of the fundamental mode that has the same frequency as the X component. Type 2 instability occurs when the frequency detuning is close to the boundary of PS. It always starts with a peak in the power spectrum at around 2 GHz. As the frequency detuning is increased a little, this frequency decreases slightly with an increasing intensity. The bandwidth of the peak as well as the low frequency shoulder in the power spectrum is wider than that of the first type of instability. The second type of fluctuation suddenly disappears when the three modes have PS simultaneously. The origin of this instability is likely due to noise induced mode hopping that typically accompanies polarization switching. For these instabilities, we take the peak in the RF power spectrum into account when its intensity is greater than 3 dB.

Figure 12.7 (c) gives the power spectrum in the stable PS regime in the stability map, in which the sharp peaks in the low frequency region are external noise. Given the coexistence of three transverse modes in this regime, there should be oscillations at the beat frequencies of the modes. Those frequencies are not observed because they are higher than the bandwidth of our detectors. Figure 12.7 (d) is in the unstable PS regime, where the fundamental mode is out of the PS regime but the two-first order modes have not. In this case, the X component and the Y component of the fundamental mode have comparable intensity. The peak in the power spectrum is very close to the frequency detuning and the low frequency part is due to polarization hopping.

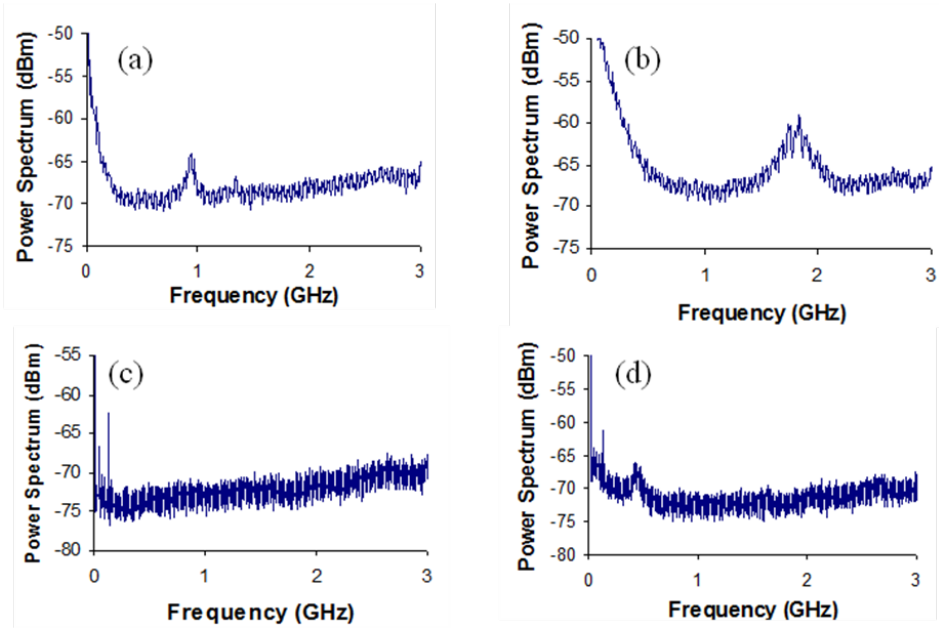

Fig. 12.7. Power spectrum of the Y polarization of V_1 subject to the two-frequency for (a) $\Delta\nu$=-8.6 GHz (type 1 instability), (b) $\Delta\nu$=-2.6 GHz (type 2 instability), (c) $\Delta\nu$=-1.8 GHz (stable PS), and (d) $\Delta\nu$=0.2 GHz (unstable PS). The injection power is 57.9 μW. The sharp peaks located at ~100 MHz or less are external noise.

12.4. Conclusions

Our results show that the partially coherent, two-frequency injection can induce PS in the total power of a multi-transverse mode VCSEL. The physical mechanisms of PS are frequency locking for the two stronger transverse modes and polarization competition for the weakest mode. This extends injection-induced PS to multi-transverse mode regime of both receiver and transmitter and may be useful for development of tunable multimode light source. The feature that the width of modal PS regime is different can be used for transverse mode selection. Instabilities include unstable PS when the three modes do not switch simultaneously and periodic oscillations before the receiver enters the stable PS regime.

CHAPTER 13

High-frequency microwave signal generation using multi-transverse mode VCSELs subject to two-frequency optical injection

In this chapter we report a new method of photonic generation of microwave signals using a multi-transverse mode VCSEL subject to two-frequency optical injection. Numerical simulations show that double injection locking involving two transverse modes can be obtained in these systems. We show that the higher-order transverse mode is excited with a much larger amplitude than that of the fundamental transverse mode. The comparison with the case of a single-transverse mode VCSEL subject to similar two-frequency optical injection shows that multi-transverse mode operation of the VCSEL enhances the performance of the photonics microwave generation system. Broad tuning ranges, extended into the THz region, and narrow linewidths are

demonstrated in our system. The maximum frequency of the generated microwave signals can be substantially increased if multimode VCSELs are used instead of single-mode VCSELs.

13.1. Introduction

Non linear dynamics of optically injected semiconductor lasers can also be used for photonic microwave generation [Chan 2008], [Chan 2007], [Chan 2010], [Chan 2006], [Qi 2011a], [Qi 2011b], [Juan 2011], [Chen 2011]. Compared with conventional microwave generation by electronic circuitry with multiple stages of frequency doubling, photonic microwave signal generation have the advantages of lower cost, longer transmission distance, higher speed, low power consumption, less system complexity and the ability to generate tunable microwave signals with higher frequencies [Qi 2011a], [Juan 2011]. Photonic microwave generation find applications in radio-over-fiber (RoF) technology that holds great promise for 4G mobile communications systems [Qi 2011a]. Both single-beam optically injected semiconductor lasers [Chan 2008], [Chan 2007], [Chan 2010], [Chan 2006], [Qi 2011a], and dual-beam, or two frequency, optically injected semiconductor lasers [Qi 2011a], [Qi 2011b],[Juan 2011], [Chen 2011] have been considered. Tunable narrow-linewidth microwave signals have been generated by using the period-one (P1) oscillations states that appear when the semiconductor laser is subject to a single-beam optical injection scheme [Qi 2011a]. Photonic microwaves from the P1 oscillation of an optically injected edge-emitter semiconductor laser have reached frequencies beyond 100 GHz [Chan 2006]. The tuning range of the generated microwave signals is limited to several tens of GHz [Juan 2011]. Recently a very high frequency (121.7 GHz) microwave signal has been generated by using a dual-beam optically injected single-mode DFB semiconductor laser [Juan 2011]. Simultaneous injection of two laser beams transforms the slave laser into a dual-wavelength laser in such a way that the frequency of the generated microwave signal can be easily tuned

by adjusting the frequency spacing between the two master lasers [Juan 2011]. Double injection locked states are observed when the slave laser is subject to strong optical injection by both master lasers in such a way that the stable locking is also observed if only light of one of the master lasers is injected [Juan 2011], [Chen 2011]. A double injection locked state has also been observed in the previous chapter in which a multi-transverse mode VCSEL is subject to orthogonal optical injection from a similar VCSEL. Experimental tuning ranges, limited by the bandwidth of the photodetector, around 20 GHz were demonstrated [Juan 2011]. Numerical calculations have shown that a wide continuous tuning range of more than 100 GHz is obtained by adjusting the detuning frequency of the two master lasers [Chen 2011].

Characterization of the maximum microwave frequency achievable in a photonic microwave system is of interest because it sets the bandwidth limit of the system [Qi 2011a]. For single-beam optically injected semiconductor lasers this limit is given by the free-spectral range (around 100 GHz) because the increase of the detuning frequency necessary to achieve higher microwave frequencies causes the laser to hop to the next mode [Qi 2011a]. The highest frequency that can be generated in a dual-beam optically injected semiconductor laser is limited by the locking range determined by the maximum injection strengths of the two master lasers [Juan 2011].

13.2. Theoretical model

The theoretical model is based on a spatially dependent dynamical model of a multi-transverse mode VCSEL subject to single-frequency optical injection [Valle 2007]. In this chapter we extend it for considering a two-frequency optical injection. The simulated cylindrically symmetric weak index-guided structure, together with the complete details of the model can be found in [Valle 2007]. The model describes the complex amplitudes of two transverse modes with their two possible linear polarizations.

Subscripts x and y will be used to denote the two orthogonal linear polarization directions. The appropriate transverse modes of the structure are the LP_{mn} modes. Here we treat the case of VCSELs that can operate in the fundamental (LP_{01}) and in the first order (LP_{11}) transverse modes. Subscripts 0,1 will be used to denote the LP_{01} and LP_{11} modes, respectively. The equations describing the polarization and transverse mode behavior of the VCSEL with a two-frequency injected optical field read [Valle 2007]:

$$\dot{E}_{0x} = k(1+i\alpha)(E_{0x}(g_{0x}-1)+iE_{0y}g_{0xy})-(\gamma_a+i\gamma_{p0})E_{0x}+\frac{k_{01}}{\tau_{in}}e^{i\Delta\omega_1 t}+\frac{k_{02}}{\tau_{in}}e^{i\Delta\omega_2 t}+\sqrt{\frac{\beta}{2}}\left(\sqrt{\overline{N}+\overline{n}}\xi_{0+}(t)+\sqrt{\overline{N}-\overline{n}}\xi_{0-}(t)\right)$$

$$\dot{E}_{0y} = k(1+i\alpha)(E_{0y}(g_{0y}-1)-iE_{0x}g_{0yx})+(\gamma_a+i\gamma_{p0})E_{0y}-i\sqrt{\frac{\beta}{2}}\left(\sqrt{\overline{N}+\overline{n}}\xi_{0+}(t)-\sqrt{\overline{N}-\overline{n}}\xi_{0-}(t)\right)$$

$$\dot{E}_{1x} = k(1+i\alpha)\left(E_{1x}\left(g_{1x}-\kappa_r\right)+iE_{1y}g_{1xy}\right)+i\gamma_p^{tr}E_{1x}-\left(\gamma_a+i\gamma_{p1}\right)E_{1x}+\frac{k_{11}}{\tau_{in}}e^{i\Delta\omega_1 t}+\frac{k_{12}}{\tau_{in}}e^{i\Delta\omega_2 t}+\sqrt{\frac{\beta}{2}}\left(\sqrt{\overline{N}+\overline{n}}\xi_{1+}(t)+\sqrt{\overline{N}-\overline{n}}\xi_{1-}(t)\right)$$

$$\dot{E}_{1y} = k(1+i\alpha)(E_{1y}(g_{1y}-\kappa_r)-iE_{1x}g_{1yx})+i\gamma_p^{tr}E_{1y}+(\gamma_a+i\gamma_{p1})E_{1y}-i\sqrt{\frac{\beta}{2}}\left(\sqrt{\overline{N}+\overline{n}}\xi_{1+}(t)-\sqrt{\overline{N}-\overline{n}}\xi_{1-}(t)\right)$$

$$\frac{\partial N(r,t)}{\partial t} = I(r)+D\nabla_\perp^2 N-\gamma_e\left[N\left(1+\sum_{i=0,1}\sum_{j=x,y}\left|E_{ij}\right|^2\psi_{ij}^2(r)\right)-in\sum_{i=0,1}\left(E_{ix}E_{iy}^*-E_{iy}E_{ix}^*\right)\psi_{ix}(r)\psi_{iy}(r)\right]$$

$$\frac{\partial n(r,t)}{\partial t} = -\gamma_s n+D\nabla_\perp^2 n-\gamma_e\left[n\sum_{i=0,1}\sum_{j=x,y}\left|E_{ij}\right|^2\psi_{ij}^2(r)-iN\sum_{i=0,1}\left(E_{ix}E_{iy}^*-E_{iy}E_{ix}^*\right)\psi_{ix}(r)\psi_{iy}(r)\right] \quad (13.1)$$

where E_{0j} and E_{1j} are the complex amplitudes of the LP_{01} and LP_{11} modes (the subindex j stands for the linear polarization state of the given mode), $N(r,t)$ is the total carrier number, n(r,t) is the difference in the carrier numbers of the two magnetic sublevels, and ψ_{0j} *and* ψ_{1j} are the modal intensity profiles of the LP_{01} and LP_{11} modes obtained by solving the Helmholtz equation [Valle 1996], [Valle 1998b], respectively. κ_r is the relative loss of the LP_{11} mode with respect to the LP_{01} mode. It determines the value of the injection current at which the LP_{11} mode begins lasing $I(r)$ represents a uniform current injection over a circular disc of 6 μm radius, and then $I(r)=I$ if $r<6\ \mu m$, and $I(r)=0$, elsewhere. The normal gain normalized to the threshold gain, g_{ij} ($i=0,1$, j=x,y), and g_{ijk}

(*i=0,1; jk=xy, yx*) are given by

$$g_{ij} = \frac{\int_0^\infty N(r,t)\psi_{ij}^2(r)\,r\,dr}{\int_0^\infty \psi_{ij}^2(r)\,r\,dr} \qquad g_{i,jk} = \frac{\int_0^\infty n(r,t)\psi_{ij}(r)\psi_{ik}(r)\,r\,dr}{\int_0^\infty \psi_{ij}^2(r)\,r\,dr} \tag{13.2}$$

In the two-frequency injection scheme the VCSEL is optically injected by a master laser 1 (ML1) and a master laser 2 (ML2), with optical frequencies ω_1 and ω_2, respectively. Two frequency detunings, $\Delta\omega_1=\omega_1-\omega_{th}$ *and* $\Delta\omega_2=\omega_2-\omega_{th}$, with respect to the central frequency between the two polarizations of the fundamental mode $\omega_{th} = (\omega_{0x}+\omega_{0y})/2$, appear in the equations. The injection terms only appear in the equations for E_{0x} and E_{1x}, hence linearly polarized optical injection in the x-direction is considered for both master lasers. In this way if the solitary VCSEL emits only in the x-linear polarization, as it will be considered in this chapter, the directions of the polarizations of optical injections and VCSEL are parallel. Optical injection terms are also characterized by the injection strengths, k_{im}, and the VCSEL roundtrip time, $\tau_{in}=2L/v_g$, where v_g is the group velocity. The injection strength k_{im} (i=0,1, m=1,2) is given by

$$k_{im} = \left(\frac{1}{\sqrt{R}} - \sqrt{R}\right)\sqrt{\eta_{inj}}\sqrt{P_{inj,im}} \tag{13.3}$$

where R is the output mirror reflectivity, η_{inj} is the coupling efficiency of the injected light to the optical field in the laser cavity and $P_{inj,im}$ is the power injected in the *i*-transverse mode by the *m*-master laser [Law 1997b]. In this work we choose the k_{im} values in relation to what should be expected when light from a multi-transverse mode VCSEL is injected into a similar device. k_{01} (k_{12}) is related to the spatial overlap integral between the profiles of the fundamental modes (the higher-order modes) of master and slave lasers. Then a reasonable choice is $k_{01}=k_{12}=k_s$, where k_s is the injection strength between similar transverse modes. k_{02} (k_{11}) is related to the spatial overlap integral between the profiles of the

fundamental mode of the slave and the higher order mode of the master (higher-order mode of the slave and the fundamental mode of the master) VCSEL. In this way we choose $k_{02}=k_{11}=k_c$, with $k_c \leqslant k_s$, where k_c is a "crossed" injection strength between transverse modes with different order. The frequency splitting between the orthogonal polarizations of the LP_{01} mode, $2\gamma_{p0}/(2\pi)$, between the orthogonal polarizations of the LP_{11} mode,$2\gamma_{p1}/(2\pi)$, and between the two transverse modes with the same polarization, $\gamma_p^{tr}/(2\pi)$, are obtained from the calculation of the waveguide modes via the Helmholtz equation [Valle 1996], [Valle 1998b]. We have chosen the values of refractive indexes $n_{core,x}$, $n_{core,y}$ and n_{cladd} in such a way that $2\gamma_{p0}/(2\pi)$=10 GHz and $\gamma_p^{tr}/(2\pi)$= 63 GHz. Spontaneous emission noise processes are modeled by the terms $\xi_{\pm}$ taken as complex Gaussian white noise sources of zero mean and delta-correlated in time. In the noise terms we consider integrated over the active region carrier distributions, and [Valle 2007] The rest of the parameters that appear in the equations and their meaning are specified in the Table 1. Time and space integration steps of 0.01 ps and 0.12 microns, respectively, have been used. The boundary conditions for the carrier distribution are taken as $N(\infty,t)=0$, $n(\infty,t)=0$. The initial conditions correspond to a below threshold stationary solution, i.e to $I=0.1I_{th}$, where I_{th} is the threshold current.

Table 1. Parameters used in the model

SYMBOL	VALUE	MEANING OF THE SYMBOL
a	6 μm	Radius of the core region
L	1 μm	Length of the cavity
$n_{core,x}$	3.5001025	Refractive index of the core region in the x-direction
$n_{core,y}$	3.5	Refractive index of the core region in the y-direction
n_{cladd}	3.41	Refractive index of the cladding region
k	300 ns^{-1}	Field decay rate
α	3	Linewidth enhacement factor
γ_e	0.55 ns^{-1}	Decay rate for the total carrier population
γ_s	1000 ns^{-1}	Spin-flip relaxation rate
D	10 cm^2s^{-1}	Diffusion coefficient
β	10^{-5} ns^{-1}	Spontaneous emission coefficient
γ_a	-0.3 ns^{-1}	Dichroism
η_{inj}	1	Coupling efficiency
R	0.995	Output-mirror reflectivity

13.3. Two-frequency optically injected VCSELs

In this section, we present the results corresponding to the two-frequency optical injection on single and multi-transverse mode VCSELs. First, we show results corresponding to a VCSEL emitting only in the fundamental transverse mode. We have chosen a value κ_f=10 to assure $LP_{01,x}$ mode operation. Results are given in terms of the separation between the frequencies of the two master lasers, $\Delta f=(\omega_2-\omega_1)/(2\pi)$, the frequency detuning of ML1 with respect to the frequency of the $LP_{01,x}$ mode, $\Delta\nu$, and the injection strength κ_s. We show in Fig. 13.1 (a) the dynamical evolution of a free-running single-transverse mode VCSEL when switched-on at time t>0 with a I=1.8 I_{th} bias current value. The VCSEL emits in the steady state in the $LP_{01,x}$ mode with a single peaked RF spectrum appearing at the relaxation oscillation frequency. Spectra are calculated after a transient time of 14 ns.

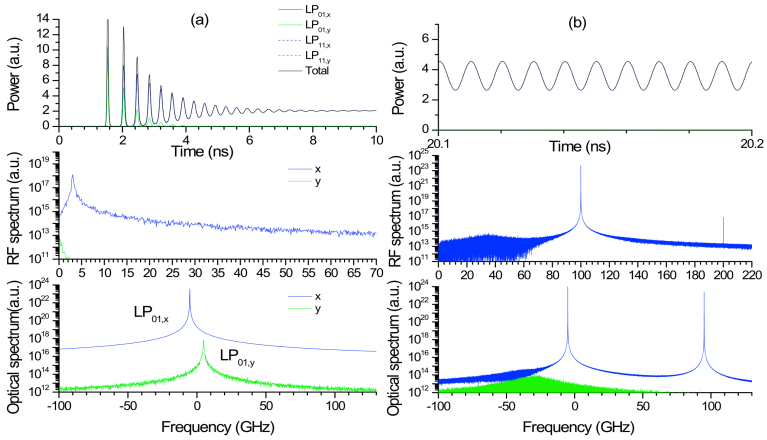

Fig. 13.1. Temporal and spectral dynamics of a single-transverse mode VCSEL when (a) no optical injection is applied, (b) Δf=100 GHz, $\Delta\nu$=0GHz, κ_s=10^{-2}, and κ_c=κ_s/2. Upper row: Time traces of the power of the polarized transverse modes. Middle row: RF spectra of the polarized powers. Lower row: x and y-polarized optical spectra.

Fig. 13.1 (b) shows the results for an injection strength of κ_s=10^{-2}, Δf=100 GHz, and with the frequency of ML1 just at the $LP_{01,x}$ mode frequency. An almost sinusoidal time trace is obtained for the power of $LP_{01,x}$ mode, that is the only mode with non negligible power. The frequency of this sinusoidal modulation is Δf. The optical spectrum consists on two well defined peaks at the ML1 and ML2 optical frequencies and the RF spectrum has a very narrow peak at Δf, the frequency separation between ML2 and ML1. This situation is similar to the double injection locking that has been obtained using a single mode DFB laser subject to dual-beam injection [Juan 2011] and in simulations using a single-mode rate equation model [Chen 2011].

We now present the results corresponding to two-frequency optical injection on a multi-transverse mode VCSEL. This laser is exactly the same than the single-transverse mode VCSEL but changing the parameter κ_f to a smaller value (κ_f=1.022) for which both transverse modes have rather similar losses. Results obtained for the solitary multimode VCSEL (κ_s=κ_c=*0*) are plotted in Fig. 13.2 (a). In this case the VCSEL shows a steady-state in which both

transverse modes, LP_{01} and LP_{11}, are excited in the x-direction. The steady-state total power in Fig. 13.2 (a) is 1.7, a similar value to the value, 2.1, that was obtained for Fig. 13.1 (a).

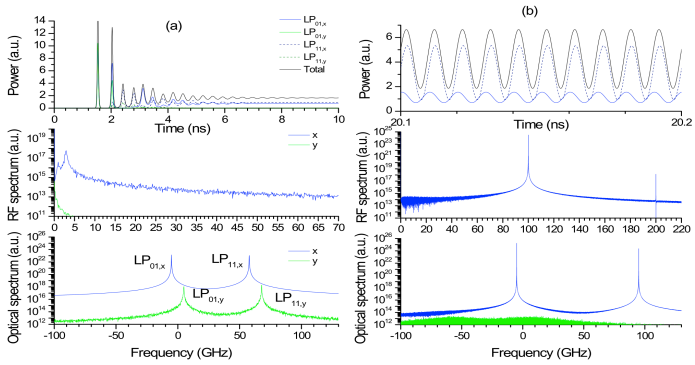

Fig. 13.2. Temporal and spectral dynamics of a multi-transverse mode VCSEL when (a) no optical injection is applied, (b) Δf=100 GHz, $\Delta\nu$=0GHz, κ_s=10^{-2}, and κ_c=κ_s/2. Upper row: Time traces of the power of the polarized transverse modes. Middle row: RF spectra of the polarized powers. Lower row: x and *y*-polarized optical spectra.

The power in the $LP_{11,x}$ mode is only slightly larger than that of $LP_{01,x}$. Fig. 13.2 (a) shows that the x-polarized RF spectrum has two peaks that appear due to the multi-transverse mode character of the VCSEL [Valle 2004]. The multimode character of the system is also clear from the optical spectra of Fig. 13.2 (a). The separation between $LP_{01,x}$ and $LP_{11,x}$ similar to the separation between $LP_{01,y}$ and $LP_{11,y}$, is around 63 GHz.

Fig. 13.2 (b) shows the results of the multi-transverse mode VCSEL subject to two-frequency optical injection. The levels of the injection strengths, Δf, and $\Delta\nu$ are equal to those considered in the single-transverse mode case (Fig. 13.1 (b)). In this way we can compare the performance of microwave generating systems using single and multi-transverse mode VCSELs. Similarly to Fig. 13.1(b), Fig. 13.2 (b) also shows the double injection locking phenomenon. Again, two well defined peaks at the frequencies of ML1 and ML2 are observed in the x-polarized optical spectrum

resulting in a RF spectrum with a narrow peak at the Δf frequency. But Fig. 13.2 (b) also shows and interesting and novel feature when compared to Fig. 13.1 (b): the high-order transverse mode $LP_{11,x}$ is excited with a much larger amplitude than that of the $LP_{01,x}$ mode. The power of both transverse modes oscillate with a phase difference near $\pi/2$. In this way the variation of the total power is nearly sinusoidal, as shown in the time traces and RF spectrum of Fig. 13.2(b). Interestingly, the amplitude of the total power is much larger than the one obtained with the equivalent single-transverse mode VCSEL case illustrated in Fig. 13.1 (b). This shows that the amplitude of the microwave signal generated by two-frequency optical injection is enhanced if multi-transverse mode operation in the VCSEL is considered instead single-transverse mode operation.

We now discuss this enhancement and the tunability of our system. Fig. 13.3 (a) shows the results of the multi-transverse mode VCSEL subject to two-frequency optical injection when increasing Δf and with similar conditions to those of Fig. 13.2 (b). Sinusoidal time traces are obtained for the two power of $LP_{01,x}$ $LP_{11,x}$ modes and total power. The amplitude of the oscillations decreases as Δf increases. We have also included the time trace corresponding to the single-transverse mode power VCSEL to show that the enhancement due to multi-mode operation is maintained. We show in Fig 13.4 (a) the peak-to-peak amplitude of the total power as a function of Δf. Results for single and multi-transverse mode VCSELs, A_{sm} and A_{mm} respectively, are included. Also results for two injection strength levels are shown.

All the cases reported in this figure have an almost sinusoidal variation of the total power. Peak-to-peak amplitudes decrease as Δf increases. An increase of the injection strength κ_S leads to larger peak-to-peak amplitudes for both, single and multi-transverse mode cases. This is also illustrated in Fig. 13.3 (b) in which κ_s is increased with respect to Fig.13.3 (a). For all the values of Δf and κ_s the amplitude of the oscillation obtained with multi-transverse mode VCSEL is larger than that obtained for single-transverse mode VCSELs as it is shown in Fig. 13.4 (a).

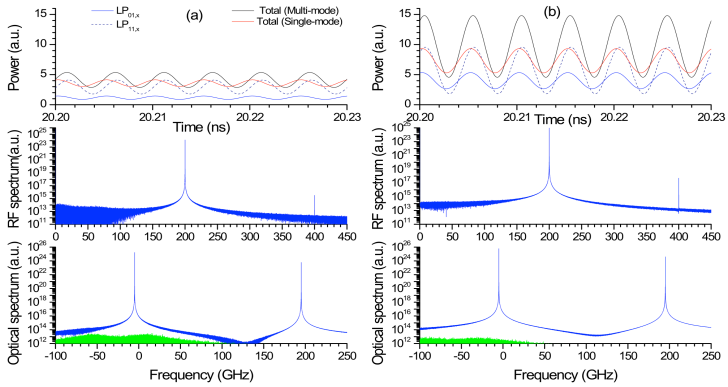

Fig. 13.3. Temporal and spectral dynamics of a multi-transverse mode VCSEL when (a) Δf=200 GHz, κ_S=10^{-2} (b) Δf=200 GHz, κ_S=$3\cdot10^{-2}$. Other parameters are $\Delta\nu$=0 GHz and κ_C= κ_S/2. Upper row. Time traces of the power of the polarized transverse modes and total power. Total power for the single mode case is also included. Middle row. RF spectra of the polarized powers. Lower row: x and *y*-polarized optical spectra.

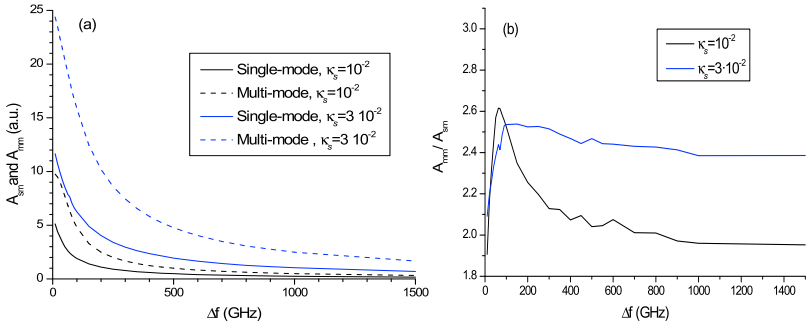

FIg. 13.4. (a) Peak-to-peak amplitude of the total power as a function of Δf. (b) Ratio between peak-to-peak amplitudes obtained with multi-transverse and single transverse-mode VCSELs. In this figure $\Delta\nu$=0 and κ_C= κ_S/2.

This enhancement is quantified in Fig. 13.4 (b) in which the ratio between peak-to-peak amplitudes of the total power obtained for multi and single-mode devices, A_{mm}/A_{sm}, is plotted as a function of Δf. A maximum value of 2.6 is obtained for κ_S=10^{-2} at Δf=63.4 GHz, value that is very near the transverse mode separation. A not so well defined maximum is obtained for κ_S=$3\cdot10^{-2}$ at Δf=100 GHz. These values are near the 63 GHz transverse mode separation

indicating the maximum enhancement is obtained when the optical frequencies of ML1 and ML2 are close to the frequencies of the free-running $LP_{01,x}$ and $LP_{11,x}$ modes, respectively.

Figure 13.4 (a) also shows that the largest variations of peak-to-peak amplitudes with Δf occur in the microwave region (<300 GHz). In Fig. 13.4 we have also considered a Δf range that goes beyond the microwave range. In this region the generated radiation has appreciable amplitude that increases as κ_s is increased. The amplitude of this modulation slightly decreases when Δf is in the THz region. An example of the dynamical evolution obtained for Δf=500 GHz, a value larger than those of the microwave region, is shown in Fig. 13.5 (a). Single and multimode VCSELs are able to respond at 500 GHz with appreciable amplitudes. The response of multimode VCSELs is such that the power of both transverse modes oscillates nearly in phase.

Fig. 13.6 (a) shows the dependence of A_{mn} and A_{sm} on the injection strength κ_s. Results are also given in terms of the injection ratio defined as the ratio of the injected optical power by the *m*-master laser, ($P_{inj,0m}$+$P_{inj,lm}$) versus the output power of the free-running multimode VCSEL. Both A_{mn} and A_{sm} increase with κ_s. Double injection locking is observed when κ_s is larger than $2.5 \cdot 10^{-3}$ and $2.9 \cdot 10^{-3}$ for single and multimode VCSELs, respectively. The curve for multi-transverse mode VCSELs has a small step near $\kappa_s=10^{-2}$ that is due to a sudden change of the phase difference between the power time series of both transverse modes: that phase difference is near π if $\kappa_s \leq 9 \cdot 10^{-3}$ and changes to a value near $\pi/2$ at $\kappa_s=10^{-2}$. Above the κ_s value for which the step in A_{mn} is observed, the ratio A_{mm}/A_{sm}, has an almost constant value of 2.6, as it is shown in Fig. 13.6 (b).

Fig. 13.7 (a) shows the dependence of A_{mn} and A_{sm} on the injection strength κ_c for two different values of κ_s. Both A_{mm} and A_{sm} increase with κ_c. Not that all amplitudes vanish when $\kappa_c \rightarrow 0$. For the single-mode VCSEL with double injection this means that the VCSEL recovers the locked state with single-frequency optical injection

characterized by a constant value of the power. For the two-mode VCSEL the situation can be explained as follows. If only injection from ML1 (ML2) with no coupling to the $LP_{11,x}$ ($LP_{01,x}$) mode is

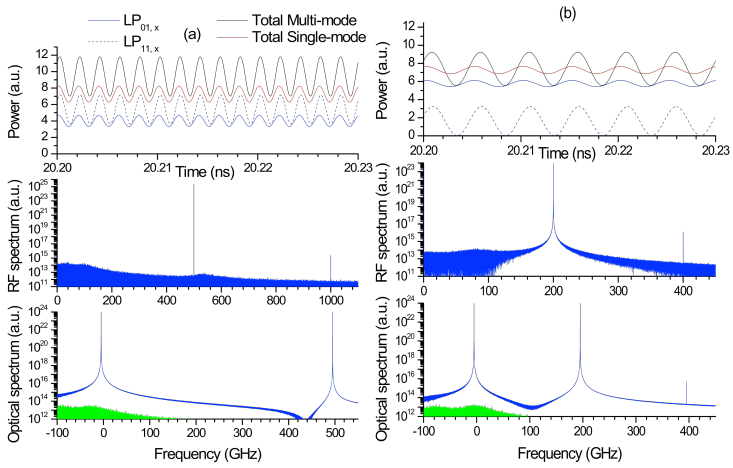

Fig. 13.5. Temporal and spectral dynamics of a multi-transverse mode VCSEL when (a) Δf=500 GHz, κ_S=3·10^{-2}, κ_C=κ_S/2, $\Delta\nu$=0 GHz. (b) Δf=200 GHz, κ_S=3·10^{-2}, κ_C=0.1κ_S, $\Delta\nu$=0 GHz. Upper row: Time traces of the power of the polarized transverse modes. Middle row: RF spectra of the polarized powers. Lower row: x and *y*-polarized optical spectra.

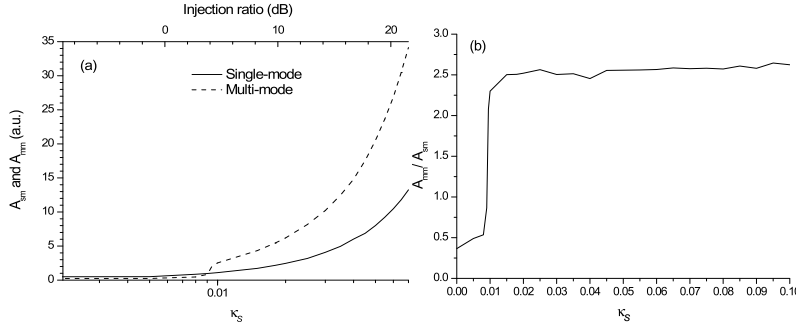

Fig. 13.6. (a) Peak-to peak amplitude of the total power as a function of κ_S. (b) Ratio between peak-to-peak amplitudes obtained with multi and single transverse-mode VCSELs. In this figure κ_C=κ_S/2, Δf=200 GHz, and $\Delta\nu$=0 GHz.

considered, for instance $\kappa_{01}=3\cdot10^{-2}$, $\kappa_{12}=\kappa_C=0$ ($\kappa_{12}=3\cdot10^{-2}$,$\kappa_{01}=\kappa_C=0$) the optical spectrum of the VCSEL consists on a single peak at the ML1 (ML2) frequency, the power of $LP_{01,x}$ ($LP_{11,x}$) is constant and the RF spectrum is flat. If injection from ML1 and ML2 is considered such that $\kappa_{01}=\kappa_{12}=3\cdot10^{-2}$, $\kappa_C=0$, the optical spectrum of the VCSEL consists on two peaks at the ML1 and ML2 frequencies, the powers of both modes, $LP_{01,x}$ and $LP_{11,x}$, are constant and the RF spectrum keeps on being flat. A nonzero value of κ_C is enough for the RF spectrum to develop a peak and for both modes to oscillate at the Δf frequency. This shows that the reason for the transverse modes power oscillations is the nonzero value of the κ_C injection strength.

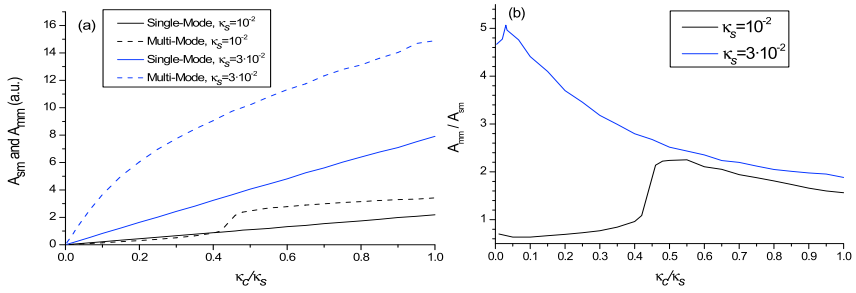

Fig. 13.7. (a) Peak-to peak amplitude of the total power as a function of κ_C/κ_S. (b) Ratio between peak-to-peak amplitudes obtained with multi and single transverse-mode VCSELs. In this figure Δf=200 GHz, and $\Delta\nu$=0 GHz.

Fig. 13.7 (a) shows that for large values of κ_S, $A_{mm}>A_{sm}$. However, for $\kappa_S=10^{-2}$, $A_{mm}\leq A_{sm}$ until the curve for multi-transverse mode VCSELs has a small step near $\kappa_C/\kappa_S=0.42$. This step is again due to a sudden change of the phase difference between the power time series of both transverse modes: that phase difference is near π if $\kappa_C/\kappa_S\leqslant0.4$ and changes to a value near $\pi/2$ at $\kappa_C/\kappa_S=0.45$. Fig. 13.7 (b) shows the ratio A_{mm}/A_{sm} corresponding to data of Fig. 13.7 (a). Larger enhancement of A_{mm} with respect to A_{sm} can be obtained when κ_C is small providing that κ_S is large enough. This situation is illustrated in Fig. 13.5 (b) for which a value of $A_{mm}/A_{sm}=4.3$ is reached.

The dependence of A_{mm} and A_{sm} on the bias current of the

VCSEL is also analyzed in Fig. 13.8 (a). Both quantities increase with the bias current. However the ratio A_{mm}/A_{sm} slightly decrease in a linear way with *I*. For instance, when $\kappa_s=3\cdot10^{-2}$, it goes from 2.6 at $I/I_{th}=1.2$ to 2.2 at $I/I_{th}=8$. We have also analyzed the effect of the frequency detuning, $\Delta\nu$ on the dynamics of the system. Dynamics obtained for the multimode case when $\Delta\nu$=5 GHz, and $\Delta\nu$=-5 GHz are very similar to those obtained when $\Delta\nu$=0 GHz, providing that the system is in the double injection locked regime. This indicates that there is an appreciable range of $\Delta\nu$ for which the enhancement of the amplitude of the generated microwave signal due to high-order transverse mode excitation does not depend on the $\Delta\nu$ value. The relative phase between the power time series corresponding to the $LP_{01,y}$ and $LP_{11,y}$ modes in the double-injection locked multi-transverse mode VCSEL can change depending on the injection conditions. Comparison between Fig. 13.3 (a) and Fig. 13.3 (b) indicates that it decreases as the value of the κ_s injection strength increases. We have also calculated the RF linewidths of the signals generated by double-injection locking of multi-transverse mode VCSELs. In this paper most spectra have been calculated with a temporal window of 1.05 μs and with a maximum frequency of 2000 GHz. Then linewidths are measured with a 0.95 MHz frequency resolution.

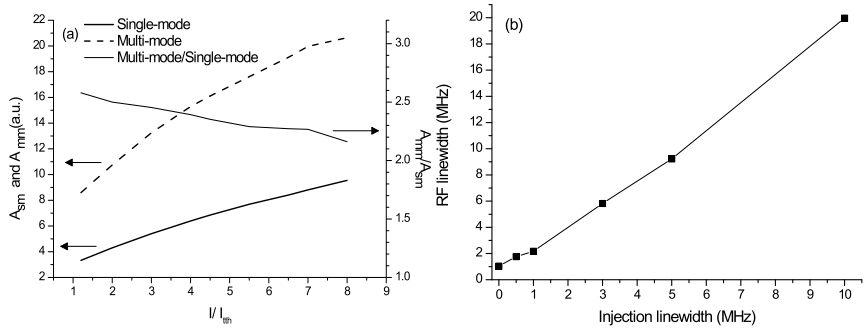

Fig. 13.8. (a) Peak-to-peak amplitude of the total power as a function of I/I_{th} when Δf=200 GHz and $\kappa_s=3\cdot10^{-2}$ (b) RF linewidth as a function of the linewidth of the master lasers when Δf=100 GHz and $\kappa s=10^{-2}$. In this figure $\kappa_C=\kappa_s/2$ and $\Delta\nu$=0GHz.

We have considered in our calculations a finite linewidth of the optical spectrum of both master lasers. This effect has been included by considering phase fluctuations in the two external signals as in Ref [Wieczorek 2009]. Equal linewidths and independent phase fluctuations have been considered for both master lasers. 3-dB RF linewidths are shown in Fig. 13.8 (b) as a function of the linewidth of the optical spectrum of one of the MLs. Narrow linewidths, in the MHz range, are demonstrated like in [Juan 2011]. In all the RF spectra the obtained sidemode suppression ratio has been more than 50 dB, like in [Juan 2011]. The second largest peak is the first harmonic corresponding to the peak that appears at Δf.

13.4. Discussion and conclusions

Peak-to-peak amplitudes in this chapter have been given in the arbitrary units used in the spin-flip model [MartinRegalado 1997b]. Our aim in this chapter has been to give qualitative trends of those amplitudes. Then we have not focused on giving their precise values. An idea of the magnitude of the power corresponding to the peak-to-peak amplitudes obtained in this work can be obtained by taking typical values of the power emitted by a VCSEL with 12 μm diameter like the one simulated in this paper. For instance, for a typical value of the total power ~0.4mW for I/I_{th}=1.8, A_{mm} (mW)=0.235 A_{mm} (a.u.). For the conditions of Fig. 13.2(b) this corresponds to a 1.1 mW peak-to-peak amplitude for 1.17 mW of power injected by each ML.

The model that we have used includes the polarization degree of freedom of transverse modes. In our case the role played by y-polarized transverse modes has been negligible because we have considered an optical injection that is parallel to the x-polarization of the solitary VCSEL. The extension of this model to consider orthogonally polarized optical injection is straightforward and should be interesting for knowing if the results obtained in this work are maintained. Experimental results obtained in the previous

chapter points out in this direction because they show that double injection locked state is observed when a multi-transverse mode VCSEL is subject to orthogonal optical injection from a similar VCSEL. This would be of interest to show that the proposed microwave signal generation system is independent on the polarization of the master lasers.

Fig. 13.4 shows that a typical increase in the amplitude obtained with multimode VCSELs with respect to single-mode VCSELs is between 2 and 3. We discuss now the corresponding increase in the maximum frequency of the generated microwave signals. Assuming that amplitudes larger than a value A are required, we calculate the maximum value of the microwave frequency obtained with the single-mode VCSEL, $\Delta f_{max,sm}$, such that $A_{sm}>A$ if $\Delta f \leq \Delta f_{max,mm}$. We also calculate the corresponding quantity for the multimode VCSEL, $\Delta f_{max,mm}$, given by $A_{mm}>A$ if $\Delta f< \Delta f_{max,mm}$. Fig. 13.9 shows the results for A=4 a.u. as a function of the injection strength or the injection ratio. The maximum frequency increases significatively when using multimode VCSELs instead of single-mode VCSELs. For instance the maximum frequency increases from 193 GHz to 578 GHz for an injection ratio of 14 dB.

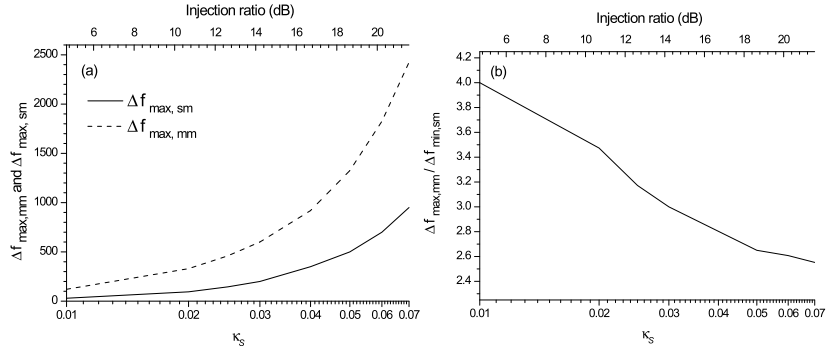

Fig. 13.9. (a) Maximum frequency of the generated microwave signals as a function of the injection strength. (b) Ratio of the maximum frequencies obtained with multimode and single-mode VCSELs. In this figure A=4 a.u., $\kappa_C=\kappa_S/2$ and $\Delta\nu$=0 GHz.

Summarizing, in this chapter we have made a theoretical study

of the dynamical properties of single and multi-transverse mode VCSELs when they are subject to two-frequency optical injection. We have focused our analysis in the double injection locking observed at large injection strengths, useful for photonic microwave signal generation. Numerical simulations of single and multi-transverse mode VCSELs have shown that the double injection locking can be obtained when these devices are subject to two frequency optical injection. For the case of multimode VCSELs we have shown that the response of multi-transverse mode VCSELs under two frequency optical injection is larger than that obtained with similar single-transverse mode VCSELs. In this way high order transverse mode excitation enhances the performance of the photonic microwave generation system based on two-frequency optical injection. This shows that while for single-frequency injection, excitation of a second mode is detrimental for generating microwave signals [Qi 2011], for two-frequency injection, excitation of a second mode is beneficial. Narrow linewidths are demonstrated in our system. Wide tuning ranges, extended into the THz band, are obtained in our system. A more realistic study of the extension into this band would require the inclusion in the model of the dynamical evolution of the macroscopic polarization of the quantum well media, as done for instance in [Javaloyes 2010]. The maximum frequency of the generated microwave signals can be substantially increased if multimode VCSELs are used instead of single-mode VCSELs.

CHAPTER 14

Conclusions and future work

Vertical-Cavity Surface-Emitting Lasers (VCSELs) are very promising light sources for all-optical signal processing due to their inherent advantages (low threshold current, circular output-beam profile, easy of fabrication of 2-D arrays, low cost, etc.). Optical injection in semiconductor lasers and in particular in VCSELs has been a subject of interest in recent years due to it is an attractive method to obtain bistable behavior and nonlinear switching. It is useful in applications whose operation principle would be based in the width of the appearing hysteresis cycles associated to the bitability, such as all-optical bistable flip-flops or bistable memory elements, etc. Also optical injection can be used to reduce the laser linewidth, the mode partition noise, or for enhancing the modulation bandwidth without modifying the semiconductor laser design.

Studies of nonlinear dynamics of optically injected semiconductor lasers have been extended to VCSELs since these

devices offer additional degrees of freedom, like the presence of multiple transverse modes and the not so well defined direction of the emitted polarization, when compared with their edge-emitting counterparts. Usually two different configurations for optical injection in VCSELs have been used. The first is known as the orthogonal optical injection configuration: linearly polarized light is injected with a polarization that is orthogonal to the linear polarization of the solitary VCSEL. The second is known as "parallel optical injection", where both the optical injected signal and the VCSEL have parallel linear polarizations. Nonlinear dynamics of VCSELs under orthogonal optical injection has been experimentally and theoretically analyzed for 850 and 1550 nm wavelength devices. Rich nonlinear dynamics, including period doubling, quasiperiodicity, injection locking, irregular behavior, and bistability have been found in short- and long-wavelength devices. Nonlinear dynamics of optically injected semiconductor lasers is interesting from a practical point of view because the period one oscillation state is one of the potential candidates for carrying message in a radio-over-fiber (RoF) system.

In this thesis our aim has been the study of the polarization switching, optical bistability and nonlinear dynamics for VCSELs when they are subject to optical injection.

In chapter 5, we have performed an experimental investigation of the relative intensity noise (RIN) spectra of multimode 1550 nm VCSELs. For a VCSEL which emits in two transverse modes, being both modes linearly polarized and having parallel polarizations, two resonance peaks appear in the noise spectra of the individual modes and total power. Qualitative dependence on those spectra on the bias current is similar to that found in previous theoretical works. For a VCSEL with three different transverse mode emission at large bias currents. The behavior is similar to the VCSEL with two transverse modes while the bias current is small, but when the bias current increases, additional peaks appear in the noise spectra. We believe that the

polarization and the higher-transverse mode rotational instabilities can play an important role in determining the structure of noise spectra in the three transverse mode regime.

In chapter 6, we have studied the polarization switching obtained in single-mode long-wavelength VCSEL subject to orthogonal optical injection. The injected power required to achieve PS is measured as a function of the frequency detuning . We have also analyzed the frequency induced polarization bistability when the injected power is around a few hundred μW and also when the injected power is increased up to a few mW. Later on, we have studied the bistability properties of the PS when we change the injected power for a fixed injected wavelength, the so called: power induced polarization bistability. Finally, we have made a theoretical study about PS and the associated bistability.

The main results in this chapter are that the injected power for PS exhibits a minimum at negative frequency detuning and a plateau at a positive detuning with respect to frequency detuning. We have also found the existence of windows where the PS disappears and then appears again. Bistable behavior of the polarization is found.

The results for the frequency induced polarization bistability show that when the injected power is low two bistable regions appear, one of them appears at short wavelength and the other one appears at long-wavelength. The widths of both bistable regions are similar and nearly independent of the injected power. The width of the region where PS takes place is shown to increase as the injected power is increased. When the injected power is high, a third bistability region appears at longer wavelength. The frequency width of this region can go beyond 37 GHZ, more than seven times larger than previously measured values.

Three different shapes of polarization bistability, including anticlokwise, X-shape and clockwise have been observed for power induced polarization bistability. Wide hysteresis cycles up to

four times higher than previously reported results have been found.

Finally, we have studied theoretically the PS appearing in these VCSELs under orthogonal optical injection finding in general, a good qualitative agreement with our experimental results. Furthermore, we have studied theoretically the wavelength-induced polarization bistability for low injected power. Two bistable regions have been found for both SW and LW PSs. We find that the widths of both bistable regions are similar and nearly independent of the injected power.

In chapter 7, we have reported an experimental study of the nonlinear dynamics appearing in a 1550 nm single-mode VCSEL subject to parallel and to orthogonal optical injection. A rich variety of nonlinear behaviors, including periodic (limit cycle, period doubling) and chaotic dynamics have been experimentally observed. For the orthogonal optical injection we have presented a theoretical study of the polarization and time resolved nonlinear dynamics. Special attention has been paid to the correlation properties of both linear polarizations emitted by the VCSEL.

For negative (positive) frequency detunings, we have obtained anticorrelated (correlated) operating regimes. We explain this behavior because there is a dynamics of competence between polarizations for $\Delta\nu<0$ while that dynamics disappears when $\Delta\nu>0$. For $\Delta\nu>0$, we have usually found that orthogonal polarization is the only polarization that contributes to the dynamics of the total power. Only correlated periodic dynamics in both linear polarizations has been found near the border of the periodic region, when the bias current is large and optical injection strength is small. For negative frequency detuning values, the correlation properties change because we find anticorrelated dynamics in both linear polarizations. This dynamical regime is characterized by a larger influence of nonlinear effects that produce anticorrelated trains of pulses in both linear polarizations. These trains of pulses have been characterized by the average and dispersion of the interpulse time thats increase as the injected power is increased.

We have also shown that the appearance of broad power spectra that characterizes the irregular dynamics is related to large values of the dispersion of the interpulse time. We have also analyzed the relative phase between the oscillations observed in the time traces of the optical power of both polarizations. Good qualitative agreement has been demonstrated between theory and experiment.

All-optical processing of high speed signals is expected to be a key technology in future photonic networks. Optical injection can be used to obtain polarization switching and polarization bistability in single transverse mode VCSELs. Based on the mechanism of PS high-speed all-optical signal regeneration and all-optical flip-flop memories have been reported.

In chapter 8, we have experimentally demonstrated all-optical inversion using PS of a long-wavelength single mode VCSEL. The dynamic behavior of the all-optical inverter under low and high frequency optical inputs has been analyzed. Experimental results show that the rise time of the parallel polarized power is much larger than the fall time of the parallel polarization. This suggests that the operation speed of the all-optical inverter is limited by the rising edges of parallel polarized pulses. A possibility to avoid that limitation is to consider small bias current values. However, the advantage of a small rise time are overshadowed by the small extinction ratio for the parallel polarized power obtained in that case. An increase of the injected optical power does not seem to solve the problem because the rise time decreases very slowly with the injected power. Nevertheless, our results show that all optical inversion can be obtained with a 2.5 Gb/s NRZ input signal with a particular 32-bit word modulation. The orthogonal polarization output shows unwanted spikes that degrade the response of the system for all optical gating operation. These results suggest that the use of orthogonal polarization to obtain all-optical gating would suffer from pattern dependent error-rate degradation.

In conclusion, the PS based all-optical inverter has been

demonstrated with a 2.5 Gb/s NRZ input signal. These results show that polarization switching in VCSELs can be useful mechanism for high-speed optical signal processing applications.

As we have already mentioned PS and transverse mode selection in VCSELs induced by external optical injection make these devices suitable for all-optical flip-flop and buffer memory operation finding then applications in all optical signal processing and optical computing.

In chapter 9, we have experimentally studied, the selection of the fundamental transverse mode of a 1550-nm multimode VCSEL induced by parallel optical injection. We have demonstrated that this selection is obtained for the VCSEL used in our experiments which is characterized by a free-running emission in two transverse modes both with parallel polarizations. The selection of the fundamental mode is accompanied by locking of that mode to the optically injected signal.

We have measured the injected power needed to select the fundamental mode as a function of the VCSEL current. In agreement with previous theoretical results, we have experimentally demonstrated that the selection of the fundamental mode by optical injection is possible for small enough values of bias current. We have also shown, again in agreement with theory that the injected power needed for modal selection grows monotonically as the VCSEL current is increased. The injected power needed for fundamental mode selection shows a minimum when measured as a function of the optical injection wavelength. The modal selection process induced by optical injection exhibits a bistable behavior. The minimum injected power and the wavelength detuning at which the selection of the fundamental mode is achieved increase with the bias current. Wide hysteresis cycles are attained when the wavelength of the optically injected signal is longer than λ_{min} and the width of the bistable region grows linearly as the wavelength of the injected signal is increased. Selection of the higher order transverse mode is

also achieved by using an optical injection of wavelength close to that of the higher order transverse mode.

In chapter 10 we have reported the experimental observation of polarization bistability in each of the transverse modes of a 1550 nm multimode VCSEL when subject to orthogonal optical injection. We have studied in detail the injected power requirements for polarization bistability. Very wide hysteresis cycles have been obtained for both transverse modes when the frequency detuning has large and negative values. The multimode emission property of the VCSEL adds new functionalities to the system in comparison to previous studies in single transverse mode devices. A squared shape with very high on-off contrast ratio and very wide associated hysteresis cycle has been measured for the I/O power characteristics of the parallel polarized high-order transverse mode. This promising result offers potential for the use of multimode VCSELs operating at 1550nm as low cost and low power consuming components for all-optical signal processing applications, such as all optical inversion and all-optical signal regeneration, in long haul optical networks.

Single-mode VCSEL-by-VCSEL optical injection locking has been recently studied as a first step for obtaining integrated low-cost high-speed communications modules. In most studies on optical injection, the injected signal comes from an external laser that operates with a single frequency. Much less attention has been paid to the injection of more than one frequency. Since optical injection changes the coupling characteristics between the electric field in the laser cavity and the charge carriers, the dynamics of a laser subject to more than one injected frequency is expected to be more complicated. Given the recent efforts in studying VCSEL by VCSEL optically injection locked systems, it is necessary to understand polarization dynamics in such a system.

Throughout this, in chapter 11, we have studied the effect of orthogonal optical injection when a multimode VCSEL emitting at 847 nm receives a single frequency injected signal provided by

another VCSEL of the same model. The birefringence parameter is around 8 GHz, a value, much smaller than the birefringence of the lasers used in previous chapters. The output from the master VCSEL is single frequency with the beam profile of the fundamental mode. The receiver VCSEL operates with four transverse modes. In contrast to previous chapters a free-space setup has been used.

Our results reveal that when the strongest mode of the receiver VCSEL, the TEM_{01} mode, is frequency-locked to the injection, polarization switching is achieved in the TEM_{01} mode as well as the other strong modes. This leads to polarization switching in the total output power of the receiver. The results imply that spatial overlapping and modal intensities play important roles in the modal polarization switching of the fundamental mode and of the TEM_{10} mode. We have identified three types of instabilities outside the modal polarization switching regime and proposed physical mechanisms for some of them.

In chapter 12 we have studied experimentally the effect of two-frequency orthogonal optical injection on a short-wavelength multimode VCSEL. The injected signal comes from another multi-transverse mode VCSEL. Our results show that with this injection, can induce PS in the total power of a multi-transverse mode VCSEL. This extends injection-induced PS to multi-transverse mode regime of both receiver and transmitter. The feature that the width of modal PS regime is different can be used for transverse mode selection. Double injection locking involving two transverse modes has been obtained in VCSELs subject to two frequency orthogonal optical injection. Instabilities include unstable PS when the three modes do not switch simultaneously and periodic oscillations before the receiver enters the stable PS regime.

Nonlinear dynamics of optically injected semiconductor lasers can also be used for photonic microwave generation. Compared with conventional microwave generation by electronic circuitry with multiple stages of frequency doubling, photonic microwave signal generation have the advantages of lower cost, longer

transmission distance, higher speed, low power consumption, less system complexity and the ability to generate tunable microwave signals with higher frequencies. Photonic microwave generation find applications in radio-over-fiber (RoF) technology that holds great promise for 4G mobile communications systems.

In chapter 13, we have made a theoretical study of the dynamical properties of single and multi-transverse mode VCSELs when they are subject to two-frequency optical injection. We have focused our analysis in the double injection locking observed at large injection strength, useful for photonic microwave signal generation. Our calculations have shown that double injection locking involving the two transverse modes can be obtained in these systems.

We have shown that the higher-order transverse mode is excited with a much larger amplitude than that of the fundamental transverse mode. The comparison with the case of a similar single-transverse mode VCSEL subject to the same two-frequency optical injection shows that the extra degree of freedom given by the multi-transverse mode operation of the VCSEL is useful for enhancing the performance of the photonic microwave generation system. In fact we have obtained that the amplitude of the total power generated by multi-transverse mode VCSELs is much larger than that obtained with a similar single-transverse mode VCSEL subject to the same two-frequency injection. This shows that while for single-frequency injection, excitation of a second mode is detrimental for photonic generation of microwave signals, for two-frequency injection, excitation of a second mode is beneficial. Wide tuning ranges, into the THz region, and narrow linewidths are also demonstrated in our system.

Throughout this thesis there are several open questions which need further work and some of them suggest new research lines.

In chapter 6, we have studied the bistability properties of the polarization switching in a single-mode 1550-nm VCSEL subject to

orthogonal optical injection and we found three different types of frequency-induced polarization bistability. Theoretical work will be performed in order to obtain a model able to explain the three forms of bistability. We have also studied the injected optical power required for PS as a function of the frequency detuning between the injected light and the orthogonal linear polarization of the VCSEL theoretically and experimentally. In general, a good overall qualitative agreement has been found between our theoretical and experimental results. However, the experimental results have not confirmed the theoretical predictions of the existence of windows where the PS disappears for positive values of detuning. Future work will be devoted to extract the working parameters of our VCSELs in order to improve the theoretical description of our experiments.

Besides, we have studied the selection of the fundamental transverse mode of a multimode VCSEL induced by parallel optical injection. Future work will be devoted to the simultaneous measurement of the selection and locking processes for different wavelength detunings and bias currents. In this way, the parameter regions in which selection and locking coincide will be determined.

We have also analyzed the effect of orthogonal optical injection when a multimode VCSEL emitting at 847 nm receives a single frequency injected signal provided by another VCSEL of the same model using a free-space setup. Dynamic analysis more comprehensive would be desirable in our system for a better understanding of the physics and bifurcations.

Finally, we have proposed a new theoretical method to generate microwave signals using a multi-transverse mode VCSEL subject to two- frequency optical injection. It would be desirable to do some experimental work to check our theoretical predictions and also more theoretical and experimental studies to know the nonlinear dynamics outside the double injection locking region.

APPENDIX A

Specifications of the experimental equipment

Optical Spectrum Analyzer (Anritsu MS9710B)

Fiber	10/125 μm SM fiber
Optical connector	FC-APC
Wavelength	Range: 600 to 1750 nm Accuracy: ±0.05 nm(1530 to 1570 nm, resolution: 0.07 to 0.2 nm, after calibration with wavelength reference light source option) Stability: ±5 pm Resolution: 0.07, 0.1, 0.2, 0.5, 1 nm Resolution accuracy: ±⩽7% (resolution: 0.1 nm, 1550±20 nm), ±⩽30% (resolution: 0.1 nm, at other wavelength)
Level	Measurement range: -90 to +10 dBm (1250 to 1600 nm, +10° to +30°C, VBW: 10 Hz, sweep averaging: 10 times) Accuracy: ±0.4 dB
Polarization dependency	±0.05 dB (1.55 μm band, resolution: ⩾0.5 nm), ±0.1 dB (1.3 μm band, resolution: ⩾0.5 nm)

Optical return loss	⩾35 dB (1.3/1.55 μm band)
Dynamic Range	70 dB(±1 nm, resolution: 0.07 nm, 1.55 μm band, high-dynamic range mode measurement, 20° to 30° C)
Operating conditions	operating temperature: 0° to 50° C

VBW	10 Hz	100 Hz	1 kHz	10 kHz	100 kHz	1 MHz
Sweep speed (typ.)	30 s	5s	0.5 s	0.5 s	0.5 s	0.5 s
Minimum light reception sensitivity	-90 dBm	-80 dBm	-70 dBm	-60 dBm	-50 dBm	-40 dBm

Table 1. Specifications for the Optical Spectrum Analyzer.

Tunable laser (Anritsu tunable laser Tunics Plus)

Tuning Characteristics	Absolute wavelength accuracy	±0.04 nm
	Wavelength stability	±5 pm/h
	Tuning repeatability (typ.)	±0.005 nm
	Wavelength setting resolution	0.001 nm
	Optical frequency fine tuning	± 2 GHz
	Tuning speed (typ.)	1s (100 nm)
Laser Output Characteristics	Power stability	±0.01 dB/h
	Side mode suppression ratio	> 45 dB
	Signal to source spontaneous-emission ratio	> 55 dB

Laser Output Characteristics	Relative intensity noise	-145 dB/Hz (typ.)
	Spectral Width (FWHM)	150 kHz (typ.)
Sweeping Mode Characteristics	Scan Speed	Adjustable from 1 to 100 nm/s
	Power repeatability from scan to scan (typ.)	±0.05 dB
	Optical connector	FC-APC
	Output fiber	SMF-28™
	Output isolation	35 dB
	Return loss	60 dB
Environment	Operating temperature range	+15° to +30° C

Table 2. Specifications for the Tunable Laser.

Oscilloscope (Agilent Technologies 54855A DSO Infiniium Oscilloscope)

Vertical

Analog bandwidth (-3 dB)	6 GHz
Input channels	4
Rise time (10% to 90%)	70 ps
Input impedance	$50\Omega \pm 2.5\%$
Sensitivity	1 mV/div to 1 V/div
Vertical resolution	8bits, 12 bits with averaging
Channel to channel isolation (any two channels with equal V/div settings)	DC to 100MHz: 40 dB 100 MHz to 1 GHz: 28 dB > 1 GHz to 6 GHz: 24 dB
DC gain accuracy	±1% of full scale at full resolution channel scale

Horizontal

Main sweep time scale range	5 ps/div to 20 s/div

Acquisition

Real time sample rate per channel	20 GSa/s
Memory depth per channel	
Standard	262,144 at all sample rates
Option 001	1,025,000 at all sample rates 32,800,000⩽2 GSa/s sample rate
Sampling modes	
Real time	Succesive single-shot acquisitions
Real time with averaging	Selectable from 2 to 4096

Measurements

FFT	
Frequency resolution	Sample rate/ memory depth=Resolution
Frequency accuracy	20 GSa/1Mpts=20 kHz

Table 3. Specifications for the Oscilloscope.

High resolution optical spectrum analyzer (Aragon Photonics BOSA 210)

Parameter	Specified value
Optical Resolution (@ 3dB)	80fm (10MHz @ 1550nm)
Wavelength Range	1528-1565 nm
Wavelength Repeatability	±1pm
Wavelength Accuracy	±1.5pm (@1550 nm)
Dynamic Range	>80 dB
Power Range	+10 to -70 dBm

Sensitivity	-70dBm/0.1 pm
Power Accuracy	±1.5 dB
Maximum Safe Total Input power	+20 dBm
Polarization Dependence	±0.5 dB
TL output power	5 dBm
Optical Input/Output	SFM; FC/APC
Power Requirement	100/110/220v, 50/60 Hz
Measurement time	1s for 10 nm
Maximum Power Consumption	140 W
Operating Temperature	+15° C to +35° C

Tunable laser output

Wavelength range	1515-1565 nm
Absolute accuracy	± 1.5 pm
Tuning speed	1-100 nm/s
Output power	4-8 dBm
Side-mode suppression	>43 dB
Relative intensity noise	< -145 dB/Hz
Laser Linewidth	<1 MHz

Table 4. Specifications for the BOSA.

Fiber Fabry-Perot Tunable Filter (Micron Optics FFP-TF2)

Mechanical Properties

Connector	FC/APC

Optical properties

Operting Wavelength Ranges	1520-1620 nm
Free Spectral Range (fixed FSR but selectable within this range)	100 to 45000 GHz (800 pm to 360 nm at 1550 nm)
Standard Finesse Values	10,40,100,200,500
3dB Bandwidth	Equals desired FSR/Finesse
Insertion loss	<1.5 dB
Polarization dependent loss	<0.2 dB
Input power (Maximum)	<100 mW (for finesse <200)
Glitch free dynamic range (GFDR)	>15 dB

Table 5. Specifications for the Fabry-Perot Interferometer.

Tunable filter controller (Micron Optics FFP-C)

Optical Properties

Input Power	-50 to -10 dBm
Input connector	FC/SPC
Detector wavelength Range- InGaAs	1000-1650 nm

Electrical Properties

Bias Tuning Voltage	5-55V
Ramp Frequency	20-100 Hz
Ramp Amplitude	5-55V
Dither Frequency	1.5-2.5 kHz
Power Supply, 15W	8-12 mV

Table 6. Specifications for the Tunable Filter Controller.

Microwave Spectrum Analyzer (Anritsu MP1800A)

Typical performance

Frequency Range	9 kHz to 20 GHz
Tuning Resolution	1 Hz
Dynamic Range	100 dB
Amplitude Accuracy	± 1.0 dB to 20 GHz
Sweep Speed	200 ms in 10 MHz Span
Attenuation Range	65 dB, 5 dB Steps

Amplitude Settings

Attenuator Range	0 to 65 dB
Attenuator Resolution	5 dB steps
Display Range	1 to 15 dB/div in 1 dB steps

Resolution and Video Bandwidth

Resolution Bandwidth	1 Hz to 3 MHz
Video Bandwidth	1 Hz to 3 MHz

Table 7. Specifications for the Microwave Spectrum Analyzer.

Fiber Optical Isolator (ISC-1550 Newport)

Specifications

Fiber Type	SFM-28
Operating wavelength (nm)	1550 nm
insertion loss (dB)	0.33 dB
Isolation (dB)	34 dB
Polarization dependent loss (dB)	0.04 dB

Polarization mode dispersion (ps)	⩽0.25 ps
Return loss, dB (input/output)	> 60/55 dB

Table 8. Specifications for the Fiber Optical Isolator

Polarization Beam Combiner/Splitters (Newport F-PBC-15-SM-FA)

Description	**Testing Data**	
	Port 2 - Port 1	Port 3 - Port 1
Insertion Loss (dB)@ 1550 nm (with connectors)	0.63	0.88
	Port 1- Port 2	Port 1- Port 3
Extinction Ratio (dB)	24	26
Return Loss (dB)	> 55	
Operating Wavelength (nm)	1550	
Operating Bandwidth (nm)	± 30	
Maximum Optical Power	500 mW	
Fiber type	Port 1 (Common Port) is SMF, Port 2 and Port 3 are PM Panda.	

Table 9. Specifications for the Polarization Beam Combiner/Splitters.

Fiber U-Bench Polarization controller (Thorlabs FBR05)

Fiber type	Single Mode
Fiber Optic Connector	FC/APC
Insertion Loss (dB)	0.5 typical

Return loss (dB)	55
Polarization Extinction Ratio (dB)	40
Operating wavelength (nm)	1260-1650

Table 10. Fiber U-Bench Polarization Controller

Fiber Optic Circulators

Parameters	Specification	Test Data
Center Wavelength (nm)	1550	1550
Operating Wavelength Range (nm)	±30	±30
Max. Insertion Loss Port 1 to 2 +0.3dB connector loss (dB)	1.2	0.91
Max. Insertion Loss Port 2 to 3 +0.3dB connector loss (dB)	1.2	0.99
Min. Isolation Port 2 to 1 (dB)	40	47
Min. Isolation Port 3 to 2 (dB)	40	48
Min Extinction ratio (Port 1 to 2 / Port 2 to 3)-2dB connector loss (dB)	20	25/29
Min. Return Loss -5 dB connector loss (dB)	50	60
Max. Optical Power (mW)	300	
Max. Tensile Load (N)	5	
Operation Temperature (°C)	-5 to 70	
Fiber Length (m)	-40 to 85	
Connector type	FC/APC	
Fiber Type	900 µm loose tube Panda Fiber	

Table 11. Specifications for the polarization maintaining optical circulator

Parameter	Test Data	
Wavelength (nm)	1550	
Insertion Loss (dB)	Port 1---> 2	0.44
	Port 2---> 3	0.49
Return Loss (dB)	Port 2---> 1	59
	Port 3---> 2	59
ISO (dB)	Port 2---> 1	54
	Port 3---> 2	59
Directivity (dB)	Port 1---> 3	60
Connector Type	FC/APC	

Table 12. Specifications for the non-polarization maintaining optical circulator.

Tunable Bandpass Fiber Optic Filter (Newport TBF-1550-1.0)

Specifications

Model	TBF-1550-1.0
Fiber Type	9/125µm Single Mode
Operatig Wavelength	1550 nm
Insertion Loss, Maximum (dB)	3.0
Back-reflection, Maximum (dB)	3.0
Back-reflection, Maximum (dB)	-50
Polarization Dependent Loss, Typical (dB)	0.05, typical at 1565 nm; 0.3 at 1535 nm

Wavelength Tuning Range	1535 to 1565
Thermal limit (dB/°C)	0.005
Tuning resolution, typical (nm)	0.05
0.5 dB Bandwidth, typical (nm)	1.0

Table 13. Specifications for the Tunable Bandpass Fiber Optic Filter.

Amplified Fiber Optic Photo Detector (PDA8GS by Thorlabs)

Detector	InGaAs Pin
Spectral Response (nm)	700-1650
Peak Response typ (A/W)	0.9 at 1550 nm
Rise/Fall Time (ps)	<50
Input	FC bulkhead fiber connector
Optical return loss (dB)	-14
Bandwidth (GHz)	DC-8 (min)
Digital Capability (Gbs)	10.7
Operating Temp	0 to 40 °C
Transimpedance Gain	500 into 50 Ω
Input Fiber (µm)	62.5 multimode
Maximum optical input power (mW)	1.0 CW

Table 14. Specifications for the Amplified Fiber Optic Photo Detector.

Single Mode, Variable Fiber Optical Attenuators: Inline (VOA50-APC Optical Attenuator by Thorlabs)

Operating wavelength (nm)	1200 to 1600

Fiber	SMF-28 e+ or equivalent, 1m per side
Attenuation Range (dB)	1.5-50
Attenuation Resolution (dB)	⩽ 0.1
Back Reflection (Return Loss) (dB)	> 55
Polarization Sensitivity (dB)	⩽ 0.2
Optical power (mW)	⩽ 300
Thermal Stability (dB/°C)	⩽ 0.03
Operating Temperature (°C)	0 to 60

Table 15. Single Mode, Variable Fiber Optical Attenuators

Optical Fiber 50/50 Coupler (Newport F-CPL-F12155)

Type	1x2 WF
Fiber type	single mode
Operating Wavelength (nm)	1550
Return Loss	55 dB
Insertion Loss, maximum	3.4 dB
Bandwidth	± 40 nm
Polarization Dependent Loss, Typical	0.1

Table 16. Specifications for Optical Fiber Coupler.

90/10 Coupler (Thorlabs 10202A-90-FC)

Center wavelength (nm)	1550
Change in wavelength (nm)	±40
Coupling ratio	90:10
Insertion Loss	12.7/0.8

Excess Loss (dB)	0.2
Polarization Dependent Loss (dB)	<0.15
Directivity (dB)	>60
Connector	FC/PC

Table 17. Specifications for 90/10 Coupler.

APPENDIX B

List of abbreviations

BS	Nonpolarizing beamsplitter
CCD	Charge coupled device camera
EEL	Edge-Emitting laser
EH	Hybrid Electric mode
FC	Fiber coupler
FFP	Fiber Fabry-Perot
FP	Fabry-Perot optical spectrum analyzer
FSR	Free Spectral Range
HE	Hybrid Magnetic mode
HH	Heavy Hole
HWP	Half-wave plate
ISO	Optical Isolator
ML	Master Laser
NDF	Neutral density filter
NRZ	Non-Return-To-Zero
OSA	Optical Spectrum Analyzer
PB	Polarization bistability
PBS	Polarization Beam Splitter
PC	Polarization Controller
PD	Photodetector

PM	Power Meter
PS	Polarization Switching
PZT	Piezoelectric element
QW	Quantum well
RMS	Root mean square
LCP	Left circularly polarized light
LH	Light Hole
LW	Long-wavelength
MBE	Molecular beam epitaxy
MOCVD	Metalorganic chemical vapor deposition
NDF	Neutral density filter
RCP	Right circularly polarized light
RIN	Relative intensity noise
SBS	Stimulated Brillouin Scattering
SFM	Spin Flip Model
SHR	Shockley-Read-Hall recombination
SMSR	Side Mode Suppression Ratio
SW	Short-wavelength
TE	Transverse Electric mode
TL	Tunable Laser
TM	Transverse Magnetic mode
VCSEL	Vertical-Cavity Surface-Emitting Lasers

Appendix C

Resumen en Castellano

Los láseres de semiconductor conocidos como VCSELs (láseres de cavidad vertical emisores de superficie) aparecen como una de las fuentes láser del futuro debido a sus excelentes prestaciones. Entre sus múltiples ventajas destacan: costes reducidos de fabricación, alta eficiencia de acoplamiento a fibras ópticas debido a su haz circular, baja divergencia, fabricación en arrays 2D, operación monomodo longitudinal y baja corriente umbral entre otras. Además de todo ésto, los dispositivos actuales están siendo fabricados con tiempos de vida de más de un millón de horas. Estas ventajas hacen a los VCSELs candidatos ideales para su uso como fuentes estables en las redes de telecomunicaciones ópticas presentes y futuras. Sin embargo, no pueden emitir más de unos pocos mW de potencia debido al pequeño tamaño de la región activa. Por esta razón son principalmente usados en redes de área local y metropolitana. Hoy en día, la tecnología permite diseñar VCSELs que operan en un amplio rango de longitudes de onda extendiéndose desde los 650 a los 1600 nm.

Los VCSELs, como mencionamos anteriormente, operan en régimen monomodo longitudinal y por lo general muestran características complejas de polarización y de dinámica multimodo transversal. Mientras la emisión en varios modos transversales suele atribuirse al fenómeno conocido como "spatial hole burning", el comportamiento de la polarización está influenciado por diferentes mecanismos físicos. La luz emitida por

un VCSEL está, comúnmente, linealmente polarizada a lo largo de dos direcciones ortogonales, y cuando la corriente o la temperatura de estos dispositivos varía, suele observarse un cambio en la polarización ("polarization switching (PS)"). Comprender y controlar la polarización de los VCSELs es crucial para su uso en aplicaciones sensibles a la polarización, como discos magneto-ópticos y sistemas de detección coherente.

El efecto de la inyección óptica en los VCSELs ha sido estudiado desde 1993 y es el principal objeto de esta Tesis. El estudio de los efectos de inyección óptica en los VCSELs es interesante porque, en contraste con los láseres de semiconductor de emisión lateral (EEL), el grado de libertad extra otorgado por la polarización, juega un papel importante en la respuesta dinámica del dispositivo bajo inyección óptica.

A lo largo de esta Tesis, fundamentalmente experimental aunque acompañada también de estudios teóricos para comprender y comparar con los resultados experimentales, analizamos la dinámica no lineal y las propiedades de polarización de los VCSELs cuando éstos son sometidos a inyección óptica. Hemos trabajado con VCSELs monomodo y multimodo transversal emitiendo usualmente a longitudes de onda cercanas a 1550 nm. Típicamente hemos empleado montajes experimentales en fibra óptica, aunque algunos resultados experimentales con VCSELs operando a una longitud de onda de 850 nm se han hecho trabajando en aire. En estos experimentos hemos estudiado la dinámica no lineal de VCSELs multimodo cuando son sometidos a una o dos frecuencias de inyección óptica.

La presente Tesis se organiza como sigue. En el capítulo 2, se describen los principios básicos de los láseres de semiconductor. Presentamos un modelo simple de su dinámica basado en una aproximación de las ecuaciones de balance para estos láseres. Estudiamos las soluciones del estado estacionario y realizamos un análisis en pequeña señal de las ecuaciones de balance.

Se describe también el concepto del ruido relativo de intensidad (RIN) y su cálculo, usando análisis de pequeña señal.

En el capítulo 3, describimos las propiedades de emisión de los VCSELs. Presentamos las características luz-corriente y además explicamos el comportamiento térmico y las propiedades de polarización de los VCSELs. Es sabido que los VCSELs pueden emitir en varios modos transversales, fenómeno atribuido al "spatial hole burning" el cual es explicado brevemente en este capítulo. Describimos el modelo de Spin-Flip que representa el modelo comúnmente usado para explicar el comportamiento de la polarización de los VCSELs y en particular del PS encontrado en estos dispositivos. El principal objetivo de esta Tesis, como ya mencionamos anteriormente, es estudiar los efectos de la inyección óptica en VCSELs, por tanto, describimos en este capítulo trabajos previos de inyección óptica en láseres de semiconductor y en particular de los VCSELs con una especial atención en el fenómeno de PS asociado a la inyección óptica.

En el capítulo 4 describimos el equipo de medida y presentamos sus características más relevantes.

En el capítulo 5, estudiamos experimentalmente el ruido relativo de intensidad para diferentes VCSELs multimodo. Hemos considerado VCSELs que emiten en dos y tres modos transversales. Para los VCSELs que emiten en dos modos transversales paralelamente polarizados, aparecen dos picos de resonancia en el espectro del ruido de los modos individuales y en la potencia total. El espectro del RIN de los VCSELs multimodo depende de la corriente aplicada de un modo similar a lo previamente encontrado en teoría. Para los VCSELs que emiten en tres modos transversales con polarizaciones diferentes hemos encontrado que la polarización de los VCSELs juega un papel importante en la determinación de la estructura multipico de los espectros de ruido.

En el capítulo 6 estudiamos teórica y experimentalmente las propiedades de biestabilidad del PS en un VCSEL monomodo

emitiendo a 1550 nm sometido a inyección óptica ortogonal. Primero estudiamos la biestabilidad en función de la desintonía (diferencia entre la frecuencia del láser maestro y la frecuencia de la polarización ortogonal del VCSEL) en frecuencia entre la luz inyectada y la polarización lineal y ortogonal del VCSEL. En segundo lugar estudiamos las propiedades de biestabilidad del PS en función de la potencia óptica inyectada. Hemos encontrado tres regiones biestables diferentes. Analizamos el ancho de las regiones biestables en función de la potencia inyectada encontrando que el ancho de una de las tres regiones biestables es más de siete veces mayor que el encontrado en trabajos previos. Encontramos tres formas diferentes de biestabilidad: antihoraria, horaria y forma de X. Se ha obtenido un buen acuerdo cualitativo entre teoría y experimento.

En el capítulo 7, analizamos la dinámica no lineal que aparece en los VCSELs monomodo emitiendo a 1550 nm sometidos a inyección óptica paralela y ortogonal. Para ambos tipos de inyección, medimos mapas de estabilidad identificando los límites entre regiones de diferente dinámica no lineal. En el caso de inyección óptica ortogonal medimos simultáneamente las trazas temporales de la salida de ambas polarizaciones lineales del VCSEL. Estudiamos la señal de salida para diferentes valores de la corriente, la potencia inyectada y diferentes desintonías. Usando las trazas simultáneas, analizamos las propiedades de correlación entre ambas polarizaciones lineales. Para desintonías en frecuencia positivas encontramos típicamente que la polarización ortogonal es la única polarización que contribuye a la dinámica de la potencia total. Sin embargo, encontramos dinámica correlacionada en ambas polarizaciones lineales para valores grandes de corriente y para pequeños valores de potencia de inyección próximos al borde de la región periódica. Para desintonías en frecuencia negativas encontramos dinámica anticorrelacionada, caracterizada por espectros de potencia anchos relacionados a su vez con grandes valores de dispersión del tiempo entre pulsos. Un buen acuerdo cualitativo se

encuentra entre teoría y experimentos.

En el capítulo 8, estudiamos las características dinámicas de un inversor todo-óptico basado en el PS en VCSELs emitiendo a 1550 nm de longitud de onda. El procesado todo-óptico de señales de alta velocidad se espera que sea la clave tecnológica en el futuro de las redes fotónicas. Usando el PS de un VCSEL monomodo a 1550 nm demostramos un inversor todo-óptico. Consideramos inyección óptica de pulsos de alta y baja frecuencia, identificando las condiciones de operación apropiadas para la inversión todo-óptica. El PS basado en inversores todo-ópticos se demuestra para una tasa de 2.5 Gb/s en formato de modulación no regreso a cero de la señal de entrada.

En el capítulo 9, la selección modal inducida por inyección óptica paralela, es estudiada experimentalmente en un VCSEL con emisión en dos modos transversales que están linealmente polarizados en una dirección que llamamos paralela. La selección del modo transversal fundamental puede conseguirse cuando los dos modos transversales tienen polarizaciones paralelas. La selección del modo fundamental es acompañada de bloqueo al modo de la señal ópticamente inyectado para valores suficientemente grandes de desintonía. También encontramos biestabilidad para este proceso cuando la longitud de onda de la inyección óptica aumenta por encima de un valor mínimo.

En el capítulo 10, dado el interés para el procesado de señal todo-óptico y aplicaciones ópticas de "switching/routing" en redes ópticas de larga distancia, hemos analizado experimentalmente la biestabilidad de la polarización en la potencia óptica inducida en VCSELs multimodo transversal de longitud de onda larga bajo inyección óptica ortogonal. Biestabilidad con ciclos de histéresis muy anchos se ha medido para los modos transversal fundamental y de orden superior del VCSEL. La forma de los ciclos de histéresis asociados es diferente para cada modo transversal. El modo transversal de orden

superior tiene forma cuadrada para las características de entrada y salida lo cual es interesante para obtener inversores y regeneradores todo ópticos de buena calidad.

En el capítulo 11 hemos estudiado el efecto de la inyección óptica ortogonal en VCSELs multimodo transversal de longitud de onda corta. El haz inyectado viene de un VCSEL similar. Ambos emiten a 850 nm de longitud de onda. En contraste con los montajes experimentales descritos anteriormente, en este caso, todos los haces láser se propagan en aire. Mostramos que cuando el VCSEL esclavo emite en varios modos transversales con polarización paralela, la inyección óptica puede inducir PS en todos ellos mientras sólo un modo esté bloqueado a la frecuencia externa. Este fenómeno es observado incluso para baja potencia (unos pocos μW) de inyección. Oscilaciones periódicas y pulsaciones irregulares de baja frecuencia se han observado.

En el capítulo 12 estudiamos los efectos de inyectar luz desde un VCSEL multimodo transversal de longitud de onda corta en otro dispositivo multimodo similar. Denominamos a este esquema de inyección como inyección óptica de dos frecuencias porque el láser maestro emite en dos modos transversales. Encontramos PS con y sin bloqueo para desintonías relativamente pequeñas. Además del PS, encontramos también dos tipos de inestabilidades. Todos ellos están representados en el plano de desintonía en frecuencia frente a la potencia inyectada.

En el capítulo 13 mostramos teóricamente un nuevo método para la generación de señales de microondas fotónicas usando un VCSEL multimodo transversal sometido a la inyección óptica de dos frecuencias. Mostramos que el bloqueo a la doble inyección involucrando dos modos transversales puede obtenerse en estos sistemas. La comparación con el caso de un VCSEL monomodo similar sometido a la inyección óptica de dos frecuencias muestra que la operación multimodo transversal del VCSEL mejora el rendimiento de los sistemas basados en la generación de señales de microondas fotónicas. Amplios rangos de sintonizabilidad,

hasta los THz, con anchos de línea estrechos se demuestran en nuestro sistema. Mostramos que la máxima frecuencia de la señal de microondas generada puede aumentar sustancialmente si se emplean VCSELs multimodo en lugar de VCSELs monomodo.

Finalmente, en el capítulo 14 presentamos una revisión de las principales conclusiones mostradas en esta Tesis.

Appendix D

Publication List

JOURNAL PUBLICATIONS

1.- A. Quirce, A. Valle and L. Pesquera, "Very Wide Hysteresis Cycles in 1550-Nm VCSELs Subject to Orthogonal Optical Injection," IEEE Photonics Technology Letters, vol. 21, no. 17, pp. 1193-1195, SEP 1, 2009.

2.- A. Hurtado, A. Quirce, A. Valle, L. Pesquera and M. J. Adams, "Power and Wavelength Polarization Bistability with very Wide Hysteresis Cycles in a 1550nm-VCSEL Subject to Orthogonal Optical Injection," Optics Express, vol. 17, no. 26, pp. 23637-23642, DEC 21, 2009.

3.- A. Hurtado, A. Quirce, A. Valle, L. Pesquera and M. J. Adams, "Nonlinear Dynamics Induced by Parallel and Orthogonal Optical Injection in 1550 Nm Vertical-Cavity Surface-Emitting Lasers (VCSELs)," Optics Express, vol. 18, no. 9, pp. 9423-9428, APR 26, 2010.

4.- A. Quirce, A. Valle, A. Hurtado, C. Gimenez, L. Pesquera and M. J. Adams, "Experimental Study of Transverse Mode Selection in VCSELs Induced by Parallel Polarized Optical Injection," IEEE J. Quant. Electron., vol. 46, no. 4, pp. 467-473, APR, 2010.

5.- M. S. Torre, A. Quirce, A. Valle and L. Pesquera, "Wavelength-Induced Polarization Bistability in 1550 Nm VCSELs Subject to Orthogonal Optical Injection," Journal of the Optical Society of America B-Optical Physics, vol. 27, no. 12, pp. 2542-2548, DEC, 2010.

6.- M. Torre, A. Hurtado, A. Quirce, A. Valle, L. Pesquera and M. Adams, "Polarization Switching in Long-Wavelength VCSELs Subject to Orthogonal Optical Injection," IEEE J. Quant. Electron., vol. 47, no. 1, pp. 92-99, JAN, 2011.

7.- A. Quirce, A. Valle, C. Gimenez and L. Pesquera, "Intensity Noise Characteristics of Multimode VCSELs," J. Lightwave Technol., vol. 29, no. 7, APR 1 2011, 2011.

8.- P. Perez, A. Quirce, L. Pesquera and A. Valle, "Polarization-Resolved Nonlinear Dynamics Induced by Orthogonal Optical Injection in Long-Wavelength VCSELs," IEEE Journal of Selected Topics in Quantum Electronics, vol. 17, no. 5, pp. 1228-1235, SEP-OCT, 2011.

9.- H. Lin, D. W. Pierce, A. J. Basnet, A. Quirce, Y. Zhang and A. Valle, "Two-Frequency Injection on a Multimode Vertical-Cavity Surface-Emitting Laser," Optics Express, vol. 19, no. 23, pp. 22437-22442, NOV 7 2011, 2011.

10.- A. Quirce, P. Perez, A. Valle and L. Pesquera, "Correlation Properties and Time-Resolved Dynamics of Linear Polarizations Emitted by Single-Mode Vertical-Cavity Surface-Emitting Lasers Subject to Orthogonal Optical Injection," Journal of the Optical Society of America B-Optical Physics, vol. 28, no. 11, NOV, 2011.

11.- A. Quirce, J. R. Cuesta, A. Valle, A. Hurtado, L. Pesquera and M. J. Adams, "Polarization Bistability Induced by Orthogonal Optical Injection in 1550-Nm Multimode VCSELs," IEEE Journal of Selected Topics in Quantum Electronics, vol. 18, no. 2, MAR-APR

2012, 2012.

12.- H. Lin, Y. Zhang, D. W. Pierce, A. Quirce and A. Valle, "Polarization Dynamics of a Multimode Vertical-Cavity Surface-Emitting Laser Subject to Orthogonal Optical Injection," Journal of the Optical Society of America B-Optical Physics, vol. 29, no. 4, APR 2012, 2012.

13.- A. Quirce, J. R. Cuesta, A. Hurtado, K. Schires, A. Valle, L. Pesquera, I.D. Henning and M. J. Adams, "Dynamic characteristics of an all-optical inverter based on polarization switching in long-wavelength VCSELs," IEEE Journal of Quantum Electronics, vol. 48, no. 5, pp. 588-595, MAY, 2012.

14.- A. Quirce and A. Valle, "High-frequency microwave signal generation using multi-transverse mode VCSELs subject to two-frequency optical injection," Optics Express, vol. 20, no. 12, pp. 13390-13401, MAY, 2012.

INTERNATIONAL PROCEEDINGS

1.- A. Hurtado, A. Quirce, A. Valle, L. Pesquera and M.J. Adams, "Different forms of polarization bistability with very wide hysteresis cycles in a 1550nm-VCSEL subject to orthogonal optical injection" *22nd Annual Meeting of the IEEE-Photonics-Society*. vols. 1 and 2, art. no. 807-808,2009.

2.- A. Quirce, A. Hurtado, A. Valle, L. Pesquera and M.J. Adams, "Nonlinear polarization dynamics induced by orthogonal optical injection in 1550nm-Vertical-Cavity Surface-Emitting Lasers." *22nd Annual Meeting of the IEEE-Photonics-Society*. vols. 1 and 2, art. no. 809-810,2009.

3.- A. Hurtado, K. Schires, N. Khan, A. Quirce, A. Valle, L. Pesquera, I. D. Henning and M. J. Adams, "Experimental Stability Maps of a 1550nm-VCSEL Subject to Polarized Optical Injection," *Physics and*

Simulation of Optoelectronic Devices Xviii, vol. 7597, art. no. 75971L, 2010.

4.- A. Quirce, A. Valle, C. Gimenez and L. Pesquera, "Experimental Study of Relative Intensity Noise of Multimode Vertical-Cavity Surface-Emitting Lasers," *Semiconductor Lasers and Laser Dynamics Iv,* vol. 7720, art. no. 772024, 2010.

5.- A. Quirce, J. R. Cuesta, A. Valle, A. Hurtado, L. Pesquera and M. J. Adams, "Polarization Bistability in Long-Wavelength Multitransverse-Mode VCSELs Induced by Orthogonal Optical Injection," *Semiconductor Lasers and Laser Dynamics Iv,* vol. 7720, art. no. 77201V, 2010.

6.-P. Perez, A. Quirce, L. Pesquera and A. Valle, "Polarization-Resolved Nonlinear Dynamics induced by orthogonal optical injection in 1550 nm-Vertical-Cavity Surface-Emitting Lasers. " *22nd IEEE International Semiconductor Laser Conference*, pp. 89-90, 2010.

7.- A. Quirce, J.R. Cuesta, A. Hurtado, K. Schires, A. Valle, L. Pesquera, I. Henning, M. J. Adams, "All-optical Inverter based on Polarization Switching in Long-wavelength VCSELs" *European Conference on Lasers and Electro-Optics. European Quantum Electronics Conference*, Munich, Germany, 22-26 May 2011.

8.- A. Quirce, A. Valle, L. Pesquera, A. Hurtado and M. J. Adams, "Transverse Mode Selection and Injection Locking in 1550-Nm Multimode VCSELs Induced by Optical Injection," *Vertical-Cavity Surface-Emitting Lasers Xv,* vol. 7952, art. no. 79520N, 2011.

9.- P. Perez, A. Quirce, L. Pesquera and A. Valle, "Polarization-Resolved Nonlinear Dynamics in Long-Wavelength Single-Mode VCSELs Subject to Orthogonal Optical Injection," *Physics and Simulation of Optoelectronic Devices Xix,* vol. 7933, art. no. 79330B,

2011.

10.- P. Perez, A. Quirce, A. Valle and L. Pesquera, "Deterministic and Stochastic Dynamics of Linear Polarizations Emitted by Single-Mode VCSELs Subject to Orthogonal Optical Injection," *Semiconductor Lasers and Laser Dynamics V,* vol. 8432, art. no. 84321B, 2012.

11.- A. Quirce, P. Perez, A. Valle and L. Pesquera, "Optical Spectral Analysis of the Nonlinear Dynamics in Long-Wavelength Single-Mode VCSELs Subject to Orthogonal Optical Injection," *Physics and Simulation of Optoelectronic Devices Xx,* vol. 8255, art. no. 825509, 2012.

12.- A. Quirce, A. Valle, H. Lin, Y. Zhang and D. W. Pierce, "Polarization Switching of Transverse Modes in VCSELs Subject to Two-Frequency Orthogonal Optical Injection," *Semiconductor Lasers and Laser Dynamics V,* vol. 8432, art. no. 84321C, 2012.

13.- A. Valle, A. Quirce. "High-Frequency Microwave Signal Generation Using Multi-Transverse Mode VCSELs Subject to Dual-Beam Optical Injection", 23rd *IEEE International Semiconductor Laser Conference*, ISLC 2012, San Diego, USA, 7-10 October.

NATIONAL PROCEEDINGS

1.- A. Quirce, A. Valle, C. Giménez and L. Pesquera, "Experimental Study of Modal Selection in Multitransverse Mode VCSELs Induced by Optical Injection" *Proceedings Reunión Española de Optoelectrónica (OPTOEL 2009)*, pp. 193-198.

2.- A. Quirce, J.R. Cuesta, K. Schires, A. Hurtado, A. Valle, L. Pesquera, I.D. Henning and M. Adams, " All-Optical Inverter with a 1550nm Vertical Cavity Surface Emitting Laser" *Proceedings Reunión Española de Optoelectrónica (OPTOEL 2011)*, pp. S2-83/1-S2-83/5.

3.- A. Quirce, P. Pérez, L. Pesquera and A. Valle, " Polarization-Resolved Nonlinear Dynamics Induced by Orthogonal Optical Injection in 1550 nm VCSELs" *Proceedings Reunión Española de Optoelectrónica (OPTOEL 2011)*, pp. S2-93/1-S2-93/6.

OTHER CONFERENCE PUBLICATIONS

1.- A. Hurtado, A. Quirce, A. Valle, L. Pesquera and M.J. Adams "Polarization bistability in 1550nm-VCSELs subject to orthogonal optical injection: very wide hysteresis cycles with different forms", *23rd Conference on Semiconductor and Integrated Optoelectronics*, SIOE'2009, Cardiff, UK, 6-8 April 2009.

2.- A. Quirce, A. Hurtado, A. Valle, L. Pesquera and M.J.Adams, "Experimental study of the nonlinear dynamics of the polarization in 1550 nm-VCSELs subject to orthogonal optical injection", 23rd *Conference on Semiconductor and Integrated Optoelectronics,* SIOE'2009*,* Cardiff, UK, 6-8 April 2009.

3.- A. Hurtado, A. Quirce, L. Pesquera, A. Valle and M.J. Adams, "Experimental study of nonlinear dynamics and chaos in a 1550nm-VCSEL subject to polarized optical injection", *The 2nd Chaotic Modeling and Simulation International Conference,* CHAOS 2009, Chania, Crete, Greece, 1-5 June 2009.

4.- A. Quirce, A. Hurtado A. Valle, L. Pesquera, M. J. Adams, "Experimental study of the nonlinear polarization dynamics induced by orthogonal optical injection in 1550 nm-Vertical-Cavity Surface- Emitting Lasers", The 2nd *Chaotic Modeling and Simulation International Conference*, CHAOS 2009, Chania, Crete, Greece,1-5 June 2009.

5.- A. Quirce, A. Hurtado A. Valle, L. Pesquera, M. J. Adams, "Polarization nonlinear dynamics of Vertical-Cavity Surface-Emitting lasers subject to orthogonal optical injection", XVI *Congreso de Física Estadística,* FisEs 2009, Huelva, Spain, 10-12

September 2009.

6.- A. Quirce, A. Valle, H. Lin, D. W. Pierce and Y. Zhang. "High-Frequency Microwave Signal Generation Using Multi-Transverse Mode VCSELs Subject to Two-Frequency Optical Injection", *International Symposium on Physics and Applications of Laser Dynamics*, IS-PALD 2012, Tainan, Taiwan, 7-9 November.

Bibliography

[Adams 2010] M. J. Adams, A. Hurtado, D. Labukhin and I. D. Henning, "Nonlinear Semiconductor Lasers and Amplifiers for all-Optical Information Processing," *Chaos,* vol. 20, no. 3, art. no. 037102, SEP, 2010.

[Agrawal 2002] G. P. Agrawal, "*Fiber-Optic Communication Systems*". Wiley-Interscience, 2002.

[Al-Hosiny 2006] N. Al-Hosiny, I. D. Henning and M. J. Adams, "Secondary Locking Regions in Laser Diode Subject to Optical Injection from Two Lasers," *Electron. Lett.,* vol. 42, no. 13, pp. 759-760, JUN 22 2006.

[Al-Seyab 2011] R. Al-Seyab, K. Schires, N. A. Khan, A. Hurtado, I. D. Henning and M. J. Adams, "Dynamics of Polarized Optical Injection in 1550-Nm VCSELs: Theory and Experiments," *IEEE Journal of Selected Topics in Quantum Electronics,* vol. 17, no. 5, pp. 1242-1249, SEP-OCT, 2011.

[Altes 2006] J. Altes, I. Gatare, K. Panajotov, H. Thienpont and M. Sciamanna, "Mapping of the Dynamics Induced by Orthogonal Optical Injection in Vertical-Cavity Surface-Emitting Lasers," *IEEE J. Quant. Electron.,* vol. 42, no. 1-2, pp. 198-207, JAN-FEB, 2006.

[Boiko 1999] D. Boiko, G. Stephan and P. Besnard, "Fast Polarization Switching with Memory Effect in a Vertical Cavity Surface Emitting Laser Subject to Modulated Optical Injection," *J. Appl. Phys.,* vol. 86, no. 8, pp. 4096-4099, OCT 15, 1999.

[Buccafusca 1996] O. Buccafusca, J. Chilla, J. Rocca, S. Feld, C. Wilmsen, V. Morozov and R. Leibenguth, "Transverse Mode Dynamics in Vertical Cavity Surface Emitting Lasers Excited by Fast Electrical Pulses," *Appl. Phys. Lett.,* vol. 68, no. 5, pp. 590-592, JAN

29, 1996.

[Chang 2003] C. Chang, L. Chrostowski and C. Chang-Hasnain, "Injection Locking of VCSELs," *IEEE Journal of Selected Topics in Quantum Electronics,* vol. 9, no. 5, pp. 1386-1393, SEP-OCT, 2003.

[Chan 2006] S. Chan, S. Hwang and J. Liu, "Radio-Over-Fiber AM-to-FM Upconversion using an Optically Injected Semiconductor Laser," *Opt. Lett.,* vol. 31, no. 15, pp. 2254-2256, AUG 1, 2006.

[Chan 2007] S. Chan, S. Hwang and J. Liu, "Radio-Over-Fiber Transmission from an Optically Injected Semiconductor Laser in Period-One State - Art. no. 646811," *Physics and Simulation of Optoelectronic Devices XV,* vol. 6468, pp. 46811-46811, 2007.

[Chan 2008] S. Chan, R. Diaz and J. Liu, "Novel Photonic Applications of Nonlinear Semiconductor Laser Dynamics," *Opt. Quant. Electron.,* vol. 40, no. 2-4, pp. 83-95, MAR 2008.

[Chan 2010] S. Chan, "Analysis of an Optically Injected Semiconductor Laser for Microwave Generation," *IEEE J. Quant. Electron.,* vol. 46, no. 3, pp. 421-428, MAR 2010.

[Changhasnain 1991] C. Changhasnain, J. Harbison, G. Hasnain, a. Vonlehmen, L. Florez and N. Stoffel, "Dynamic, Polarization, and Transverse-Mode Characteristics of Vertical Cavity Surface Emitting Lasers," *IEEE J. Quant. Electron.,* vol. 27, no. 6, pp. 1402-1409, JUN, 1991.

[Chavezpirson 1993] A. Chavezpirson, H. Ando, H. Saito and H. Kanbe, "Polarization Properties of a Vertical-Cavity Surface-Emitting Laser using a Fractional Layer Superlattice Gain Medium," *Appl. Phys. Lett.,* vol. 62, no. 24, JUN 14 1993.

[Chen 2011] Y. Chen, Y. Juan and F. Lin, "High-Frequency Microwave Signal Generation in a Semiconductor Laser Under Double Injection Locking," *Rf and Millimeter-Wave Photonics,* vol. 7936, art. no. 793609, 2011.

[Choquette 1995] K. Choquette, R. Schneider, K. Lear and R. Leibenguth, "Gain-Dependent Polarization Properties of Vertical-

Cavity Lasers," *IEEE Journal of Selected Topics in Quantum Electronics,* vol. 1, no. 2, pp. 661-666, JUN, 1995.

[Chrostowski 2006] L. Chrostowski, X. X. Zhao and C. J. Chang-Hasnain, "Microwave Performance of Optically Injection-Locked VCSELs," *IEEE Trans. Microwave Theory Tech.,* vol. 54, no. 2, pp. 788-796, FEB 2006.

[Chrostowski 2011]. Chrostowski, B. Faraji, W. Hofmann, M. Amann and S. Wieczorek, "40 GHz Bandwidth and 64 GHz Resonance Frequency in Injection-Locked 1.55 Mu m VCSELs ," *IEEE Journal of Selected Topics in Quantum Electronics,* vol. 13, no. 5, pp. 1200-1208, SEP-OCT, 2007.

[Coldren 1995] L. A. Coldren and S. W. Corzine, "*Diode Lasers and Photonic Integrated Circuits.*" New York: John Wiley & Sons, 1995.

[Freund 2010] R. E. Freund, C. A. Bunge, N. N. Ledentsov, D. Molin and C. Caspar, "High-Speed Transmission in Multi-Mode Fibers", *J. Lightwave Technol.*, vol. 28, no. 4, pp. 569-570-586, 2010.

[Gatare 2006a] I. Gatare, J. Buesa, H. Thienpont, K. Panajotov and M. Sciamanna, "Polarization Switching Bistability and Dynamics in Vertical-Cavity Surface-Emitting Laser Under Orthogonal Optical Injection," *Opt. Quant. Electron.,* vol. 38, no. 4-6, pp. 429-443, MAR, 2006.

[Gatare 2006b] I. Gatare, M. Sciamanna, J. Buesa, H. Thienpont and K. Panajotov, "Nonlinear Dynamics Accompanying Polarization Switching in Vertical-Cavity Surface-Emitting Lasers with Orthogonal Optical Injection," *Appl. Phys. Lett.,* vol. 88, no. 10, art. no. 101106, MAR 6, 2006.

[Gatare 2007a] I. Gatare, K. Panajotov and M. Sciamanna, "Frequency-Induced Polarization Bistability in Vertical-Cavity Surface-Emitting Lasers with Orthogonal Optical Injection," *Physical Review A,* vol. 75, no. 2, art. no. 023804, FEB, 2007.

[Gatare 2007b] I. Gatare, M. Sciamanna, M. Nizette and K. Panajotov, "Bifurcation to Polarization Switching and Locking in

Vertical-Cavity Surface-Emitting Lasers with Optical Injection," *Physical Review A,* vol. 76, no. 3, art. no. 031803, SEP, 2007.

[Gatare 2008] I. Gatare, "Polarization Switching, Locking and Synchronization in VCSELs with Optical Injection", PhD Thesis. Vrije Universiteit Brussel, Brussels, Belgium and Supélec, LMOPS, Metz, France, 2008.

[Gatare 2009] I. Gatare, M. Sciamanna, M. Nizette, H. Thienpont and K. Panajotov, "Mapping of Two-Polarization-Mode Dynamics in Vertical-Cavity Surface-Emitting Lasers with Optical Injection," *Physical Review E,* vol. 80, no. 2, art. no. 026218, AUG, 2009.

[Gholami 2006] A. Gholami, Z. Toffano, A. Destrez, S. Pellevrault, M. Pez and F. Quentel, "Optimization of VCSEL Spatiotemporal Operation -in MMF Links for 10-Gb Ethernet," *IEEE Journal of Selected Topics in Quantum Electronics,* vol. 12, no. 4, pp. 767-775, JUL-AUG 2006.

[Giacomelli 1998] G. Giacomelli and F. Marin, "Statistics of Polarization Competition in VCSELs," *Quantum and Semiclassical Optics,* vol. 10, no. 3, pp. 469-476, JUN 1998.

[Gu 2008] Q. Gu, W. Hofmann, M. Amann and L. Chrostowski, "Optically Injection-Locked VCSEL as a Duplex transmitter/ receiver," *IEEE Photonics Technology Letters,* vol. 20, no. 5-8, pp. 463-465, MAR-APR, 2008.

[Hahn 1993] K. H. Hahn, M. R. Tan, Y. M. Houng and S. Y. Wang, "Large-Area Multitransverse-Mode VCSELs for Modal Noise-Reduction in Multimode Fiber Systems," *Electron. Lett.,* vol. 29, no. 16, pp. 1482-1483, AUG 5 1993.

[Hahn 1994] K. H. Hahn, M. R. Tan and S. Y. Wang, "Intensity Noise of Large-Area Vertical-Cavity Surface-Emitting Lasers in Multimode Optical-Fiber Links," *Electron. Lett.,* vol. 30, no. 2, pp. 139-140, JAN 20 1994.

[Hasebe 2006] K. Hasebe and F. Koyama, "Modeling of all-Optical-Signal Processing Devices Based on Two Mode Injection-Locked Vertical-Cavity Surface-Emitting Laser," *Japanese Journal of*

Applied Physics Part 1-Regular Papers Brief Communications & Review Papers, vol. 45, no. 8B, pp. 6697-6703, AUG, 2006.

[Hayat 2009] A. Hayat, A. Bacou, A. Rissons, J. Mollier, V. Iakovlev, A. Sirbu and E. Kapon, "Long Wavelength VCSEL-by-VCSEL Optical

Injection Locking," *IEEE Trans. Microwave Theory Tech.,* vol. 57, no. 7, pp. 1850-1858, JUL 2009.

[Hermier 2001] J. P. Hermier, A. Bramati, A. Z. Khoury, V. Josse, E. Giacobino, P. Schnitzer, R. Michalzik and K. J. Ebeling, "Noise Characteristics of Oxide-Confined Vertical-Cavity Surface-Emitting Lasers," *IEEE J. Quant. Electron.,* vol. 37, no. 1, pp. 87-91, JAN 2001.

[Hong 2000a] Y. Hong, K. Shore, A. Larsson, M. Ghisoni and J. Halonen, "Pure Frequency-Polarization Bistability in Vertical Cavity Surface Emitting Semiconductor Lasers," *Leos 2000 - IEEE Annual Meeting Conference Proceedings, Vols.1 & 2,* pp. 888-889, 2000.

[Hong 2000b] Y. Hong, K. Shore, A. Larsson, M. Ghisoni and J. Halonen, "Pure Frequency-Polarisation Bistability in Vertical Cavity Surface-Emitting Semiconductor Laser Subject to Optical Injection," *Electron. Lett.,* vol. 36, no. 24, pp. 2019-2020, NOV 23, 2000.

[Hong 2001] Y. Hong, K. Shore, A. Larsson, M. Ghisoni and J. Halonen, "Polarization Switching in a Vertical Cavity Surface Emitting Semiconductor Laser by Frequency Detuning," *IEE Proceedings-Optoelectronics,* vol. 148, no. 1, pp. 31-34, FEB, 2001.

[Hong 2002] Y. Hong, P. Spencer, P. Rees and K. Shore, "Optical Injection Dynamics of Two-Mode Vertical Cavity Surface-Emitting Semiconductor Lasers," *IEEE J. Quant. Electron.,* vol. 38, no. 3, pp. 274-278, MAR, 2002.

[Hong 2003] Y. Hong, P. Spencer, S. Bandyopadhyay, P. Rees and K. Shore, "Polarisation-Resolved Chaos and Instabilities in a Vertical Cavity Surface Emitting Laser Subject to Optical Injection," *Opt. Commun.,* vol. 216, no. 1-3, pp. 185-189, FEB 1, 2003.

[Hurtado 2006] A. Hurtado, A. Gonzalez-Marcos, J. Martin-Pereda and M. Adams, "Two-Wavelength Switching with a Distributed-Feed

Back Semiconductor Optical Amplifier (DFBSOA)," *IEE Proceedings-Optoelectronics,* vol. 153, no. 1, pp. 21-27, FEB, 2006.

[Hurtado 2007] A. Hurtado, I. D. Henning and M. J. Adams, "Two-Wavelength Switching with 1.55 Mu m VCSOA," *Electron. Lett.,* vol. 43, no. 16, pp. 887-889, AUG 2, 2007.

[Hurtado 2008a] A. Hurtado, I. D. Henning and M. J. Adams, "Differences in the Injection Locking Bandwidth in 1550nm-VCSELs Subject to Parallel and Orthogonal Optical Injection". *21st IEEE International Semiconductor Laser Conference*, pp. 87-88, ISLC 2008.

[Hurtado 2008b] A. Hurtado, I. D. Henning and M. J. Adams, "Two-Wavelength Switching with a 1550 Nm VCSEL Under Single Orthogonal Optical Injection," *IEEE Journal of Selected Topics in Quantum Electronics,* vol. 14, no. 3, pp. 911-917, MAY-JUN, 2008.

[Hurtado 2009a] A. Hurtado, D. Labukhin, F. D. Henning and M. J. Adams, "Injection Locking Bandwidth in 1550-Nm VCSELs Subject to Parallel and Orthogonal Optical Injection," *IEEE Journal of Selected Topics in Quantum Electronics,* vol. 15, no. 3, pp. 585-593, MAY-JUN, 2009.

[Hurtado 2009b] A. Hurtado, I. D. Henning and M. J. Adams, "Different Forms of Wavelength Polarization Switching and Bistability in a 1.55 Mu m Vertical-Cavity Surface-Emitting Laser Under Orthogonally Polarized Optical Injection," *Opt. Lett.,* vol. 34, no. 3, pp. 365-367, FEB 1, 2009.

[Hurtado 2009c] A. Hurtado, I. D. Henning and M. J. Adams, "Wavelength Polarization Switching and Bistability in a 1550-Nm VCSEL Subject to Polarized Optical Injection," *IEEE Photonics Technology Letters,* vol. 21, no. 15, pp. 1084-1086, AUG 1, 2009.

[Iga 2000] K. Iga, "Surface-Emitting Laser - its Birth and Generation of New Optoelectronics Field," *IEEE Journal of Selected Topics in Quantum Electronics,* vol. 6, no. 6, pp. 1201-1215, NOV-DEC, 2000.

[Inoue 1987] K. Inoue, "All-Optical Flip-Flop Operation in an Optical Bistable Device using 2 Lights of Different Frequencies," *Opt. Lett.,*

vol. 12, no. 11, pp. 918-920, NOV, 1987.

[Javaloyes 2010] J. Javaloyes and S. Balle, "Quasiequilibrium Time-Domain Susceptibility of Semiconductor Quantum Wells," *Physical Review A,* vol. 81, no. 6, art. no. 062505, JUN 10 2010.

[Jeong 2008] K. H. Jeong, K. H. Kim, S. H. Lee, M. H. Lee, B. Yoo and K. A. Shore, "Optical Injection-Induced Polarization Switching Dynamics in 1.5 Mu m Wavelength Single-Mode Vertical-Cavity Surface-Emitting Lasers," *IEEE Photonics Technology Letters,* vol. 20, no. 9-12, pp. 779-781, MAY-JUN, 2008.

[Jewell 1989] J. L. Jewell, A. Scherer, S. L. Mccall, Y. H. Lee, S. Walker, J. P. Harbison and L. T. Florez, "Low-Threshold Electrically Pumped Vertical-Cavity Surface-Emitting Microlasers," *Electron. Lett.,* vol. 25, no. 17, AUG 17 1989.

[Juan 2011] Y. Juan and F. Lin, "Photonic Generation of Broadly Tunable Microwave Signals Utilizing a Dual-Beam Optically Injected Semiconductor Laser," *IEEE Photonics Journal,* vol. 3, no. 4, pp. 644-650, AUG 2011.

[Jungo 2003] M. Jungo, "*Spatiotemporal VCSEL Model for Advanced Simulations of Optical Links*". Series in Quantum Electronics, 2003.

[Kaiser 2002] J. Kaiser, C. Degen and W. Elsasser, "Polarization-Switching Influence on the Intensity Noise of Vertical-Cavity Surface-Emitting Lasers," *Journal of the Optical Society of America B-Optical Physics,* vol. 19, no. 4, pp. 672-677, APR 2002.

[Kaplan 2009] A. M. Kaplan, G. P. Agrawal and D. N. Maywar, "All-Optical Flip-Flop Operation of VCSOA," *Electron. Lett.,* vol. 45, no. 2, pp. 127-128, JAN 15, 2009.

[Katayama 2008a] T. Katayama, T. Ooi and H. Kawaguchi, "Optical buffer memory with shift register function using 1,55-um polarization bistable VCSELs," in *The 21st Annual Meeting of the IEEE Lasers & Electro-Optics Society (LEOS 2008),* Newport Beach, USA, 2008, pp. 739-740.

[Katayama 2008b] T. Katayama, T. Kitazawa and H. Kawaguchi, "All-optical flip-flop operation using 1.55 um polarization bistable VCSELs," in *Conference on Lasers and Electro-Optics/Quantum Electronics and Laser Science Conference (CLEO/QELS 2008), CME5,* San Jose, USA, 2008.

[Kawaguchi 1994] H. Kawaguchi, "*Bistabilities and Nonlinearities in Laser Diodes*". *Boston:* Artech House, 1994.

[Kawaguchi 1995a] H. KAWAGUCHI and I. HIDAYAT, "Gigahertz all-Optical Flip-Flop Operation of Polarization-Bistable Vertical-Cavity Surface-Emitting Lasers," *Electron. Lett.,* vol. 31, no. 14, pp. 1150-1151, JUL 6, 1995.

[Kawaguchi 1995b] H. Kawaguchi, I. Hidayat, Y. Takahashi and Y. Yamayoshi, "Pitchfork Bifurcation Polarization Bistability in Vertical-Cavity Surface-Emitting Lasers," *Electron. Lett.,* vol. 31, no. 2, pp. 109-111, JAN 19, 1995.

[Kawaguchi 1997] H. Kawaguchi, "Bistable Laser Diodes and their Applications: State of the Art," *IEEE Journal of Selected Topics in Quantum Electronics,* vol. 3, no. 5, pp. 1254-1270, OCT, 1997.

[Kawaguchi 2006] H. Kawaguchi, T. Mori, Y. Sato and Y. Yamayoshi, "Optical Buffer Memory using Polarization-Bistable Vertical-Cavity Surface-Emitting Lasers," *Japanese Journal of Applied Physics Part 2-Letters & Express Letters,* vol. 45, no. 33-36, pp. L894-L897, SEP, 2006.

[Kelleher 2011] B. Kelleher, C. Bonatto, G. Huyet and S. P. Hegarty, "Excitability in Optically Injected Semiconductor Lasers: Contrasting Quantum-Well- and Quantum-Dot-Based Devices," *Physical Review E,* vol. 83, no. 2, art. no. 026207, FEB 24, 2011.

[Koyama 2006] F. Koyama, "Recent Advances of VCSEL Photonics," *J. Lightwave Technol.,* vol. 24, no. 12, pp. 4502-4513, DEC, 2006.

[Kuchta 1993] D. M. Kuchta, J. Gamelin, J. D. Walker, J. Lin, K. Y. Lau, J. S. Smith, M. Hong and J. P. Mannaerts, "Relative Intensity Noise of Vertical Cavity Surface Emitting Lasers," *Appl. Phys. Lett.,* vol. 62, no. 11, pp. 1194-1196, MAR 15 1993.

[Lau 2008] E. K. Lau, X. Zhao, H. Sung, D. Parekh, C. Chang-Hasnain and M. C. Wu, "Strong Optical Injection-Locked Semiconductor Lasers Demonstrating > 100-GHz Resonance Frequencies and 80-GHz Intrinsic Bandwidths," *Optics Express,* vol. 16, no. 9, pp. 6609-6618, APR 28, 2008.

[Law 1997a] J. Y. Law and G. P. Agrawal, "Mode-Partition Noise in Vertical-Cavity Surface-Emitting Lasers," *IEEE Photonics Technology Letters,* vol. 9, no. 4, pp. 437-439, APR 1997, 1997.

[Law 1997b] J. Law, G. vanTartwijk and G. Agrawal, "Effects of Transverse-Mode Competition on the Injection Dynamics of Vertical-Cavity Surface-Emitting Lasers," *Quantum and Semiclassical Optics,* vol. 9, no. 5, pp. 737-747, OCT, 1997.

[Lear 1997] K. Lear, V. Hietala, H. Hou, M. Ochiai, J. Banas, B. Hammons, J. Zolper and S. Kilcoyne, "Small and Large Signal Modulation of 850 Nm Oxide-Confined Vertical-Cavity Surface-Emitting Lasers," *OSA Trends in Optics and Photonics,* vol. 15, pp. 69-70-74, 1997.

[Lee 2008] T. T. Lee, P. G. Lim, J. S. Harris Jr., K. V. Shenoy and S. J. Smith, "Low-Frequency Noise Characterization of Near-IR VCSELs for Functional Brain Imaging - Art. no. 68422T," *Photonic Therapeutics and Diagnostics IV,* vol. 6842, pp. T8422-T8422, 2008.

[Lee 2010a] S. H. Lee, H. W. Jung, K. H. Kim and M. H. Lee, "All-Optical Flip-Flop Operation Based on Polarization Bistability of Conventional-Type 1.55-Mu m Wavelength Single-Mode VCSELs," *Journal of the Optical Society of Korea,* vol. 14, no. 2, pp. 137-141, JUN, 2010.

[Lee 2010b] S. H. Lee, H. W. Jung, K. H. Kim, M. H. Lee, B. Yoo, J. Roh and K. A. Shore, "1-GHz all-Optical Flip-Flop Operation of Conventional Cylindrical-Shaped Single-Mode VCSELs Under Low-Power Optical Injection," *IEEE Photonics Technology Letters,* vol. 22, no. 23, pp. 1759-1761, DEC 1, 2010.

[Lee 1989] Y. H. Lee, J. L. Jewell, A. Scherer, S. L. Mccall, J. P. Harbison and L. T. Florez, "Room-Temperature Continuous-Wave

Vertical-Cavity Single-Quantum-Well Microlaser Diodes," *Electron. Lett.,* vol. 25, no. 20, SEP 28 1989.

[Li 1996] H. Li, T. Lucas, J. McInerney, M. Wright and R. Morgan, "Injection Locking Dynamics of Vertical Cavity Semiconductor Lasers Under Conventional and Phase Conjugate Injection," *IEEE J. Quant. Electron.,* vol. 32, no. 2, pp. 227-235, FEB, 1996.

[Li 1994] L. L. Li and K. Petermann, "Small-Signal Analysis of Optical-Frequency Conversion in an Injection-Locked Semiconductor-Laser," *IEEE J. Quant. Electron.,* vol. 30, no. 1, pp. 43-48, JAN 1994.

[Liu 2005] J. Liu, "*Photonic Devices*". Cambridge University Press, 2005.

[Mahon 1993] C. J. Mahon, M. L. Majewski, M. G. Peters, F. H. Peters and L. A. Coldren, *Relative Intensity Noise and Modulation Distortion Characteristics of Vertical-Cavity Surface-Emitting Laser-Diodes.* IEEE Lasers and Electro-Optics Society Annual Meeting, pp. 556-557, (LEOS),1993.

[Marki 2008] C. F. Marki, S. Moro, D. R. Jorgesen, P. Wen and S. C. Esener, "Cascadable Optical Inversion using 1550 Nm VCSEL," *Electron. Lett.,* vol. 44, no. 4, pp. 292-293, FEB 14, 2008.

[MartinRegalado 1996] J. MartinRegalado, M. S. Miguel, N. B. Abraham and F. Prati, "Polarization Switching in Quantum-Well Vertical-Cavity Surface-Emitting Lasers," *Opt. Lett.,* vol. 21, no. 5, pp. 351-353, MAR 1 1996.

[MartinRegalado 1997a] J. MartinRegalado, S. Balle and M. SanMiguel, "Polarization and Transverse-Mode Dynamics of Gain-Guided Vertical-Cavity Surface-Emitting Lasers," *Opt. Lett.,* vol. 22, no. 7, pp. 460-462, APR 1 1997.

[MartinRegalado 1997b] J. MartinRegalado, F. Prati, M. SanMiguel and N. Abraham, "Polarization Properties of Vertical-CavitySurface-Emitting Lasers," *IEEE J. Quant. Electron.,* vol. 33, no. 5, pp. 765-783, MAY, 1997.

[Maywar 2001] D. Maywar, G. Agrawal and Y. Nakano, "All-Optical Hysteresis Control by Means of Cross-Phase Modulation in Semiconductor Optical Amplifiers," *Journal of the Optical Society of America B-Optical Physics,* vol. 18, no. 7, pp. 1003-1013, JUL, 2001.

[Miller 1998] A. Miller, M. Ebrahimzadeh, D. M. Finlayson, *"Semiconductor quantum optoelectronics. From Quantum Physics to Smart Devices,"* Proceedings of the Fiftieth Scottish Universities Summer School in Physics, St. Andrews. Bristol: Scottish Universities Summer School in Physics; Philadelphia: Institute of Physics.

[Mogensen 1985] F. Mogensen, H. Olesen and G. Jacobsen, "Locking Conditions and Stability Properties for a Semiconductor-Laser with External Light Injection," *IEEE J. Quant. Electron.,* vol. 21, no. 7, pp. 784-793, 1985.

[Molitor 2010] A. Molitor, M. Blazek, J. M. Ostermann, R. Michalzik, P. Debernardi and W. Elsaesser, "Investigations on the Intensity Noise of Surface Grating Relief VCSELs," *IEEE J. Quant. Electron.,* vol. 46, no. 4, pp. 554-561, APR 2010.

[Mori 2006] T. Mori, Y. Yamayoshi and H. Kawaguchi, "Low-Switching-Energy and High-Repetition-Frequency all-Optical Flip-Flop Operations of a Polarization Bistable Vertical-Cavity Surface-Emitting Laser," *Appl. Phys. Lett.,* vol. 88, no. 10, art. no. 101102, MAR 6, 2006.

[Mori 2008] T. Mori, Y. Sato and H. Kawaguchi, "Timing Jitter Reduction by all-Optical Signal Regeneration using a Polarization Bistable VCSEL," *J. Lightwave Technol.,* vol. 26, no. 13-16, pp. 2946-2953, JUL-AUG, 2008.

[Mulet 2001] J. Mulet, C. Mirasso and M. Miguel, "Polarization Resolved Intensity Noise in Vertical-Cavity Surface-Emitting Lasers," *Physical Review A,* vol. 64, no. 2, art. no. 023817, AUG, 2001.

[Mulet 2002a] J. Mulet and S. Balle, "Transverse Mode Dynamics in Vertical-Cavity Surface-Emitting Lasers: Spatiotemporal Versus Modal Expansion Descriptions," *Physical Review A,* vol. 66, no. 5,

art. no. 053802, NOV, 2002.

[Mulet 2002b] J. Mulet and S. Balle, "Spatio-Temporal Modeling of the Optical Properties of VCSELs in the Presence of Polarization Effects," *IEEE J. Quant. Electron.,* vol. 38, no. 3, pp. 291-305, MAR 2002.

[Nagler 2003] B. Nagler, M. Peeters, J. Albert, G. Verschaffelt, K. Panajotov, H. Thienpont, I. Veretennicoff, J. Danckaert, S. Barbay, G. Giacomelli and F. Marin, "Polarization-Mode Hopping in Single-Mode Vertical-Cavity Surface-Emitting Lasers: Theory and Experiment," *Physical Review A,* vol. 68, no. 1, art. no. 013813, JUL, 2003.

[Nishikawa 1995] Y. Nishikawa, A. Tackeuchi, S. Nakamura, S. Muto and N. Yokoyama, "All-Optical Picosecond Switching of a Quantum-Well Etalon using Spin-Polarization Relaxation," *Appl. Phys. Lett.,* vol. 66, no. 7, FEB 13 1995.

[Nizette 2009] M. Nizette, M. Sciamanna, I. Gatare, H. Thienpont and K. Panajotov, "Dynamics of Vertical-Cavity Surface-Emitting Lasers with Optical Injection: A Two-Mode Model Approach," *Journal of the Optical Society of America B-Optical Physics,* vol. 26, no. 8, pp. 1603-1613, AUG, 2009.

[Olejniczak 2010] OleL. Olejniczak, K. Panajotov, H. Thienpont and M. Sciamanna, "Self-Pulsations and Excitability in Optically Injected Quantum-Dot Lasers: Impact of the Excited States and Spontaneous Emission Noise," *Physical Review A,* vol. 82, no. 2, art. no. 023807, AUG 17, 2010.

[Onishi 2004a] Y. Onishi and F. Koyama, "All-Optical Regeneration using a Vertical-Cavity Surface-Emitting Laser with External Light Injection," *IEICE Trans. Electron.,* vol. E87C, no. 3, pp. 409-415, MAR, 2004.

[Onishi 2004b] Y. Onishi, F. Koyama, N. Nishiyama, C. Caneau and C. Zah, "Nonlinear Optical Input-Output Characteristics of 1.55 μm Injection-Locked Vertical-Cavity Surface-Emitting Lasers," *Appl. Phys. Lett.,* vol. 84, no. 17, pp. 3247-3249, APR 26, 2004.

[Onishi 2004c] Y. Onishi, N. Nishiyama, C. Caneau, F. Koyama and C. Zah, "Dynamic Behavior of an all-Optical Inverter using Transverse-Mode Switching in 1.55-Mu m Vertical-Cavity Surface-Emitting Lasers," *IEEE Photonics Technology Letters,* vol. 16, no. 5,pp. 1236-1238, MAY, 2004.

[Onishi 2005] Y. Onishi, N. Nishiyama, C. Caneau, F. Koyama and C. Zah, "All-Optical Inverter Based on Long-Wavelength Vertical-Cavity Surface-Emitting Laser," *IEEE Journal of Selected Topics in Quantum Electronics,* vol. 11, no. 5, pp. 999-1005, SEP-OCT, 2005.

[Osborne 2009] S. Osborne, A. Amann, K. Buckley, G. Ryan, S. P. Hegarty, G. Huyet and S. O'Brien, "Antiphase Dynamics in a Multimode Semiconductor Laser with Optical Injection," *Physical Review A,* vol. 79, no. 2, art. no. 023834, FEB, 2009.

[Pakdeevanich 1999] Pakdeevanich and M. Adams, "Measurements and Modeling of Reflective Bistability in 1.55-Mu m Laser Diode Amplifiers," *IEEE J. Quant. Electron.,* vol. 35, no. 12, pp. 1894-1903, DEC, 1999.

[Pakdeevanich 2000]. Pakdeevanich and M. Adams, "Switching Powers for Optical Bistability in a Semiconductor Laser Above and Below Threshold," *Opt. Commun.,* vol. 176, no. 1-3, pp. 195-198, MAR 15, 2000.

[Pan 1993] Z. Pan, S. Jiang, M. Dagenais, R. Morgan, K. Kojima, M. Asom, R. Leibenguth, G. Guth and M. Focht, "Optical-Injection Induced Polarization Bistability in Vertical-Cavity Surface-Emitting Lasers," *Appl. Phys. Lett.,* vol. 63, no. 22, pp. 2999-3001, NOV 29, 1993.

[Panajotov 1998]. Panajotov, B. Ryvkin, J. Danckaert, M. Peeters, H. Thienpont and I. Veretennicoff, "Polarization Switching in VCSEL's due to Thermal Lensing," *IEEE Photonics Technology Letters*, vol. 10, no. 1, JAN 1998.

[Panajotov 2009]. Panajotov, I. Gatare, A. Valle, H. Thienpont and M. Sciamanna, "Polarization- and Transverse-Mode Dynamics in Optically Injected and Gain-Switched Vertical-Cavity Surface-

Emitting Lasers," *IEEE J. Quant. Electron.*, vol. 45, no. 11, pp. 1473-1481, NOV, 2009.

[Parekh 2008] D. Parekh, X. Zhao, W. Hofmann, M. C. Amann, L. A. Zenteno and C. J. Chang-Hasnain, "Greatly Enhanced Modulation Response of Injection-Locked Multimode VCSELs," *Optics Express,* vol. 16, no. 26, pp. 21582-21586, DEC 22, 2008.

[Park 2006] M. Park, O. Kwon, W. Han, K. Lee, S. Park and B. Yoo, "All-Monolithic 1.55 Mu m InAlGaAs/InP Vertical Cavity Surface Emitting Lasers Grown by Metal Organic Chemical Vapor Deposition," *Japanese Journal of Applied Physics Part 2-Letters & Express Letters,* vol. 45, no. 1-3, pp. L8-L10, JAN, 2006.

[Peeters 2003] M. Peeters, "Polarization Switching in Vertical-Cavity Surface-Emitting Lasers. A Modeling Perspective," PhD Thesis. Vrije Universiteit Brussel. Faculteit Toegepaste Wetenschappen,APR, 2003.

[Principato 2006] F. Principato, S. Costa, G. Ferrante and F. Marin, "Electrical and Optical Low Frequency Noises in Multimodal Vertical Cavity Surface Emitting Lasers," *Laser Physics Letters,* vol. 3, no. 10, pp. 474-479, OCT 2006.

[Qi 2011a] X. Qi and J. Liu, "Photonic Microwave Applications of the Dynamics of Semiconductor Lasers," *IEEE Journal of Selected Topics in Quantum Electronics,* vol. 17, no. 5, pp. 1198-1211, SEP-OCT 2011.

[Qi 2011b] X. Qi and J. Liu, "Dynamics Scenarios of Dual-Beam Optically Injected Semiconductor Lasers," *IEEE J. Quant. Electron.,* vol. 47, no. 6, pp. 762-769, JUN 2011.

[Raddatz 1994] L. Raddatz, I. H. White, K. H. Hahn, M. R. Tan and S. Y. Wang, "Noise Performance of Multimode Vertical-Cavity Surface-Emitting Lasers," *Electron. Lett.,* vol. 30, no. 23, pp. 1991-1992, NOV 10 1994.

[Ryvkin 1999] B. Ryvkin, K. Panajotov, A. Georgievski, J. Danckaert, M. Peeters, G. Verschaffelt, H. Thienpont and I. Veretennicoff, "Effect of Photon-Energy-Dependent Loss and Gain Mechanisms

on Polarization Switching in Vertical-Cavity Surface-Emitting Lasers," *Journal of the Optical Society of America B-Optical Physics,* vol. 16, no. 11, pp. 2106-2113, NOV, 1999.

[Ryvkin 2004] B. Ryvkin, K. Panajotov, E. Avrutin, I. Veretennicoff and H. Thienpont, "Optical-Injection-Induced Polarization Switching in Polarization-Bistable Vertical-Cavity Surface-Emitting Lasers," *J. Appl. Phys.,* vol. 96, no. 11, pp. 6002-6007, DEC 1, 2004.

[Sakaguchi 2010a] J. Sakaguchi, T. Katayama and H. Kawaguchi, "All-Optical Memory Operation of 980-Nm Polarization Bistable VCSEL for 20-Gb/s PRBS RZ and 40-Gb/s NRZ Data Signals," *Optics Express,* vol. 18, no. 12, pp. 12362-12370, JUN 7, 2010.

[Sakaguchi 2010b] J. Sakaguchi, T. Katayama and H. Kawaguchi, "High Switching-Speed Operation of Optical Memory Based on Polarization Bistable Vertical-Cavity Surface-Emitting Laser," *IEEE J. Quant. Electron.,* vol. 46, no. 11, pp. 1526-1534, NOV, 2010.

[Saleh 1991] B.E.A. Saleh, M.C. Teich, "*Fundamentals of photonics*". John Wiley & sons, 1991.

[Salvide 2011] M. Fernando Salvide, M. Susana Torre, A. Valle and L. Pesquera, "Transverse Mode Selection and Bistability in Vertical-Cavity Surface-Emitting Lasers Induced by Parallel Polarized Optical Injection," *IEEE J. Quant. Electron.,* vol. 47, no. 5, pp. 723-730, MAY 2011.

[San Miguel 1995] M. Sanmiguel, Q. Feng and J. Moloney, "Light-Polarization Dynamics in Surface-Emitting Semiconductor-Lasers," *Physical Review A,* vol. 52, no. 2, pp. 1728-1739, AUG, 1995.

[Satuby 1998] Y. Satuby and M. Orenstein, "Small-Signal Modulation of Multitransverse Modes Vertical-Cavity Surface-Emitting Semiconductor Lasers," *IEEE Photonics Technology Letters*, vol. 10, no. 6, JUN 1998.

[Satuby 1999] Y. Satuby and M. Orenstein, "Mode-Coupling Effects on the Small-Signal Modulation of Multitransverse-Mode Vertical-Cavity Semiconductor Lasers," *IEEE J. Quant. Electron.,* vol. 35, no. 6, pp. 944-954, JUN 1999.

[Schires 2011a] K. Schires, A. Hurtado, I. D. Henning and M. J. Adams, "Comprehensive Experimental Analysis of Nonlinear Dynamics in an Optically-Injected Semiconductor Laser," *Aip Advances*, vol. 1, no. 3, art. no. 032131, SEP, 2011.

[Schires 2011b] K. Schires, A. Hurtado, I. D. Henning and M. J. Adams, "Polarization and Time-Resolved Dynamics of a 1550-Nm VCSEL Subject to Orthogonally Polarized Optical Injection," *IEEE Photonics Journal,* vol. 3, no. 3, pp. 555-563, JUN, 2011.

[Sciamanna 2006] M. Sciamanna and K. Panajotov, "Route to Polarization Switching Induced by Optical Injection in Vertical-Cavity Surface-Emitting Lasers," *Physical Review A,* vol. 73, no. 2, art. no. 023811, FEB, 2006.

[Ser 1995] J. H. Ser, Y. G. Ju, J. H. Shin and Y. H. Lee, "Polarization Stabilization of Vertical-Cavity Top-Surface-Emitting Lasers by Inscription of Fine Metal-Interlaced Gratings," *Appl. Phys. Lett.,* vol. 66, no. 21, MAY 22 1995.

[Simpson 1997] T. B. Simpson, J. M. Liu, K. F. Huang and K. Tai, "Nonlinear Dynamics Induced by External Optical Injection in Semiconductor Lasers," *Quantum and Semiclassical Optics,* vol. 9, no. 5, OCT 1997.

[Simpson 2003] T. Simpson, "Mapping the Nonlinear Dynamics of a Distributed Feedback Semiconductor Laser Subject to External Optical Injection," *Opt. Commun.,* vol. 215, no. 1-3, pp. 135-151, JAN 1, 2003.

[Stevens 2001] R. STEVENS, "Modulation Properties of Vertical Cavity Light Emitters," PhD thesis. Laboratory of Photonics and Microwave Engineering. Department of Microelectronics and Information Technology. Royal Institute of Technology. Sweden, 2001.

[Thrush 2004] E. Thrush, O. Levi, W. Ha, G. Carey, L. J. Cook, J. Deich, S. J. Smith, W. E. Moerner and J. S. Harris, "Integrated Semiconductor Vertical-Cavity Surface-Emitting Lasers and PIN Photodetectors for Biomedical Fluorescence Sensing," *IEEE J. Quant. Electron.,* vol. 40, no. 5, pp. 491-498, MAY 2004.

[Toomey 2012] J. P. Toomey, C. Nichkawde, D. M. Kane, K. Schires, I. D. Henning, A. Hurtado and M. J. Adams, "Stability of the Nonlinear Dynamics of an Optically Injected VCSEL." *Optics Express,* vol. 20, no. 9, 2012-APR-23, 2012.

[Torre 2004] M. Torre, C. Masoller and K. Shore, "Numerical Study of Optical Injection Dynamics of Vertical-Cavity Surface-Emitting Lasers," *IEEE J. Quant. Electron.,* vol. 40, no. 1, pp. 25-30, JAN, 2004.

[Torre 2006] M. Torre, A. Valle and L. Pesquera, "Polarization and Transverse Mode Behaviour of VCSELs Under Optical Injection," *Opt. Quant. Electron.,* vol. 38, no. 4-6, pp. 445-465, MAR, 2006.

[Torre 2010] M. S. Torre, A. Valle and L. Pesquera, "Transverse Mode Selection in Vertical-Cavity Surface-Emitting Lasers with Optical Injected Signal," *IEEE J. Quant. Electron.,* vol. 46, no. 1, pp. 105-111, JAN, 2010.

[Troger 1999] J. Troger, L. Thevenaz, P. A. Nicati and P. A. Robert, "Theory and Experiment of a Single-Mode Diode Laser Subject to External Light Injection from several Lasers," *J. Lightwave Technol.,* vol. 17, no. 4, pp. 629-636, APR 1999.

[Vakhshoori 1993] D. Vakhshoori, J. Wynn, G. Zydzik, R. Leibenguth, M. Asom, K. Kojima and R. Morgan, "Top-Surface Emitting Lasers with 1.9 V Threshold Voltage and the Effect of Spatial Hole Burning on their Transverse-Mode Operation and Efficiencies," *Appl. Phys. Lett.,* vol. 62, no. 13, pp. 1448-1450, MAR 29, 1993.

[Valle 1995] A. Valle, J. Sarma and K. A. Shore, "Spatial Holeburning Effects on the Dynamics of Vertical-Cavity Surface-Emitting Laser-Diodes," *IEEE J. Quant. Electron.,* vol. 31, no. 8, pp. 1423-1431, AUG 1995.

[Valle 1996] A. Valle, K. Shore and L. Pesquera, "Polarization Selection in Birefringent Vertical-Cavity Surface Emitting Lasers," *J. Lightwave Technol.,* vol. 14, no. 9, pp. 2062-2068, SEP, 1996.

[Valle 1997] A. Valle, L. Pesquera and K. Shore, "Polarization Behavior of Birefringent Multitransverse Mode Vertical-Cavity Surface-Emitting Lasers," *IEEE Photonics Technology Letters,* vol. 9,

no. 5, pp. 557-559, MAY, 1997.

[Valle 1998a] A. Valle, "Selection and Modulation of High-Order Transverse Modes in Vertical-Cavity Surface-Emitting Lasers," *IEEE J. Quant. Electron.*, vol. 34, no. 10, pp. 1924-1932, OCT 1998.

[Valle 1998b] A. Valle, J. Martin-Regalado, L. Pesquera, S. Balle and M. San Miguel, "Polarization Dynamics of Birefringent Index-Guided Vertical Cavity Surface-Emitting Lasers," *Physics and Simulation of Optoelectronic Devices Vi, Pts 1 and 2,* vol. 3283, pp. 280-291, 1998.

[Valle 2001] A. Valle and L. Pesquera, "Relative Intensity Noise of Multitransverse-Mode Vertical-Cavity Surface-Emitting Lasers," *IEEE Photonics Technology Letters,* vol. 13, no. 4, pp. 272-274, APR 2001.

[Valle 2002] A. Valle and L. Pesquera, "Analytical Calculation of Transverse-Mode Characteristics in Vertical-Cavity Surface-Emitting Lasers," *Journal of the Optical Society of America B-Optical Physics,* vol. 19, no. 7, pp. 1549-1557, JUL 2002.

[Valle 2004] A. Valle and L. Pesquera, "Theoretical Calculation of Relative Intensity Noise of Multimode Vertical-Cavity Surface-Emitting Lasers," *IEEE J. Quant. Electron.,* vol. 40, no. 6, pp. 597-606, JUN 2004.

[Valle 2007] A. Valle, I. Gatare, K. Panajotov and M. Sciamanna, "Transverse Mode Switching and Locking in Vertical-Cavity Surface-Emitting Lasers Subject to Orthogonal Optical Injection," *IEEE J. Quant. Electron.*, vol. 43, no. 3-4, pp. 322-333, MAR-APR, 2007.

[Valle 2008] A. Valle, M. Gomez-Molina and L. Pesquera, "Polarization Bistability in 1550 Nm Wavelength Single-Mode Vertical-Cavity Surface-Emitting Lasers Subject to Orthogonal Optical Injection," *IEEE Journal of Selected Topics in Quantum Electronics,* vol. 14, no. 3, pp. 895-902, MAY-JUN, 2008.

[Vantartwijk 1995] G. Vantartwijk and D. Lenstra, "Semiconductor-Lasers with Optical-Injection and Feedback," *Quantum and Semiclassical Optics,* vol. 7, no. 2, pp. 87-143, APR, 1995.

[Vey 1999] J. L. Vey, C. Degen, K. Auen and W. Elsasser, "Quantum

Noise and Polarization Properties of Vertical-Cavity Surface-Emitting Lasers," *Physical Review A,* vol. 60, no. 4, pp. 3284-3295, OCT 1999.

[Wieczorek 2005] S. Wieczorek, B. Krauskopf, T. Simpson and D. Lenstra, "The Dynamical Complexity of Optically Injected Semiconductor Lasers," *Physics Reports-Review Section of Physics Letters,* vol. 416, no. 1-2, pp. 1-128, SEP, 2005.

[Wieczorek 2009] S. Wieczorek and W. W. Chow, "Bifurcations and Chaos in a Semiconductor Laser with Coherent Or Noisy Optical Injection," *Opt. Commun.,* vol. 282, no. 12, pp. 2367-2379, JUN 15 2009.

[Willemsen 1999] M. B. Willemsen, M. U. F. Khalid, M. P. van Exter and J. P. Woerdman, "Polarization Switching of a Vertical-Cavity Semiconductor Laser as a Kramers Hopping Problem," *Phys. Rev. Lett.,* vol. 82, no. 24, pp. 4815-4818, JUN 14 1999.

[Willner 2012] A. E. Willner, R. L. Byer, C. J. Chang-Hasnain, S. R. Forrest, H. Kressel, H. Kogelnik, G. J. Tearney, C. H. Townes and M. N. Zervas, "Optics and Photonics: Key Enabling Technologies," *Proceedings of the IEEE,* vol. 100, pp. 1604-1643, MAY 13th, 2012.

[Wipiejewski 1999] T. Wipiejewski, H. D. Wolf, L. Korte, W. Huber, G. Kristen, C. Hoyler, H. Hedrich, O. Kleinbub, M. Popp, J. Kaindl, A. Rieger, T. Albrecht, J. Mueller, A. Orth, Z. Spika, S. Lutgen, H. Pflaeging and J. Harrasser, "*Performance and Reliability of Oxide Confined VCSELs*". *1999 Proceedings. IEEE 49th Electronic components and Technology Conference*, pp. 741-746.

[Yu 2003] S. F. Yu, "*Analysis and Design of Vertical Cavity Surface Emitting Lasers*". New Jersey: Wiley-Interscience, 2003.

[Zakharov 2001] S. M. Zakharov, "The Thermal Cross-Interference Effects in the Arrays of Vertical-Cavity Surface-Emitting Lasers," *Semiconductors,* vol. 35, no. 4, 2001.

[Zei 2001] L. G. Zei, S. Ebers, J. R. Kropp and K. Petermann, "Noise Performance of Multimode VCSELs," *J. Lightwave Technol.,* vol. 19, no. 6, pp. 884-892, JUN 2001.

[Zhang 2004] H. Zhang, G. Mrozynski, A. Wallrabenstein and J. Schrage, "Analysis of Transverse Mode Competition of VCSELs Based on a Spatially Independent Model," *IEEE J. Quant. Electron.*, vol. 40, no. 1, pp. 18-24, JAN, 2004.

[Zhang 2009a] B. Zhang, X. Zhao, D. Parekh, Y. Yue, W. Hofmann, M. Amann, C. Chang-Hasnain and A. Willner, "Multifunctional and Reconfigurable 10-GHz Operation of an Optical Injection-Locked VCSEL". *Conference on Lasers and Electro-Optics/Quantum Electronics and Laser Science Conference, pp.1-2 (CLEO/QELS 2009)*

[Zhang 2009b] W. L. Zhang and S. F. Yu, "Optical Flip-Flop using Bistable Vertical-Cavity Semiconductor Optical Amplifiers with Anti-Resonant Reflecting Optical Waveguide," *J. Lightwave Technol.*, vol. 27, no. 21, pp. 4703-4710, NOV 1, 2009.